Jordan Journal of Mechanical and Industrial Engineering (JJMIE)

JJMIE is a high-quality scientific journal devoted to fields of Mechanical and Industrial Engineering. It is published by Hashemite University in cooperation with the Jordanian Scientific Research and Innovation Support Fund, Ministry of Higher Education and Scientific Research.

SUBMISSION ADDRESS:

Prof. Moh'd Sami Ashhab, Editor-in-Chief
Jordan Journal of Mechanical & Industrial Engineering,
Hashemite University,
PO Box 330127, Zarqa, 13133 , Jordan
E-mail: jjmie@hu.edu.jo

Hashemite Kingdom of Jordan

Hashemite University

Jordan Journal of Mechanical and Industrial Engineering

JJMIE

An International Peer-Reviewed Scientific Journal

Financed by Scientific Research Support Fund

http://jjmie.hu.edu.jo/

ISSN 1995-6665

Jordan Journal of Mechanical and Industrial Engineering (JJMIE)

JJMIE is a high-quality scientific journal devoted to fields of Mechanical and Industrial Engineering. It is published by Hashemite University in cooperation with the Jordanian Scientific Research and Innovation Support Fund, Ministry of Higher Education and Scientific Research.

Introduction: The Editorial Board is very committed to build the Journal as one of the leading international journals in mechanical and industrial engineering sciences in the next few years. With the support of the Ministry of Higher Education and Scientific Research and Jordanian Universities, it is expected that a heavy resource to be channeled into the Journal to establish its international reputation. The Journal's reputation will be enhanced from arrangements with several organizers of international conferences in publishing selected best papers of the conference proceedings.

Aims and Scope: *Jordan Journal of Mechanical and Industrial Engineering* (JJMIE) is a refereed international journal to be of interest and use to all those concerned with research in various fields of, or closely related to, mechanical and industrial engineering disciplines. *Jordan Journal of Mechanical and Industrial Engineering* aims to provide a highly readable and valuable addition to the literature which will serve as an indispensable reference tool for years to come. The coverage of the journal includes all new theoretical and experimental findings in the fields of mechanical and industrial engineering or any closely related fields (Materials, Manufacturing, Management, Design, Thermal, Fluid, Energy, Control, Mechatronics, and Biomedical). The journal also encourages the submission of critical review articles covering advances in recent research of such fields as well as technical notes.

Guide for Authors

Manuscript Submission:
High-quality submissions to this new journal are welcome now and manuscripts may be either submitted online or email.

Online: For online and email submission upload one copy of the full paper including graphics and all figures at the online, submission site, accessed via http://jjmie.hu.edu.jo. The manuscript must be written in MS Word Format. All correspondence including notification of the Editor's decision and requests for revision, takes place by e-mail and via the Author's homepage, removing the need for a hard-copy paper trail

Submission address and contact :

Prof. Moh'd Sami Ashhab
Editor-in-Chief
Jordan Journal of Mechanical & Industrial Engineering, Hashemite University
PO Box 330127, Zarqa, 13115, Jordan
E-mail: jjmie@hu.edu.jo

Types of contributions*:* Original research papers and Technical reports

Corresponding author: Clearly indicate who is responsible for correspondence at all stages of refereeing and publication, including post-publication. Ensure that telephone and fax numbers (with country and area code) are provided in addition to the e-mail address and the complete postal address. Full postal addresses must be given for all co-authors.

Original material: Submission of an article implies that the work described has not been published previously (except in the form of itstan abstract or as part of a published lecture or academic thesis), that it is not under consideration for publication elsewhere, tha publication is approved by all authors and that, if accepted, it will not be published elsewhere in the same form, in English or in any other language, without the written consent of the Publisher. Authors found to be deliberately contravening the submission guidelines on originality and exclusivity shall not be considered for future publication in this journal.

Withdrawing: If the author chooses to withdraw his article after it has been assessed, he shall reimburse JJMIE with the cost of reviewing the paper.

Manuscript Preparation:

General: Editors reserve the right to adjust style to certain standards of uniformity. Original manuscripts are discarded after .publication unless the Publisher is asked to return original material after use. Please use MS Word for the text of your manuscript

Structure: Follow this order when typing manuscripts: Title, Authors, Authors title, Affiliations, Abstract, Keywords, Introduction, Main text, Conclusions, Acknowledgements, Appendix, References, Figure Captions, Figures and then Tables. Please supply figures imported into the text AND also separately as original graphics files. Collate acknowledgements in a separate section at the end of the article and do not include them on the title page, as a footnote to the title or otherwise.

Text Layout: Use 1.5 line spacing and wide (3 cm) margins. Ensure that each new paragraph is clearly indicated. Present tables and figure legends on separate pages at the end of the manuscript. If possible, consult a recent issue of the journal to become familiar with layout and conventions. All footnotes (except for table and corresponding author footnotes) should be identified with superscript Arabic numbers. To conserve space, authors are requested to mark the less important parts of the paper (such as records of experimental results) for printing in smaller type. For long papers (more than 4000 words) sections which could be deleted without destroying either the sense or the continuity of the paper should be indicated as a guide for the editor. Nomenclature should conform to that most frequently used in the scientific field concerned. Number all pages consecutively; use 12 or 10 pt font size and standard fonts.

Corresponding author: Clearly indicate who is responsible for correspondence at all stages of refereeing and publication, including post-publication. The corresponding author should be identified with an asterisk and footnote. Ensure that telephone and fax numbers (with country and area code) are provided in addition to the e-mail address and the complete postal address. Full postal addresses must be given for all co-authors. Please consult a recent journal paper for style if possible.

Abstract: A self-contained abstract outlining in a single paragraph the aims, scope and conclusions of the paper must be supplied.

Keywords: Immediately after the abstract, provide a maximum of six keywords (avoid, for example, 'and', 'of'). Be sparing with abbreviations: only abbreviations firmly established in the field may be eligible.

Symbols: All Greek letters and unusual symbols should be identified by name in the margin, the first time they are used.

Units: Follow internationally accepted rules and conventions: use the international system of units (SI). If other quantities are mentioned, give their equivalent quantities in SI

Maths: Number consecutively any equations that have to be displayed separately from the text (if referred to explicitly in the text).

References: All publications cited in the text should be presented in a list of references following the text of the manuscript.

Text: Indicate references by number(s) in square brackets in line with the text. The actual authors can be referred to, but the reference number(s) must always be given.

List: Number the references (numbers in square brackets) in the list in the order in which they appear in the text.

Examples:

Reference to a journal publication:

[1] M.S. Mohsen, B.A. Akash, "Evaluation of domestic solar water heating system in Jordan using analytic hierarchy process". Energy Conversion & Management, Vol. 38 (1997) No. 9, 1815-1822.

Reference to a book:

[2] Strunk Jr W, White EB. The elements of style. 3rd ed. New York: Macmillan; 1979.

Reference to a conference proceeding:

[3] B. Akash, S. Odeh, S. Nijmeh, "Modeling of solar-assisted double-tube evaporator heat pump system under local climate conditions". 5th Jordanian International Mechanical Engineering Conference, Amman, Jordan, 2004.

Reference to a chapter in an edited book:

[4] Mettam GR, Adams LB. How to prepare an electronic version of your article. In: Jones BS, Smith RZ, editors. Introduction to the electronic age, New York: E-Publishing Inc; 1999, p. 281-304

Free Online Color : If, together with your accepted article, you submit usable color and black/white figures then the journal will ensure that these figures will appear in color on the journal website electronic version.

Tables: Tables should be numbered consecutively and given suitable captions and each table should begin on a new page. No vertical rules should be used. Tables should not unnecessarily duplicate results presented elsewhere in the manuscript (for example, in graphs). Footnotes to tables should be typed below the table and should be referred to by superscript lowercase letters.

Notification: Authors will be notified of the acceptance of their paper by the editor. The Publisher will also send a notification of receipt of the paper in production.

Copyright: All authors must sign the Transfer of Copyright agreement before the article can be published. This transfer agreement enables Jordan Journal of Mechanical and Industrial Engineering to protect the copyrighted material for the authors, but does not relinquish the authors' proprietary rights. The copyright transfer covers the exclusive rights to reproduce and distribute the article, including reprints, photographic reproductions, microfilm or any other reproductions of similar nature and translations.

Proof Reading: One set of page proofs in MS Word format will be sent by e-mail to the corresponding author, to be checked for typesetting/editing. The corrections should be returned within **48 hours**. No changes in, or additions to, the accepted (and subsequently edited) manuscript will be allowed at this stage. Proofreading is solely the author's responsibility. Any queries should be answered in full. Please correct factual errors only, or errors introduced by typesetting. Please note that once your paper has been proofed we publish the identical paper online as in print.

Author Benefits:

No page charges: Publication in this journal is free of charge.

Free offprints: One journal issues of which the article appears will be supplied free of charge to the corresponding author and additional offprint for each co-author. Corresponding authors will be given the choice to buy extra offprints before printing of the article.

JJMIE

Volume 12, Number 4, December. 2018
ISSN 1995-6665
Pages 245 - 251

Jordan Journal of Mechanical and Industrial Engineering

Availability Analysis of an Industrial System using Supplementary Variable Technique

Munish Mehta[a*], Jujhar Singh[b], Shubham Sharma[b,c]

[a]*School of Mechanical Engineering, Lovely Professional University, Phagwara, 144411, India*
[b]*Deptt. of Mechanical Engineering, I. K. Gujral Punjab Technical University, Kapurthala, 144603, India*
[c] *Deptt. of Mechanical Engineering, CSIR-Central Leather Research Institute, RCED, Leather Complex, Jalandhar, 144021, India*

Received 25 October. 2017

Abstract

The objective of this research is to develop a mathematical model for analyzing the availability of a butteroil production system. The industrial system consists of four subsystems; viz heater, clarifier, filling and granulation. From the state transition diagram of the system, using mnemonic rule and under the assumption of constant failure rates and variable repair rates, Chapman-Kolmogorov differential equations have been derived by applying supplementary variable techniques. These equations have been solved by Lagrange's method and availability of the system has been computed for various choices of failure and repair rates using Runge-Kutta fourth order method. Mean time between failure has been calculated numerically. Finally, criticality analysis has been done to get some ideas of the maintenance priority and assist the plant management in deciding maintenance priorities for optimum utilization of the resources.

Keywords: Availability; Supplementary Variable Technique; Lagrange's method; Runge-Kutta; MTBF;

NOMENCLATURE

H, C, F	Respective subsystems are working at full capacity
h, c, f	Respective subsystems are in failed state
C_s, F_s	One respective subsystem has failed
$P_0(t)$	Probability that at time't', all the units are working
$P_i(x,t)$	Probability that at time't', the system is in state i and having an elapsed repair time x
Δt	Time increment
$\frac{\partial}{\partial t}$	Derivative w.r.t. 't'

Greek Symbols

α_i $(i = 1\ to\ 3)$	Failure rates of subsystems H,C and F
β_i $(i = 1\ to\ 3)$	Repair rates of subsystems H,C and F

1. Introduction

It is important for an industrial system to run failure free for long duration of time without many interruptions. Availability of the system can be increased either by providing enough redundant parts or by increasing the reliability of its components. Although redundancy can be considered a best option but being very expensive, it is not always desirable. On the other hand, continuous monitoring of parts, provision of enough repair facilities and prompt response to any breakdown seems to be a better option. The purpose is to bring the failed system back to work in the shortest possible time. Study of butteroil production system in this paper has been undertaken under these considerations.

Reliability of various systems has been analyzed by various researchers using different techniques. [1] analyzed the availability of steam generation system of a thermal power plant taking constant failure and repair rates and derived expressions for steady state availability and Mean Time Between Failure (MTBF). [2] presented Markov models to derive the transient reliability and MTBF for repairable K-out-of-N: G systems subject to two failure modes. [3] developed a procedure based on graph theory and matrix approach for the reliability evaluation and selection of a rolling element bearing. [4] developed a multi-modal adaptive importance sampling method for reliability analysis of a vehicle body–door subsystem with respect to wind noise. [5] proposed an expression and an algorithm for computing reliability of K-out-of-N system. [6] studied the steady-state availability and the mean up-time of a series–parallel repairable system under the assumption of constant failure rate and arbitrary repair time, by using Supplementary Variable Technique (SVT) and vector Markov process theory. [7] introduced a fourth-order, implicit, low-dispersion, and low-dissipation Runge-Kutta scheme. [8] investigated the reliability analysis of a multi-state manufacturing system with different performance levels. [9] constructed a fifth-order explicit

* Corresponding author e-mail: munishmehta1@rediffmail.com.

exponential Runge-Kutta method and proved its convergence for semi linear parabolic problems.

[10] presented a type of mixed Runge-Kutta methods by combining the underlying Runge-Kutta methods and the compound quadrature rules. [11] used Universal Generating Function (UGF) technique for reliability analysis of lithium-ion battery pack. [12] proposed a reliability analysis method of a multi-state system based on fuzzy Bayesian networks. [13] obtained some reliability measures of two cold standby units of a computer system using a semi-Markov process and a regenerative point technique. [14] worked on k-out-of-n standby subsystems with exponentially distributed component lifetimes and analyzed system reliability, mean time to failure, and steady-state availability as a function of the component failure rates. [15] developed performance model based on Markov birth-death process and calculated reliability, availability, maintainability, dependability, MTBF, Mean Time to Repair (MTTR) and dependability ratio for each subsystem of skim milk powder production system. [16] analyzed the availability of an engineering system by incorporating waiting time to repair and using supplementary variable technique, Laplace transformation and Gumbel-Hougaard family of copula. [17] extended the matrix-based system reliability method to k out of N systems by modifying the formulations of event and probability vectors. [18] proposed a reliability, availability and maintainability (RAM) model to quantify the values of RAM indices and to identify the most critical equipment which mainly affects the system performance. [19] adopted six sigma and Gauss-Legendre quadrature formula to propose a generalized dynamic reliability model for calculating system reliability under complex load.

With a view to maximize availability and hence production; in this paper; reliability of the butteroil production system has been evaluated by considering constant failure rate and variable repair rate. System of differential equations has been developed using SVT and availability has been calculated using Runge-Kutta fourth order method. MTBF has been calculated using Simpson's 3/8 rule. In the conclusion part, criticality analysis of all the subsystems has been done to decide the maintenance priority of different subsystems.

The rest of this paper is organized as follows: Section 2 consists of brief description of the system and assumptions made in the analysis. Differential equations have been derived and solved in Section 3. In Section 4, transient state availability of the system has been computed by Runge-Kutta fourth order method using different combinations of failure and repair rates. MTBF has also been calculated in each case. Finally, conclusions have been drawn in Section 5.

2. Butteroil production system

Butteroil or ghee refers to the clarified butter fat obtained mainly from butter by means of removing all the water and SNF (solids-not-fat) contents. It is the richest source of milk fat and is prepared either by butter or cream. Butteroil production system consists of four subsystems i.e. heater, clarifier, filling and granulation. Out of these, except granulation subsystem, all the units are subject to random failures. Figure 1 gives us the flow chart of butteroil making process.

2.1. System description

2.1.1. Heater subsystem (H): It consists of a kettle in which temperature of butter is raised slowly with the help of steam. The final temperature is monitored to be not more than 107-109°C till its color is reddish brown. Ghee along with the residue can settle down for 25-30 minutes in the kettle before filtration. It consists of two units in series. Hence, if one unit fails, system fails.

2.1.2. Clarifier subsystem (C): Clarification is carried out at around 70°C in order to clarify all the residue particles from ghee. It consists of two units in parallel. Partial failure of this system reduces the capacity of the system. Major failure occurs only when both units fail.

2.1.3. Filling subsystem (F): In this section, ghee tins are filled, weighed and sealed simultaneously. The filling temperature is strictly watched to remain between 40-45°C. There are two filling units. Failure of any one unit reduces the working capacity while system completely fails when both units break down.

2.1.4. Granulation subsystem (G): This subsystem consists of a refrigerating unit where temperature is maintained between 15-20°C. This section rarely fails and hence has not been considered for analysis.

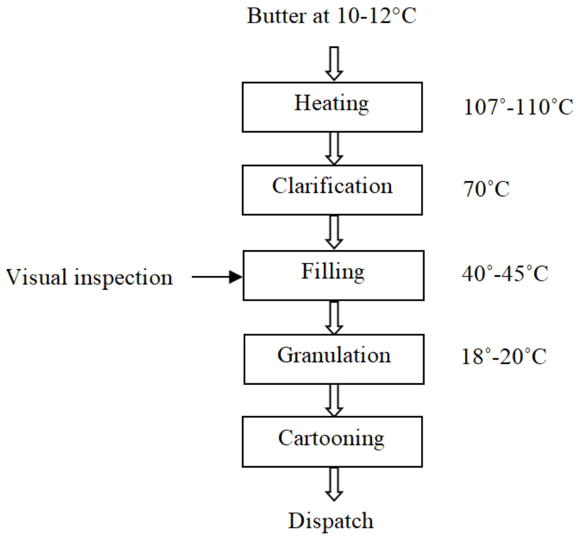

Figure 1. Schematic diagram of butteroil production system

2.2. Assumptions

Following assumptions have been made in the current analysis:

1. Failure and repair rates are constant and independent of each other and their unit is taken as per day.
2. In case of assessment of availability using SVT, repair rates are considered variable and failure rates as constant.
3. After repair, old unit is as good as new.
4. Enough repair/ maintenance facilities are available.
5. There are no simultaneous failures.
6. System may work at reduced capacity.

3. Mathematical Formulation of the System

To determine the reliability of the butteroil production system, Chapman-Kolmogorov differential equations have been developed by applying supplementary variable technique. A supplementary variable 'x' is added to change the non-Markovian event into Markovian event. Probability considerations, using mnemonic rule, give us the following set of differential equations associated with the transition diagram (Fig. 2) of the system at time (t+Δt):

$$P_0(t+\Delta t) = [1-\alpha_1\Delta t-\alpha_2\Delta t-\alpha_3\Delta t]P_0(t) + \int \beta_1(x)P_6(x,t)dx\Delta t + \int \beta_2(x)P_2(x,t)dx\Delta t + \int \beta_3(x)P_1(x,t)dx\Delta t$$

$$P_0(t+\Delta t) - P_0(t) = -[\alpha_1\Delta t+\alpha_2\Delta t+\alpha_3\Delta t]P_0(t) + \int \beta_1(x)P_6(x,t)dx\Delta t + \int \beta_2(x)P_2(x,t)dx\Delta t + \int \beta_3(x)P_1(x,t)dx\Delta t$$

Dividing both sides by Δt, we get

$$\frac{P_0(t+\Delta t)-P_0(t)}{\Delta t} = -[\alpha_1+\alpha_2+\alpha_3]P_0(t) + \int \beta_1(x)P_6(x,t)dx + \int \beta_2(x)P_2(x,t)dx + \int \beta_3(x)P_1(x,t)dx$$

$$\left[\frac{\partial}{\partial t} + L_0\right] P_0(t) = M_0(t) \quad (1)$$

$$\left[\frac{\partial}{\partial t} + \frac{\partial}{\partial x} + L_1(x)\right] P_1(x,t) = M_1(x,t) \quad (2)$$

$$\left[\frac{\partial}{\partial t} + \frac{\partial}{\partial x} + L_2(x)\right] P_2(x,t) = M_2(x,t) \quad (3)$$

$$\left[\frac{\partial}{\partial t} + \frac{\partial}{\partial x} + L_3(x)\right] P_3(x,t) = M_3(x,t) \quad (4)$$

$$\left[\frac{\partial}{\partial t} + \frac{\partial}{\partial x} + \beta_1(x)\right] P_j(x,t) = 0; \quad j = 4,6,7,11 \quad (5)$$

$$\left[\frac{\partial}{\partial t} + \frac{\partial}{\partial x} + \beta_2(x)\right] P_k(x,t) = 0; \quad k = 5,8 \quad (6)$$

$$\left[\frac{\partial}{\partial t} + \frac{\partial}{\partial x} + \beta_3(x)\right] P_l(x,t) = 0; \quad l = 9,10 \quad (7)$$

Where,

$L_0 = \sum_{i=1}^{3} \alpha_i$

$L_1(x) = \sum_{i=1}^{3} \alpha_i + \beta_3(x)$

$L_2(x) = \sum_{i=1}^{3} \alpha_i + \beta_2(x)$

$L_3(x) = \sum_{i=1}^{3} \alpha_i + \beta_2(x) + \beta_3(x)$

$M_0(t) = \int P_1(x,t)\beta_3(x)dx + \int P_2(x,t)\beta_2(x)dx + \int P_6(x,t)\beta_1(x)dx$

$M_1(x,t) = \alpha_3 P_0(t) + \int P_3(x,t)\beta_2(x)dx + \int P_{10}(x,t)\beta_3(x)dx + \int P_{11}(x,t)\beta_1(x)dx$

$M_2(x,t) = \alpha_2 P_0(t) + \int P_3(x,t)\beta_3(x)dx + \int P_4(x,t)\beta_1(x)dx + \int P_5(x,t)\beta_2(x)dx$

$M_3(x,t) = \alpha_2 P_1(t) + \alpha_3 P_2(t) + \int P_7(x,t)\beta_1(x)dx + \int P_8(x,t)\beta_2(x)dx + \int P_9(x,t)\beta_3(x)dx$

Initial Conditions

$P_0(0) = 1$

$P_i(x,0) = 0 \qquad (i = 1,2,3 \ldots\ldots\ldots\ldots..11)$

Boundary Conditions

$P_1(0,t) = \alpha_3 P_0(t)$

$P_2(0,t) = \alpha_2 P_0(t)$

$P_3(0,t) = \int \alpha_2 P_1(x,t)dx + \int \alpha_3 P_2(x,t)dx$

$P_4(0,t) = \int \alpha_1 P_2(x,t)dx$

$P_5(0,t) = \int \alpha_2 P_2(x,t)dx$

$P_6(0,t) = \alpha_1 P_0(t)$

$P_7(0,t) = \int \alpha_1 P_3(x,t)dx$

$P_8(0,t) = \int \alpha_2 P_3(x,t)dx$

$P_9(0,t) = \int \alpha_3 P_3(x,t)dx$

$P_{10}(0,t) = \int \alpha_3 P_1(x,t)dx$

$P_{11}(0,t) = \int \alpha_1 P_1(x,t)dx$

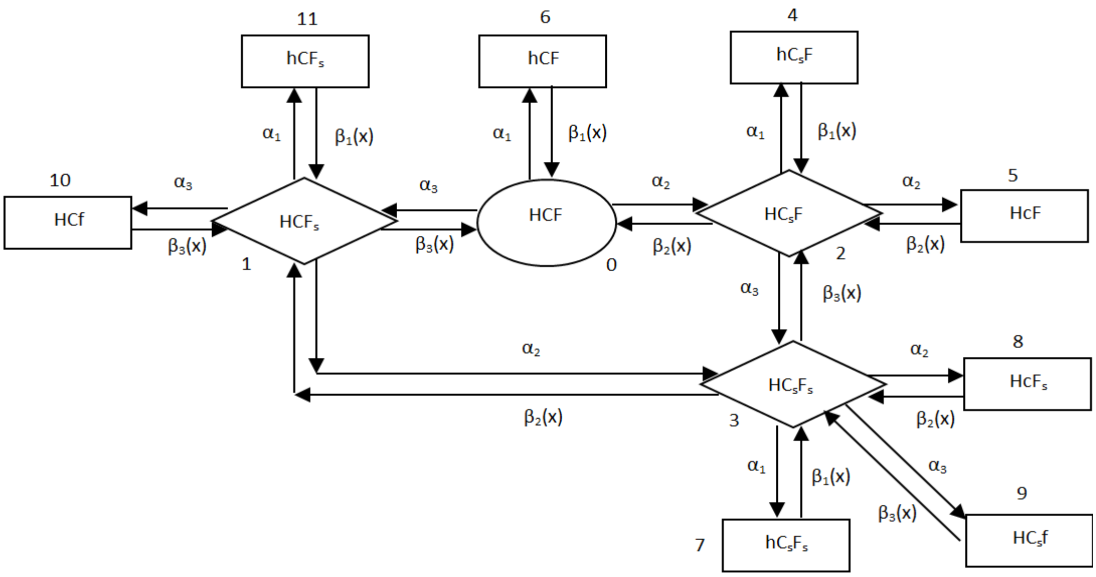

Figure 2. Transition diagram of butteroil production system

Set of differential equations from (1) to (7) along with initial conditions and boundary conditions is called Chapman-Kolmogorov differential difference equations Equation (1) is a linear differential equation of first order and eqs. (2) to (7) are linear partial differential equations of first order (Lagrange's type). All these equations have been solved using Lagrange's method. The probabilities of each state and expression of availability has been derived as follows:

$P_0(t) = e^{-L_0 t}[1 + \int M_0(t)e^{L_0 t}\, dt]$

$P_1(x,t) = e^{-L_1(x)dx}[\int M_1(x,t)e^{\int L_1(x)dx}\, dx + \alpha_3 P_0(t-x)]$

$P_2(x,t) = e^{-L_2(x)dx}[\int M_2(x,t)e^{\int L_2(x)dx}\, dx + \alpha_2 P_0(t-x)]$

$P_3(x,t) = e^{-L_3(x)dx}[\int M_3(x,t)e^{\int L_3(x)dx}\, dx + \alpha_3 P_0(t-x)]$

$P_4(x,t) = e^{-\int \beta_1(x)dx} \int \alpha_1 P_2(x,t-x)dx$

$P_5(x,t) = e^{-\int \beta_2(x)dx} \int \alpha_2 P_2(x,t-x)dx$

$P_6(x,t) = e^{-\int \beta_1(x)dx} \alpha_1 P_0(t-x)$

$P_7(x,t) = e^{-\int \beta_1(x)dx} \int \alpha_1 P_3(x,t-x)dx$

$P_8(x,t) = e^{-\int \beta_2(x)dx} \int \alpha_2 P_3(x,t-x)dx$

$P_9(x,t) = e^{-\int \beta_3(x)dx} \int \alpha_3 P_3(x,t-x)dx$

$P_{10}(x,t) = e^{-\int \beta_3(x)dx} \int \alpha_3 P_1(x,t-x)dx$

$P_{11}(x,t) = e^{-\int \beta_1(x)dx} \int \alpha_1 P_1(x,t-x)dx$

Finally, the expression of time dependent availability A(t) is obtained by summation of probabilities of all the working states and reduced capacity states, i.e.

$$A(t) = P_0(t) + \int \textstyle\sum_{i=1}^{3} P_i(x,t)dx \tag{8}$$

Availability expression of the butteroil production system as given by equation (8) can be solved using constant failure rates and variable repair rates collected from the concerned plant.

3.1. Performance modeling of the system

As we have seen in the previous case, it is difficult to solve the problem analytically if either failure or repair rates are varied. Hence, in order to simplify the problem, failure and repair rates are considered constant. In this case, the system of equations (1) to (7) can be represented as follows:

$$P_0(t)\left[\frac{\partial}{\partial t} + \textstyle\sum_{i=1}^{3} \alpha_i\right] = P_6(t)\beta_1 + P_2(t)\beta_2 + P_1(t)\beta_3 \tag{9}$$

$$P_1(t)\left[\frac{\partial}{\partial t} + \textstyle\sum_{i=1}^{3} \alpha_i + \beta_3\right] = P_{11}(t)\beta_1 + P_3(t)\beta_2 + P_{10}(t)\beta_3 + P_0(t)\alpha_3 \tag{10}$$

$$P_2(t)\left[\frac{\partial}{\partial t} + \textstyle\sum_{i=1}^{3} \alpha_i + \beta_2\right] = P_4(t)\beta_1 + P_5(t)\beta_2 + P_3(t)\beta_3 + P_0(t)\alpha_2 \tag{11}$$

$$P_3(t)\left[\frac{\partial}{\partial t} + \textstyle\sum_{i=1}^{3} \alpha_i + \beta_2 + \beta_3\right] = P_7(t)\beta_1 + P_8(t)\beta_2 + P_9(t)\beta_3 + P_1(t)\alpha_2 + P_2(t)\alpha_3 \tag{12}$$

$$P_i(t)\left[\frac{\partial}{\partial t} + \beta_1\right] = P_j(t)\alpha_1 \tag{13}$$

$$P_i(t)\left[\frac{\partial}{\partial t} + \beta_2\right] = P_j(t)\alpha_2 \tag{14}$$

$for\ i = 5, j = 2; i = 8, j = 3$

$$P_i(t)\left[\frac{\partial}{\partial t} + \beta_3\right] = P_j(t)\alpha_3 \tag{15}$$

$for\ i = 9, j = 3; i = 10, j = 1$

Initial Conditions

$P_i(t) = 1 \quad for\ i = 0$

$\quad = 0 \quad for\ i \neq 0$

To examine the effect of failure and repair rates on the availability in transient state, the system of differential equations (9) to (15) with initial conditions has been solved numerically using Runge-Kutta fourth order method. Analysis has been done for a period of 360 days divided over an interval of 30 days and the data has been tabulated in tables 1-6. These tables present the effect of failure and repair rates of various subsystems on the reliability of the system. MTBF, which has been computed using Simpson's 3/8 rule, with corresponding failure/repair rates, has been given in the last row of each table.

4. Results and Analysis

4.1. Effect of failure rate of heater (α_1) on system availability

By varying failure rate α_1 from 0.005 to 0.025 and keeping α_2 = 0.01, α_3 = 0.002857, β_1 = 0.10, β_2 = 0.05 and β_3 = 0.04, the availability of the system has been computed and compiled in Table 1, which shows that there is a decrease in availability up to 14.55 percent. Also, availability decreases by up to 1.98 percent as number of days increase from 30 to 360. MTBF shows a decline of around 50 days with the increase in failure rate from 0.005 to 0.025.

Table 1. Effect of failure rate of heater (α_1) on availability

Time ↓ (days) / α_1 →	0.005	0.01	0.015	0.02	0.025
30	0.9388	0.8980	0.8604	0.8255	0.7933
60	0.9258	0.8850	0.8476	0.8132	0.7815
90	0.9214	0.8809	0.8439	0.8098	0.7784
120	0.9199	0.8795	0.8425	0.8085	0.7771
150	0.9193	0.8790	0.8420	0.8080	0.7767
180	0.9191	0.8788	0.8418	0.8078	0.7765
210	0.9191	0.8787	0.8417	0.8077	0.7764
240	0.9191	0.8787	0.8417	0.8077	0.7764
270	0.9190	0.8787	0.8417	0.8077	0.7763
300	0.9190	0.8787	0.8417	0.8077	0.7763
330	0.9190	0.8787	0.8417	0.8077	0.7763
360	0.9190	0.8787	0.8417	0.8077	0.7763
MTBF	332.75	318.65	305.71	293.81	282.83

4.2. Effect of failure rate of clarifier (α_2) on system availability

As presented in Table 2, if failure rate α_2 increases from 0.01 to 0.033 and the values of α_1, α_3, β_1, β_2 and β_3 are kept at 0.005, 0.002857, 0.10, 0.05 and 0.04 respectively, availability goes down by 16 percent. However, availability decreases by up to 8.13 percent as time increases from 30 to 360 days. It is seen that MTBF also decreases by approximately 53 days as failure rate increases.

Table 2. Effect of failure rate of clarifier (α_2) on availability

Time (days) ↓ / α_2 →	0.01	0.01575	0.0215	0.02725	0.033
30	0.9388	0.9206	0.8972	0.8702	0.8405
60	0.9258	0.8970	0.8618	0.8232	0.7831
90	0.9214	0.8889	0.8502	0.8086	0.7663
120	0.9199	0.8862	0.8464	0.8040	0.7613
150	0.9193	0.8853	0.8452	0.8026	0.7599
180	0.9191	0.8850	0.8448	0.8021	0.7594
210	0.9191	0.8848	0.8446	0.8020	0.7593
240	0.9191	0.8848	0.8446	0.8019	0.7592
270	0.9190	0.8848	0.8446	0.8019	0.7592
300	0.9190	0.8848	0.8446	0.8019	0.7592
330	0.9190	0.8848	0.8446	0.8019	0.7592
360	0.9190	0.8848	0.8446	0.8019	0.7592
MTBF	332.75	321.60	308.37	294.19	279.83

4.3. Effect of failure rate of filling subsystem (α_3) on system availability

Next, the effect of failure rate of filling subsystem on the overall system availability has been analyzed. The results shown in Table 3 indicate that by varying failure rate α_3 = 0.002857, 0.004643, 0.006428, 0.008214 and 0.01 and taking α_1 = 0.005, α_2 = 0.01, β_1 = 0.10, β_2 = 0.05 and β_3 = 0.04, the availability decreases by 3.67 percent. It is also observed that this decrease is 4.15 percent with the increase in time from 30 to 360 days. In this case, MTBF decreases by 11 days with the increase in failure rate.

Table 3. Effect of failure rate of filling subsystem (α_3) on availability

Time (days) ↓ / α_3 →	0.002857	0.004643	0.006428	0.008214	0.01
30	0.9388	0.9365	0.9331	0.9289	0.9239
60	0.9258	0.9214	0.9153	0.9077	0.8988
90	0.9214	0.9160	0.9086	0.8995	0.8888
120	0.9199	0.9141	0.9061	0.8963	0.8849
150	0.9193	0.9133	0.9051	0.8950	0.8834
180	0.9191	0.9131	0.9047	0.8945	0.8828
210	0.9191	0.9130	0.9046	0.8943	0.8825
240	0.9191	0.9129	0.9045	0.8943	0.8824
270	0.9190	0.9129	0.9045	0.8942	0.8824
300	0.9190	0.9129	0.9045	0.8942	0.8824
330	0.9190	0.9129	0.9045	0.8942	0.8824
360	0.9190	0.9129	0.9045	0.8942	0.8824
MTBF	332.75	330.84	328.20	324.96	321.44

4.4. Effect of repair rate of heater (β_1) on system availability

The results presented in Table 4 indicate the availability of the system when repair rate β_1 of the heater subsystem is varied from 0.10 to 0.40. Taking values of α_1 = 0.005, α_2 = 0.01, α_3 = 0.002857, β_2 = 0.05 and β_3 = 0.04, it is observed that availability improves up to 3.32 percent. Whereas, there is a decrease of 1.94-1.98 percent in availability as number of days increase from 30 to 360. MTBF increases by around 11 days with the increase in repair rate.

Table 4. Effect of repair rate of heater (β_1) on availability

Time (days) ↓ / β_1 →	0.10	0.175	0.25	0.325	0.40
30	0.9388	0.9563	0.9641	0.9685	0.9712
60	0.9258	0.9445	0.9522	0.9564	0.9590
90	0.9214	0.9399	0.9476	0.9517	0.9543
120	0.9199	0.9384	0.9460	0.9501	0.9527
150	0.9193	0.9378	0.9454	0.9495	0.9521
180	0.9191	0.9376	0.9452	0.9493	0.9519
210	0.9191	0.9375	0.9451	0.9493	0.9519
240	0.9191	0.9375	0.9451	0.9492	0.9519
270	0.9190	0.9375	0.9451	0.9492	0.9518
300	0.9190	0.9375	0.9451	0.9492	0.9518
330	0.9190	0.9375	0.9451	0.9492	0.9518
360	0.9190	0.9375	0.9451	0.9492	0.9518
MTBF	332.75	339.17	341.83	343.28	344.19

4.5. Effect of repair rate of clarifier (β_2) on system availability

Table 5 presents the effect of repair rate of clarifier (β_2) on the system availability. As β_2 is varied from 0.05 to 0.20 in five steps and the values of failure and repair rates of other subsystems i.e. α_1, α_2, α_3, β_1 and β_3 are taken as 0.005, 0.01, 0.002857, 0.10 and 0.04 respectively, it is observed that availability of the system decreases by 0.49-1.98 percent with the increase in time from 30 to 360 days. But, it increases by 2.69 percent as repair rate increases from 0.05 to 0.20. In this case, MTBF increases by around 9 days.

Table 5. Effect of repair rate of clarifier (β_2) on availability

Time (days) ↓ / β_2 →	0.05	0.0875	0.125	0.1625	0.20
30	0.9388	0.9450	0.9481	0.9498	0.9508
60	0.9258	0.9394	0.9442	0.9463	0.9473
90	0.9214	0.9383	0.9433	0.9454	0.9465
120	0.9199	0.9379	0.9430	0.9451	0.9462
150	0.9193	0.9378	0.9429	0.9450	0.9460
180	0.9191	0.9377	0.9428	0.9449	0.9460
210	0.9191	0.9377	0.9428	0.9449	0.9460
240	0.9191	0.9377	0.9428	0.9449	0.9460
270	0.9190	0.9377	0.9428	0.9449	0.9459
300	0.9190	0.9377	0.9428	0.9449	0.9459
330	0.9190	0.9377	0.9428	0.9449	0.9459
360	0.9190	0.9377	0.9428	0.9449	0.9459
MTBF	332.75	338.60	340.30	341.02	341.38

4.6. Effect of repair rate of filling subsystem (β_3) on system availability

Table 6 shows the effect of improvement of repair rate of filling subsystem (β_3) on the system availability. It is observed that as β_3 increases from 0.04 to 0.16 and the value of failure and repair rates of other subsystems are kept at $\alpha_1 = 0.005$, $\alpha_2 = 0.01$, $\alpha_3 = 0.002857$, $\beta_1 = 0.10$ and $\beta_2 = 0.05$, availability increases by 0.38 percent. But as the number of days increase from 30 to 360, there is a decrease in availability of around 1.72-1.98 percent. MTBF increases by just 1 day with the increase in repair rate.

Table 6. Effect of repair rate of filling subsystem (β_3) on availability

Time (days) ↓ / β_3 →	0.04	0.07	0.10	0.13	0.16
30	0.9388	0.9394	0.9397	0.9399	0.9400
60	0.9258	0.9274	0.9280	0.9283	0.9284
90	0.9214	0.9236	0.9243	0.9246	0.9247
120	0.9199	0.9224	0.9230	0.9233	0.9234
150	0.9193	0.9219	0.9226	0.9229	0.9230
180	0.9191	0.9218	0.9225	0.9227	0.9229
210	0.9191	0.9217	0.9224	0.9227	0.9228
240	0.9191	0.9217	0.9224	0.9227	0.9228
270	0.9190	0.9217	0.9224	0.9227	0.9228
300	0.9190	0.9217	0.9224	0.9227	0.9228
330	0.9190	0.9217	0.9224	0.9227	0.9228
360	0.9190	0.9217	0.9224	0.9227	0.9228
MTBF	332.75	333.56	333.78	333.888	333.92

5. Conclusion

Tables 1-6 depict the effects of varying failure and repair rates of different subsystems on the availability of butteroil production system. On careful examination of these Tables, it reveals that failure rate of clarifier subsystem and repair rate of heater subsystems make maximum impact on availability of the system. This has also been demonstrated in Figures 3 and 4. However, in comparison to clarifier and heater subsystems, variation in failure/repair rate of filling subsystem makes lesser impact on system availability. Hence, we conclude that:

1. Utmost importance must be given to failure rate of Clarifier subsystem in order to improve system availability, since it decreases the system availability by 16 percent (more than any other subsystem)
2. Improvement in repair rate of Heater subsystem improves the system availability by 3.32 percent (more than any other subsystem). Hence, this subsystem should be repaired as soon as possible.
3. Based on failure rates, maintenance priority must be as per the following order:
   3.1. Clarifier subsystem
   3.2. Heater subsystem
   3.3. Filling subsystem
4. Similarly, based on repair rates, maintenance priority must be as per the following order:
   4.1. Heater subsystem
   4.2. Clarifier subsystem
   4.3. Filling subsystem

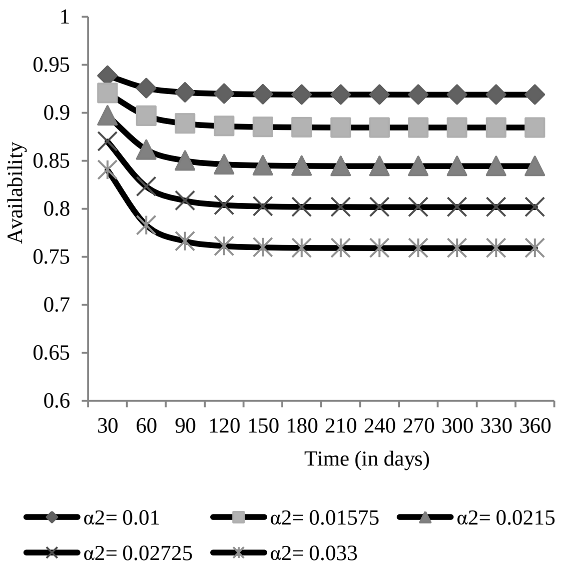

Figure 3. Effect of failure rate of Clarifier on system availability

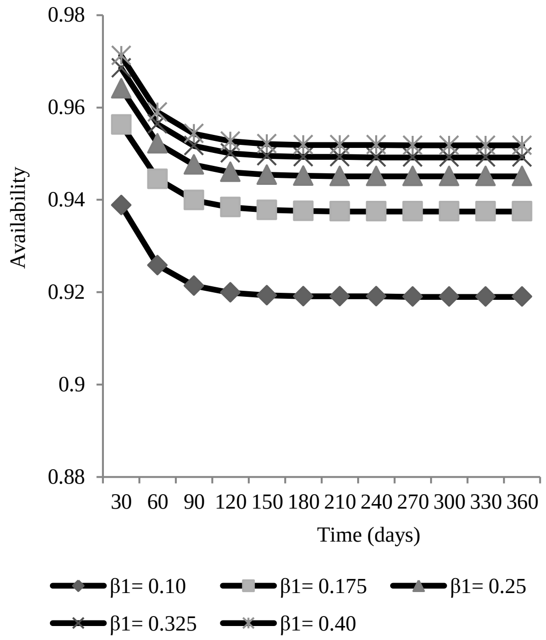

Figure 4. Effect of repair rate of heater on system availability

References

[1] P. Gupta, A. K. Lal, R. K. Sharma and J. Singh, "Analysis of reliability and availability of serial processes of plastic-pipe manufacturing plant: A case study". International Journal of Quality and Reliability Management. Vol. 24, No. 4 (2007), 404- 419.

[2] S. Garg, J. Singh and D. V. Singh, "Availability analysis of crank-case manufacturing in a two-wheeler automobile industry", Applied Mathematical Modelling. Vol. 34 (2010), 1672-1683.

[3] S. Garg, J. Singh and D. V. Singh, "Mathematical modelling and performance analysis of combed yarn production system: based on few data", Applied Mathematical Modelling. Vol. 34, No. 11 (2010), 3300-3308.

[4] P. Gupta and A. Goyal, "Availability assessment of a multi-state repairable bubble gum production system", IEEE

International Conference on Industrial Engineering and Engineering Management, Macao, 2010, 631-635.

[5] S. Shakuntla, A. K. Lal, S. S. Bhatia and J. Singh, "Reliability analysis of polytube industry using supplementary variable technique", Applied Mathematics and Computation. Vol. 218, No. 8 (2011), 3981-3992.

[6] W. Wu, Y. Tang M. Yu and Y. Jiang, "Reliability analysis of a *k*-out-of-*n*:*G* repairable system with single vacation", Applied Mathematical Modelling. Vol. 38, No. 24 (2014), 6075-6097.

[7] F. Zheng, S. Xu and X. Li, "Numerical solution of the steady-state probability and reliability of a repairable system with three unites", Applied Mathematics and Computation. Vol. 263 (2015), 251-267.

[8] B. Cekyay and S. Ozekici, "Reliability, MTTF and steady-state availability analysis of systems with exponential lifetimes", Applied Mathematical Modelling. Vol. 39, No. 1 (2015), 284-296.

[9] L. Li, H. Yan and X. Wu, "Numerical analysis on the reliability of space tracking, telemetering and command system based on the sparse matrix storage schemes", International Conference on Quality, Reliability, Risk, Maintenance, and Safety Engineering, Chengdu, 2012, 240-244.

[10] V. T Luan and A. Ostermann, "Explicit exponential Runge-Kutta methods of high order for parabolic problems", Journal of Computational Applied Mathematics. Vol. 256 (2014), 168-179.

[11] C. Zhang and T. Qin, "The mixed Runge-Kutta methods for a class of nonlinear functional-integro-differential equations", Journal of Applied Mathematics and Computation. Vol. 237 (2014), 396-404.

[12] R. Zhang, W. Yang and X. Wang, "The reliability analysis of horizontal vibration of elevator based on multi-state fuzzy Bayesian network", Jordan Journal of Mechanical and Industrial Engineering. Vol. 8, No. 1 (2014), 43-49.

[13] Kumar and S. C. Malik, "Reliability modelling of a computer system with priority to H/W repair over replacement of H/W and up-gradation of S/W subject to MOT and MRT", Jordan Journal of Mechanical and Industrial Engineering. Vol. 8, No. 4 (2014), 233-241.

[14] S. Nugraha, "The selection of time step in Runge-Kutta fourth order for determine deviation in the weapon arm vehicle", Energy Procedia. Vol. 68 (2015), 363-369.

[15] Amann and K. Kadau, "Numerically efficient modified Runge-Kutta solver for fatigue crack growth analysis", Engineering Fracture Mechanics. Vol. 161 (2016), 55-62.

[16] K. Hussain, F. Ismail and N. Senu, "Solving directly special fourth-order ordinary differential equations using Runge-Kutta type method", Journal of Computational and Applied Mathematics. Vol. 306 (2016), 179–199.

[17] J. Byun, H. Noh and J. Song, "Reliability growth analysis of K out of N systems using matrix-based system reliability method", Reliability Engineering and system safety, Vol. 165 (2017), 410-421.

[18] M. F. Aly, I. H. Afefy, R. K. Abdel-Magied and E. K. A. Elhalim, "A comprehensive model of reliability, availability and maintainability (RAM) for industrial systems evaluations", Jordan Journal of Mechanical and Industrial Engineering. Vol. 12, No. 1 (2018), 59-67.

[19] X. Zhang, H. Gao. H. Huang, Y. Li and J. Mi, "Dynamic reliability modeling for system analysis under complex load", Reliability Engineering and system safety, Vol. 180 (2018), 345-351.

JJMIE

Volume 12, Number 4, December. 2018
ISSN 1995-6665
Pages 253 - 260

Jordan Journal of Mechanical and Industrial Engineering

Earth’s Magnetic Field Measurements Data Accuracy Evaluation on Board of the Small Spacecraft "AIST" Flight Model

A.V. Sedelnikov, A.S. Filippov, T.A. Ivashova

Samara National Research University

Received 1 Feb. 2018

Abstract

The article suggests a data accuracy test of Earth's magnetic field measurements performed with the magnetometer scientific instrument MAGKOM. The measurements were carried out on board of a small spacecraft "AIST" flight model starting from April 20, 2013 up to May 20 of the same year. The test is based on checking stationarity of the vector magnitude of the magnetic induction average value with unlimited measurement information volume increase. With the help of the proposed test, it is possible to arrive at conclusions about magnetometers operation correctness, and to assign the weight of various measurement channels when they are combined.

Keywords: Magnetometer, small spacecraft, measurements accuracy test;

1. Introduction

Earth's magnetic field measuring during the orbital flight of a spacecraft is produced with various purposes. Most often they are used as primary information to estimate the parameters of spacecraft motion around the cog. This information is necessary to control a spacecraft orbital motion [1-3], to evaluate the microacceleration level in the working area of technological equipment [4-7], to spot characteristics of the gravity-sensitive processes behavior in their implementation on board spacecraft [8-9] etc. Therefore, the task of Earth’s magnetic field measurements data accuracy evaluation is an important and urgent task for measuring equipment monitoring at the operations phase of a spacecraft.

To solve this problem, various tools are used. In the paper [1] the problem of small spacecrafts stabilizing by measuring the Earth's magnetic field using engine flywheel is solved. The paper [2] also liquid rocket thrusters for spacecraft orientation is used. For small spacecrafts there are restrictions on the use of effectors of the control system [10]. Therefore, the solutions proposed in papers [1] and [2] are not always suitable for small spacecrafts. Especially when it comes to small spacecraft without a complete control system for orbital motion by classification [10]. A vivid example of the applicability of solutions [1] and [2] is the Aist-2D small spacecraft. From the perspective of the author of the paper [10], such small spacecrafts are practically in no way inferior to spacecraft of the middle class and are unlikely to find a mass application in view of the high cost of realizing their mission.

However, we should soon expect a massive use of small spacecraft in various areas of research. The most promising application, according to the authors [4, 10] are space technologies. At the same time for the successful implementation of technological processes, it is necessary to comply with the requirements for micro-acceleration [8]. These requirements are associated not only with the design of the smallest spacecrafts (this is detailed in [6]), but also with the quality of the measurement data. Thus, the proposed in the work [5] a method of reducing accelerations can be used in view of evaluations [4] and features of measuring only for small spacecraft type Aist-2D with a complete traffic control system [9].

For example, the authors of the works [3, 11] compare the significance of the magnetic field measurement data differences with the Earth's magnetosphere standard model. This comparison allowed the authors to conclude that the measuring equipment operated correctly onboard of the flight and technological samples of AIST and to detect significant differences between measurements of two different magnetometers. The results of the tests performed that the magnetometer No. 1 data differs from the magnetosphere standard model wider than the magnetometer No. 2 data for both small spacecrafts.

So, the authors decided not to consider the magnetometer No. 1 data in small spacecrafts motion estimation around the cog.

The detailed statistical studies of the measuring equipment operation accuracy on the technological sample of the Aist small spacecraft are performed in the paper [12]. They include the verification of the correspondence between the measuring channels of two different magnetometer sensors, the confidence spans

* Corresponding author e-mail: axe_backdraft@inbox.ru.

superimposing of corresponding measuring channels monitoring, the study of the statistical hypotheses of the significance of the differences between the numerical parameters of the measuring channels. Based on the analysis, the authors draw conclusions about measuring equipment operation accuracy and the presence of an average sampled value significant shift of the corresponding measuring channels.

The general approach of these works can be considered the data analysis that was run based on measurements on separate channels. The integrated test is proposed by the authors involving the research of the Earth's magnetic field vector magnitude dynamics rather than its individual components. Such approach supplements the statistical studies proposed in the works and allows us to make valid conclusions about the operation accuracy of on-board the earth's magnetic field measuring equipment.

2. Materials and methods

The subject of this study is Earth's magnetic field, the means of measuring, which are the part of the scientific equipment of MAGKOM (figure 1).

The spacecraft on board of which the MAGKOM scientific equipment operates is the flight model of the Aist small spacecraft (figure 2).

It was launched on April 19, 2013 as a hitchhiker payload with the spacecraft of middle class "Bion–M" No. 1 launch into orbit 21.04.2013 the Aist small spacecraft flight model was separated from the injection module (in-out box) and began an autonomous flight in a near-circular orbit with the height of approximately 575 km high. The service life of the Aist small spacecraft flight model is 3 years. Currently, the center for receiving and processing information of the Samara National Research University was named after Academician S.P. Korolev is still receiving the signal from this small spacecraft. The main characteristics, goals and objectives of this small spacecraft mission are presented in work [3] in details.

For processing, the primary information from the magnetometer sensors were used (figure 1d). It was a time series. For example, the measurements performed on 29.04.13 are shown in figure 3 for the first sensor and in figure 4 for the second sensor.

Three-component magnetometers (figure 1d) during optimal operation had a rated accuracy of $\pm 0{,}5\ \mu T$ and made measurements of the earth's magnetic field at 6 s intervals. The scientific equipment MAGKOM nuanced characteristics are performed in the paper [13].

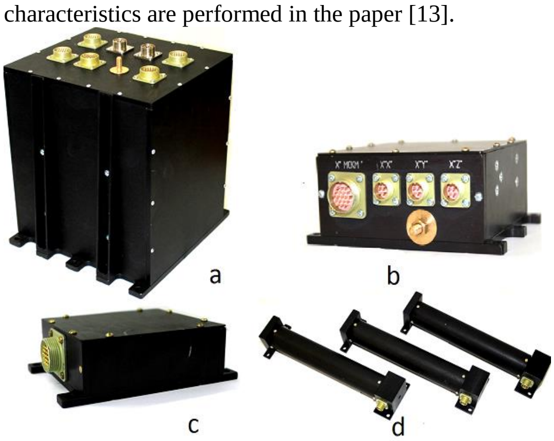

Figure 1. Scientific equipment MAGKOM (cited according to [11]): a-electronics unit; b- control unit for electromagnets; c- three-component magnetometer; d- electromagnets

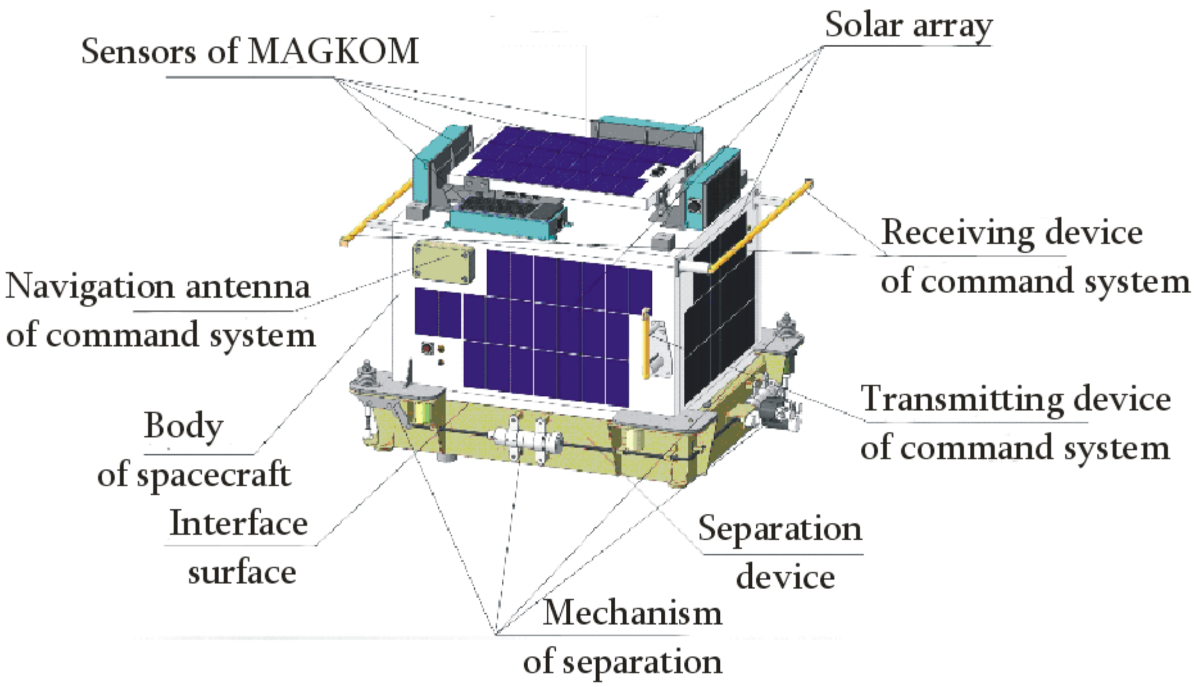

Figure 2. General view of the Aist small spacecraft flight model

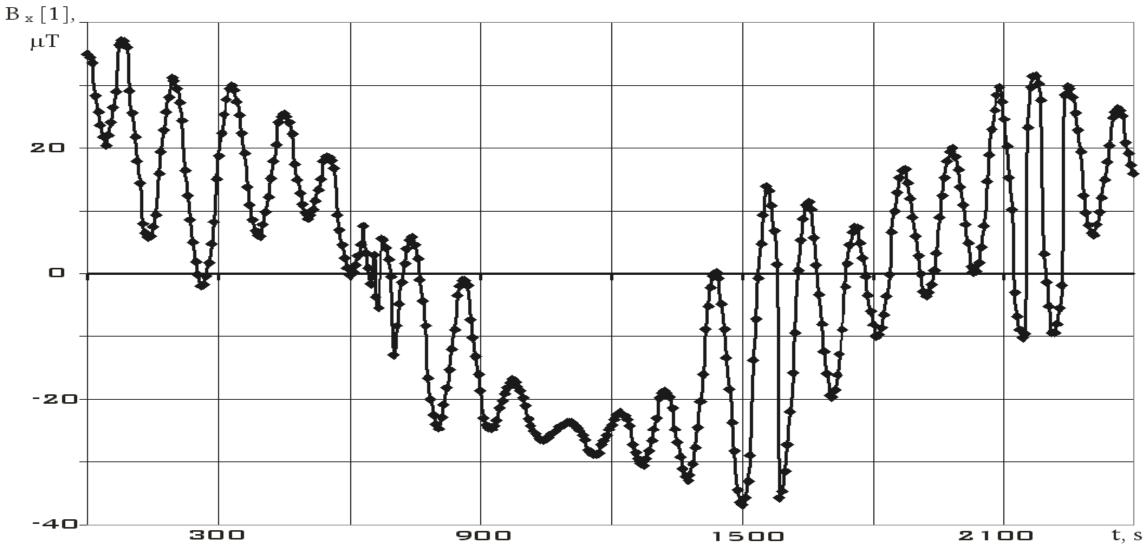

Figure 3a. The Earth's magnetic field measurements data form the sensor No. 1 on the channel B_x[1] 29.04.2013

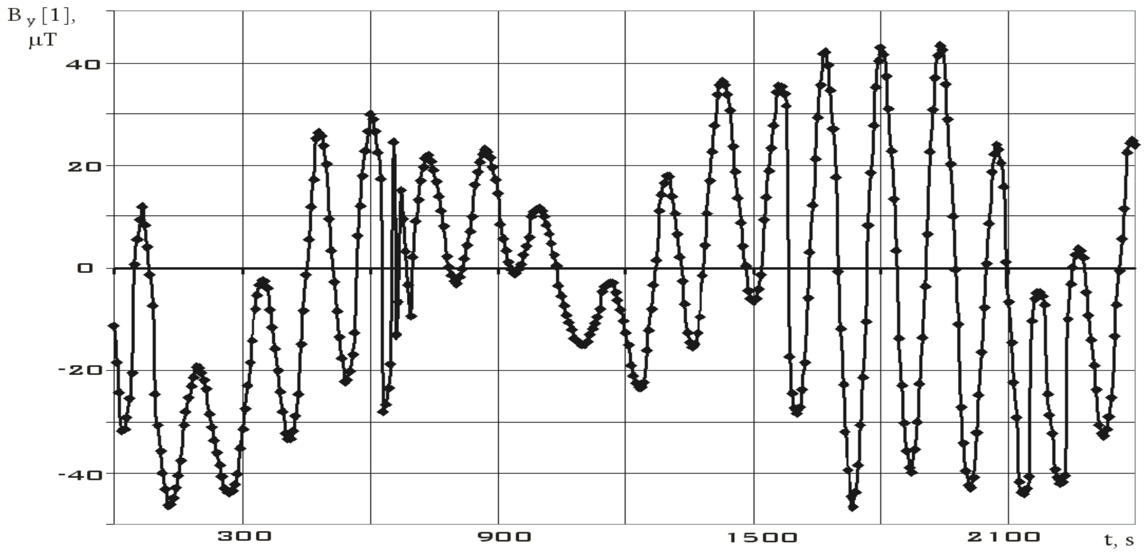

Figure 3b. The Earth's magnetic field measurements data from the sensor No. 1 on the channel B_y[1] 29.04.2013

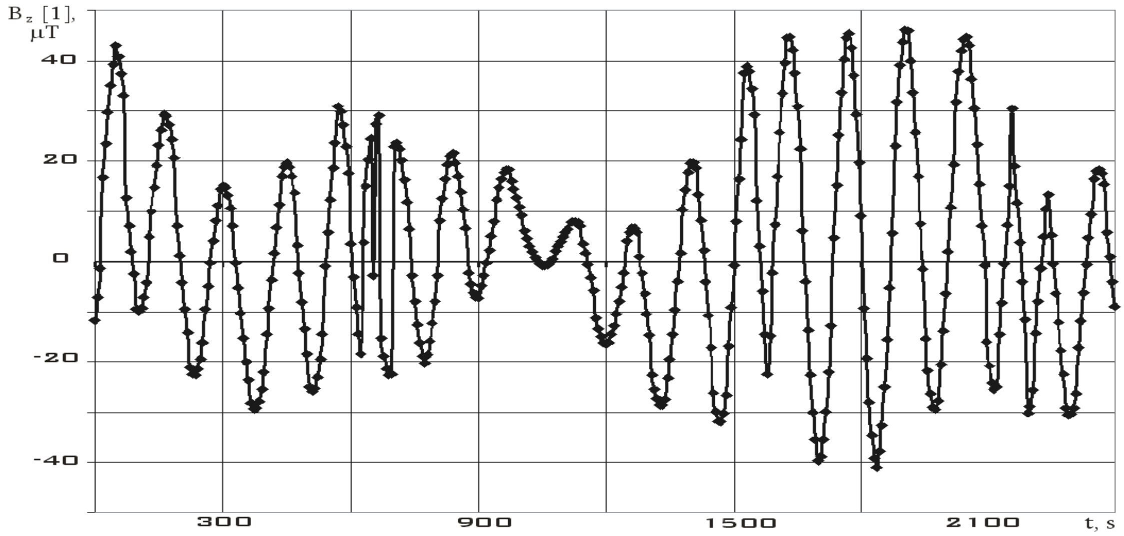

Figure 3c. The Earth's magnetic field measurements data from the sensor No. 1 on the channel B_z[1] 29.04.2013

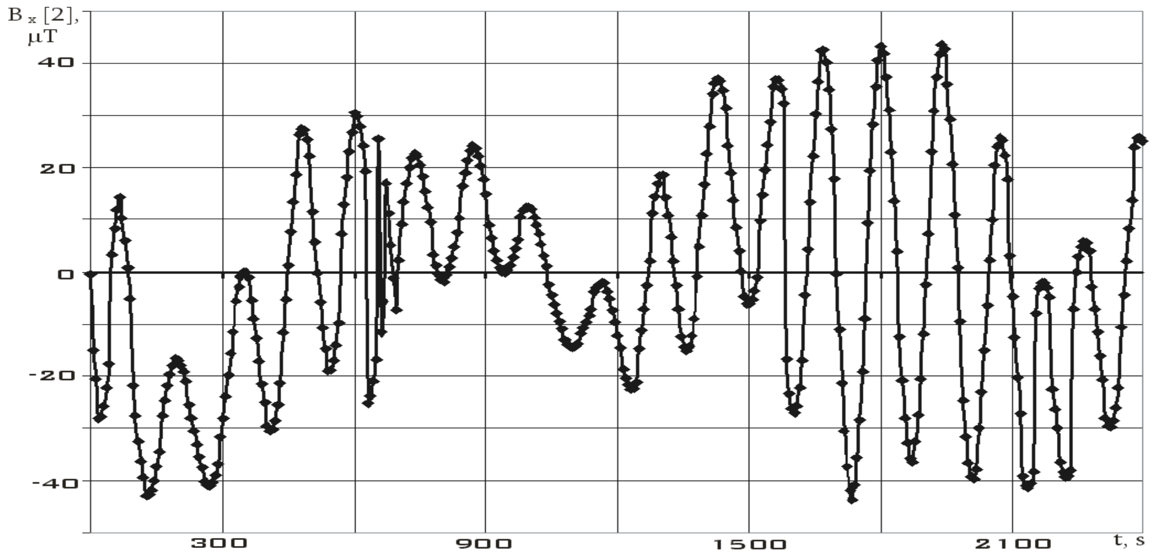

Figure 4a. The Earth's magnetic field measurements data from the sensor No. 2 on the channel B_x[2] 29.04.2013

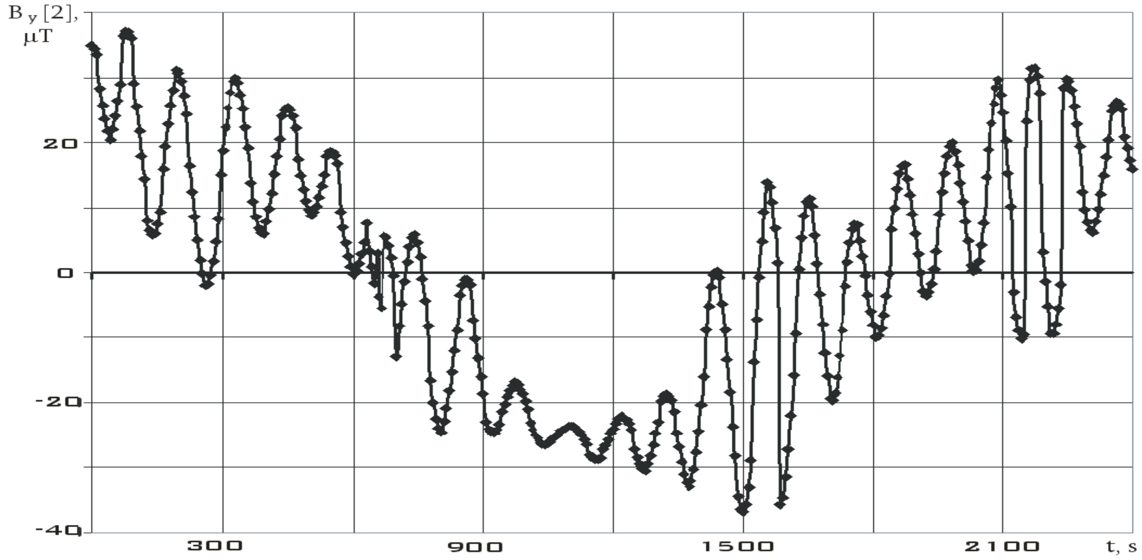

Figure 4b. The Earth's magnetic field measurements data from the sensor No. 2 on the channel B_y[2] 29.04.2013

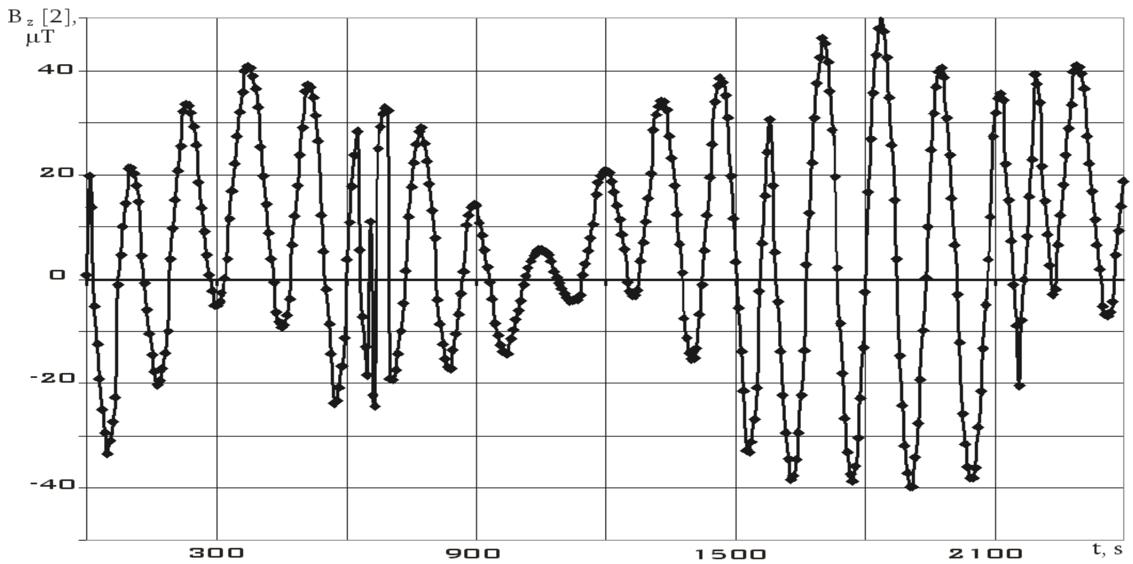

Figure 4c. The Earth's magnetic field measurements data from the sensor No. 2 on the channel B_z[2] 29.04.2013

While processing of measurement data, time series ejections, mostly associated with incorrect transmission, reception or telemetric information decryption, have been removed.

3. Integral accuracy validation test

The test assumes the modulus of the Earth's magnetic field induction vector analysis, calculated from measurements using magnetometers. The test is based on the following considerations:

3.1. Stationarity condition.

As first approximation, the modulus of the Earth's magnetic field induction vector average value along the orbit of the spacecraft can be regarded as permanent. Especially when it comes to measurements carried out in a relatively short period of time. The orbit of the spacecraft in this time interval should not vary significantly. In case of orbit variation, the test can be applied to the series of measurements before and after the variation separately. For higher accuracy testing, one can abandon the premises of the average value stationarity and use, for example, the global magnetic field model WMM 2005 to estimate the time history of the induction module average volume along the spacecraft's orbit over a measurable time interval.

3.2. The condition of representativeness.

During one measurement session, the spacecraft makes several turns or measurement sessions are selected in such a way that the orbit sections with the different values of the induction module meet uniformly in the total sample. The magnetic field of the Earth has fundamentally different characteristics at the poles and the equator (figure 5). If you select measurement sessions performed in part 1 or part 2, then the average value of the induction module will be overestimated. Appropriately, the choice of measurement sessions from part 3 or part 4 will result in a lower average value. Because of measurement sessions mismatching, the stationarity condition may be violated. Indeed, let us imagine that we have successively 100 measurements from part 1, part 2, part 3 and part 4. Without disturbing the time history of measurements, we provide the total sample from them. In this case, the average value for the first 100 sessions will be conservative, then the value will be decreased by adding part 2 measurement data, it will become conservative again after the addition of the part 3 data and finally decreased by adding the part 4 data.

In this case, testing the significance of changes in the induction module hypothesis can come to good. However this significance may not be related to the measurements, but may result from the incorrect arrangement of separate measurement sessions into the total sample. In this case, to properly form a common sample, you should evenly distribute the measurement data of part 1, part 2, part 3 and part 4, disturbing the measurements time history.

3.3. The property of consistency.

The increase of measurement sessions number in the total sample, subject to the condition of representativeness under measuring equipment correct operation condition, must serve to come sample average of the magnetic induction module arbitrarily close to its steady-state value adopted within the framework of the stationarity condition:

$$\lim_{n\to\infty}\left(\left|\hat{\vec{B}}\right| - \left|\bar{\vec{B}}\right|\right) = 0 , \qquad (1)$$

where $\left|\bar{\vec{B}}\right|$ – the average value of the induction module along the spacecraft orbit, $\left|\hat{\vec{B}}\right|$ – the sample average of the induction modulus, n – number of measurements.

And the variance of the sample average should also arbitrarily come to decrease:

$$\lim_{n\to\infty} D\left|\hat{\vec{B}}\right| = 0 \qquad (2)$$

Thus, the estimated mean $\left|\hat{\vec{B}}\right|$ of the induction module along the spacecraft's orbit under measuring equipment correct operation condition can be considered as a consistent bias in small samples (figure 6).

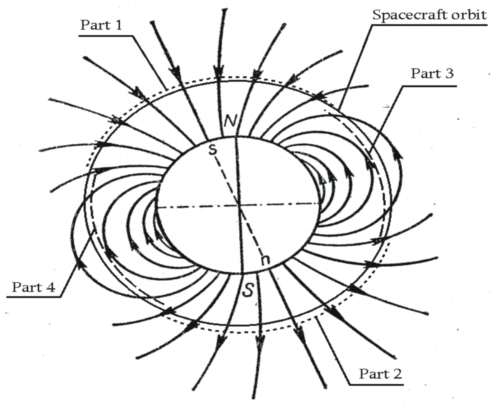

Figure 5. Scheme of the magnetic field lines of the Earth

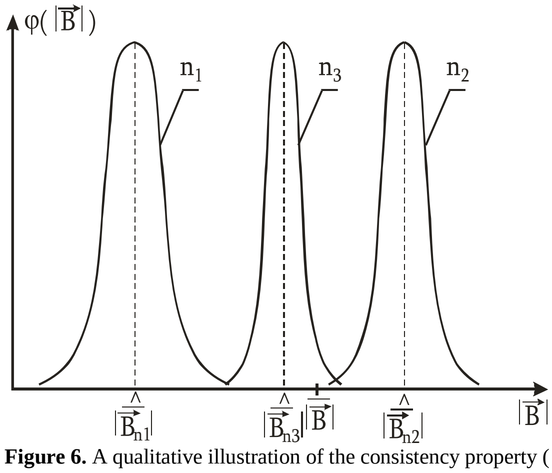

Figure 6. A qualitative illustration of the consistency property ($n_1 < n_2 < n_3$)

To use the integral test, the following algorithm is proposed:

1. Checking the time interval for measuring the stationarity condition.
2. Receding the initial measurement data outlier.
3. Calculating the modulus of the Earth's magnetic field induction vector from measurements.
4. Analyzing the spacecraft position in orbit at the time intervals when measurements were being taken.
5. Arranging the total sample of measurement data taking into account the condition of representativeness.
6. Verification the consistency of estimator condition of the modulus of the magnetic induction vector average orbital value from measurement data.
7. Estimating of the statistical analysis accuracy.
8. Forming the conclusions about the measuring equipment operation accuracy.

4. The results of checking the measuring equipment operation accuracy of the Aist small spacecraft flight model

To estimate the measuring equipment operation accuracy, the data obtained during the measurement sessions were used and the basic parameters of which are presented in Table 1.

Checking the time intervals of measurements according to paragraph 1 of the algorithm shows that only for the measurement session on 29.04.2013, the spacecraft performed less than one turn. Therefore, the measurements data validation integral test might be well-adjusted for the measurement sessions presented in Table 1. Outlier indicated in the third and the fourth columns of Table 1 were receded from the total sample in accordance with paragraph 2 of the algorithm. The calculation of the magnetic induction vector modulus provided the results presented in figure 7.

Table 1. The basic parameters of the Earth's magnetic field measurement sessions samples

Date	Volume of sample	Outlier		Turns number at a measurement session	Total sample volume	
		Sensor 1	Sensor 2		Sensor 1	Sensor 2
27.04.2013	1150	1	1	1,2	1149	1149
29.04.2013	400	0	1	0,6	1549	1548
10.05.2013	1350	0	0	1,7	2899	2898
14.05.2013	2350	1	2	2,6	5248	5246
16.05.2013	1699	221	228	2,1	6726	6717
20.05.2013	1750	42	41	2,3	8434	8426
27.04.2013	1150	1	1	1,2	1149	1149
29.04.2013	400	0	1	0,6	1549	1548

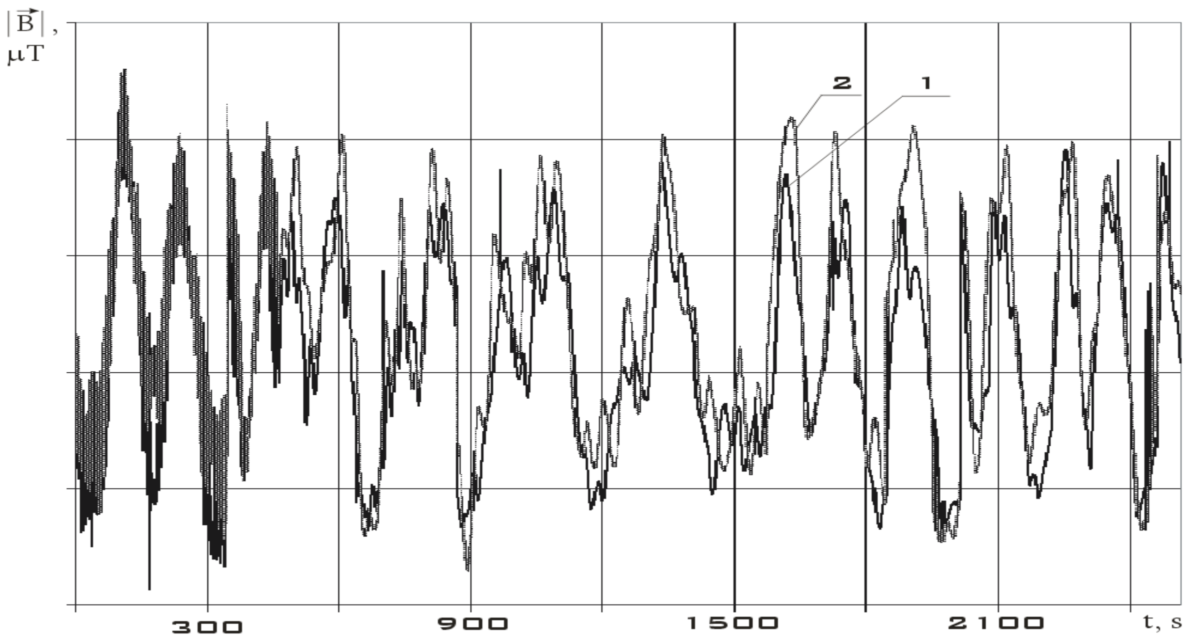

Figure 7. The modulus of the Earth's magnetic field induction vector on the measurements data 29.04.2013: 1) sensor No. 1; 2) sensor No. 2

To arrange the total sample, we will take the easiest rout without breaking the time history of measurements. We obtain the total sample by successive docking of the measurement sessions data given in Table 1. Let us check the consistency of estimator condition of the modulus of the magnetic induction vector average orbital value from measurement data using the expressions (1) and (2). The behavior patterns of an average value and of the total sample variance are shown in Figures 8 and 9.

Analysis of the obtained relationship shows that the sample variance decreases while the sample number increases. So, for $n = 1000$ the average orbital value of the Earth's field magnetic induction vector modulus can be represented as $|\vec{B}| = 33{,}2 \pm 4{,}5\ \mu T$ (Sensor No. 1) and $|\vec{B}| = 35{,}0 \pm 3{,}8\ \mu T$ (Sensor No. 2), and for $n = 8000$ – $|\vec{B}| = 31{,}7 \pm 1{,}9\ \mu T$ (Sensor No. 1) and $|\vec{B}| = 34{,}3 \pm 1{,}7\ \mu T$ (Sensor No. 2). This fully corresponds to figure 6, showing the average orbital value consistency of estimator. Since the measurement sessions have been carried out in a monthly time interval the average orbital value in this interval can be considered stationary. In this context the analytical error does not exceed the measurement error which is $\pm 0{,}5\,\mu T$ according to the developers of the measuring equipment. So, it is a fair assumption that both sensors on the Aist small spacecraft flight sample in the considered measurement sessions are operated correctly. The variation between measurement data (figure 8) is not discussed by the authors of the article. One of the possible reasons for this variation is the effect of the battery operation [12, 14, 15] that requires more careful analysis.

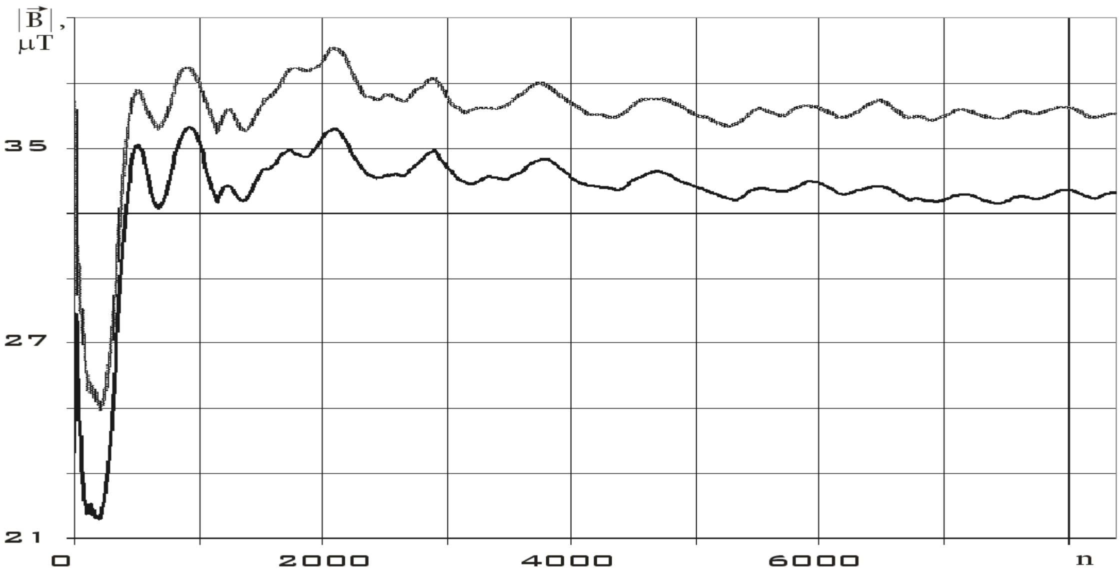

Figure 8. The behavior pattern of a total sample average value for the sensor No. 1 (the upper curve) and for the sensor No. 2 (the lower curve)

Figure 9. The behavior pattern of the total sample variance for the sensor No. 1 (the upper curve) and for the sensor No. 2 (the lower curve)

Conclusions

1. The advantage of the presented test is its integration that lies in all measuring channels validation at once. This saves time spent on analysis, and simplifies the test performance. However it is impossible to identify what measurement channel gives in correct data. The test is used successfully in the case of smooth operation of all measuring instruments for assigning the separate measurement channels weight when implementing joint processing of measurement data.
2. While arranging the sample volume of measurement data, measurement chrono sequence disarrangement may not allow to date the moment of the measuring instrument failure accurately. To solve this problem, it is necessary to test hypotheses of homogeneity of separate measurements samples. In this case, the series of measurements for part 1, part 2, part 3 and part 4 (figure 5) should be sorted and the hypothesis of homogeneity should be checked only within one of the parts.
3. The failure test can not only be a result of measuring equipment failed operation, but also with activating of other spacecraft equipment during the measurement session that can be significantly affected the magnetometer sensors readings. Therefore the proposed test can state the significance of the spacecraft operation systems and equipment impact on Earth's magnetic-field measurement with onboard tools.
4. The presented results of the time period since 20.04.2013 to 27.04.2013 show that onboard Earth's magnetic-field measuring equipment of the Aist small spacecraft flight sample operated perfectly.
5. A comparative analysis (benchmark analysis) of two sensors measurements shows that in the total sample while keeping the measurement sessions chronosequence of the second sensor sampling variance is lower than the first sensor. This suggests that more accurate evaluation of the magnetic induction vector components by means of a second sensor. The authors of [3] came to the same conclusion, that made further evaluation of the spacecraft evolution parameters around the center of mass center only on the basis of the second sensor measurements.

References

[1] V.V. Lyubimov, V.S. Lashin, "External stability of a resonance during the descent of a spacecraft with a small variable asymmetry in the martian atmosphere". Advances in Space Research, Vol. 59, No. 6, 2017, 1607–1613.

[2] A.I. Belousov, A.V. Sedelnikov, K.I. Potienko, "Study of effective application of electric jet engine as a mean to reduce microacceleration level". International Review of Aerospace Engineering, Vol. 8, No. 4, 2015, 157–160.

[3] V.I. Abrashkin, K.E. Voronov, A.V. Piyakov, Yu. Ya. Puzin, V.V. Sazonov, N.D. Semkin, A.S. Filippov, S. Yu. Chebukov, "Uncontrolled rotational motion of the Aist small spacecraft prototype". Cosmic Research, Vol. 55, No. 2, 2017, 128–141.

[4] A.V. Sedelnikov, "Fractal assessment of microaccelerations at weak damping of natural oscillation in spacecraft elastic elements. II". Russian Aeronautics, Vol. 50, No. 3, 2007, 322–325.

[5] A.V. Sedelnikov, A.A. Kireeva, "Alternative solution to increase the duration of microgravity calm period on board the space laboratory". Acta Astronautica, Vol. 69, No. 6–7, 2011, 480–484.

[6] A.I. Belousov, A.V. Sedelnikov, "Problems in formation and control of a required microacceleration level at spacecraft design, tests, and operation". Russian Aeronautics, Vol. 57, No. 2, 2014, 111–117.

[7] A.V. Sedelnikov, K.I. Potienko, "How to estimate microaccelerations for spacecraft with elliptical orbit". Microgravity Science and Technology, Vol. 28, No. 1, 2016, 41–48.

[8] M.M. Al-Maghalseh, "Investigate the Natural Convection Heat Transfer in A PCM Thermal Storage System Using ANSYS/FLUENT". Jordan Journal of Mechanical and Industrial Engineering, Vol. 11, No. 4, 2015, 119–127.

[9] A.V. Sedelnikov, "Classification of microaccelerations according to methods of their control". Microgravity Science and Technology, Vol. 27, No. 3, 2015, 245–251.

[10] A.V. Sedelnikov, "Mean of microaccelerations estimate in the small spacecraft internal environment with the use of fuzzy sets". Microgravity Science and Technology, Vol. 30, No. 4, 2018, 1–7.

[11] V.I. Abrashkin, K.E. Voronov, A.V. Piyakov, Yu. Ya. Puzin, V.V. Sazonov, N.D. Semkin, A.S. Filippov, S. Yu. Chebukov, "Definition of rotary motion of the satellite AIST according to onboard measurements of the Earth's magnetic field". Preprint of Keldysh Institute of Applied Mathematics Russian Academy of Sciences, No. 17, 2014, 1–38.

[12] A.V. Sedelnikov, A.S. Filippov, A.S. Gorozhankina, "Problems of data processing of magnetic field of the Earth measuring instruments of the scientific equipment MAGKOM". Instruments and Systems: Monitoring, Control, and Diagnostics, No. 6, 2017, 33–40.

[13] N.D. Semkin, I.V. Piyakov, "Results of operation of scientific hardware Space system of microacceleration compensation". Vestnik of the Samara State Aerospace University, Vol. 15, No. 1, 2016, 107–114.

[14] A.I. Belousov, N.D. Semkin, A.V. Sedelnikov, Yu.Ya. Puzin, K.E. Voronov, A.V. Piyakov, A.S. Philippov, "Analysis of rotary motion of small spacecrafts of the Aist series". Aerospace Instrument-Making, No. 8, 2017, 3–10.

[15] A.V. Sedelnikov, "Evaluation of the level of microaccelerations on-board of a small satellite caused by a collision of a space debris particle with a solar panel". Jordan Journal of Mechanical and Industrial Engineering, Vol. 11, No. 2, 2017, 121–127.

JJMIE

Volume 12, Number 4, December. 2018
ISSN 1995-6665
Pages 261 - 268

Jordan Journal of Mechanical and Industrial Engineering

Effect of Castor Biodiesel on Diesel Engine Performance, Emissions, and Combustion Characteristics

Sameh Nada[a], Ali M. Attia[a], M. S. Gad[b,*]

[a]*Mechanical Engineering Department, Faculty of Engineering, Banha University, Egypt.*
[b]*Mechanical Engineering Department, Faculty of Engineering, Fayoum University, Egypt.*

Received 12 July. 2018

Abstract

In this work, castor oil was used to produce biodiesel by transesterification process. The aim of this work was to study the performance, emissions and combustion characteristics of castor biodiesel blend B20 compared to diesel fuel using four stroke, single cylinder diesel engine. Diesel- biodiesel mixture B20 gives reasonable viscosity near to diesel oil. Brake thermal efficiency of castor biodiesel blend was higher than diesel oil by about 2%. Biodiesel blend B20 achieved higher exhaust gas temperature about diesel fuel. The smoke point increased with the blending ratio increase. Blend B20 achieved increase in smoke point by 30% about crude diesel. Cylinder pressure is higher for castor biodiesel blend compared to diesel oil at all loads. Performance and combustion characteristics of a diesel engine using biodiesel blends up to 20% with diesel fuel were close to diesel fuel. Non-edible castor oil which produced biodiesel could be a good substitute to diesel fuel in diesel engine.

Keywords: Castor biodiesel, Diesel engine, Performance, Smoke, Combustion characteristics;

1. Introduction

The problem of fossil fuel depletion and environmental degradation can be solved by using crude biodiesel or blends with diesel fuel. Biodiesel is fatty acid ethyl or methyl ester from vegetable oils or animal fats [1]. At different engine loads, biodiesel blends of 5, 20 and 35% for castor diesel -biodiesel blends were studied. At higher biodiesel concentration in the fuel, an increase in fuel consumption was shown [1, 2].

Small percentages of castor biodiesel blends with diesel fuel of 5, 10, 15 and 20% by volume were used. Biodiesel blends showed higher engine exhaust gas temperatures in comparison with diesel fuel [3]. Engine emission analysis and performance were performed using castor biodiesel blends of 2, 5 and 10% by volume at different loads. Specific fuel consumption and thermal efficiency of 10% castor biodiesel percentage were close to diesel fuel. Higher viscosity and lower net calorific value led to increase in specific fuel consumption for castor biodiesel blends about diesel oil [4]. Higher viscosities and lower net calorific value are the major problems associated with using vegetable oils. Thermal efficiency is slightly decreased, exhaust gas temperature and specific fuel consumption increased compared to diesel fuel for all biodiesel blends [5].

At different engine loads, castor biodiesel was run in a diesel engine. Transesterification was used for vegetable oil viscosity reduction. The increase in biodiesel concentration led to increase of exhaust gas temperature [7]. Blend B80 has the highest thermal efficiency and lowest specific fuel consumption. Blend B80 shows the overall optimum performance when used in diesel engine [8]. Castor biodiesel blends were prepared by blending biodiesel with different volumes of diesel fuel. Castor biodiesel blends of B5, B10, B20 and B30 were studied. Biodiesel fuel was evaluated in terms of its physical and chemical properties such as flash point, viscosity, density and lower heating value. Results showed that biodiesel has similar properties with diesel fuel [9].

Castor biodiesel blends of 5, 10, 15, 20, 30% by volume were investigated at various loads. The maximum increase in specific fuel consumption when compared to diesel fuel is 10.7 for B30 at half engine load, respectively. Blends B15 and B20 at full load operation gave the best specific fuel consumption of diesel engine [10]. Castor biodiesel blends with diesel oil from 0 to 40% by volume were investigated to examine engine performance and exhaust emissions. Transesterification process was used to produce biodiesel from castor oil. Specific fuel consumption of biodiesel blends increased with the blend percentage increase. Reduction in exhaust emissions and improvement in performance parameters made the blend of caster biodiesel reach up to 20% which is a suitable alternative fuel for diesel engine. Blend B20 can be selected due to its better combustion and lower emissions compared to diesel fuel [11].

* Corresponding author e-mail: mgad27@yahoo.com.

Effect of castor biodiesel blends on diesel engine performance and emissions was studied. Specific fuel consumption, thermal efficiency, and exhaust emissions were analyzed. Volume percentages of biodiesel with diesel fuel of 5, 10, 15, 20 and 30% were used. Lower blends of biodiesel provide acceptable engine performance. Exhaust emissions were decreased. Castor biodiesel blend B15 was the optimum blend of biodiesel-diesel blends [12]. Specific consumption increased for castor biodiesel blends compared to diesel fuel. Using biodiesel blends from castor oil of B10 and B20 showed satisfactory results in comparison to diesel fuel [13]. A single cylinder diesel engine was used to run with diesel and various blends of castor biodiesel. Performance parameters and emission tests were compared for various blends of castor biodiesel with diesel fuel. At blend B60, specific fuel consumption was the lowest with the highest exhaust gas temperature as compared to other biodiesel blends. B60 showed the optimum performance for its use in diesel engines. Vegetable oils are alternative fuels for diesel engines. Use of vegetable oils in diesel engine causes problems due to their higher viscosity and poor volatility. Blending diesel oil with vegetable oils reduces the viscosity of these oils [14]. Thermal efficiencies of biodiesel blends were lower compared to diesel fuel [15].

The reduction of kinematic viscosity by seven times about diesel oil was due to the presence of ricin oleic acid. Up to 20% of castor biodiesel can be blended within the accepted standard range of viscosity. Diesel oil has lower net calorific value compared to castor biodiesel [16]. Diesel oil has lower surface tension about biodiesel. Biodiesel blend has higher pressure rise rate during the rapid combustion phase about diesel oil due to higher reactivity of biodiesel [17]. The engine fueled with 20% castor biodiesel performs better and does not require any change in engine design [18]. Biodiesel is a good alternative in winter conditions. Castor biodiesel has a very low pour and cloud points; therefore, castor biodiesel has a lower cetane number compared to diesel [19, 20].

Poor breakup, evaporation properties and oxygen content have effects on castor biodiesel emissions [21, 22]. Higher value of specific fuel consumption was related to B5 at 1500 and 2000 rpm [23]. The optimal reaction conditions at a molar ratio of 5.4:1, KOH concentration of 0.73%, reaction temperature of 64°C, reaction time of 2.5 hour and stirring rate of 320 rpm resulting in 97.82% biodiesel yield. Increase of biodiesel percentage led to significant reductions in exhaust emissions [24, 25, 26].

Due to its higher oil yield, castor oil is one of the most promising non-edible oil. Due to limited castor oil biodiesel performance and emissions studies, it is evident that further research is recommended. Non-edible oil was taken as a feedstock for biodiesel production from Egyptian castor because of its ecological, reproductive, and supportable nature. Literature review did not show the smoke points and flame visualization, but it was considered. In this study, transesterification process was used for production of castor biodiesel from crude oil. Castor biodiesel at volume percentage of 20% was blended with diesel fuel. Chemical and physical properties of castor biodiesel blend were compared to diesel fuel. Experiments were also conducted to investigate its effect on the performance, emissions and combustion characteristics of diesel engine.

2. Production of castor biodiesel

Biodiesel was made from castor oil by base catalyzed transesterification. In a round bottom flask, the oil is heated up to 70 °C and stirred vigorously. The triglyceride of castor oil reacted with potassium hydroxide NaOH which was mixed with methanol in molar ratio of 6:1 in a separate vessel. The mixture was poured into round bottom flask while stirring the mixture continuously and maintained at atmospheric pressure and 65°C for 90 minutes to form an ester and glycerol. Under gravity for 24 hours, the mixture was left to settle in a separating funnel. The bottom layer consisted of glycerin, excess alcohol, catalyst, impurities and traces of unreacted oil. The upper layer was biodiesel. The fatty acid methyl ester (FAME) was water washed with air-bubbling to remove unreacted methoxide. The mixture was then heated to remove the water traces to obtain clear biodiesel of 92% yield [27, 28].

3. Experimental Setup

Experimental tests were done using a single cylinder, four stroke diesel engines with a developing power of 5.775 kW at 1500 rpm. Technical specifications of tested diesel engine were given in Table 1. The experimental set up schematic diagram was shown in Fig. 1. DC generator had been connected to the tested engine output shaft with flexible coupling. AC voltage from the power supply was controlled with variac. The received voltage was converted into DC excitation voltage by a rectifier circuit and measured using a digital voltammeter (model DT9205A) with a resolution of 1 volt in the range up to 750 volt (AC). Voltage was measured using a digital voltammeter (clamp multi-meter model 266, measurement range 0-750 DC volt, and 1-volt resolution). The generator output current was measured using an ammeter. Series of heaters which hot water flowing through a water tank was used to measure the electric output power of DC generator. Six electric heaters (each of 19.5Ω resistance) were connected to the generator output terminals. The excitation voltage was regulated to produce generator power output that would be equal the expected power output. A burette in the front side of the panel was used to measure fuel flow rate and selection between both diesel and biodiesel fuels. The air flow was measured using MERIAM- 50MC2 laminar flow element equipped with digital differential pressure transducer. The adoption of damping air box with large volume reduced the pressure fluctuations across the airflow measurement device to negligible values. A digital stroboscope (model DS-303) optical tachometer was used for engine speed measurements. The tachometer had been placed directly toward the engine flywheel. A strip of reflective tape was applied to the engine flywheel. A light beam was generated from the digital stroboscope with specific frequency towards the flywheel circumference. This optical tachometer had a measurement range up to 9999 rpm with a resolution of 1 rpm. Thermocouples K connected to digital thermometer (Omega-model 650) was used to measure the ambient air, exhaust gas and intake air temperatures. A cooled piezoelectric pressure sensor (model 6061B of pressure range up to 25 MPa and sensitivity of -2.75 pc/MPa) connected with NEXUS charge amplifier (Type 2690-A-OS4) was used to measure the cylinder pressure. The piston top dead center (TDC) marking was done by using proximity switch (model LM12-3004NA) installed at detecting distance of 4 mm supplied with DC voltage up to 36 V. A digital linear displacement (Sony-Magnescale LY-1115) detected the location of TDC relative to the position of the proximity. Data-Acquisition Card (DAQ model NI PCI-6251 with terminal block SCB-68) installed on PC computer controlled by LABVIEW software was used to acquire the signals from charge amplifier and proximity switch. The average cylinder pressure for at least 25 cycles was taken. At engine load variation from zero to full load and constant speed of 1500 rpm, the tests were carried out.

Table 1. Engine specification

Type	DEUTZ F1L511
Number of cylinders	1
Number of strokes	Four stroke
Cooling type	Air cooled
Bore (mm)	100
Stroke (mm)	105
Compression ratio	17.5:1
Fuel injection advance angle	24° BTDC
Rated brake power (kW)	5.775 at 1500 rpm
Number of nozzle holes	1
Injector opening pressure (bar)	175

4. Results and discussion

4.1. Effect castor biodiesel blends on viscosity

Due to the higher viscosity of biodiesel, it cannot be used directly in diesel engine. Therefore, it can be preheated or blended with the fossil fuels to be able to supply fuel blend without engine modifications. Preheat of fuel needs the addition of the eaters and the corresponding controllers, while the use of fuel blending does not need any additional equipment for engine [29, 30]. The mixture viscosity had been affected by the effect of the blend percentage as shown in Fig.2. Viscosity is directed proportional with the castor biodiesel increase in blends. Viscosity of methyl ester is higher compared with standard biodiesel value. The ratios of biodiesel blend and diesel oil viscosities are 5.7, 16.7, 29.6, 42.4, 58.1, 73, 113.3 and 387% for B5, B10, B15, B20, B25, B30, B40 and B100. We use biodiesel blend B20 because it gave reasonable viscosity according to literature review made by the researcher. Net calorific value of castor biodiesel blend was lower than diesel oil. Castor biodiesel achieved higher flash point compared to diesel oil, so, it is safer than crude diesel in handling and storage. Chemical and physical properties of diesel and castor biodiesel blends are shown in Table 2.

Table 2. Physical and chemical properties of diesel and castor biodiesel blends.

Properties	Method	Biodiesel B100	Diesel oil	Biodiesel blend B20
Density @ 15.56°C	ASTM D-4052	925	835	845
Kinematic viscosity, cSt, @ 40° C	ASTM D-445	16	2.5	4
Flash point, °C	ASTM D-93	148	72	82
Cetane number	----------------	58	50	52
Net calorific value kJ/ kg	ASTM D-224	41000	44000	43000

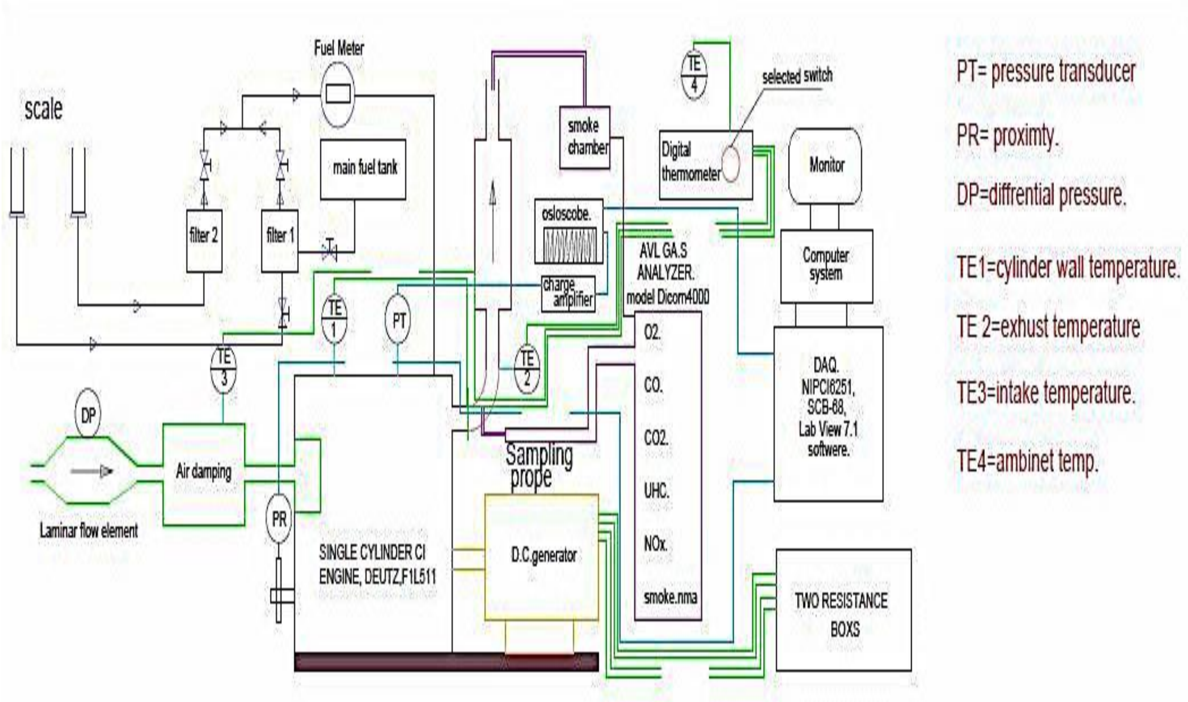

Figure1. Schematic of the experimental setup.

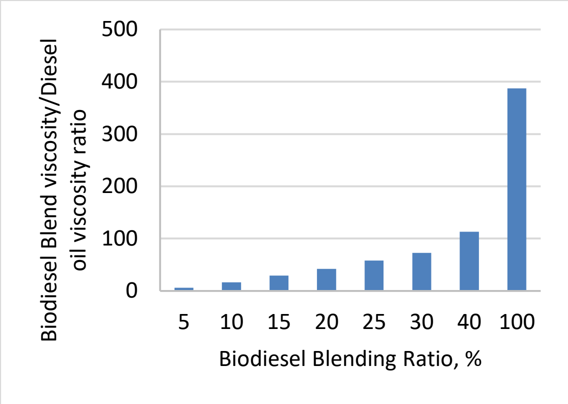

Figure 2. Effect of biodiesel blends on fuel viscosity

4.2. Brake specific fuel consumption (BSFC)

The variation in brake specific fuel consumption with respect to change in engine load for castor biodiesel blend and fossil diesel was shown in Fig. 3. The heat generated in the cylinder increased as the load increased. BSFC of castor biodiesel blend B20 was lower at all loads in comparison to diesel oil due to net calorific value of biodiesel blend B20 was near to diesel fuel. The engine consumes less fuel than compared to diesel oil to produce the same power. Lower viscosity, higher volatility led to combustion characteristics improvement of biodiesel blend. Castor biodiesel blend has lower density near to diesel oil. The fuel injection system operates on a volume metering system, so the oil density has an effect on engine performance. The reduction in specific fuel consumption for B20 about diesel oil is about 2% at 50% of engine load. The results are similar with literature [17, 31].

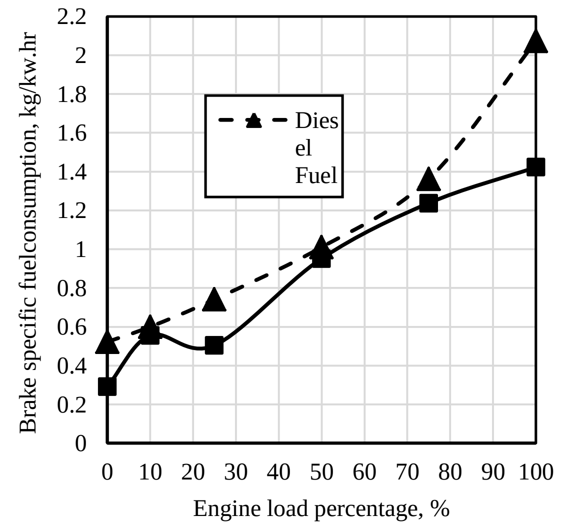

Figure 3. Variation of specific fuel consumption with engine brake power.

4.3. Brake thermal efficiency (BTE)

Figure 4 portrayed the brake thermal efficiency variation with engine load for diesel and biodiesel blend B20. Thermal efficiency of diesel and castor biodiesel blend increased with engine brake power increase due to fuel consumption increase. The increase in engine load led to increasing of heat generated in the cylinder. BTE was slightly higher for biodiesel blend B20 at all loads due to its net calorific value, density and viscosity near to diesel oil. The same displacement of the injection pump plunger with less discharge fuel for due to lower bulk modulus of biodiesel blend was shown. Value of biodiesel blend viscosity was near to diesel oil that gave a good atomization and efficient mixing of air and fuel. The higher lubricity and oxygen present in biodiesel improved the thermal efficiency. The increase in BTE for biodiesel blend was 2% about diesel oil at 50% of engine load. The results matched with these references [17, 31].

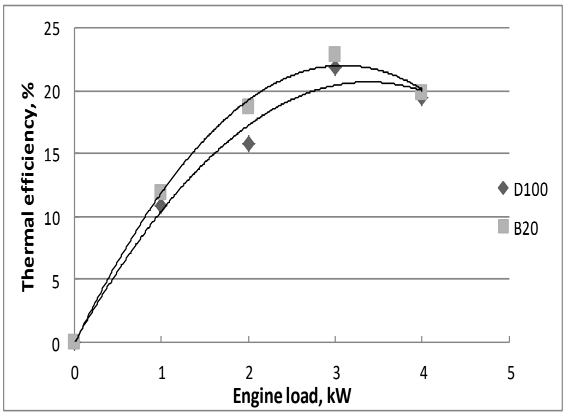

Figure 4. Variation of thermal efficiency with engine brake power.

4.4. Exhaust gas temperature (Texh.)

It describes the combustion status and shows the heat amount going waste in the exhaust gases. Figure 5 illustrated the exhaust gas temperature variation with engine brake power for diesel and castor biodiesel blend fuels. The increase in exhaust gas temperature with engine load increase was due to the increase in fuel consumption and cylinder temperature. Higher bulk modulus of biodiesel and heat loss increase of biodiesel blend B20 about diesel oil. Using biodiesel blends more than 20% led to higher increases of T_{exh} about diesel oil. Castor biodiesel blend B20 showed higher exhaust gas temperature compared to diesel oil. $T_{exh.}$ for diesel and biodiesel blend are 394 and 491°C, respectively at full load. The results confirmed with literature [17, 31]

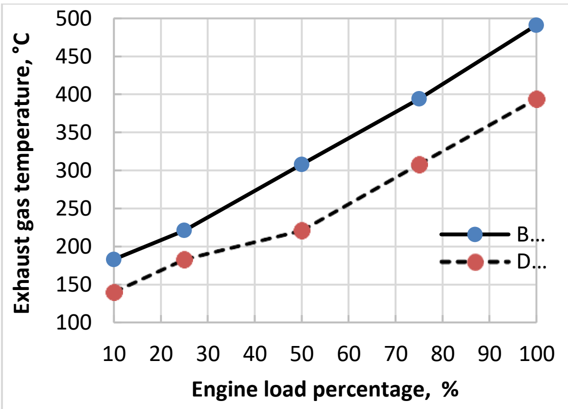

Figure 5. Variation of exhaust gas temperature with engine brake power.

4.5. Effect of biodiesel blends on smoke point

The smoke point is the maximum flame height produced by a specific wick fed lamp at which the flame starts to soot as stated by ASTMD1322-12 and as shown in Fig.6. The level A was above the smoke point, the level B at the smoke point and the level C below the smoke point. The flame in the wick feed lamb is laminar diffusion flame. The fuel flowed through the wick by the capillary effect. It was vaporized before entering the pre-combustion zone due to higher temperature then broke down in the preheat zone of the flame forming soot. As the temperature was raised at the flame front, the formed soot was oxidized and the combustion was completed. The completeness of soot oxidation depends on the amount of cracked hydrocarbons and the reaction rate. The existence of oxygen leads to higher reaction rate as a result of active radical formation in particular OH. The same results can be obtained if the hydrocarbon contents were reduced as already done by the transesterification process where the R-group was replaced by OH-group [32].

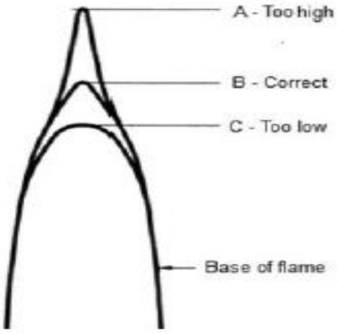

Figure 6. Smoke point evaluation

The candle was washed by methanol and left it until dry. The extracted oil was soaked and dried wick not less than 125 mm long in the sample. Then, it was placed in the candle wick tube. After that, the burning end of the wick was resoaked in the sample. The wick tube was placed in the candle. The candle was lighted and adjusted the wick until the flame was approximately 10 mm high and allowed the wick to burn for 5 min. The candle was raised until a smoky tail appear, then the candle was lowered slowly. The end of wick should be burned at the start of ruler. The observed layer of flame was flame A which was an elongated, pointed tip with the sides of the tip appearing concave upward (orange), Flame B was a blunted flame observed near the true flame tip and Flame C which is the downward white layer (white). The height of flame tip was determined. Smoke points for castor biodiesel blends were shown in Table 3 [33].

This method showed the relative smoke of diesel oil and it`s blends with castor biodiesel in a diffusion flame. The combustion products radiant heat transfer of the fuel was responsible quantitatively for the smoke point. The smoke point increased with blending ratio because of higher oxygen content in castor biodiesel as shown in Fig.7. The smoke points for biodiesel blends were affected by the oxygen content. The Smoke points increase about diesel oil which were23, 30, 40, 55 and 257% for B10, B20, B30, B40 and B100, respectively.

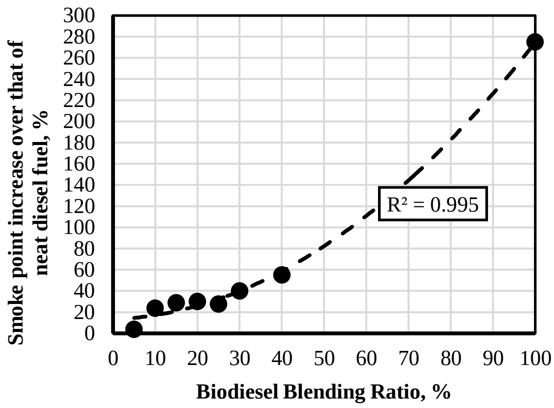

Figure 7. Smoke points for castor biodiesel blends.

Table 3. Smoke point for castor biodiesel blends.

Biodiesel blend	Diesel oil	B10	B20
Smoke point	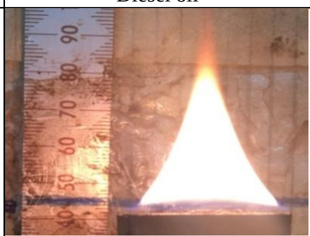		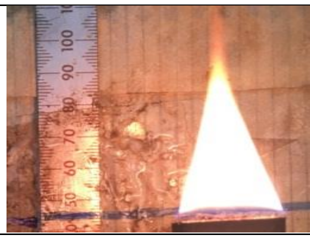
Biodiesel blend	B30	B40	B100
Smoke point	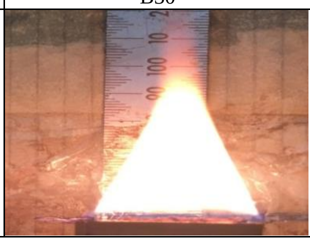		

4.6. Variation of cylinder pressure with crank angle

Cylinder pressure describes the ability of the fuel to mix well with air. The large amount of fuel burnt in premixed combustion stage was related to the maximum rate of pressure rise and higher peak pressure. Figure 8 (A, B, C and D) showed the cylinder pressure variation with crank angle for diesel and castor biodiesel blend B20 at different engine loads of 10, 25, 75 and 100%. Castor biodiesel blend B20 followed by a cylinder pressure pattern similar to diesel fuel at load variation. Cylinder pressure was higher for biodiesel blend compared to diesel oil due to lower cetane number, longer ignition delay and less fuel burnt in diffusion stage of castor biodiesel blend. Higher cylinder pressure for biodiesel blend about diesel oil was due to more fuel burnt in premixed stage, improved reaction rate, higher heat release, air-fuel mixing and improved combustion characteristics. The cylinder peak pressure for diesel fuel is 55 MPa was attained at a crank angle of 5° before TDC. In case of biodiesel blend, the cylinder peak pressure was 65 MPa at a crank angle of 5° after TDC at full load. These results matched with references [17, 31].

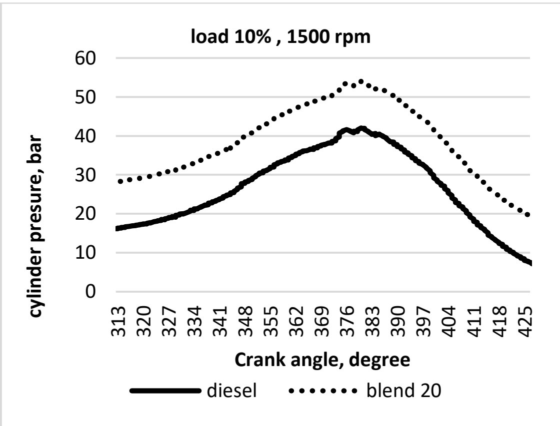

(A)

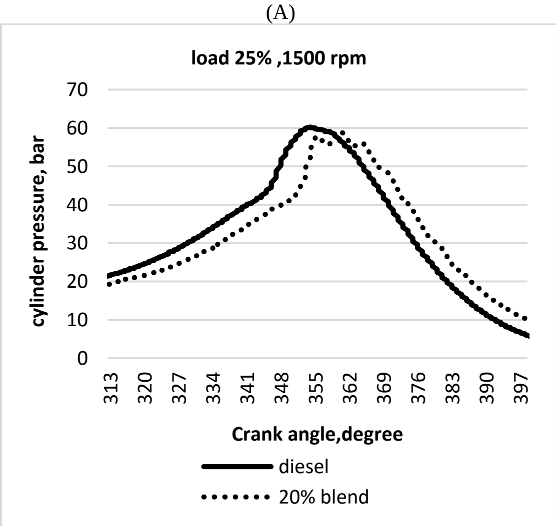

(B)

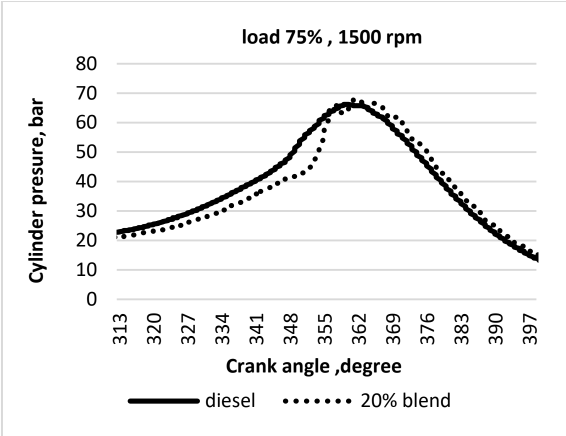

(C)

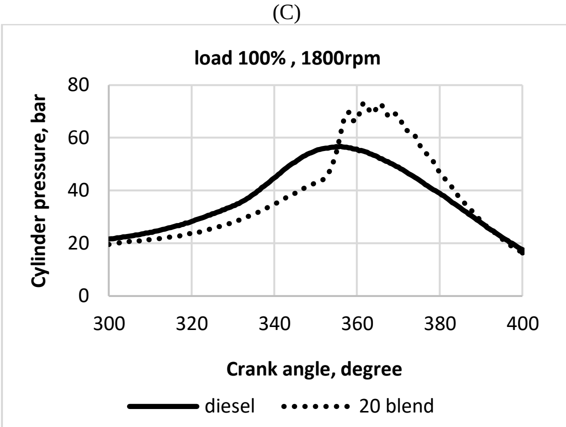

(D)

Figure 8. Variation of cylinder pressure with crank angle for diesel and biodiesel blend at 10, 25, 75 and 100% of engine load.

Conclusions

Biodiesel produced from castor oil can be used as alternative fuel in diesel engines. Castor biodiesel blend B20 was tested in a diesel engine at a constant engine speed of 1500 rpm and variable engine loads. Castor biodiesel was produced from raw oil by transesterification process. Experimental results were compared with diesel fuel and show the following**:**

- Methanol to oil molar ratio 6:1, 70 min reaction time, and 70 ^{o}C reaction temperature were the best conditions for castor biodiesel production using transesterification process.
- Viscosity is directly proportional with increase amount of castor biodiesel in blends. Castor biodiesel viscosity was higher compared with standard diesel. We use biodiesel blend B20 because it gave reasonable viscosity near to diesel.
- Castor biodiesel blend B20 showed a decrease in specific fuel consumption with respect to diesel fuel by about 2% at 50% of engine load.
- Biodiesel blend B20 showed an increase in engine thermal efficiency in comparison to diesel fuel by about 2% at 50% of engine load.
- There was an increase in exhaust gas temperature for biodiesel blend about diesel fuel. Its values for diesel and biodiesel blend were 394 and 491°C at full load.
- The smoke points for biodiesel blends were affected by the oxygen content. Increase in smoke points about

diesel oil are 23, 30, 40, 55 and 257% for B10, B20, B30, B40 and B100.

- The cylinder peak pressure for diesel fuel was 55 MPa at a crank angle of 5° before TDC. In case of biodiesel blend, the cylinder peak pressure was 65 MPa at a crank angle of 5° after TDC at full load.
- Castor biodiesel blends can be run up to 20% biodiesel volume with diesel fuel without any engine modifications because of engine performance, emission and combustion were close to diesel fuel.
- Biodiesel produced from non-edible castor oil could be a good alternative fuel for diesel engine without any modification.

References

[1] Balat M., " Current alternative engine fuels", Energy Sources 2005, 27(6): 569-77.

[2] O. S. Valente, M. J. da Silva, V. M. Pasa, C. R. Belchior, J. R. Sodre "Fuel consumption and emissions from a diesel power generator fuelled with castor oil and soybean biodiesel", Fuel, Vol.89, pp.3637-3642, 2010.

[3] H. Y. Shrirame, N. L. Panwar, B.R. Bamniya, "Bio Diesel from Castor Oil-A Green Energy Option", Low Carbon Economy Journal, Vol.2, pp.1-6, 2011.

[4] D. Vashist, M. Ahmad, "Performance of single-cylinder compression ignition engine with indigenous castor oil bio diesel", International Journal of Automotive Engineering and Technologies, Vol.3, No.2, pp.45-53, 2014.

[5] P. Lingfa, "A Comparative Study on Performance and Emission Characteristics of Compression Ignition Engine using Biodiesel derived from Castor Oil", International Journal of Innovative Research in Science, Engineering and Technology, Vol.3, No.4, pp.124-128, March 2014.

[6] M. M. Kulkarni, V. S. Dhumal, "Performance Characteristics of Single Cylinder DI Diesel Engine Fueled with Castor Biodiesel", International Journal of Engineering Research and Technology, Vol.1, No.10, pp.1-3, December 2012.

[7] Ingle S., Nandedkar V. M.,"Indigenous Castor Oil Biodiesel an alternative fuel for Diesel Engines", International Journal of Mechanical and Industrial Engineering (IJMIE), Vol.2, No.2, pp.62-64, 2012.

[8] P. Sreenivas, V. R. Mamilla, K. C. Sekhar, "Development of Biodiesel from Castor Oil", International Journal of Energy Science, Vol.1, No.3, pp.192-197, 2011.

[9] S. S. Ingle, V.M. Nandedkar, "Castor oil Biodiesel an alternative fuel for Diesel in Compression Ignition Engine", IOSR Journal of Mechanical and Civil Engineering (IOSR-JMCE), Vol.1, No.10, pp.10-13, December 2012.

[10] M. S. Soliman, Hany A. Mohamed, O.A. Abdelhafez, A.M. Nassibe, "Production and characterization of biodiesel fuels from castor oil utilizing methanol", International Research Journal of Engineering Science, Technology and Innovation, Vol.3, No.2, pp.17-23, April 2014.

[11] S. Jafarmadar, J. Pashae,"Experimental Study of the Effect of Castor Oil Biodiesel Fuel on Performance and Emissions of Turbocharged DI Diesel", International Journal of Engineering, Vol.26, No.8, pp.905-912, August 2013.

[12] M. S. Islam, A. Ahmed, A. Islam, S. Abdul Aziz, L. C. Xian, M. Mridha, "Study on Emission and Performance of Diesel Engine using Castor Biodiesel", Hindawi Publishing Corporation, Journal of Chemistry, Vol.1, No.10, pp.1-8, December 2014.

[13] M.H. Shojaeefard, M. Efgahni, F. Meisami, A. Barari, "Experimental Investigation on Performance and Exhaust Emissions of Castor Oil Biodiesel from a diesel Engine", Environmental Technology Journal, Vol.34, Issue 13-14, pp.2019-2026, 2013.

[14] L. D. Monteiro, G. P. Junior, J. A. Velasquez, D. S. Rocha, A. V. Bueno, "Performance Impact of the application of castor oil biodiesel in diesel engines", Eng. Agric., Jabooticabal, Vol.33, No.6, pp.1165-1171, November 2013.

[15] A. S. Kumara, D. Maheswar, K. K. Reddy, " Comparision of Diesel Engine Performance and Emissions from Neat and Transesterified Cotton Seed Oil ", Jordon Journal of Mechanical and Industrial Engineering ,Vol.3, No.3, pp.190-197, 2009.

[16] A. Amin, A. Gadallah, A.K. El Morsi, N.N. El-Ibiari, G.I. El-Diwani, "Experimental and empirical study of diesel and castor biodiesel blending effect, on kinematic viscosity, density and calorific value", Egyptian Journal of petroleum, Vol.25, pp.509-514, 2016.

[17] M. Das, M. Sarkar, A. Datta, A. K. Santra, " An experimental study on the combustion, performance and emission characteristics of a diesel engine fuelled with diesel-castor oil biodiesel blends", Renewable Energy, Vol.119, pp.174-184, 2018.

[18] A. Deep, S. S. Sandhu, S. Chander, " Experimental investigations on the influence of fuel injection timing and pressure on single cylinder C.I. engine fueled with 20% blend of castor biodiesel in diesel", Fuel, Vol.210, pp.15-22, 2017.

[19] S.T. Keera, S.M. El Sabagh, A.R. Taman, " Castor oil biodiesel production and optimization", Egyptian journal of Petroleum, Vol.27, pp.979-984, 2018.

[20] P. Berman, S. Nizri, Z. Wiesman, " Castor oil biodiesel and its blends as alternative fuel", Biomass and Bioenergy, Vol.35, pp.2861-2866, 2011.

[21] A.V. Bueno, M. P. Pereira, J. V. Pontes, F. M. de Luna, C. L. Jr, " Performance and emissions characteristics of castor oil biodiesel fuel blends", Applied Thermal Engineering, Vol.125, pp.559-566, 2017.

[22] M. Arunkumar, M. Kannan, G. Murali, " Experimental studies on engine performance and emission characteristics using castor biodiesel as fuel in CI engine", Renewable Energy, Vol.131, pp.737-744, 2019.

[23] S. A. Hajlari, B. Najafi, S. F. Ardabili, " Castor oil, a source for biodiesel production and its impact on the diesel engine performance", Renewable Energy Focus, Vol.28, pp.1-10, 2019.

[24] O. Aboelazayem, N. Sh. El-Gendy, A. A. Abdel-Rehim, F. Ashour, M. A. Sadek, " Biodiesel production from castor oil in Egypt: Process optimization, kinetic study, diesel engine performance and exhaust emissions analysis", Energy, Vol.157, pp.843-852, 2018.

[25] S. S. Ingle, V. M. Nandedkar, M. V. Nagarhalli, "Prediction of Performance and Emission of Castor Oil Biodiesel in Diesel Engine", International Journal of Mechanical and Production Engineering, Vol.1, No.1, pp.16-18, July 2013.

[26] D. Vashist, M. Ahmad," Comparative Study of Performance and Emission characteristics of a Diesel Engine fueled by Castor and Jatropha Methyl Ester with the help of T Test", International Journal of Automotive Engineering , Vol.2, No.2, pp.61-67, April 2012.

[27] R. S. Kumbar, P. S. Patil, O. Hebbal, "Experimental Investigation of Performance and Combustion Characteristics on a single cylinder LHR Engine using Diesel, and Castor Biodiesel", International Journal of Research in Engineering and Technology, Vol.2, No.7, pp.207-211, July 2013.

[28] N. L. Panwar, H. Y. Shrirame, N. S. Rathore, S. Jindal, A. K. Kurchania, "Performance evaluation of a diesel engine fueled with methyl ester of castor seed oil", Applied Thermal Engineering , Vol.30, pp.245-249, 2010.

[29] M. H. Shojaeefard, M. M. Etghani, M. Akbari, A. Khalkhali, B. Ghobadian, "Artificial neural networks based prediction of performance and exhaust emissions in direct injection engine using castor oil biodiesel- diesel blends", Journal of

Renewable and Sustainable Energy,Vol.4, 063130, pp.1-19, 2012.

[30] E. I. Bello, A. Makanju, "Production, Characterization and Evaluation of Castor oil Biodiesel as Alternative Fuel for Diesel Engines", Journal of Emerging Trends in Engineering and Applied Sciences (JETEAS),Vol.2, No.3, pp.525-530, 2011.

[31] S. V. Lahane, K. Subramanian, " Effect of different percentages of biodiesel-diesel blends on injection, spray, combustion, performance and emission characteristics of a diesel engine", Fuel ,Vol.139, No.10, pp. 537-545, 2015.

[32] ASTM D1322-12., "Standard test method for smoke point of kerosene and aviation turbine fuel", ASTM International, West Conshohocken, 2012, pp. 527-533.

[33] M. O. Kareem, G. D. Pena, A Raj, M. M. Alrefaai, S. Stephen, T. Anjana, "Effects of Neem Oil-Derived Biodiesel Addition to Diesel on the Reactivity and Characteristics of Combustion-Generated Soot ", Energy and Fuels,Vol.31, No.10, pp. 10822-10832, 2017.

JJMIE

Volume 12, Number 4, December. 2018
ISSN 1995-6665
Pages 269 - 279

Jordan Journal of Mechanical and Industrial Engineering

Mathematical Modelling for Reliability Measures to Sugar Mill Plant Industry

Amit Kumar[a], Mangey Ram[b*]

[a]Department of Mathematics, Lovely Professional University, Punjab, India
[b]Department of Mathematics; Computer Science and Engineering, Graphic Era Deemed to be University Dehradun, Uttarakhand, India
Received 1 Feb. 2018

Abstract

The present paper aims to investigate a sugar mill plant for obtaining its various performance measures. A sugar plant comprises many components, such as feeding system, evaporation system and crystallization system. These systems relate to each other in series configuration. Further, the feeding system consists of cutting, crushing, bagasse system, and heat generating system as well. After the raw material pass through the feeding system, output goes to be evaporated and then pass through the crystallization for the final output, which is sugar. A mathematical mode is devoloped, using Markov process, for evaluating the various reliability measures e.g. availability, reliability, MTTF and expected profit, of the sugar plant. Critical components is obtained through sensitivity analysis for the same. The information regarding failure rates and repair rate of various subsystems are taken from their past records. The results of this research show that the reliability of the sugar mill plant is equally sensitive with respect to all considered failures except bagesses carrying system. Also, the MTTF of the sugar mill are the most affected by the failiure of evaporation and crystallization process.

Keywords: Performance measures; supplementary variable technique; Markov birth-death process; transition state probability; crystallization system; feeding system;

1. Introduction

As technology grows, the complications of the industrial systems increase rapidly. So, to maintain this devolvement, one must make the systems reliable (as much as possible). Therefore, the main task of the management of the system is to optimize the reliability for the same. A lot of research has been done in context of industrial system for improving the various performance measures of the systems [1, 2, and 3]. Sugar plant is one of the examples of such type of system. The role of reliability theory in complex industrial systems is widely studied in the literature of reliability. A sugar plant is such a complex system which is studied in this work. Many researchers, including Kakar et. al [4] studied a sulphate juice pump (SJP) system working in a sugar mill with the assumption that repair equipment may also fail during the repair and found the availability, MTSF and busy period of the system. Sachdeva et. al [5] presented a reliability study of the pulping system of paper industry using Petri nets technique and found the maintenance strategies to enhance the performance of the pulping system, and thus found ‘how the maintenance and operation cost reduce?’. Tiwari et. al [6] developed a mathematical model for a steam generating system of thermal power plant and analyzed the performance of various subsystems of them. Gupta et. al [7] found the various reliability measures of a coal handling unit of a thermal power plant using Markov process. Khanduja et. al [8] have discussed the performance evaluation for washing unit of a paper plant and analysed the digesting system for the same by using genetic algorithm. Besides, the effect of genetic algorithm, various system parameters, such as steady state availability is also calculated. Kumar and Ram [9] evaluated some important reliability characteristics of a coal handling unit of a thermal power plant. They also found the expected profit for the same. Ram et. al [10] analysed and evaluated the reliability measures for various engineering models under the concept of Gumbel-Hougaard family copula. Mariajayaprakash and Senthilvelan [11] discussed the failures of the fuel feeding system which is frequently occurring in the co-generation boiler, of a sugar mill, and gives the solution to overcome these failures. Gonzalez et. al [12] gave a practical view about the behaviour of an industrial (Bioethanol plant) system to access its reliability and availability and conclude that cost estimation is a key factor that should be considered. Kumar et. al [13] analysed the crushing system of a sugar mill with general repair distribution and constant failure rates and draw some important reliability measures. Kumar et. al [14] discussed refining system of a sugar mill which consist four subsystems and analysed the performance. Bakhshesh et. al [15] investigated the accumulation and deposition of solid particles in a pipeline with asymmetric branches by using Lagrangian method and find the effects of some

* Corresponding author e-mail: drmrswami@yahoo.com.

Important parameters on it, and concluded that the dependency is higher at high flow velocities. Patel and Singh [16] studied a four stroke diesel engine using blended methyl ester (B50) in order to optimize nitrous oxide emission with addition of di-tert-butyl peroxide with cetane improver and found 1% di-tert-butyl peroxide would give the optimum results for nitrous oxide reduction in the diesel engine.

Here, in this paper the authors have developed a mathematical model of a sugar plant which consists of feeding system, evaporation and crystallization process. The considered system may work in three different states, which are good state, degraded state, and failed state, throughout the process of sugar making. The flow diagram and transition state diagram are shown in Fig. 1(a) and 1(b) respectively.

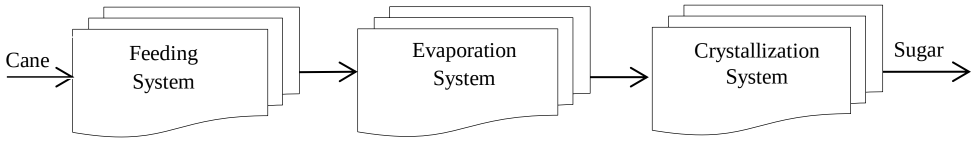

Figure 1(a). System configuration

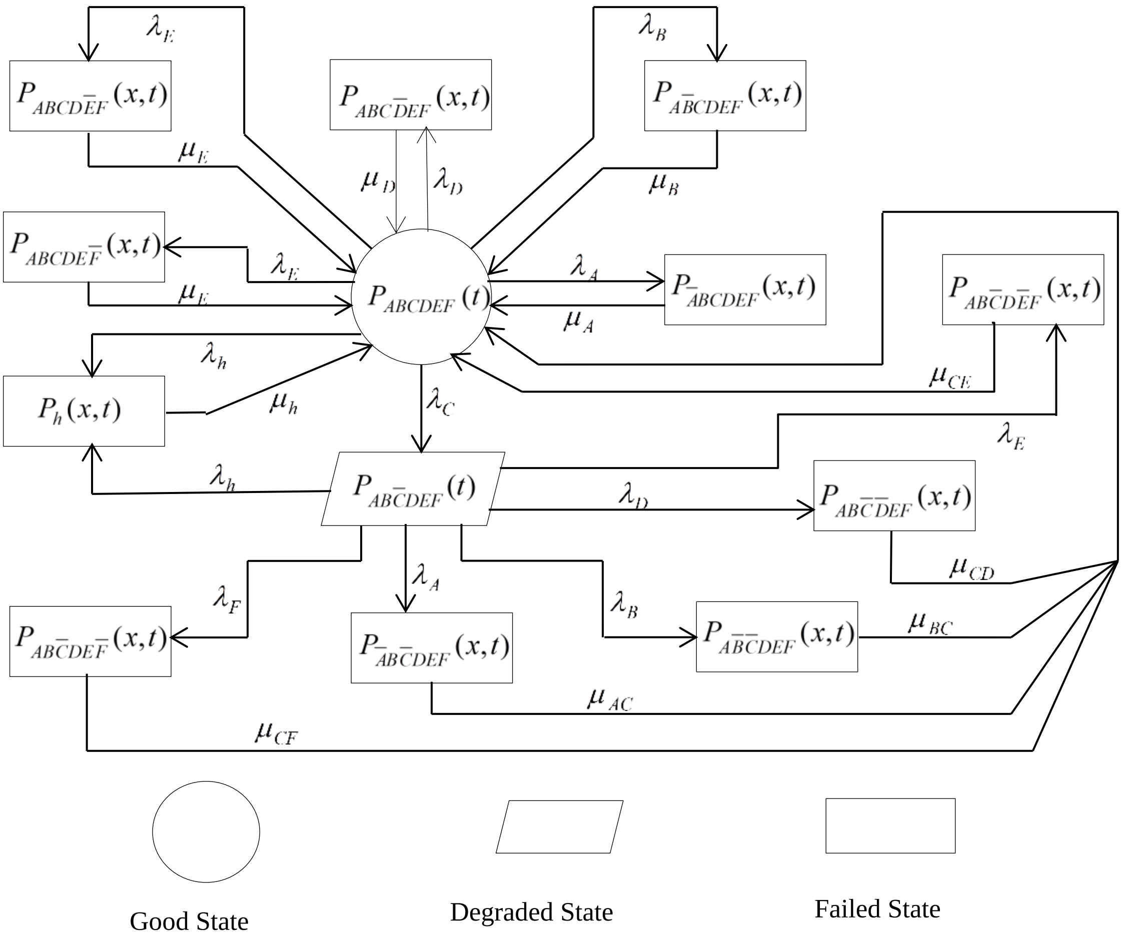

Figure 1(b). Transition State diagram

2. Assumptions and Notations

The following assumptions are used throughout the modelling

Initially all the components of the considered system are in good condition and hence it will work with full efficiency.

The system can also work in a reduced capacity (i.e. in degraded state).

At every instant repair, facilities are available.

All repair and failure rates are taken to be constant.

Raw material (i.e. cane) is always available to produce sugar.

The following notations have been used throughout the problem

$P_{ABCDEF}(t)$	The probability that at any instant *t* the plant is working with full efficiency.
$P_{AB\bar{C}DEF}(t)$	The probability that at any instant *t*, the plant is working in degraded state with failed bagasse carrying system.
$P_{\bar{A}BCDEF}(x,t)$	The probability that at any instant *t*, the plant is failed by the failure of cutting process.
$P_{A\bar{B}CDEF}(x,t)$	The probability that at any instant *t*, the plant is failed by the failure of crushing process.
$P_{ABC\bar{D}EF}(x,t)$	The probability that at any instant *t*, the plant is failed by the failure of heat generating process.
$P_{ABCD\bar{E}F}(x,t)$	The probability that at any instant *t*, the plant is failed by the failure of evaporation process.
$P_{ABCDE\bar{F}}(x,t)$	The probability that at any instant *t*, the plant is failed by the failure of crystallization process.
$P_{\bar{A}B\bar{C}DEF}(x,t)$	The probability that at any instant *t*, the plant is failed by the failure of cutting process and bagasse carrying process.
$P_{A\bar{B}\bar{C}DEF}(x,t)$	The probability that at any instant *t*, the plant is failed by the failure of crushing process and bagasse carrying process.
$P_{AB\bar{C}\bar{D}EF}(x,t)$	The probability that at any instant *t*, the plant is failed by the failure of heat generating process and bagasse carrying process.
$P_{AB\bar{C}D\bar{E}F}(x,t)$	The probability that at any instant *t*, the plant is failed by the failure of evaporation process and bagasse carrying process.
$P_{AB\bar{C}DE\bar{F}}(x,t)$	The probability that at any instant *t*, the plant is failed by the failure of crystallization process and bagasse carrying process.
$P_h(x,t)$	The probability that at any instant *t*, the plant is failed by the human error.
$\lambda_A / \lambda_B / \lambda_C / \lambda_D / \lambda_E / \lambda_F / \lambda_h$	Failure rate of cutting process/crushing process/ bagasse carrying process/ heat generating process/evaporation process/crystallization process/human error.
$\mu_A / \mu_B / \mu_C / \mu_D / \mu_E / \mu_F / \mu_h$	Repair rate of cutting process/ crushing process/ bagasse carrying process/ heat generating process/ evaporation process/ crystallization process/ human failure.
$\mu_{AC} / \mu_{BC} / \mu_{CD} / \mu_{CE} / \mu_{CF}$	Simultaneous repair rate of cutting process and bagasse carrying process/ crushing process and bagasse carrying process/ heat generating process and bagasse carrying process/ evaporation process and bagasse carrying process/ crystallization process and bagasse carrying process.
K_1 / K_2	Revenue/service cost per unit time from the plant.
t/s	Time scale variable in years/ Laplace transforms variable.

3. Mathematical Formulation and Solution of the Considered Sugar Plant System

With the aid of Markov birth-death process the following set of intro-differential equation is developed

$$\left(\frac{\partial}{\partial t}+\lambda_A+\lambda_B+\lambda_C+\lambda_D+\lambda_E+\lambda_F+\lambda_h\right)P_{ABCDEF}(t)=\sum_{i,j}\int_0^\infty \mu_i P_j(x,t)dx \tag{1}$$

where $i = A, B, D, E, F, h, CF, AC, BC, CD, CE;\ j = \bar{A}BCDEF,$
$A\bar{B}CDEF, ABC\bar{D}EF, ABCD\bar{E}F, ABCDE\bar{F}, h, AB\bar{C}DE\bar{F},$
$\bar{A}B\bar{C}DEF, A\bar{B}\bar{C}DEF, AB\bar{C}\bar{D}EF, AB\bar{C}D\bar{E}F$

$$\left(\frac{\partial}{\partial t}+\lambda_A+\lambda_B+\lambda_D+\lambda_E+\lambda_F+\lambda_h\right)P_{AB\bar{C}DEF}(t)=\lambda_C P_{ABCDEF}(t) \tag{2}$$

$$\left(\frac{\partial}{\partial x}+\frac{\partial}{\partial t}+\mu_k\right)P_l(x,t)=0 \tag{3}$$

where $k = A, B, D, E, F, h, CF, AC, BC, CD, CE;$
$l = \bar{A}BCDEF, A\bar{B}CDEF, ABC\bar{D}EF, ABCD\bar{E}F, ABCDE\bar{F}, h, AB\bar{C}DE\bar{F},$
$\bar{A}B\bar{C}DEF, A\bar{B}\bar{C}DEF, AB\bar{C}\bar{D}EF, AB\bar{C}D\bar{E}F$

Boundary conditions

$$P_j(0,t)=\lambda_k P_l(t) \tag{4}$$

where $j = \bar{A}BCDEF, A\bar{B}CDEF, ABC\bar{D}EF, ABCD\bar{E}F, ABCDE\bar{F}, h,$
$AB\bar{C}DE\bar{F}, \bar{A}B\bar{C}DEF, A\bar{B}\bar{C}DEF, AB\bar{C}\bar{D}EF, AB\bar{C}D\bar{E}F;$
$k = A, B, D, E, F, h, F, A, B, D, E;$
$l = ABCDEF, ABCDEF, ABCDEF, ABCDEF, ABCDEF, ABCDEF,$
$AB\bar{C}DEF, AB\bar{C}DEF, AB\bar{C}DEF, AB\bar{C}DEF, AB\bar{C}DEF$

Initial condition

$$P_{ABCDEF}(t)=\begin{cases}1 & ,t=0\\ 0 & ,\text{othetwise}\end{cases}$$ and all other state probabilities are zero at t = 0 (5)

Taking Laplace transformation from equations (1) to (4), one gets

$$(s+\lambda_A+\lambda_B+\lambda_C+\lambda_D+\lambda_E+\lambda_F+\lambda_h)\bar{P}_{ABCDEF}(s)=1+\sum_{i,j}\int_0^\infty \mu_i \bar{P}_j(x,s)dx \tag{6}$$

$$(s+\lambda_A+\lambda_B+\lambda_D+\lambda_E+\lambda_F+\lambda_h)\bar{P}_{AB\bar{C}DEF}(s)=\lambda_C\bar{P}_{ABCDEF}(s) \tag{7}$$

$$\left(\frac{\partial}{\partial x}+s+\mu_k\right)\bar{P}_l(x,s)=0 \tag{8}$$

Boundary conditions

$$P_j(0,t)=\lambda_k P_l(t) \tag{9}$$

Solving equations from (6) to (8) with the help of boundary conditions, we get the transition state probabilities as

$$\bar{P}_{ABCDEF}(s)=\frac{1}{[H_1-H_3-H_4]} \tag{10}$$

$$\bar{P}_{AB\bar{C}DEF}(s)=\frac{\lambda_C}{H_2}\bar{P}_{ABCDEF}(s) \tag{11}$$

$$\bar{P}_{\bar{A}BCDEF}(s)=\frac{\lambda_A}{(s+\mu_A)}\bar{P}_{ABCDEF}(s) \tag{12}$$

$$\bar{P}_{A\bar{B}CDEF}(s)=\frac{\lambda_B}{(s+\mu_B)}\bar{P}_{ABCDEF}(s) \tag{13}$$

$$\bar{P}_{ABC\bar{D}EF}(s)=\frac{\lambda_D}{(s+\mu_D)}\bar{P}_{ABCDEF}(s) \tag{14}$$

$$\bar{P}_{ABCD\bar{E}F}(s)=\frac{\lambda_E}{(s+\mu_E)}\bar{P}_{ABCDEF}(s) \tag{15}$$

$$\bar{P}_{ABCDE\bar{F}}(s)=\frac{\lambda_F}{(s+\mu_F)}\bar{P}_{ABCDEF}(s) \tag{16}$$

$$\bar{P}_h(s)=\frac{\lambda_h}{(s+\mu_h)}\bar{P}_{ABCDEF}(s) \tag{17}$$

$$\bar{P}_{AB\bar{C}DE\bar{F}}(s)=\frac{\lambda_C\lambda_F}{H_2(s+\mu_{CF})}\bar{P}_{ABCDEF}(s) \tag{18}$$

$$\bar{P}_{\bar{A}B\bar{C}DEF}(s)=\frac{\lambda_A\lambda_C}{H_2(s+\mu_{AC})}\bar{P}_{ABCDEF}(s) \tag{19}$$

$$\overline{P}_{A\overline{B}\overline{C}DEF}(s)=\frac{\lambda_B\lambda_C}{H_2(s+\mu_{BC})}\overline{P}_{ABCDEF}(s) \tag{20}$$

$$\overline{P}_{AB\overline{C}\overline{D}EF}(s)=\frac{\lambda_C\lambda_D}{H_2(s+\mu_{CD})}\overline{P}_{ABCDEF}(s) \tag{21}$$

$$\overline{P}_{AB\overline{C}D\overline{E}F}(s)=\frac{\lambda_C\lambda_E}{H_2(s+\mu_{CE})}\overline{P}_{ABCDEF}(s) \tag{22}$$

Where

$$H_1=(s+\lambda_A+\lambda_B+\lambda_C+\lambda_D+\lambda_E+\lambda_F+\lambda_h),\ H_2=(s+\lambda_A+\lambda_B+\lambda_D+\lambda_E+\lambda_F+\lambda_h)$$

$$H_3=\frac{\lambda_A\mu_A}{(s+\mu_A)}-\frac{\lambda_B\mu_B}{(s+\mu_B)}-\frac{\lambda_D\mu_D}{(s+\mu_D)}-\frac{\lambda_E\mu_E}{(s+\mu_E)}-\frac{\lambda_F\mu_F}{(s+\mu_F)}-\frac{\lambda_h\mu_h}{(s+\mu_h)}$$

$$H_4=\frac{\lambda_C\lambda_F\mu_{CF}}{H_2(s+\mu_{CF})}-\frac{\lambda_A\lambda_C\mu_{AC}}{H_2(s+\mu_{AC})}-\frac{\lambda_B\lambda_C\mu_{BC}}{H_2(s+\mu_{BC})}-\frac{\lambda_C\lambda_D\mu_{CD}}{H_2(s+\mu_{CD})}-\frac{\lambda_C\lambda_E\mu_{CE}}{H_2(s+\mu_{CE})}$$

From the transition state diagram, the probability that the sugar plant system is in up and downstate is given by

$$\overline{P}_{up}(s)=\overline{P}_{ABCDEF}(s)+\overline{P}_{AB\overline{C}DEF}(s) \tag{23}$$

$$\overline{P}_{down}(s)=\sum_j \overline{P}_j(s) \tag{24}$$

where $j=\overline{A}BCDEF,\ A\overline{B}CDEF,\ ABC\overline{D}EF,\ ABCD\overline{E}F,\ ABCDE\overline{F},\ \overline{A}B\overline{C}DEF,$
$A\overline{B}\overline{C}DEF,\ AB\overline{C}\overline{D}EF,\ AB\overline{C}D\overline{E}F,\ AB\overline{C}DE\overline{F},\ h$

4. Particular Cases and Numerical Computations

4.1. Availability Assessment

The time dependent availability of the sugar mill plant can be obtained (as given below) by putting the value different failure rates as $\lambda_E=0.21,\ \lambda_F=0.21,$ $\lambda_h=0.11\ \lambda_A=0.04, \lambda_B=0.04,$ $\lambda_C=0.045, \lambda_D=0.09$ and all the repair are taken as one (i.e. 100% maintenance are taken into consideration) in (23) then taking inverse Laplace transform, we get the availability of sugar mill plant as

$$P_{up}(t)=0.4107799801\,e^{(-1.703033898t)} - 0.0025783751\ 0e^{(-0.7380277981t)} + 0.5917983951e^{(-0.0039383035\ \ 45\ t)} \tag{25}$$

Varying time unit t in the equation (25), we get the following Table 1 and Fig. 2 for availability for the sugar plant system.

Table 1. Availability vs. Time

Time (t)	Availatbility
0	1
1	0.66305
2	0.60019
3	0.58704
4	0.58286
5	0.58027
6	0.57796
7	0.57569
8	0.57343
9	0.57118
10	0.56894

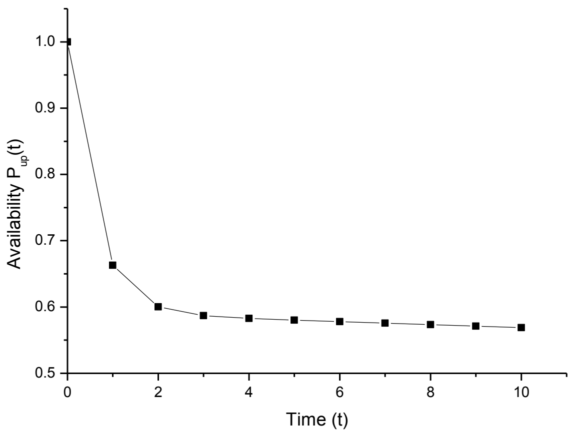

Figure 2. Availability vs. of Time

4.2. Reliability Assessment

Reliability investigation is one of the fundamental measures of ensuring safety in various industry/operations. However, the reliability assessment of these systems is too complex due to their multistate break down and multistate functionality. Reliability of a system is likelihood for performing its function for a given period of time under some specific/operating conditions. The reliability of the sugar mill plant will be obtained by taking its various failure rates as

$$\lambda_h=0.11, \lambda_A=0.04, \lambda_B=0.04, \lambda_C=0.045,$$
$$\lambda_D=0.09, \lambda_E=0.21, \lambda_F=0.21$$

and all repairs as zero (i.e. for calculating reliability of the considered system, the maintenance of its units are not taken into consideration) in (23) and taking the inverse Laplace transform, the reliability of the system is given as

$$R(t)=\mathrm{e}^{(-0.7450t)}+2\mathrm{e}^{(0.7225t)}\sinh(0.0225\ t) \tag{26}$$

Now varying time unit t in the equation (26), one gets the Table 2 and Fig. 3 for reliability.

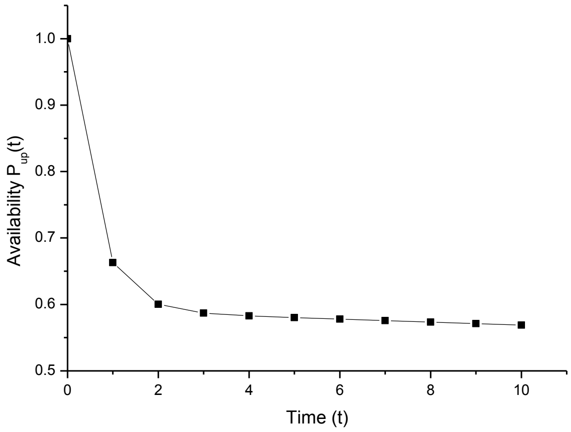

Figure 3. Reliability vs. Time

Table 2. Reliability vs. Time

Time (t)	Reliability $R(t)$
0	1.00000
1	0.49658
2	0.24659
3	0.12245
4	0.06081
5	0.03019
6	0.01499
7	0.00744
8	0.00369
9	0.00183
10	0.00091

4.3. Mean Time to Failure (MTTF) Assessment

Basically MTTF is the average failure time for an individual component. Mathematically it is calculated as

$$MTTF = \int_0^\infty t f(t)dt = \int_0^\infty R(t)dt = \lim_{s\to 0} \overline{R}(s)$$

Where $f(t)$ is the probability density function and $R(t)$ is system reliability

The MTTF of the considered system can be obtained by using (23) in the above expression of MTTF. Varying the failure rates one by one in the MTTF expression obtained in this step, Table 3 and corresponding Fig. 4 is obtained for MTTF of the considered system as:

4.4. Sensitivity Assessment

a) Sensitivity of Reliability

We carry out the sensitivity assessment of the reliability of sugar plant by differentiating the reliability expression with respect to various failure rates, and then setting

$$\lambda_A = 0.04, \lambda_B = 0.04, \lambda_C = 0.045, \lambda_D = 0.09,$$
$$\lambda_E = 0.21, \lambda_F = 0.21, \lambda_h = 0.11$$

we get

$$\frac{\partial R(t)}{\partial \lambda_A}, \frac{\partial R(t)}{\partial \lambda_B}, \frac{\partial R(t)}{\partial \lambda_C}, \frac{\partial R(t)}{\partial \lambda_D}, \frac{\partial R(t)}{\partial \lambda_E}, \frac{\partial R(t)}{\partial \lambda_F}, \frac{\partial R(t)}{\partial \lambda_h}.$$

Now, setting t = 0 to 10 units of time in these partial derivatives, one can obtain the Table 4 and Fig. 5 respectively.

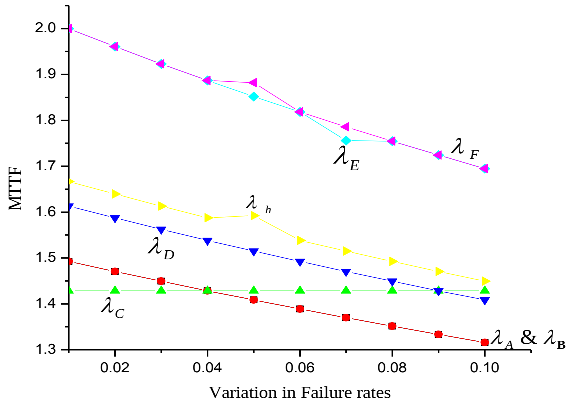

Figure 4. MTTF vs. Failure rates

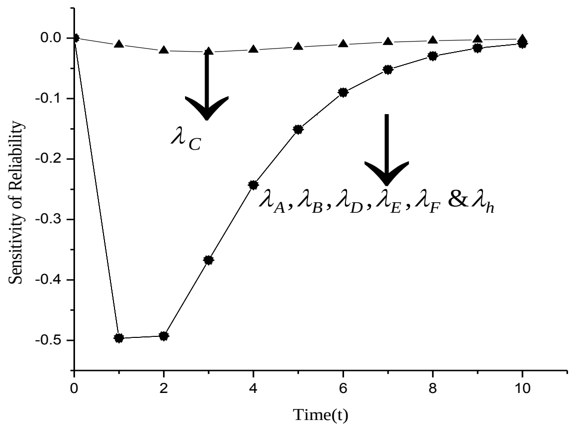

Figure 5. Sensitivity of Reliability vs. Time

Table 3. MTTF vs. Failure rates

Variations in	MTTF with respect to failure rates						
$\lambda_A, \lambda_B, \lambda_C, \lambda_D, \lambda_E, \lambda_F, \lambda_h$	λ_A	λ_B	λ_C	λ_D	λ_E	λ_F	λ_h
0.01	1.49253	1.49253	1.42857	1.61290	2.00000	2.00000	1.66666
0.02	1.47058	1.47058	1.42857	1.58730	1.96078	1.96078	1.63934
0.03	1.44927	1.44927	1.42857	1.56250	1.92307	1.92307	1.61290
0.04	1.42857	1.42857	1.42857	1.53846	1.88679	1.88679	1.58730
0.05	1.40845	1.40845	1.42857	1.51515	1.85185	1.88185	1.59250
0.06	1.38888	1.38888	1.42857	1.49253	1.81818	1.81818	1.53846
0.07	1.36986	1.36986	1.42857	1.47058	1.75571	1.78571	1.51515
0.08	1.35135	1.35135	1.42857	1.44927	1.75438	1.75438	1.49253
0.09	1.33333	1.33333	1.42857	1.42857	1.72413	1.72413	1.47058
0.10	1.31578	1.31578	1.42857	1.40845	1.69491	1.69491	1.44927

b) Sensitivity of MTTF Assessment

By differentiating MTTF expression with respect to failure rates and then putting various failure rates as $\lambda_A = 0.04, \lambda_B = 0.04, \lambda_C = 0.045, \lambda_D = 0.09$ $, \lambda_E = 0.21, \quad \lambda_F = 0.21, \lambda_h = 0.11$ we get the values of

$$\frac{\partial(MTTF)}{\partial\lambda_A}, \frac{\partial(MTTF)}{\partial\lambda_B}, \frac{\partial(MTTF)}{\partial\lambda_C}, \frac{\partial(MTTF)}{\partial\lambda_D}, \frac{\partial(MTTF)}{\partial\lambda_E}, \frac{\partial(MTTF)}{\partial\lambda_F}, \frac{\partial(MTTF)}{\partial\lambda_h}.$$

Varying the failure rates one by one as 0.01, 0.02, 0.03, 0.04, 0.05, 0.06, 0.07, 0.08, 0.09 in these partial derivatives, one can obtain the Table 5 and Fig. 6 respectively.

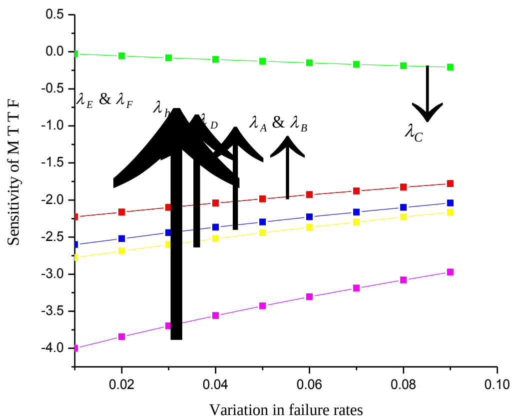

Figure 6. Sensitivity of MTTF vs. Failure rates

4.5. Expected Profit Assessment

The profit function [7] for the sugar plant during the time duration [0,t) is given as

$$E_P(t) = K_1 \int_0^t P_{up}(t)dt - tK_2 \tag{27}$$

Using Equation (25) in (27), profit function for the same set of parameters is given by

$$\begin{aligned} E_p(t) = \{K_1[&-0.2412048172\ e^{(-1.703033\,898\ t)} \\ &+ 0.0034936016\,05e^{(-0.7380277981\ )} \\ &- 150.2673393\ e^{(-0.003938303545\ t)} \\ &+ 150.5050505] - K_2\, t\} \end{aligned} \tag{28}$$

Now taking K_1= 1 and K_2 as 0.1, 0.2, 0.3, 0.4, 0.5 and 0.6 respectively than varying t in (28) one get the Table 6 and correspondingly Fig. 7.

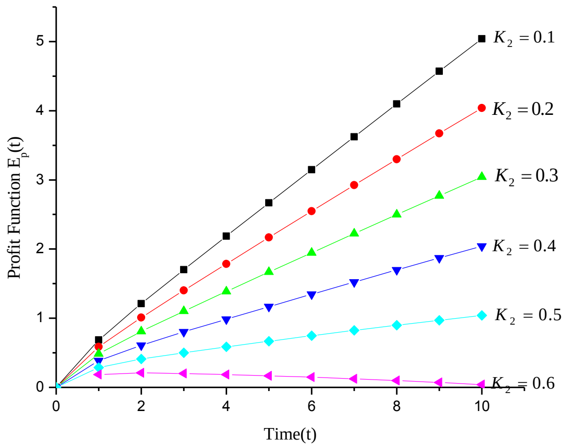

Figure 7. Expected profit vs. Failure rates

Table 4. Sensitivity of Reliability vs. Time

Time (t)	$\frac{\partial R(t)}{\partial\lambda_A}$	$\frac{\partial R(t)}{\partial\lambda_B}$	$\frac{\partial R(t)}{\partial\lambda_C}$	$\frac{\partial R(t)}{\partial\lambda_D}$	$\frac{\partial R(t)}{\partial\lambda_E}$	$\frac{\partial R(t)}{\partial\lambda_F}$	$\frac{\partial R(t)}{\partial\lambda_h}$
0	0	0	0	0	0	0	0
1	-0.49658	-0.49658	-0.01084	-0.49658	-0.49658	-0.49658	-0.49658
2	-0.49319	-0.49319	-0.02090	-0.49319	-0.49319	-0.49319	-0.49319
3	-0.36736	-0.36736	-0.02267	-0.36736	-0.36736	-0.36736	-0.36736
4	-0.24324	-0.24324	-0.01943	-0.24324	-0.24324	-0.24324	-0.24324
5	-0.15098	-0.15098	-0.01464	-0.15098	-0.15098	-0.15098	-0.15098
6	-0.08997	-0.08997	-0.01016	-0.08997	-0.08997	-0.08997	-0.08997
7	-0.05212	-0.05212	-0.00667	-0.05212	-0.05212	-0.05212	-0.05212
8	-0.02958	-0.02958	-0.00420	-0.02958	-0.02958	-0.02958	-0.02958
9	-0.01652	-0.01652	-0.00256	-0.01652	-0.01652	-0.01652	-0.01652
10	-0.00911	-0.00911	-0.00152	-0.00911	-0.00911	-0.00911	-0.00911

Table 5. Sensitivity of MTTF vs. Failure rates

Variations in λ_A, λ_B, λ_h, λ_E, λ_{CCF}, λ_S	$\frac{\partial(MTTF)}{\partial\lambda_A}$	$\frac{\partial(MTTF)}{\partial\lambda_B}$	$\frac{\partial(MTTF)}{\partial\lambda_C}$	$\frac{\partial(MTTF)}{\partial\lambda_D}$	$\frac{\partial(MTTF)}{\partial\lambda_E}$	$\frac{\partial(MTTF)}{\partial\lambda_F}$	$\frac{\partial(MTTF)}{\partial\lambda_h}$
0.01	-2.22766	-2.22766	-0.02833	-2.60145	-4.00000	-4.00000	-2.77777
0.02	-2.16262	-2.16262	-0.05511	-2.51952	-3.84467	-3.84467	-2.68744
0.03	-2.10039	-2.10039	-0.08042	-2.44140	-3.69822	-3.69822	-2.60145
0.04	-2.04081	-2.04081	-0.10435	-2.36686	-3.55998	-3.55998	-2.51952
0.05	-1.98373	-1.98373	-0.12698	-2.29568	-3.42935	-3.42935	-2.44140
0.06	-1.92901	-1.92901	-0.14839	-2.22766	-3.30578	-3.30578	-2.36686
0.07	-1.87652	-1.87652	-0.16866	-2.16262	-3.18877	-3.18877	-2.29568
0.08	-1.82615	-1.82615	-0.18784	-2.10039	-3.07787	-3.07787	-2.22766
0.09	-1.77777	-1.77777	-0.20601	-2.04081	-2.97265	-2.97265	-2.16262

Table 6. Expected profit vs. Failure rates

Time(t)	Expected Profits					
	$K_2 = 0.1$	$K_2 = 0.2$	$K_2 = 0.3$	$K_2 = 0.4$	$K_2 = 0.5$	$K_2 = 0.6$
0	0	0	0	0	0	
1	0.68608	0.58608	0.48608	0.38608	0.28608	0.18608
2	1.20945	1.00945	0.80945	0.60945	0.40945	0.20945
3	1.70158	1.40158	1.10158	0.80158	0.50158	0.20158
4	2.18627	1.78627	1.38627	0.98627	0.58627	0.18627
5	2.66779	2.16779	1.66779	1.16779	0.66779	0.16779
6	2.14691	2.54691	1.94691	1.34691	0.74691	0.14691
7	3.62373	2.92373	2.22373	1.52373	0.82373	0.12373
8	4.09830	3.29830	2.49830	1.69830	0.89830	0.09830
9	4.57061	3.67061	2.77061	1.87061	0.97061	0.07061
10	5.04067	4.04067	3.04067	2.04067	1.04067	0.04067

5. Result Discussion

Keeping in mind the above figures we have:

- From Fig 2, it has been observed that the availability of the system is first decreasing rapidly and then swiftly as time passes.
- From Fig 3, the reliability of the system decreases smoothly as time passes.
- From Fig 4, it has been observed that the MTTF of the system is decreasing with respect to all type of failures except the failure rate of bagasse carrying unit. MTTF with respect failure rate of bagasse carrying system is approximate constant.
- Fig 5 shows the sensitivity assessment with respect to system reliability. From this one can see that the sensitivity of reliability is approximate constant with respect to failure rate of bagasse carrying system and for remaining failure rates of the system it first decrees and then increase.
- Fig 6 shows the sensitivity of MTTF. It reflects that the MTTF of sugar mill plant is equally sensitive with respect to the failure rate of cutting and crushing system, evaporation and crystallization and it is approximately constant with respect to failure rate of bagasse carrying system.
- From, Fig. 7, it is very clear that the profit decreases as the service cost increases with the passage of time unit.

6. Conclusion

In this work, the feeding system, evaporation system, and crystallization process of a sugar plant have been discussed. Based on the above calculation, we have concluded that the failure rate of bagasse carrying system has not so much impact on the production of the sugar mill plant and MTTF of the same is much sensitive with respect to the failure rate of sub parts of feeding system (cutting and crusher system). Also, the most surprising thing is that the reliability has same characteristics with respect to all types of failures Except bagasse carrying system. So, to make the sugar plant system more reliable, the managers and engineers must consider these points, and should try to reduce the failure rates for more production of sugar.

From this work, one could improve the sugar plant overall performance by restricting its failure rates and to make it less sensitive. Further, it asserts that the finding of this paper is highly advantageous to the management of the sugar plant industry.

References

[1] V. Kolhe, R. E. Shelke and S. S.Khandare, "Combustion Modeling with CFD in Direct Injection CI Engine Fuelled with Biodiesel". Jordan Journal of Mechanical and Industrial Engineering, Vol. 9 (2015) No. 1, 61-66.

[2] A. Goyal, S. Dhiman, S. Kumar and R. Sharma, "A Study of Experimental Temperature Measuring Techniques used in Metal Cutting". Jordan Journal of Mechanical and Industrial Engineering, Vol. 8 (2014) No. 2, 82-93.

[3] V. Kolhe, R. E. Shelke, S. S. Khandare, "Performance and Combustion Characteristics of a DI Diesel Engine Fueled With Jatropha Methyl Esters and Its Blends". Jordan Journal of Mechanical and Industrial Engineering, Vol. 8 (2014) No. 1, 7-12.

[4] M. Kakar, A. K. Chitkar, and J. Bhatti, "Probability analysis of a complex system working in a sugar mill with repair equipment failure and correlated life time". Mathematical Journal of Interdisciplinary Science, Vol. 1 (2012) No. 1, 57-66.

[5] A. Sachdeva, D. Kumar and P. Kumar, "Reliability Analysis of pulping system using Petri nets". International Journal of Quality and Reliability Management, Vol. 25 (2008) No. 8, 860-877.

[6] P. C. Tewari, S. Kajal and R. Khanduja, "Performance evaluation and availability analysis of steam generating system in a thermal power plant". In Proceedings of the World Congress on Engineering, Vol. 3 (2012), 4-6.

[7] S. Gupta, P. C. Tewari and A. K. Sharma, "A Markov model for performance evaluation of a coal handling unit of a thermal power plant". Journal of Industrial and System Engineering, Vol. 3 (2009) No. 2, 85-96.

[8] R. Khanduja, P. C. Tewari and D. Kumar, "Mathematical modelling and performance optimization for the digesting system of a paper plant". International Journal of Engineering, Vol. 23 (2010) No. 3&4, 215-225.

[9] A. Kumar, M. Ram, "Reliability measure improvement and sensitivity analysis of a coal handling unit for a thermal power plant". International Journal of Engineering, Vol. 26 (2013) No. 9, 1059-1066.

[10] M. Ram, S. B. Singh and V. V. Singh, "Stochastic analysis of a standby system with waiting repair strategy". IEEE Transactions on Systems, Man, and Cybernetics: Systems, Vol. 43 (2013) No. 3, 698-707.

[11] A. Mariajayaprakash, T. Senthilvelan, "Failure detection and optimization of sugar mill boiler using FMEA and Taguchi method". Engineering Failure Analysis, Vol. 30 (2013), 17-26.

[12] V. Gonzalez, J. F. Gomez, M. Lopez, A. Crespo and P. M. de Leon, "Availability and reliability assessment of industrial complex systems: A practical view applied on a bioethanol plant simulation". Safety, Reliability and Risk Analysis: Theory, Methods and Applications–Martorell et al.(eds); 2009, 687-695.

[13] D. Kumar, J. Singh and P. C. Pandey, "Design and cost analysis of a refining system in the sugar industry". Microelectronics Reliability, Vol. 30 (1990) No. 6, 1025-1028.

[14] D. Kumar, J. Singh, and I. P. Singh, "Availability of the feeding system in the sugar industry". Microelectronics Reliability, Vol. 28 (1988) No. 6, 867-871.

[15] M. Bakhshesh, E. G. Rad and M. Mehrvar, "Effect of Asymmetric Branches on Solid Particles Distribution in Central Gas Stations (CGSs)". Jordan Journal of Mechanical and Industrial Engineering, Vol. 8 (2014) No. 2, 56-65.

[16] N. K. Patel and R. N. Singh, "Optimization of NOx Emission from soya Biodiesel Fuelled Diesel Engine using cetane Improver". Jordan Journal of Mechanical and Industrial Engineering, Vol. 8 (2014) No. 4, 213-217.

Appendix A

Markov Birth-death process

Markov process or Markov birth-death process is a very useful tool for analysing random events which are dependent on each other. It is the most powerful technique in the field of reliability, which helps us to evaluate the system's various performance measures. It is named after the Russian mathematician "Andrei Andreyevich Markov".

It is a process in which transition from one state to another state (future state) depends only on the present state of the system and does not depend on the past state or one can say that the transition does not depend on what happened in the past with the system or we can say that the future stage is dependent only on the present state. As the part of the process, initially based on system configuration a state transition diagram is created, then by the Markov process, a number of differential equations are generated (on the basis of input and output or repair and failure) and then by solving these equations with the help of Laplace transformation, we get the required system's transition state probabilities. Now with the help of these transition state probabilities, the various reliability measures are calculated.

Let us consider a system having only one element. The element can be in one of two states, s_0 or s_1 (i.e., functioning or non-functioning states as shown in following figure). Since the system considered is repairable, a transition is possible from state s_1 to state s_0.

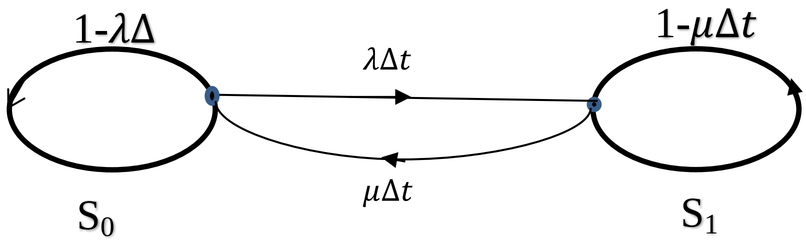

The equation which represents the state S_0 is given as

$p_{s_0}(t+\Delta t) = (1-\lambda\Delta t)p_{s_0}(t) + p_{s_1}(t)\mu\Delta t$

Similarly, the equation for the state S_1 can be developed.

Appendix B

Formulation of the intro-differential equations for the various state of sugar mill plant

Using Markov birth–death process, we can find the probability of the system to be in initial state in the interval $(t, t+\Delta t)$ as

For the state good state $P_{ABCDEF}(t)$

$$P_{ABCDEF}(t+\Delta t) = (1-\lambda_A\Delta t)(1-\lambda_B\Delta t)(1-\lambda_C\Delta t)(1-\lambda_D\Delta t)(1-\lambda_E\Delta t)(1-\lambda_F\Delta t)$$

$$(1-\lambda_h\Delta t)P_{ABCDEF}(t) + \sum_{i,j}\int_0^\infty \mu_i P_j(x,t)dx$$

$$\frac{P_{ABCDEF}(t+\Delta t) - P_{ABCDEF}(t)}{\Delta t} + (\lambda_A+\lambda_B+\lambda_C+\lambda_D+\lambda_E+\lambda_F+\lambda_h)P_{ABCDEF}(t)$$

$$= \sum_{i,j}\int_0^\infty \mu_i P_j(x,t)dx$$

Now taking $\lim_{\Delta t\to 0}$, we get

$$\lim_{\Delta t\to 0}\frac{P_{ABCDEF}(t+\Delta t) - P_{ABCDEF}(t)}{\Delta t} + (\lambda_A+\lambda_B+\lambda_C+\lambda_D+\lambda_E+\lambda_F+\lambda_h)P_{ABCDEF}(t)$$

$$= \sum_{i,j}\int_0^\infty \mu_i P_j(x,t)dx$$

$$\left(\frac{\partial}{\partial t}+\lambda_A+\lambda_B+\lambda_C+\lambda_D+\lambda_E+\lambda_F+\lambda_h\right)P_{ABCDEF}(t) = \sum_{i,j}\int_0^\infty \mu_i P_j(x,t)dx \quad (1)$$

$$\text{where } i = A, B, D, E, F, h, CF, AC, BC, CD, CE;\ j = \bar{A}BCDEF, A\bar{B}CDEF, ABC\bar{D}EF, ABCD\bar{E}F, ABCDE\bar{F}, h, AB\bar{C}DE\bar{F}, \bar{A}B\bar{C}DEF, A\bar{B}\bar{C}DEF, AB\bar{C}\bar{D}EF, AB\bar{C}D\bar{E}F$$

For degraded state (when the Sugar mill plant is working in degraded state due to failure of bagasse carrying process) $P_{AB\bar{C}DEF}(t)$

$$P_{AB\bar{C}DEF}(t+\Delta t) = (1-\lambda_A \Delta t)(1-\lambda_B \Delta t)(1-\lambda_D \Delta t)(1-\lambda_E \Delta t)(1-\lambda_F \Delta t)(1-\lambda_h \Delta t)P_{AB\bar{C}DEF}(t) + \lambda_C P_{ABCDEF}(t)$$

$$\frac{P_{AB\bar{C}DEF}(t+\Delta t) - P_{AB\bar{C}DEF}(t)}{\Delta t} + (\lambda_A + \lambda_B + \lambda_D + \lambda_E + \lambda_F + \lambda_h)P_{AB\bar{C}DEF}(t) = \lambda_C P_{ABCDEF}(t)$$

Now taking $\lim\limits_{\Delta t \to 0}$, we get

$$\lim_{\Delta t \to 0} \frac{P_{AB\bar{C}DEF}(t+\Delta t) - P_{AB\bar{C}DEF}(t)}{\Delta t} + (\lambda_A + \lambda_B + \lambda_D + \lambda_E + \lambda_F + \lambda_h)P_{AB\bar{C}DEF}(t) = \lambda_C P_{ABCDEF}(t)$$

$$\left(\frac{\partial}{\partial t} + \lambda_A + \lambda_B + \lambda_D + \lambda_E + \lambda_F + \lambda_h\right)P_{AB\bar{C}DEF}(t) = \lambda_C P_{ABCDEF}(t) \tag{2}$$

For Failed states (states which occurs due to complete failure of cutting process/crushing process/heat generating process/ evaporation process/ crystallization process/ human error) $P_i(x,t)$

$$P_i(x+\Delta x, t+\Delta t) = \{1-\mu_k \Delta t\}P_i(x,t)$$

$$\Rightarrow \frac{P_i(x+\Delta x, t+\Delta t) - P_i(x,t)}{\Delta t} + \mu_k P_i(x,t) = 0$$

Taking $\operatorname*{limit}\limits_{\Delta x \to 0, \Delta t \to 0}$, we get

$$\Rightarrow \operatorname*{limit}_{\Delta x \to 0, \Delta t \to 0} \frac{P_i(x+\Delta x, t+\Delta t) - P_i(x,t)}{\Delta t} + \mu_k P_i(x,t) = 0$$

$$\left(\frac{\partial}{\partial x} + \frac{\partial}{\partial t} + \mu_k\right)P_l(x,t) = 0 \tag{3}$$

$$\text{where } k = A, B, D, E, F, h, CF, AC, BC, CD, CE;$$

$$i = \bar{A}BCDEF, A\bar{B}CDEF, ABC\bar{D}EF, ABCD\bar{E}F, ABCDE\bar{F}, h, AB\bar{C}DE\bar{F}, \bar{A}B\bar{C}DEF, A\bar{B}\bar{C}DEF, AB\bar{C}\bar{D}EF, AB\bar{C}D\bar{E}F$$

Boundary conditions of the system are obtained corresponding to transitions between the states where transition from a state with and without elapsed repair time exists, with elapsed repair times *x* and 0. Hence we have the following boundary/initial conditions:

$$P_j(0,t) = \lambda_k P_l(t) \tag{4}$$

$$\text{where } j = \bar{A}BCDEF, A\bar{B}CDEF, ABC\bar{D}EF, ABCD\bar{E}F, ABCDE\bar{F}, h, AB\bar{C}DE\bar{F}, \bar{A}B\bar{C}DEF, A\bar{B}\bar{C}DEF, AB\bar{C}\bar{D}EF, AB\bar{C}D\bar{E}F;$$

$$k = A, B, D, E, F, h, F, A, B, D, E;$$

$$l = ABCDEF, ABCDEF, ABCDEF, ABCDEF, ABCDEF, ABCDEF, AB\bar{C}DEF, AB\bar{C}DEF, AB\bar{C}DEF, AB\bar{C}DEF, AB\bar{C}DEF$$

Initial condition

$$P_{ABCDEF}(t) = \begin{cases} 1 & , t = 0 \\ 0 & , \text{othetwise} \end{cases} \quad \text{and all other state probabilities are zero at t = 0} \tag{5}$$

JJMIE

Volume 12, Number 4, December. 2018
ISSN 1995-6665
Pages 281 - 292

Jordan Journal of Mechanical and Industrial Engineering

Investigations on the Mechanical, Wear and Corrosion Properties of Cold Metal Transfer Welded and Friction Stir Welded Aluminium Alloy AA2219

M. N. Abijith[a], Adithya Rajeev Nair[a], M. Aadharsh[a], R. Vaira Vignesh[a]

R. Padmanaban[*, a], M. Arivarasu[b]

[a]*Department of Mechanical Engineering, Amrita School of Engineering, Coimbatore, Amrita Vishwa Vidyapeetham, India.*
[b]*Center for Innovative Manufacturing and Research, Vellore Institute of Technology, Vellore, India.*

Received 1 August. 2018

Abstract

Aluminium – Copper alloy AA2219 finds application in aerospace and automotive components because of its high strength to weight ratio and corrosion resistance. However, joining of the alloy by conventional welding techniques results in poor property profile. In this study, AA2219 rolled plates of thickness 5.5 mm are joined by cold metal transfer welding process and friction stir welding process. The microstructure, mechanical, corrosion and wear properties of the welded plates are analyzed. The results indicate that cold metal transfer welded specimens have high hardness and tensile strength than the friction stir welded specimens. However, the corrosion resistance and wear resistance of friction stir welded specimens are higher than the base material and cold metal transfer welded specimens.

Keywords: Aluminium alloy, Friction stir welding, Cold metal transfer welding, Corrosion, Wear;

Introduction

Aluminium alloys are the preferred materials for light weighting of engineering components. Aluminium – Copper alloy AA2219 is widely used in aerospace and aircraft components because of its good strength to weight ratio and corrosion resistance. The high strength and fracture toughness of AA2219 alloy are attributable to the grain boundary layers [1]. The solidification cracking resistance of AA2219 alloy enabled joining of different components by welding techniques [2, 3]. Though AA2219 alloy has better weldability than other hardenable aluminium alloys, conventional welding results in unfavorable defects such as liquation cracking, porosity, and weldment distortion [4]. For an example, the tensile strength and fatigue strength of conventionally welded AA2219 alloy were much lower than the base material [5-8].

Cold metal transfer welding is one of the emerging areas in welding, which is a modified form of the gas metal arc welding process. During the welding process, at the instance of the electrode wire tip contacting the molten pool, the servomotor reverses the direction of the welding torch and retracts the wire electrode. This enables the fall of a single drop of the molten wire electrode over the joint line. A sound joint is produced by the fusion of wire electrode material and the base material in the weldment. The advantage of cold metal transfer welding process is its higher electrode melting coefficient than other welding processes [9]. As the current drops to near-zero during the metal transfer, cold metal transfer welding has less spattering effect compared to other short-circuit welding techniques [10]. Hence, the wire feed rate affects the phase duration and short-circuit duration. An increase in the short-circuit duration increases the grain size of the post-welded material [11] and slow welding speeds lead to the formation of heat-affected zone, which increases the vulnerability to liquation cracking [12].

In this study, the AA2219 alloy plates were cold metal transfer welded by varying the process parameters (welding current and welding speed). Defect-free joint with high depth of penetration was chosen as the criteria for optimizing the cold metal transfer welding process parameters. To assess the performance of the cold metal transfer welded AA2219 alloy plates, A2219 alloy plates were joined by the friction stir welding process. The friction stir welding process is one of the preferred industrial techniques for welding AA2219 alloy. In this process, a rotating non-consumable tool is plunged into the workpiece and traversed along the welding line. The action of load and traverse of the rotating tool in the workpiece generates frictional heat, which plasticizes the material enabling a joint in the solid state [13, 14]. Friction stir welding process parameters significantly influence the evolution of microstructure and henceforth the properties of the weldments [15]. The incorporation of right welding parameters avoids melting of aluminium alloys, reduce the formation of intermetallic compounds and help to achieve desirable properties [16]. Friction stir welded aluminium alloys have negligible issues such as cracking and porosity when compared to other arc welding techniques [17-19]. The microstructural constituents in cold metal transfer welded and friction stir welded specimens were characterized using microstructural analysis and X-ray diffraction analysis. The microhardness, tensile strength, and impact strength of the welded plates were evaluated. The fractograph of the tensile and impact test specimens were obtained using field emission – scanning electron microscope to deduce the fracture mechanism. The surface morphology of the specimens post corrosion and wear test was observed using field emission - scanning electron microscope to understand the corrosion mechanism and wear mechanism. This article presents a comparative study on the performance of the AA2219 alloy plates joined by cold metal transfer welding and friction stir welding process.

Materials and Methods

Material

Aluminium alloy AA2219 forged plate of thickness 5.5 mm was used in this study. The alloy was received in the annealed condition and its chemical composition is given in Table 1.

Table 1. Composition of AA2219

Element	Mn	Mg	Fe	Si	Cr	Zn	Ti	Cu	Al
Composition (Weight %)	0.229	0.007	0.108	0.079	0.130	0.046	0.040	5.959	Balance

Cold metal transfer welding

The AA2219 alloy plate was cut into workpieces of dimension 150 mm × 50 mm × 5.5 mm and degreased using acetone. The bead on trials and experimental welding trials were carried out using Fronius cold metal transfer welding machine. Aluminium alloy AA4024 wire of diameter 1.2 mm was used as filler material for the cold metal transfer welding process. Argon gas at a flow rate of 15 liters.min^{-1} shielded the weld pool from the atmosphere. The filler wire was fed at a rate of 7.6 m.min^{-1} and the stick out distance was 10 mm. The cold metal transfer welding trials were performed by varying the current and welding speed as per the experimental layout in Table 2. The penetration depth of the weldments is measured at each parametric combinations of current and welding speed.

Table 2. Process parameters for bead-on trials of AA2219 (Cold metal transfer welding)

Sl.	Current (A)	Speed mm.min^{-1}	Depth of Penetration (mm)	Sl.	Current (A)	Speed mm.min^{-1}	Depth of Penetration (mm)
1	70	800	0.550	11	132	1000	0.930
2	70	900	0.640	12	148	800	1.370
3	70	1000	0.900	13	148	1000	1.220
4	80	800	0.450	14	162	800	1.680
5	80	900	0.680	15	170	700	3.660
6	80	100	1.000	16	170	800	2.780
7	90	800	0.450	17	170	900	2.440
8	90	900	0.590	18	170	1000	1.830
9	90	1000	0.790	19	180	700	3.240
10	132	800	1.180				

Friction stir welding

The friction stir welding trials were performed by varying the welding speed as per the experimental layout in Table 3. The workpieces were cleaned and degreased with acetone. Friction stir welding trials were carried out in friction stir welding competent computer numerical control milling machine. The experimental procedures to perform friction stir welding trials were discussed elsewhere [20, 21].

Table 3. Experimental layout of Friction Stir Welding trials

Sl.	Tool rotation speed (rpm)	Welding Speed (mm.min^{-1})	Plunge depth (mm)
1	1600	45	5.3
2	1600	60	5.3
3	1600	75	5.3

Microstructural analysis

The specimens for microstructural analysis were cut from the base material, cold metal transfer welded workpiece and friction stir welded workpiece. The cut specimens were prepared and polished as per the ASTM E3-11 standard. The etchant was prepared, and the specimens were etched as per the guidelines of the ASTM E407-07 standard. The microstructure of the specimens was observed using an optical microscope (Carl Zeiss).

Mechanical tests

The specimen for microhardness test was prepared from the base material, cold metal transfer welded workpiece and friction stir welded specimens according to the IS 1501:2002 standard. Vicker's microhardness was measured using a microhardness tester (Mitutoyo) with a test load of 50 N for a time period of 10s. Three tensile test specimens were fabricated from each of the base material, cold metal transfer welded workpiece and friction stir welded workpiece as per the ASTM E8/8M-15a standard. The tensile strength was calculated from the stress-strain graph, which was obtained from the computerized tensile testing machine (Tinius Olsen). For measuring the maximum impact load, three specimens each from the base material, cold metal transfer welded workpiece and friction stir welded workpiece were prepared and subjected to Charpy impact test as outlined by the ASTM E23-12c standard.

Wear test

The specimens were cut from the base material, cold metal transfer welded workpiece and friction stir welded workpiece and were mounted in a hollow steel tube using a cold setting compound. The wear test was conducted as per the ASTM G99-95a standard, in a pin on disc tribometer (Ducom) with the specimen as pin and counter disc made of EN316 steel. The wear test parameters were chosen as follows: track diameter of 60 mm, sliding velocity of 1.5 $m.s^{-1}$ and sliding distance of 900 m. An uninterrupted contact was established between the specimen and the counter disc by applying a load of 9.80 N through a lever system. The mass of the specimens before and after the wear test was measured using a precision balance of readability 0.0001 g.

Corrosion tests

Immersion corrosion test

The specimens were prepared from the base material, cold metal transfer welded workpiece and friction stir welded workpieces as per the directions outlined in the Microstructure section. The specimens were cleaned and subjected to immersion test as per the ASTM G31-72 standard. The immersion tests were performed in artificial seawater solution (3.5 weight % sodium chloride solution) at room temperature T1 = 27°C and at an elevated temperature T2 = 45°C. The temperature of the solution was maintained using a water bath, which was fitted with a digital temperature controller with a sensitivity of 0.1°C. After the immersion period, the corrosion products were cleaned using the cleaning solution as per the ASTM G1-03 standard. The cleaning solution was prepared by mixing 25 ml of phosphoric acid and 10 g of chromium trioxide in 500 ml of water. The specimens were immersed in the cleaning solution (heated and maintained at 80°C) for 300 s, to remove all the corrosion products. Then the specimens were rinsed in nitric acid for 60 s. The specimens were dried in a blast of hot air and then weighed in the precision balance of readability 0.0001 g to calculate the mass loss of the specimens.

Electrochemical corrosion test

Electrochemical corrosion tests were performed for the base material and the workpieces welded by both cold metal transfer welding and friction stir welding techniques to calculate their corrosion potential and corrosion current in artificial seawater solution. The specimens were prepared as per the ASTM G102 standard. The surface of the specimens was prepared as described in the *Microstructure section*. The specimens were masked using an insulation tape, such that an area of 1 mm^2 was exposed to the electrolyte (artificial seawater solution). Electrochemical cell setup was built using calomel electrode as the reference electrode, a platinum wire as the counter electrode and the specimen as the working electrode. The electrodes were connected to the electrochemical workstation (CH Instruments). An open circuit potential was established for each specimen and the specimens were potentiodynamically polarized with reference to open circuit potential at a scan rate of 5 $mV.s^{-1}$.

Surface morphology, Elemental composition, Phase analysis

The specimens subjected to wear and corrosion test were preserved in a desiccator. The surface morphology of the specimens was observed using field emission scanning electron spectroscopy (Zeiss Sigma). The images were obtained at an electron acceleration potential of 10kV and a wide range of magnifications. The elemental composition of the worn out and corroded specimens were analyzed using energy-dispersive X-ray spectroscopy (Bruker). The spectra were obtained at an electric acceleration potential of 20kV over a small region of the corroded specimen. The X-ray diffractometer (Rigaku) was used to analyze the constitutional phases present in the cold metal transfer welded workpiece and friction stir welded workpiece using Copper-K α radiation in continuous scanning mode at a scan rate of 2° min^{-1}.

Results and Discussions

Macrostructure

Cold Metal Transfer Welding

Cold metal transfer welding trials were conducted by varying the cold metal transfer welding process parameters (welding current and welding speed). The corresponding penetration depth of the weldments was measured and given in Table 2. The mathematical relationship between the process variables and response variables could be devised using a standard statistical regression equation [22]. However, the penetration depth exhibited complex non-linear characteristics with cold metal transfer welding the process parameters. Hence, a hybrid model integrating the polynomial function and radial basis function was developed to relate the cold metal transfer welding process parameters (welding current and welding speed) with the response variable (depth of penetration) using Matlab ® technical computing environment. The details regarding the development of model are discussed elsewhere [23]. Since the input variables are discrete, a multiquadratic variant of radial basis function model was used. The radial basis function had two centers, a global width of 0.029147 and the regularization parameter was 0.0001. The developed polynomial – radial basis function model using coded levels of welding current (I) and welding speed (S) is given in equation (1).

$$\begin{aligned} Depth\ of\ penetraion &= 0.13896 + 1.5654 \times I \\ &- 0.51265 \times S + 0.27861 \\ &\times I^2 - 0.7344 \times I \times S \\ &- 0.34034 \times S^2 + RBF \end{aligned} \quad (1)$$

Where RBF is radial basis function.

The coefficient of determination (R2) and root mean squared error (RMSE) values of the developed model were 0.98 and 0.064 respectively. The closeness of coefficient of determination to 1 and root mean squared error value to

0, indicates that the developed model is efficient in prediction [23]. Figure 1 shows the contour plot depicting the influence of welding current and welding speed on the penetration depth of the welds. The heat input to the material is proportional to the magnitude of current. Therefore, the high magnitude of welding current melted the material along its depth to a greater extent than the low magnitude of welding current. It is observed that penetration depth increased with increase in welding current from 70 A to 170 A. However, a welding current greater than 170 A resulted in visible weld defects. Hence the experimental trials were limited to welding current of 170 A. Heat input has an inverse relationship with the welding speed. At higher welding speed of 800 mm-min^{-1}, 900 mm-min^{-1}, and 1000 mm-min^{-1}, the amount of heat generated was insufficient to melt the material. So, the specimens processed at high welding speed had low penetration depth, at any level of current. A maximum penetration of 3.66 mm was obtained for 170A welding current and welding speed 700 mm-min^{-1}. Hence, they were chosen as optimum process parameter for cold metal transfer welding of AA2219. At this optimum parametric condition, the specimens were joined by cold metal transfer welding (push method and drag method). For the same penetration depth, the specimen welded by drag method had lesser porosity compared with the specimen welded by push method. Hence, it is established that the drag method is the best choice for cold metal transfer welding of AA2219 alloy (square butt configuration). Repeating the drag method cold metal transfer welding process on the other side of the plate resulted in a complete penetration of 5.5 mm. No visible defects were observed in the macro-structure of the cold metal transfer welded specimen as shown in Figure 2 (a).

Friction Stir Welding

Friction stir welding of the AA2219 alloy at a low welding speed of 45 mm.min^{-1} resulted in visible surface defects and a high welding speed of 75 mm.min^{-1} resulted in incomplete penetration. A complete penetration and defectless weld were obtained in a single automated pass with at tool rotation speed of 1600 rpm and a welding speed of 60 mm.min^{-1}, as shown in Figure 2 (b). Hence, the optimum friction stir welding process parameters for joining AA2219 alloy is established as follows: tool rotation speed of 1600 rpm and a welding speed of 60 mm.min^{-1}.

Microstructure

Figure 3 (a) shows the dispersed Al_2Cu particles (dark region) in irregular shapes and sizes in the microstructure of the base material. The needle-like continuous structures in the microstructure of AA4024 alloy corresponds to secondary β-(Al, Fe, Si) precipitates (dark region), as shown in Figure 3 (b). Figure 3 (c) shows a clear distinguished weld interface between the matrix of filler material and base material. The microstructural image shows Al2Cu of the base material, weld interface and β-(Al, Fe, Si) precipitates of the filler material in the cold metal transfer weld specimen. In friction stir welded specimen, the Al2Cu particles are dispersed on the surface of the and no significant change was observed in the dispersion of Al_2Cu particles, as observed in Figure 3 (d). In X-ray diffraction, the cold metal transfer welded specimen produced significant peaks corresponding to distinct phases α-Al, Al_2Cu, and β-(Al, Fe, Si), as shown in Figure 4 (a). It corresponds to the phases present in the base material (AA2219) and filler material (AA4024). The X-ray diffraction analysis of the friction stir welded specimen revealed the presence of two distinct phases in the matrix α-Al and Al_2Cu, as shown in Figure 4 (b). The X-ray diffraction results are consistent with the aforesaid microstructural analysis.

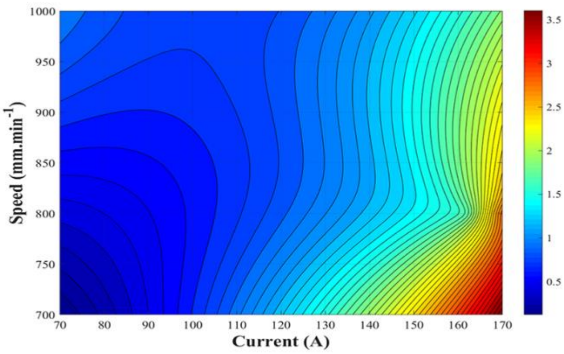

Figure 1. Effect of current and welding speed on the depth of penetration in cold metal transfer welding process

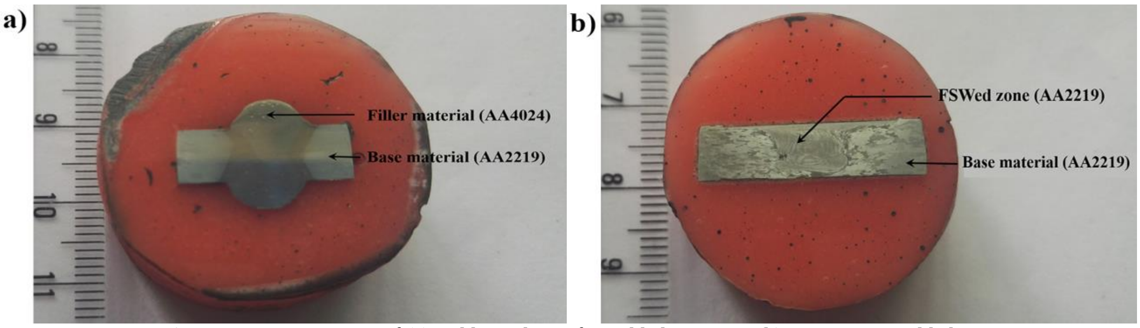

Figure 2. Macrostructure of (a) Cold metal transfer welded specimen (b) Friction stir welded specimen

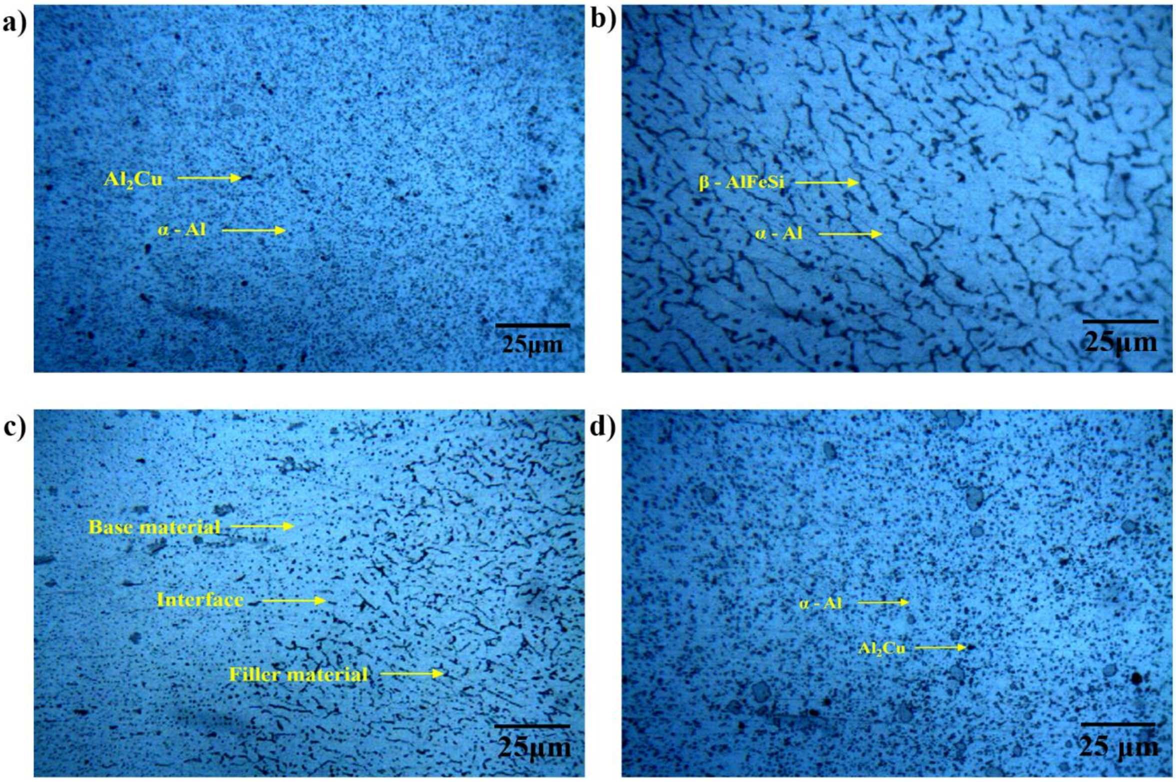

Figure 3. Microstructure of (a) Base material AA2219 (b) Filler material AA4024 (c) Cold metal transfer welded specimen (d) Friction stir welded specimen

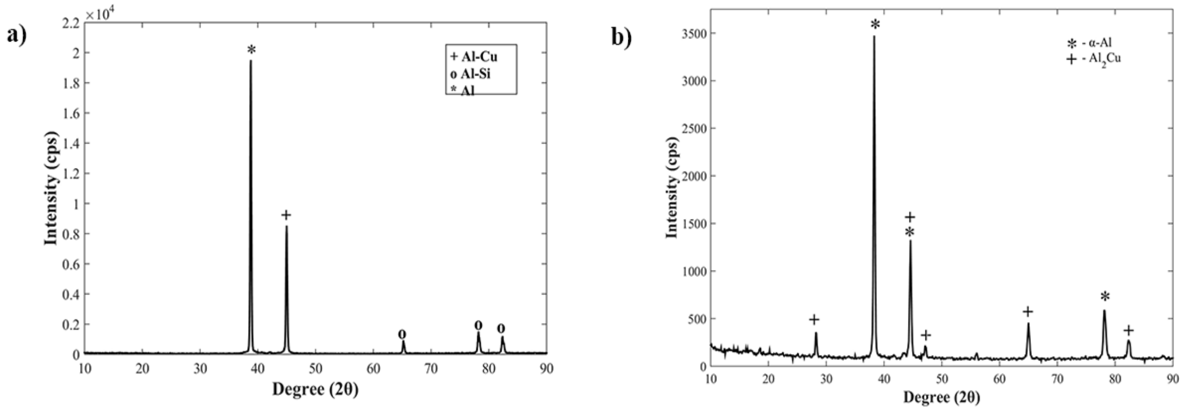

Figure 4. X-ray diffraction analysis of (a) Cold metal transfer welded specimen (b) Friction stir welded specimen

Microhardness

The microhardness of the base material was measured to be 82 Hv. The high microhardness is attributed to Al_2Cu particles in the matrix, which were obstacles for dislocation motion. As observed in the microstructure of cold metal transfer welded specimen, the volume fraction of intermetallic is comparatively higher in the weld zone and weld interface than the base material and filler material. These intermetallic phases acted as barriers to dislocation movement, which increased the microhardness of the material. Hence, the weld zone and weld interface had a higher average microhardness of 110 Hv and 140 Hv respectively. The variation in microhardness of the cold metal transfer welded specimen at the cap-section, mid-section, and root-section of the weldment is shown in Figure 5(a). In the case of the friction stir welded specimens, the microhardness was ~20% lesser than the microhardness of base material. The partial dissolution of Al_2Cu phase attributes to the low microhardness of the friction stir welded region than the base material. The microhardness plot of the friction stir welded specimen is shown in Figure 5 (b). The microhardness test indicates that the microhardness of cold metal transfer welded specimen is ~41% higher than the microhardness of the friction stir welded specimen.

Tensile Strength

The tensile strength of the specimens was determined using the tensile testing machine and the results are presented in Table 4. The load was applied axially to the tensile test specimens until there was a visible rupture. The average tensile strength and rupture load of the base material specimen were found to be 158.20 MPa and 5.525 kN respectively. The tensile fractograph of the base material is shown in Figure 6 (a), which revealed a few secondary cracks and dimple features. However, a quite large deformation zone was observed indicating a high tensile strength. The average tensile strength of the friction stir welded specimen was found to be 86.975 MPa and the average load at rupture was found to be 3.0375kN. The tensile fractograph of the friction stir welded specimen indicates the presence of cracks and quasi-cleavage dimples, as shown in Figure 6 (b). The small deformation zone and wide cracks indicated the least tensile strength of the friction stir welded specimen. The average tensile strength and the average load at rupture of the cold metal transfer welded specimen were found to be 159.02 MPa and 5.553 kN respectively. It is observed that the tensile strength of cold metal transfer welded specimen was ~83% higher than the tensile strength of friction stir welded specimens. A large deformation zone with quasi-cleavage dimples was observed in the tensile fractograph of the cold metal transfer welded specimen, as shown in Figure 6 (c). This demonstrated the highest tensile strength of the cold metal transfer welded specimen. Aforesaid microstructural analysis revealed the presence of huge volume fraction of secondary phases in the cold metal transfer welded specimen, which accounted for its high tensile strength. The tensile test results indicate that the cold metal transfer weldments had the higher ultimate tensile strength and rupture load.

Impact strength

The average impact strength of the base material was calculated to be 0.3123 J.mm^{-2}. As observed Figure 7 (a), the impact fractograph of the base material displayed a comparatively smaller deformation zone, more cleavage steps and tearing ridges than the fractograph of friction stir welded specimens and cold metal transfer welded specimens. It is observed that average impact strength of friction stir welded specimen was 0.3209 J.mm^{-2}. As shown in Figure 7 (b), more tearing ridges were observed in the impact fractograph of the friction stir welded specimen than the tensile fractograph of the friction stir welded specimen. Many cleavage steps and small deformation zone indicated the lowest impact strength of the friction stir welded specimen. In line with the observations of tensile strength, the impact strength of cold metal transfer welded specimens was higher than the impact strength of the base material and friction stir welded specimen. The average impact strength of cold metal transfer welded specimen was observed be 0.4242 J.mm^{-2}. It is attributed to the strong bonding of the filler material with the base material. Figure 7 (c) shows the impact fractograph of the cold metal transfer welded specimen. Quasi-cleavage dimples and large deformation zone indicated quasi-cleavage fracture feature in the cold metal transfer welded specimen, which demonstrated the highest impact strength of the cold metal transfer welded specimens.

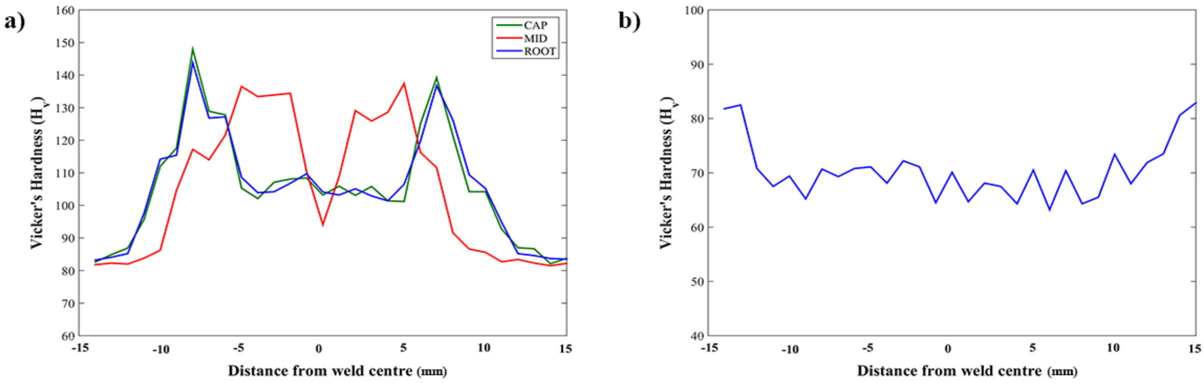

Figure 5. Microhardness plot of (a) Cold metal transfer welded specimen (b) Friction stir welded specimen

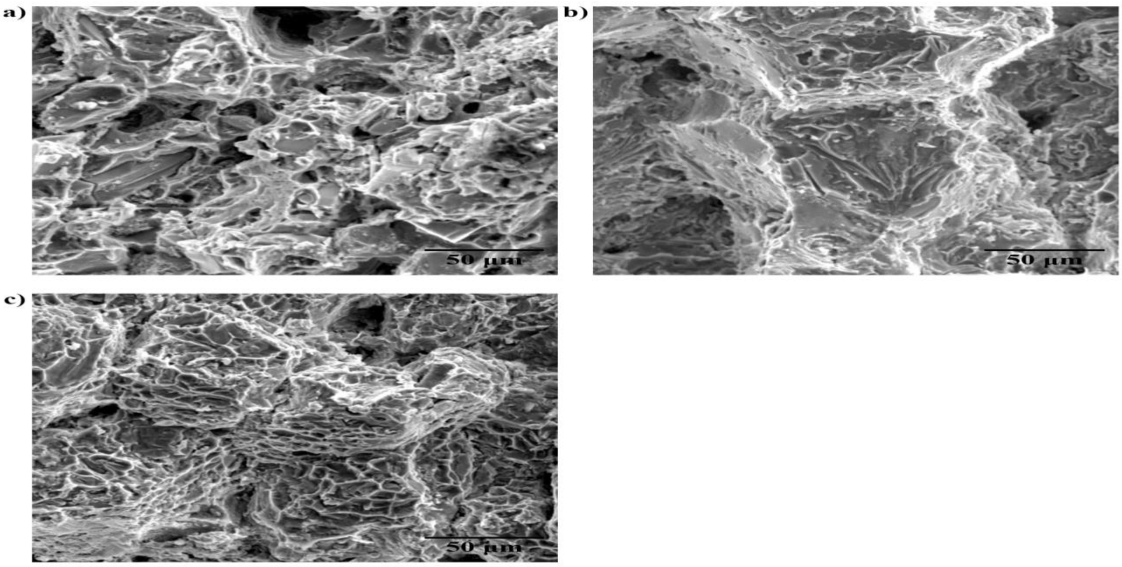

Figure 6. Tensile Fractograph of (a) Base material (b) Friction stir welded specimen (c) Cold metal transfer welded specimen

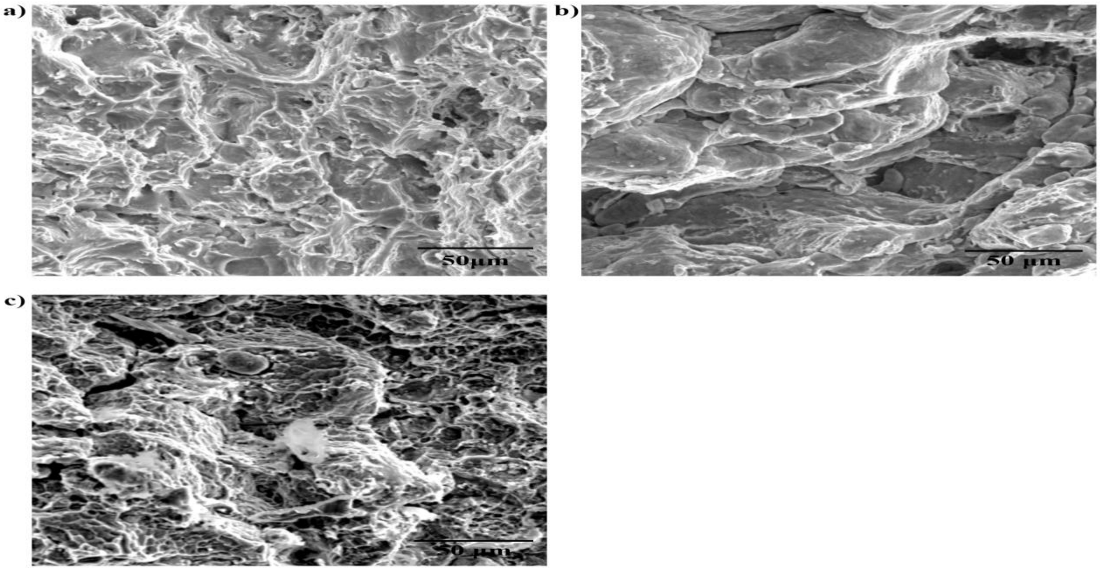

Figure 7. Impact Fractograph of (a) Base material (b) Friction stir welded specimen (c) Cold metal transfer welded specimen

Table 4. Summary of the mechanical, tribological and corrosion tests performed on the base material, cold metal transfer welded and friction stir welded specimen

Sl.	Specimen	Ultimate Tensile Strength (MPa)	Impact Strength (J.mm^{-2})	Wear rate ($\times10^{-7}$ kg.N^{-1}.m^{-1})	Corrosion test: *Immersion test* Corrosion rate (10^{-5} mm/year) 27°C	Corrosion test: *Immersion test* Corrosion rate (10^{-5} mm/year) 45°C	Corrosion test: *Potentiodynamic polarization* Corrosion potential (V)	Corrosion test: *Potentiodynamic polarization* Corrosion current ($\times10^{-3}$A)
1	Base material	158.483± 1.431	0.312± 0.019	2.906± 0.628	2.856± 0.040	5.711± 0.090	-(0.559± 0.004)	5± 0.224
2	Cold metal transfer welded specimen	159.020± 1.145	0.425± 0.022	2.802± 0.328	2.128± 0.034	8.820± 0.136	-(0.621± 0.004)	14.643± 1.905
3	Friction stir welded specimen	86.975± 0.495	0.321± 0.015	4.213± 0.296	2.094± 0.027	3.822± 0.066	-(0.601± 0.012)	6.003± 0.127

Wear rate

The wear test was conducted for the base material, cold metal transfer welded and friction stir welded specimens ant the wear rate of the specimens was calculated using equation (2) [21]. The wear rate of the specimens is summarized in Table 4.

$$Wear\ rate = \frac{\Delta m}{F \times L}\ \left({}^{g}/_{Nm}\right) \qquad (2)$$

Where Δm is mass loss in g, F is load in N and L is sliding distance in m.

A minimum wear rate of 2.905×10^{-7} g/(Nm) was observed for the base material, closely followed by the cold metal transfer welded specimen. The surface morphology of the worn cold metal transfer welded specimen is shown in Figure 8 (a). Loose wear debris and feeble wear tracks were observed on the worn out region, as the result of delamination of the surface oxide layer and subsurface material layer (adhesive wear). The friction stir welded specimens exhibited the highest wear rate and lowest wear coefficient. The wear track was prominent and the surface had deep continuous grooves on the surface as observed in Figure 8 (b). The worn surface had massive deformation and a large amount of wear debris, which indicated the domination of severe wear regime (abrasive wear). The softness of the matrix, as evident from the hardness test results, resulted in high wear rate of the specimens [24]. It is observed that wear coefficient of the base material and the cold metal transfer welded specimen was more fluctuating in comparison to the friction stir welded specimen. The fluctuation in the cold metal transfer welding specimen was attributed to the more fraction of hard intermetallics in the matrix. In the base material, the frequency of fluctuation was low in the initial phases and increased towards the end. The results indicate that cold metal transfer welded specimens had high wear resistance.

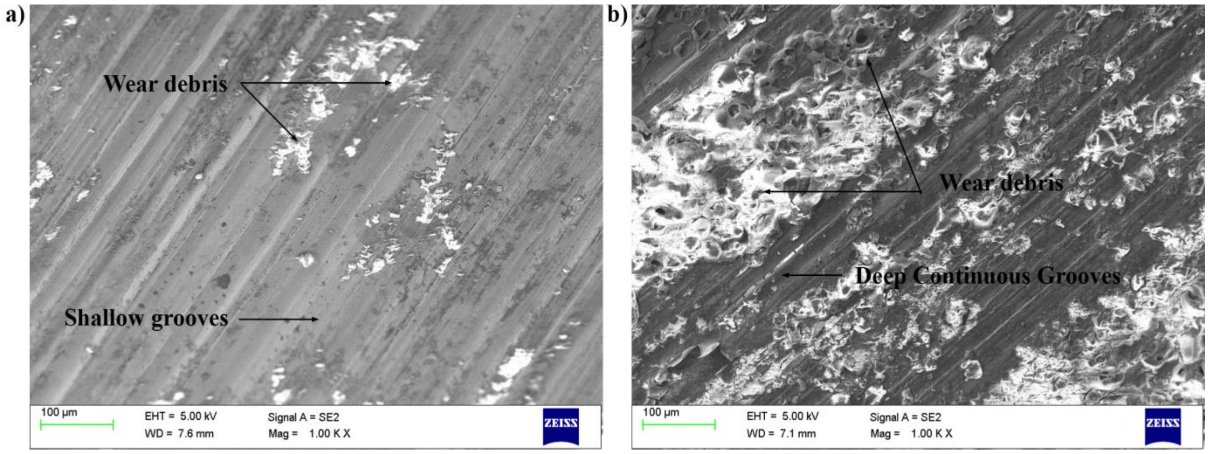

Figure 8. Worn out surface of (a) Cold metal transfer welded specimen (b) Friction stir welded specimen

Corrosion

Immersion corrosion

The immersion corrosion test was performed at room temperature and at an elevated temperature of 45°C. The corrosion rate of the specimens (base material, friction stir welded specimen and cold metal transfer welded specimen) was calculated from the mass loss of the specimens and displayed in Table 4. The corrosion rate of the base material at room temperature was 2.8549×10-5 mm/year. The corrosion rate decreased by ~25% in both friction stir welded specimen and the cold metal transfer welded specimen at room temperature. It is observed that increase in temperature increased the corrosion rate of the specimens. At the elevated temperature, cold metal transfer welded specimens exhibited the highest corrosion rate of 8.8350×10^{-5} mm/year. The corrosion rate of the cold metal transfer welded specimen was ~54% higher than the base material at elevated temperature. The friction stir welded specimen exhibited the least corrosion rate of 3.8142×10^{-5} mm/year at elevated temperature, which is ~32% lesser than the corrosion rate of the base material at elevated temperature.

The corrosion mechanism of the specimens is described as follows. Aluminium reacts with water as described by the Equation (3), Equation (4) and Equation (5) [23].

$$\mathrm{Al + 3H_2O \rightarrow Al(OH)_3 + 3H^+ + 3e^-} \tag{3}$$

$$\mathrm{Al + 2H_2O \rightarrow AlO(OH) + 3H^+ + 3e^-} \tag{4}$$

$$\mathrm{Al + \frac{3}{2}H_2O \rightarrow Al_2O_3 + 3H^+ + 3e^-} \tag{5}$$

But the aggressive chloride ions in the electrolyte transforms aluminium hydroxide to aluminium chloride as per the Equation (6), Equation (7), and Equation (8).

$$\mathrm{Al(OH)^{2+} + Cl^- \rightarrow Al(OH)Cl^+} \tag{6}$$

$$\mathrm{Al(OH)Cl^+ + H_2O \rightarrow Al(OH)_2Cl + H^+} \tag{7}$$

$$\mathrm{2Al(OH)_2Cl + 4Na^+ + 4Cl^- \rightarrow 2AlCl_3 + 4NaOH} \tag{8}$$

Aluminium hydroxide is transformed into $\mathrm{Al(OH)_2Cl}$ in the presence of chloride ion, as given by Equation (7). Hydrolysis of $\mathrm{Al(OH)Cl^+}$ yields an unstable compound, which on further reaction with chloride ion forms aluminium chloride, as per the Equation (8). Aluminium chloride dissolves into solution and exposes a fresh area of the metal surface to the electrolyte. This process of salt formation, its dissolution, and exposure to fresh surface increase the corrosion rate of the specimen. Figure 9 (a) shows the corroded surface of the base material, which showed the striations on the surface. In agreement with the highest corrosion rate, the cold metal transfer welded specimen had many cracked layers on the surface, as shown in Figure 9 (b). The friction stir welded specimen had the least corrosion rate among the tested specimens. Hence, meager corrosion products were observed on the surface as shown in Figure 9 (c). The results indicate that the corrosion resistance of friction stir welded specimen is higher than the corrosion resistance of cold metal transfer welded specimen.

Electrochemical corrosion

The corrosion characteristics of the base material, cold metal transfer welded and friction stir welded plates were studied using potentiodynamic polarization technique. The Tafel plots for the specimens are shown in Figure 10, which sufficiently prove that pitting occurs only at very high positive potentials. The corrosion current and corrosion potential were extrapolated from the Tafel region and presented in Table 4. The formation of aluminium oxide layer limits the flow of current, decreasing the corrosion rate. The corrosion potential of the base material is nobler (more positive) than the cold metal transfer welded and friction stir welded specimens. Comparing the welding techniques, friction stir welded specimen exhibited a noble corrosion potential of -0.585 V. The cold metal transfer welded specimen exhibited the highest corrosion potential of -0.615 V. The anodic reaction on the surface of the specimen is the formation of aluminium ion, as per the Equation (9).

$$\mathrm{Al \rightarrow Al^{3+} + 3e^-} \tag{9}$$

The principal cathodic reaction in pitting corrosion of aluminium-magnesium alloys, in the marine environment, is the formation OH^- ions [25]. The cathodic reaction is the reduction of atmospheric oxygen in the electrolyte, as per the Equation (10).

$$O_2 + 2H_2O + 4e^- \rightarrow 4\mathrm{OH^-} \tag{10}$$

The existence of a potential difference between the intermetallics and the matrix created local galvanic sites, which decreased the corrosion potential of cold metal transfer welded specimens. This is attributed to the high-volume fraction of intermetallic present in the cold metal transfer welded specimen than the base materials and friction stir welded specimen. The cold metal transfer welded specimen had more corrosion products than the base material and friction stir welded specimens, as observed in Figure 11. Pitting corrosion is the dominant mechanism in the corrosion of cold metal transfer welded specimen. The energy dispersive X-ray spectroscopy analysis justified that the corrosion products consisted of aluminium, copper, silicon, sodium, oxygen, and chlorine atoms. The EDS spectra are shown in Figure 12 and Table 5 shows the elemental composition of the corrosion products. The probable corrosion products are chlorides of aluminium, copper, and oxides of aluminium, copper, silicon. Sodium came from the electrolyte, which was made by dissolving the sodium chloride in distilled water. The predominant corrosion product in base material and friction stir welded specimen is aluminium chloride as evidenced by a higher concentration of aluminium and chlorine. The electrochemical corrosion test also reveals that the corrosion resistance of friction stir welded specimen is higher than the corrosion resistance of the cold metal transfer welded specimen.

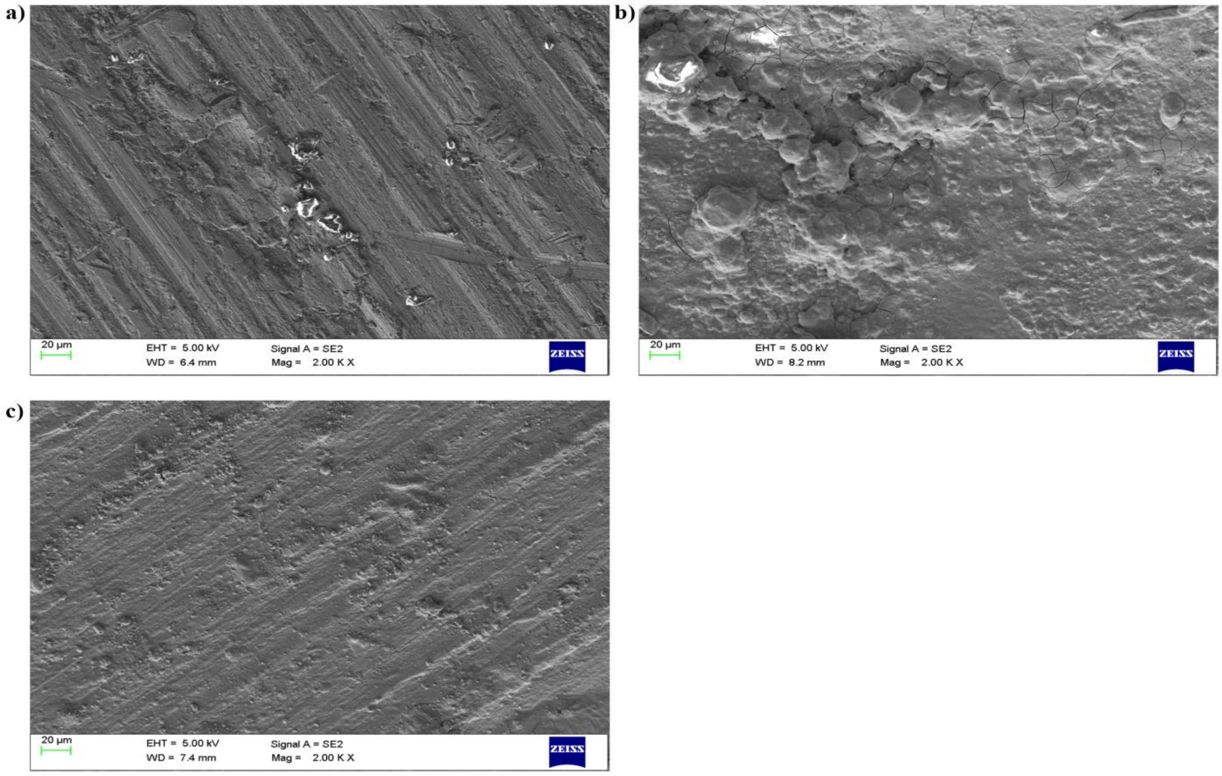

Figure 9. Surface morphology of the corroded (a) Base material (b) Cold metal transfer welded specimen (c) Friction stir welded specimen

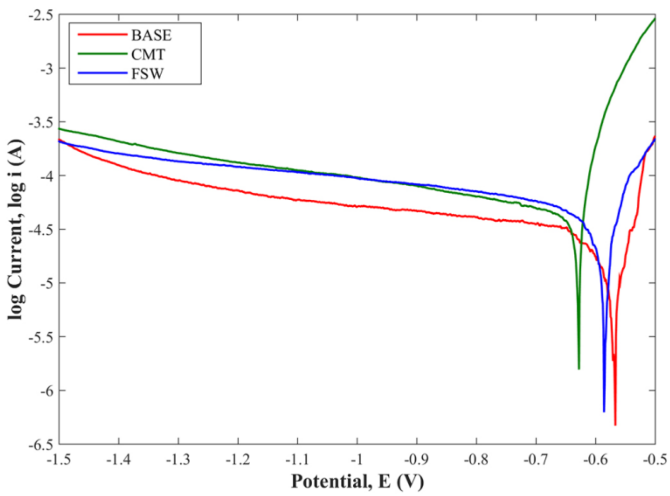

Figure 10. Tafel plot of the base material, Cold metal transfer welded and Friction stir welded specimens

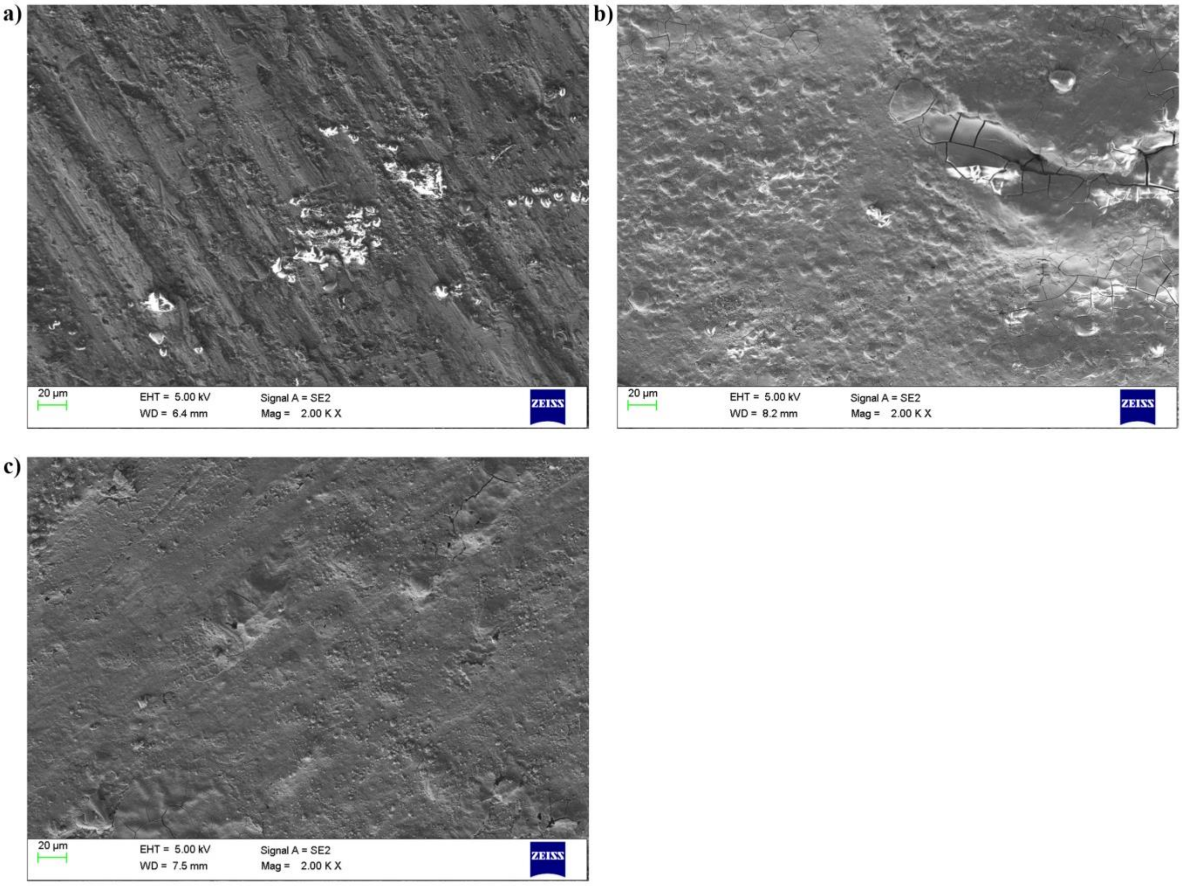

Figure 11. Surface morphology of the corroded (a) Base material (b) Cold metal transfer welded specimen (c) Friction stir welded specimen

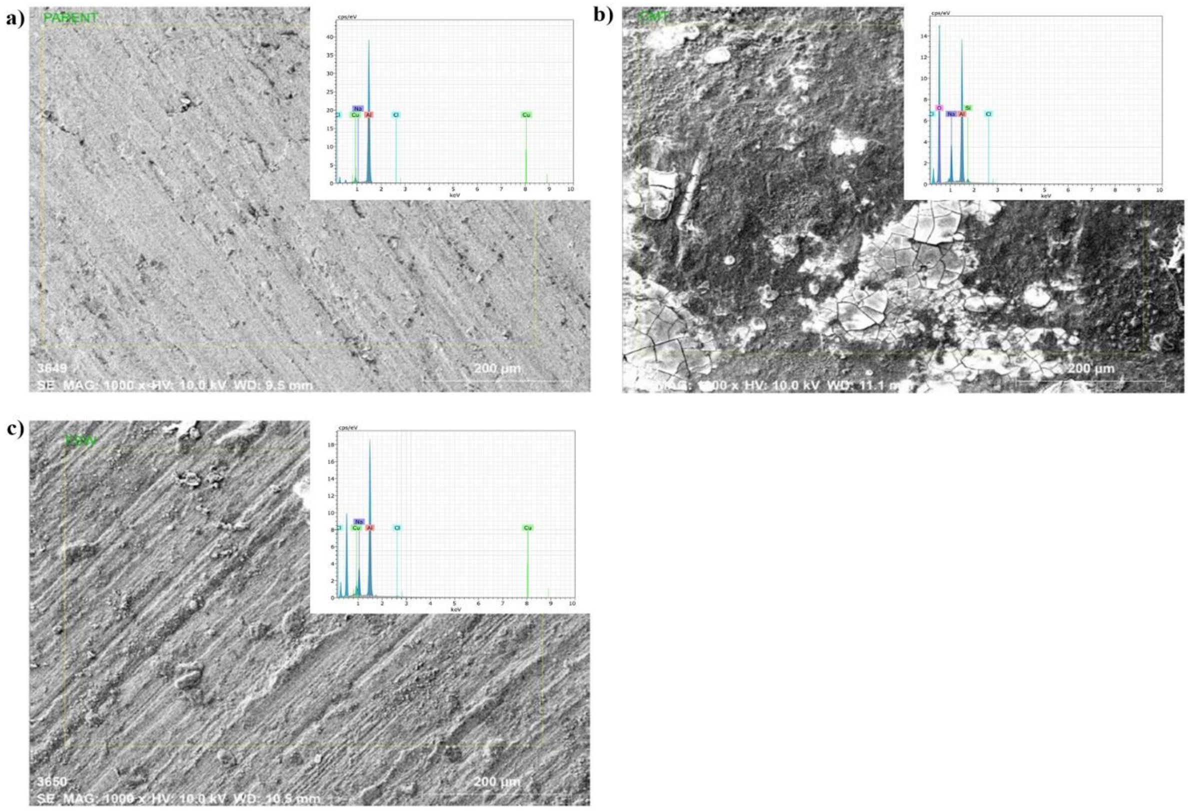

Figure 12. Energy dispersive X-ray spectroscopy analysis of the corroded specimens (a) Base material (b) Cold metal transfer welded specimen (c) Friction stir welded specimen

Table 5. Energy dispersive X-ray analysis of the corroded specimens

Sl.	Element	Normalized concentration Wt. %			Atomic concentration Wt. %			Error (3 σ) Wt. %		
		Base	*CMTW*	*FSW*	*Base*	*CMTW*	*FSW*	*Base*	*CMTW*	*FSW*
1	Aluminium	92.49	36.79	77.47	96.40	26.83	80.01	10.97	3.83	5.67
2	Copper	7.07	-	9.05	3.13	-	3.97	2.81	-	2.22
3	Sodium	0.29	9.59	12.72	0.35	8.21	15.42	0.14	1.38	1.30
4	Chlorine	0.16	0.19	0.76	0.13	0.11	0.60	0.11	0.11	0.15
5	Silicon	-	1.63	-	-	1.14	-	-	0.26	
6	Oxygen	-	51.80	-	-	63.71	-	-	13.56	
Total		100	100	100	100	100	100	100	-	

CMTW – Cold Metal Transfer Welding; FSW – Friction Stir Welding

Conclusion

Aluminium alloy 2219 plates were welded by cold metal transfer welding and friction stir welding process. The weldments were characterized for microstructure, microhardness, tensile strength, rupture load, impact strength, wear rate, and corrosion rate. The results demonstrated the following.

- The optimum parameters for complete penetration in cold metal transfer welding process were current of 170 A and welding speed of 700 $mm.min^{-1}$. The optimum parameters for complete penetration in friction stir welding process were tool rotation speed of 1600 rpm and a welding speed of 60 $mm.min^{-1}$. The results demonstrated the following.
- The microstructure of the base material AA2219 had Al_2Cu particles, cold metal transfer welded specimens had Al_2Cu and β-(Al, Fe, Si) particles. The friction stir welded specimens had Al_2Cu particles.
- The microhardness of the cold metal transfer welded specimens were found to be higher than the base material and friction stir welded specimens. High microhardness was attributed to the presence of both β-(Al, Fe, Si) and Al_2Cu phases.
- The cold metal transfer welded specimen was dominated by severe wear and the friction stir welded specimen was dominated by mild wear.
- Electrochemical corrosion test revealed that the corrosion rate of the cold metal transfer welded specimens was higher than that of the friction stir welded specimens, which was accredited to the presence of large volumes of inter-metallics with a significant difference in corrosion potential. The results are consistent with the immersion test results.

The results indicated that cold metal transfer welded specimens had high hardness, tensile strength, impact strength, and wear resistance than the friction stir welded specimens. However, the corrosion resistance of cold metal transfer welded specimens was lower than the friction stir welded specimens.

References

[1] V. Sharma, K. S. Kumar, B. N. Rao, and S. Pathak, "Effect of microstructure and strength on the fracture behavior of AA2219 alloy," *Materials Science and Engineering A,* vol. 502, pp. 45-53, 2009.

[2] S. Tosto, F. Nenci, and J. Hu, "Microstructure and properties of electron beam welded and post-welded 2219 aluminium alloy," *Materials Science and Technology,* vol. 12, pp. 323-328, 1996.

[3] W. Xu, J. Liu, and H. Zhu, "Pitting corrosion of friction stir welded aluminum alloy thick plate in alkaline chloride solution," *Electrochimica Acta,* vol. 55, pp. 2918-2923, 2010.

[4] G. Dance, "Comparative evaluation of mechanical properties of TIG, MIG, EBW and VPPA welded AA2219 aluminum alloy," *Welding and Metal Fabrication,* vol. 24, pp. 216-222, 1994.

[5] S. Malarvizhi and V. Balasubramanian, "Fatigue crack growth resistance of gas tungsten arc, electron beam and friction stir welded joints of AA2219 aluminium alloy," *Materials and Design,* vol. 32, pp. 1205-1214, 2011.

[6] S. Malarvizhi, K. Raghukandan, and N. Viswanathan, "Effect of post weld aging treatment on tensile properties of electron beam welded AA2219 aluminum alloy," *International Journal of Advanced Manufacturing Technology,* vol. 37, pp. 294-301, 2008.

[7] D. Dittrich, J. Standfuss, J. Liebscher, B. Brenner, and E. Beyer, "Laser beam welding of hard to weld Al alloys for a regional aircraft fuselage design–first results," *Physics Procedia*, vol. 12, pp. 113-122, 2011.

[8] P. B. Srinivasan, K. Arora, W. Dietzel, S. Pandey, and M. Schaper, "Characterisation of microstructure, mechanical properties and corrosion behaviour of an AA2219 friction stir weldment," *Journal of Alloys Compounds,* vol. 492, pp. 631-637, 2010.

[9] C. G. Pickin, S. W. Williams, and M. Lunt, "Characterisation of the cold metal transfer (CMT) process and its application for low dilution cladding," *Journal of Materials Processing Technology*, vol. 211, pp. 496-502, 2011.

[10] P. Almeida and S. Williams, "Innovative process model of Ti–6Al–4V additive layer manufacturing using cold metal transfer (CMT)," in *Proceedings of the twenty-first annual international solid freeform fabrication symposium, University of Texas at Austin, Austin, TX, USA*, 2010.

[11] P. Wang, S. Hu, J. Shen, and Y. Liang, "Characterization the contribution and limitation of the characteristic processing

parameters in cold metal transfer deposition of an Al alloy," *Journal of Materials Processing Technology,* vol. 245, pp. 122-133, 2017.

[12] H. Zhang, S. Hu, Z. Wang, and Y. Liang, "The effect of welding speed on microstructures of cold metal transfer deposited AZ31 magnesium alloy clad," *Materials and Design,* vol. 86, pp. 894-901, 2015.

[13] R. V. Vignesh and R. Padmanaban, "Modelling tensile strength of friction stir welded aluminium alloy 1100 using fuzzy logic," in *Intelligent Systems and Control (ISCO), 2017 11th International Conference on*, 2017, pp. 449-456.

[14] R. V. Vignesh, R. Padmanaban, M. Arivarasu, S. Thirumalini, J. Gokulachandran, and M. S. S. S. Ram, "Numerical modelling of thermal phenomenon in friction stir welding of aluminum plates," *IOP Conference Series: Materials Science and Engineering,* vol. 149, p. 012208, 2016.

[15] H. Fujii, L. Cui, M. Maeda, and K. Nogi, "Effect of tool shape on mechanical properties and microstructure of friction stir welded aluminum alloys," *Materials Science and Engineering A,* vol. 419, pp. 25-31, 2006.

[16] M. Dehghani, A. Amadeh, and S. A. Mousavi, "Investigations on the effects of friction stir welding parameters on intermetallic and defect formation in joining aluminum alloy to mild steel," *Materials and Design,* vol. 49, pp. 433-441, 2013.

[17] P. Cavaliere, A. De Santis, F. Panella, and A. Squillace, "Effect of welding parameters on mechanical and microstructural properties of dissimilar AA6082–AA2024 joints produced by friction stir welding," *Materials and Design,* vol. 30, pp. 609-616, 2009.

[18] T. Chen and W.-B. Lin, "Optimal FSW process parameters for interface and welded zone toughness of dissimilar aluminium–steel joint," *Science and Technology of Welding and Joining,* vol. 15, pp. 279-285, 2010.

[19] S. K. Rao, G. M. Reddy, K. S. Rao, M. Kamaraj, and K. P. Rao, "Reasons for superior mechanical and corrosion properties of 2219 aluminum alloy electron beam welds," *Materials characterization,* vol. 55, pp. 345-354, 2005.

[20] V. V. Ramalingam and P. Ramasamy, "Modelling Corrosion Behavior of Friction Stir Processed Aluminium Alloy 5083 Using Polynomial: Radial Basis Function," *Transactions of the Indian Institute of Metals,* vol. 70, pp. 2575-2589, December 01 2017.

[21] R. Vaira Vignesh, R. Padmanaban, and M. Datta, "Influence of FSP on the microstructure, microhardness, intergranular corrosion susceptibility and wear resistance of AA5083 alloy," *Tribology - Materials, Surfaces & Interfaces,* pp. 1-13, 2018.

[22] Sivaraos, K. R. Milkey, A. R. Samsudin, A. K. Dubey, and P. Kidd, "Comparison between taguchi method and response surface methodology (RSM) in modelling CO2 laser machining," *Jordan Journal of Mechanical and Industrial Engineering,* vol. 8, pp. 35-42, 2014.

[23] V. V. Ramalingam and P. Ramasamy, "Modelling Corrosion Behavior of Friction Stir Processed Aluminium Alloy 5083 Using Polynomial: Radial Basis Function," *Transactions of the Indian Institute of Metals,* vol. DOI: 10.1007/s12666-017-1110-1, April 11 2017.

[24] V. Ramakoteswara Rao, N. Ramanaiah, and M. M. M. Sarcar, "Optimization of volumetric wear rate of Aa7075-Tic metal matrix composite by using taguchi technique," *Jordan Journal of Mechanical and Industrial Engineering,* vol. 10, pp. 189-198, 2016.

[25] A. K. Jafarzadeh, T. Shahrabi, S. M. M. Hadavi, and M. G. Hosseini, "Role of Chloride Ion and Dissolved Oxygen in Electrochemical Corrosion of AA5083-H321 Aluminum-Magnesium Alloy in NaCl Solutions under Flow Conditions," *Journal of Materials Science & Technology,* vol. 23, 2007.

JJMIE

Volume 12, Number 4, December. 2018
ISSN 1995-6665
Pages 293 - 312

Jordan Journal of Mechanical and Industrial Engineering

Nonlinear Vibration and Frequency Analysis of Functionally Graded- Piezoelectric Cylindrical Nano-shell with Surface Elasticity

Sayyid H. Hashemi Kachapi

Department of Mechanical Engineering, Babol Noshirvani University of Technology, P.O.Box484, Shariati Street, Babol, Mazandaran47148-71167, Iran

Received 3 August. 2018

Abstract

The size-dependent effects on the nonlinear dynamic response and frequency analysis of functionally graded-piezoelectric cylindrical nano-shell (FG-PCNS) as Nano resonator are investigated in the current paper. The Nano resonator is embedded in visco-Pasternak medium and harmonic force. To this end, Gurtin–Murdoch surface elasticity and von-karman-Donnell's theory are used. The governing equations and boundary conditions are derived using Hamilton's principle. Also, the assumed mode method is used for changing the partial differential equations into ordinary differential equations. Complex averaging method combined with arc-length continuation is used to achieve an approximate solution for the nonlinear frequency response and stability analysis of the FG-PCNS. The convergence, accuracy and reliability of the current formulation are validated by comparisons with existing experimental and numerical results published in the literature, with excellent agreements achieved. The detailed parametric study is conducted, focusing on the effects of parameters such as the effects of geometrical parameters and material properties, visco-Pasternak medium and harmonic force with surface energy effects and principle parametric resonance on the nonlinear dynamic response and frequency analysis of the piezoelectric nanoresonator.

Keywords: Surface elasticity, functionally graded- piezoelectric cylindrical nano-shell, natural frequency, nonlinear dynamic response, visco-Pasternak medium, harmonic force, stability analysis, complex averaging method, arc-length continuation;

Nomenclature: Notation and symbols

symbols	Description	symbol	Description
h_N	Thickness of nanoshell	h_p	Thickness of piezoelectric layer
L	Piezoelectric nanoshell Length	E_p	Young modulus of piezoelectric layer
R	The mid-surface radius	υ_p	Poisson ratio of piezoelectric layer
x	Axial direction	ρ_p	Mass density of piezoelectric layer
θ	Circumferential direction	e_{31p}, e_{32p}	Piezoelectric constants
z	Radius direction	η_{33p}	Dielectric constant
E_N	Young modulus of nanoshell	s_2	outer surface of piezoelectric layer
υ_N	Poisson ratio of nanoshell	λ^{s_2}, μ^{s_2}	Lamé's constants of piezoelectric layer
ρ_N	Mass density of nanoshell	$\bar{E}_p$	Electric field
S_1	Inner surface of nanoshell	D_{zp}	Electric displacement
λ^{s_1}, μ^{s_1}	Lamé's constants of nanoshell	$\tau_0^{s_2}$	Residual stress of piezoelectric layer

$\tau_0^{s_1}$	Residual stress of nanoshell	$e_{31p}^{s_2}, e_{32p}^{s_2}$	Surface piezoelectric constants
ρ^{s_1}	Nanoshell surface mass density	ρ^{s_2}	Piezoelectric layer surface mass density
C_{ijN}	Elastic constant of nanoshell	C_{ijp}	Elastic constant of piezoelectric layer
σ_{ijN}	Middle stress of nanoshell	σ_{ijp}	Middle stress of piezoelectric layers
$\kappa_{(x,\theta)}$	Curvature components	V_p	Piezoelectric voltage
$\varepsilon^0_{(x,\theta)}, \gamma^0_{x\theta}$	Middle surface strains	π	Total strain energy
u	Displacement of x direction	T	Total kinetic energy
v	Displacement of θ direction	I	Mass moments of inertia
w	Displacement of z direction	C_w	Damping coefficient
∇	Laplace operator	K_w	Winkler modulus
ω	Natural frequency	K_p	Shear modulus of pasternak foundation
M	Total mass matrix	W	Total work
C	Total damping coefficient	K	Total stiffness matrix
f	Harmonic excitation amplitude		

* Corresponding author e-mail: sha.hashemi.kachapi@gmail.com.

1. Introduction

In recent years, piezoelectric materials with direct and converse effects play an important role for several applications such as nano-beams, nano-plates, nano-membranes and nano-shells have been fabricated and they attract worldwide attention in nanoelectromechanical systems (NEMS) [1-3]. As a result, investigation on the electromechanical characteristics of piezoelectric structures at nanoscale is crucial for NEMS design. The vibration of micro/nano-electromechanical systems is crucial for absorbing the ambient mechanical resources and producing the electric power. To design the nano-sized shell and obtain the desired properties, the vibration character should be addressed. Both molecular dynamics simulation and experimental investigation have invariably shown that the nano-sized effects in the analysis of vibration character of nanostructures cannot be neglected, and since the classical continuum theory is scale-free, it fails to predict the size-dependent response of nano-structures. Consequently, to consider the small-scale effect, some non-classical continuum theories have been introduced to develop the size-dependent continuum models [4-9].

In nanostructures for which the ratio of surface-to-volume is high, atoms at or near a free surface have different equilibrium requirements as compared to those within the bulk of material in consequence of dissimilar environmental conditions. This leads to the presentation of surface stresses that can considerably influence the mechanical behavior of nanostructures at very small sizes. So as to incorporate the surface stress effect into the continuum mechanics, Gurtin and Murdoch developed a non-classical elasticity theory named as surface elasticity theory [8, 9].

According to surface energy effect, free vibration analysis and nonlinear buckling and postbuckling behavior of nano-sized piezoelectric shell structures are studied by Fang et al. [10-12]. Recently, Hashemi Kachapi et al. presented Gurtin–Murdoch surface/interface theory to investigate the effects of the surface energy on the natural frequencies analysis of double-walled piezo-viscoelastic cylindrical nanoshell [13]. They showed that considering surface effects in the nanoscale system without considering the SD, the maximum frequency will be obtained and this case will be considered as the critical state of the system. In another works by Hashemi Kachapi et al., nonlinear vibration and stability analysis of piezoelectric nanoresonator subjected to electrostatic and harmonic excitations is investigated using the Gurtin–Murdoch surface/interface theory and complex averaging method combined with arc-length continuation [14, 15]. It is found that increasing or decreasing of surface/interface parameters lead to increasing or decreasing the resonance amplitude, resonant frequency, the system's instability, nonlinear behavior and bandwidth. Liu et al. utilized a new finite element method for modeling thin structures with surface effects by using layered shell elements [16]. They studied surface effects on kirigami of soft sheets as a potential application of the proposed method.

Karimipour et al investigated the size dependent vibration and pull-in instability analysis of thin plate actuator using nonclassical theories [17]. It is found that the significant difference between the pull-in instability parameters in the nonclassical and the classical theory are merely due to the consideration of the size effect parameters. Pourkiaee et al. investigated the nonlinear vibration and stability analysis of a doubly clamped piezoelectric nanobeam by using the multiple scales method [18]. The influence of van der Waals forces, piezoelectric voltages and surface effects are investigated on the static equilibria, pull-in voltages and dynamic primary resonances of the nano resonator. Rouhi et al. worked on nonlinear free vibration analysis of circular cylindrical nanoshell with considering Gurtin–Murdoch surface stress theory and shear deformation effects [19]. Also, based on electro-elasticity surface/interface theory, Zhu et al. investigated torsional buckling behavior of FG cylindrical nano-shell covered with piezoelectric nano-layers [20]. The effects of small scale and surface effects on nonlinear vibration of boron nitride nano sheet were showed by Ghorbanpour Arani et al. [21]. In another work by Ghorbanpour Arani et al., dynamic stability of double-walled boron nitride nanotubes conveying viscose fluid by incorporating Euler–Bernoulli beam, Timoshenko beam and cylindrical shell theories are investigated using nonlocal piezoelasticity theory [22]. Nonlinear vibration of smart nano-sandwich viscoelastic structure conveying visco-fluid considering surface effects was studied by Fereidoon et al. [23]. The nonlinear buckling and postbuckling behaviors of shear deformable nano-shell under radial compressive load were studied by Sahmani et al. based on the surface elasticity theory, and the effect of surface free energy on the critical buckling load and end-shortening was discussed [24]. Zhu et al. investigated on influences of surface energy effect for nonlinear free vibration behavior of orthotropic piezoelectric cylindrical nano-shells [25].

In the present study, the free and force vibration analysis of a functionally graded- piezoelectric cylindrical nano-shell with arbitrary boundary conditions is investigated. For this purpose, Hamilton's principle, assumed mode method and complex averaging method combined with arc-length continuation are used to drive the governing equations and boundary conditions, changing the partial differential equations into ordinary differential equations and also to achieve an approximate solution for the nonlinear frequency response and stability analysis of the FG-PCNS. A variety of new vibration results including the effects of geometrical parameters and material properties, visco-Pasternak medium and harmonic force with surface energy effects on natural frequency, nonlinear dynamic response and stability analysis for FG-PCNS with non-classical restraints are presented. Also, the solution method used in this paper, i.e., Complex averaging method combined with Arc-length continuation, is rarely taken into consideration, while in contrast to other methods used to get the frequency response, for any number of equations of motion with each the desired mode gains an acceptable answer.

2. Mathematical formulation

A cylindrical nano shell embedded with a piezoelectric layer is depicted, as shown in Fig. 1. The length of nanoshell is $L\,nm$, the geometrical parameters of the cylindrical shell are mid-surface radius R, thickness of cylindrical shell $2h_N$ thickness of piezoelectric material layer h_p. In Figure 1, harmonic force (fcosωt) is applied to the piezoelectric nanoshell by a compressive force where f and ω are the amplitude and angular frequency of the external excitation. With the origin of coordinate system located on the middle surface of nano-shell, the coordinates of a typical point in the axial, circumferential and radius directions are described by x, θ, and z, respectively. Also, K_w ,K_p and C_w are stiffness coefficient of Winkler foundation, shear layer of Pasternak foundation and the damping factor of the visco medium for the transverse motion, respectively.

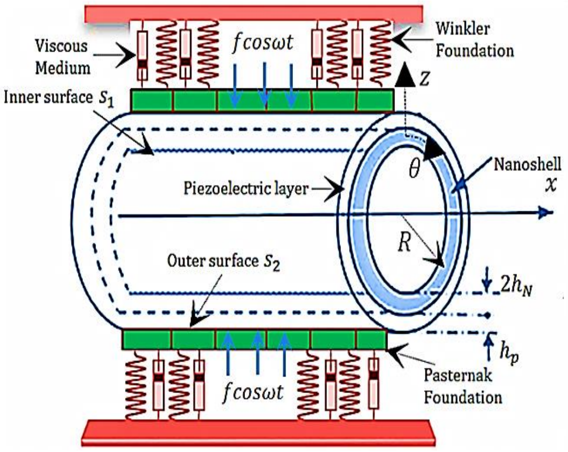

Figure 1. A functionally graded- piezoelectric cylindrical nano-shell with inner and outer surfaces

E_N, υ_N and ρ_N represent Young modulus, Poisson ratio and the mass density of cylindrical nano-shell. In the present nano-shell, it is assumed that the material properties E_N, υ_N and ρ_N vary through the thickness of nano-shell according to the power-law function. They are written as

$$E_N = (E_T - E_B)\left(\frac{2z + h_N}{2h_N}\right)^q + E_B \tag{1}$$

$$\upsilon_N = (\upsilon_T - \upsilon_B)\left(\frac{2z + h_N}{2h_N}\right)^q + \upsilon_B \tag{2}$$

$$\rho_N = (\rho_T - \rho_B)\left(\frac{2z + h_N}{2h_N}\right)^q + \rho_B \tag{3}$$

where q is the power-law exponent. The subscripts T and B represent the properties of the nano-shell at the upper and lower layers, respectively.

Young modulus, Poisson ratio, piezoelectric and dielectric constants and the mass density of piezoelectric layer are $E_p, \upsilon_p, e_{31p}, e_{32p}, \eta_{33p}$ and ρ_p. Due to the nano-sized property, the ratio of surface to the volume becomes large, and the surface energy around the shell expresses significant effect on the vibration of nano-structure. According to the electro-elastic surface/interface theory, the surface/interface region adhered to the neighboring solids is several atomic sizes and has its own electromechanical properties. The surface at the outer piezoelectric layer is denoted by s_2, and the inner surface is denoted by s_1, as shown in Fig. 1. The material properties of surface s_2 are Lamé's constants λ^{s_2}, μ^{s_2}, residual stress $\tau_0^{s_2}$ and piezoelectric constants $e_{31p}^{s_2}, e_{32p}^{s_2}$. Those of the inner surface are Lame's constants λ^{s_1}, μ^{s_1}, and residual stress $\tau_0^{s_1}$.

Due to the character of nano-shell, the state of generalized plane stress of shells is assumed, and the normal stress in the radial direction is zero. In the cylindrical nano-shell, the constitutive relation can be expressed as [26, 27];

$$\begin{Bmatrix}\sigma_{xxN}\\ \sigma_{\theta\theta N}\\ \tau_{x\theta N}\end{Bmatrix} = \begin{bmatrix}C_{11N} & C_{12N} & 0\\ C_{21N} & C_{22N} & 0\\ 0 & 0 & C_{66N}\end{bmatrix}\begin{Bmatrix}\varepsilon_{xx}\\ \varepsilon_{\theta\theta}\\ \gamma_{x\theta}\end{Bmatrix}, \quad or \quad \{\sigma_N\} = [C_N]\{\varepsilon\}, \tag{4}$$

In the outside piezoelectric shell, the constitutive relation can be expressed as [26, 27]

$$\begin{Bmatrix}\sigma_{xxp}\\ \sigma_{\theta\theta p}\\ \tau_{x\theta p}\end{Bmatrix} = \begin{bmatrix}C_{11p} & C_{12p} & 0\\ C_{21p} & C_{22p} & 0\\ 0 & 0 & C_{66p}\end{bmatrix}\begin{Bmatrix}\varepsilon_{xx}\\ \varepsilon_{\theta\theta}\\ \gamma_{x\theta}\end{Bmatrix} - \begin{bmatrix}0 & 0 & e_{31p}\\ 0 & 0 & e_{32p}\\ 0 & 0 & 0\end{bmatrix}\begin{Bmatrix}\bar{E}_{xp}\\ \bar{E}_{\theta p}\\ \bar{E}_{zp}\end{Bmatrix}, \tag{5}$$

or $\{\sigma_p\} = [C_p]\{\varepsilon\} - [e_p]\{\bar{E}_p\}$,

in which the subscripts N and P represent the cylindrical nano-shell and piezoelectric layers, respectively. $\{\bar{E}_p\}$ is the vector of electric field for piezoelectric layers. $[C_N]$ and $[C_p]$are the matrixes of elastic constants, and they can be denoted as

$$C_{11N} = \frac{E_N}{1-\upsilon_N^2} = C_{22N}, \quad C_{12N} = \frac{\upsilon_N E_N}{1-\upsilon_N^2} = C_{21N}, \quad C_{66N} = \frac{E_N}{2(1+\upsilon_N)} \tag{6}$$

$$C_{11p} = \frac{E_p}{1-\upsilon_p^2} = C_{22p}, \quad C_{12p} = \frac{\upsilon_p E_p}{1-\upsilon_p^2} = C_{21p}, \quad C_{66p} = \frac{E_p}{2(1+\upsilon_p)} \tag{7}$$

Since the piezoelectric layers are very thin, $\bar{E}_{xp}$and $\bar{E}_{\theta p}$are assumed to be zero ($\bar{E}_{xp} = \bar{E}_{\theta p} = 0$), and only the radial component of electric field $\bar{E}_{zp}$is considered. Consequetly, $\{\bar{E}_p\}$ can be written as

$$\bar{E}_{zp} = V_p/h_p, \tag{8}$$

where V_p is the voltage applied to piezoelectric layers. In addition, the voltages at the piezoelectric surface $S_2(z = h_N + h_p)$ and $S_1(z = h_N)$ are $+V_p$ and $-V_p$, respectively. Based on these assumptions mentioned above, the radial component of electric displacement D_{zp} can be presented as

$$D_{zp} = e_{31p}\varepsilon_{xx} + e_{32p}\varepsilon_{\theta\theta} + \eta_{33p}\bar{E}_{zp} \tag{9}$$

3. Non- classical Shell theory

Within the framework of classical shell theory, the displacement fields of the nano-shell can be written as [27]

$$u_x(x,\theta,z) = u(x,\theta) - z\frac{\partial w(x,\theta)}{\partial x}, \tag{10}$$

$$u_\theta(x,\theta,z) = v(x,\theta) - \frac{z}{R}\frac{\partial w(x,\theta)}{\partial \theta}, \tag{11}$$

$$u_z(x,\theta,z) = w(x,\theta), \tag{12}$$

where u, v and w stand for the middle surface displacements in the x , θ and z directions, respectively. The nonlinear deflection and curvatures are defined by Von-Karman-Donnell's theory as [26, 27]

$$\begin{Bmatrix}\varepsilon_{xx}\\ \varepsilon_{\theta\theta}\\ \gamma_{x\theta}\end{Bmatrix}=\begin{Bmatrix}\varepsilon_{xx}^0\\ \varepsilon_{\theta\theta}^0\\ \gamma_{x\theta}^0\end{Bmatrix}+z\begin{Bmatrix}\kappa_{xx}\\ \kappa_{\theta\theta}\\ \kappa_{x\theta}\end{Bmatrix}=\begin{Bmatrix}\frac{\partial u}{\partial x}+\frac{1}{2}\left(\frac{\partial w}{\partial x}\right)^2\\ \frac{1}{R}\left(\frac{\partial v}{\partial\theta}+w\right)+\frac{1}{2R^2}\left(\frac{\partial w}{\partial\theta}\right)^2\\ \frac{1}{R}\frac{\partial u}{\partial\theta}+\frac{\partial v}{\partial x}+\frac{1}{R}\frac{\partial w}{\partial x}\frac{\partial w}{\partial\theta}\end{Bmatrix}-z\begin{Bmatrix}\frac{\partial^2 w}{\partial x^2}\\ \frac{1}{R^2}\frac{\partial^2 w}{\partial\theta^2}\\ \frac{2}{R}\frac{\partial^2 w}{\partial x\partial\theta}\end{Bmatrix}\tag{13}$$

in which ε_{xx}^0 ،$\varepsilon_{\theta\theta}^0$ and $\gamma_{x\theta}^0$ are the middle surface strains, and κ_{xx} ,$\kappa_{\theta\theta}$ and $\kappa_{x\theta}$ are the curvature components of the nano-shell.

Since the dimension of the shell is at nanometer scale, the surface effect needs to be considered. On based of the Gurtin–Murdoch surface elasticity theory, the constitute relations for surfaces can be written as [8, 9]

$$\begin{aligned}\sigma_{\alpha\beta}^{s_2}&=\tau_0^{s_2}\delta_{\alpha\beta}+\left(\tau_0^{s_2}+\lambda^{s_2}\right)\varepsilon_{qq}\delta_{\alpha\beta}+2\left(\mu^{s_2}-\tau_0^{s_2}\right)\varepsilon_{\alpha\beta}+\tau_0^{s_2}u_{\alpha,\beta}^{s_2}-e_p^{s_2}E_{zp},\\ \sigma_{\alpha z}^{s_2}&=\tau_0^{s_2}u_{z,\alpha}^{s_2}, \quad \sigma_{\alpha z}^{s_1}=\tau_0^{s_1}u_{z,\alpha}^{s_1}, (\alpha,\beta=x,\theta)\\ \sigma_{\alpha\beta}^{s_1}&=\tau_0^{s_1}\delta_{\alpha\beta}+\left(\tau_0^{s_1}+\lambda^{s_1}\right)\varepsilon_{qq}\delta_{\alpha\beta}+2\left(\mu^{s_1}-\tau_0^{s_1}\right)\varepsilon_{\alpha\beta}+\tau_0^{s_1}u_{\alpha,\beta}^{s_1},\end{aligned}\tag{14}$$

in which $\delta_{\alpha\beta}$ is the Kronecker delta function. Furthermore, the components of stress at the surfaces can be expressed as

$$\begin{aligned}\sigma_{xx}^{s_2}&=(\lambda^{s_2}+2\mu^{s_2})\varepsilon_{xx}+\left(\tau_0^{s_2}+\lambda^{s_2}\right)\varepsilon_{\theta\theta}-\frac{\tau_0^{s_2}}{2}\left(\frac{\partial w}{\partial x}\right)^2+\tau_0^{s_2}-e_{31p}^{s_2}E_{zp},\\ \sigma_{\theta\theta}^{s_2}&=\left(\tau_0^{s_2}+\lambda^{s_2}\right)\varepsilon_{xx}+(\lambda^{s_2}+2\mu^{s_2})\varepsilon_{\theta\theta}-\tau_0^{s_2}\left(\frac{w}{R}+\frac{1}{2R^2}\left(\frac{\partial w}{\partial\theta}\right)^2\right)+\tau_0^{s_2}-e_{32p}^{s_2}E_{zp},\\ \sigma_{xx}^{s_1}&=(\lambda^{s_1}+2\mu^{s_1})\varepsilon_{xx}+\left(\tau_0^{s_1}+\lambda^{s_1}\right)\varepsilon_{\theta\theta}-\frac{\tau_0^{s_1}}{2}\left(\frac{\partial w}{\partial x}\right)^2+\tau_0^{s_1},\\ \sigma_{\theta\theta}^{s_1}&=\left(\tau_0^{s_1}+\lambda^{s_1}\right)\varepsilon_{xx}+(\lambda^{s_1}+2\mu^{s_1})\varepsilon_{\theta\theta}-\tau_0^{s_1}\left(\frac{w}{R}+\frac{1}{2R^2}\left(\frac{\partial w}{\partial\theta}\right)^2\right)+\tau_0^{s_1}\\ \sigma_{x\theta}^{s_i}&=\mu^{s_i}\gamma_{x\theta}-\tau_0^{s_i}\left(\frac{\partial v}{\partial x}+\frac{1}{2R}\frac{\partial w}{\partial x}\frac{\partial w}{\partial\theta}-\frac{z}{R}\frac{\partial^2 w}{\partial x\partial\theta}\right),\sigma_{xz}^{s_i}=\tau_0^{s_i}\frac{\partial w}{\partial x},\\ \sigma_{\theta x}^{s_i}&=\mu^{s_i}\gamma_{x\theta}-\tau_0^{s_i}\left(\frac{1}{R}\frac{\partial u}{\partial\theta}+\frac{1}{2R}\frac{\partial w}{\partial x}\frac{\partial w}{\partial\theta}-\frac{z}{R}\frac{\partial^2 w}{\partial x\partial\theta}\right),\sigma_{\theta z}^{s_i}=\frac{\tau_0^{s_i}}{R}\frac{\partial w}{\partial\theta},(i=1,2)\end{aligned}\tag{15}$$

Based on the classical continuum models, σ_{zz} is neglected due to its small value as compared to other normal stress components. But, in the present nonclassical continuum model, this assumption does not satisfy the surface conditions. Thus, it is supposed that σ_{zz} varies linearly through the thickness, and satisfies the balance conditions on the surfaces [8-15], i.e.

$$\begin{aligned}\sigma_{zz}=&\frac{1}{2}\left(\left(\frac{\partial\sigma_{xz}^{s_2}}{\partial x}+\frac{1}{R}\frac{\partial\sigma_{\theta z}^{s_2}}{\partial\theta}-\rho^{s_2}\frac{\partial^2 w}{\partial t^2}\right)-\left(\frac{\partial\sigma_{xz}^{s_1}}{\partial x}+\frac{1}{R}\frac{\partial\sigma_{\theta z}^{s_1}}{\partial\theta}-\rho^{s_1}\frac{\partial^2 w}{\partial t^2}\right)\right)\\ &+\frac{1}{2h_N+h_p}\left(\left(\frac{\partial\sigma_{xz}^{s_2}}{\partial x}+\frac{1}{R}\frac{\partial\sigma_{\theta z}^{s_2}}{\partial\theta}-\rho^{s_2}\frac{\partial^2 w}{\partial t^2}\right)+\left(\frac{\partial\sigma_{xz}^{s_1}}{\partial x}+\frac{1}{R}\frac{\partial\sigma_{\theta z}^{s_1}}{\partial\theta}-\rho^{s_1}\frac{\partial^2 w}{\partial t^2}\right)\right)z\end{aligned}\tag{16}$$

For simplification, the material properties of surfaces and interfaces are selected as

$$\tau_0^{s_1}=\tau_0^{s_2}=\tau_0^s,\ \lambda^{s_1}=\lambda^{s_2}=\lambda^s,\ \mu^{s_1}=\mu^{s_2}=\mu^s,\ e_{31p}^{s_2}=e_{31p}^s,\ e_{32p}^{s_2}=e_{32p}^s\tag{17}$$

By means of Eqs. (15) and (16), σ_{zz} can be rewritten as

$$\sigma_{zz}=\left(\frac{\left(\tau_0^{s_2}-\tau_0^{s_1}\right)}{2}+\frac{z\left(\tau_0^{s_2}+\tau_0^{s_1}\right)}{2h_N+h_p}\right)\left(\frac{\partial^2 w}{\partial x^2}+\frac{1}{R^2}\frac{\partial^2 w}{\partial\theta^2}\right)+\left(\frac{(\rho^{s_1}-\rho^{s_2})}{2}-\frac{z(\rho^{s_1}+\rho^{s_2})}{2h_N+h_p}\right)\frac{\partial^2 w}{\partial t^2},\tag{18}$$

According to Eq. (18), the normal stresses σ_{xx} and $\sigma_{\theta\theta}$ Eqs. (4) and (5) can be rewritten ten as

$$\sigma_{xxN}=C_{11N}\varepsilon_{xx}+C_{12N}\varepsilon_{\theta\theta}+\frac{\upsilon_N\sigma_{zz(N,p)}}{1-\upsilon_N},\tag{19a}$$

$$\sigma_{\theta\theta N}=C_{21N}\varepsilon_{xx}+C_{22N}\varepsilon_{\theta\theta}+\frac{\upsilon_N\sigma_{zz(N,p)}}{1-\upsilon_N},\tag{19b}$$

$$\sigma_{x\theta N}=C_{66N}\gamma_{x\theta},\tag{19c}$$

$$\sigma_{xxp}=C_{11p}\varepsilon_{xx}+C_{12p}\varepsilon_{\theta\theta}-e_{31p}\bar{E}_{xp}+\frac{\upsilon_p\sigma_{zz(N,p)}}{1-\upsilon_p},\tag{19d}$$

$$\sigma_{\theta\theta p}=C_{21p}\varepsilon_{xx}+C_{22p}\varepsilon_{\theta\theta}-e_{32p}\bar{E}_{\theta p}+\frac{\upsilon_N\sigma_{zz(N,p)}}{1-\upsilon_p},\tag{19e}$$

$$\sigma_{x\theta p}=C_{66p}\gamma_{x\theta},\tag{19f}$$

4. Governing equations

In this section, the governing equations of motion of the piezoelectric cylindrical nanoshell are obtained by applying the assumed mode method. The total strain energy considering the surface stress effect is expressed as:

$$\pi=\frac{1}{2}\int_0^L\int_0^{2\pi}\int_{-h_N}^{h_N}(\sigma_{ijN}\varepsilon_{ij})Rdzd\theta dx+\frac{1}{2}\int_0^L\int_0^{2\pi}\int_{h_N}^{h_N+h_p}(\sigma_{ijp}\varepsilon_{ij}-\bar{E}_{zp}D_{zp})Rdzd\theta dx$$
$$+\frac{1}{2}\int_0^L\int_0^{2\pi}(\sigma_{ij}^{s_2}\varepsilon_{ij}-\bar{E}_{zp}D_i^{s_2})(R+h_N+h_p)d\theta dx+\frac{1}{2}\int_0^L\int_0^{2\pi}(\sigma_{ij}^{s_1}\varepsilon_{ij})(R-h_N)d\theta dx \tag{20}$$
$$=\frac{1}{2}\int_0^L\int_0^{2\pi}\{N_{xx}\varepsilon_{xx}^0+N_{\theta\theta}\varepsilon_{\theta\theta}^0+N_{x\theta}\gamma_{x\theta}^0+M_{xx}\kappa_{xx}+M_{\theta\theta}\kappa_{\theta\theta}+M_{x\theta}\kappa_{x\theta}+\eta_{33}\bar{E}_{zp}^2h_p\}Rd\theta dx\,.$$

In Eq. (20), the stresses and moment resultants are defined in Appendixes A and B.

In addition, the kinetic energy of the nanoshell can be formulated as:

$$T=\frac{1}{2}\iint\left\{I\left(\left(\frac{\partial u}{\partial t}\right)^2+\left(\frac{\partial v}{\partial t}\right)^2+\left(\frac{\partial w}{\partial t}\right)^2\right)\right\}Rd\theta dx \tag{21}$$

where

$$I=\int_{-h_N}^{h_N}\rho_N\,dz+\rho_ph_p+\rho^{s_2}|_{z=-h_N}+\rho^{s_1}|_{z=h_N+h_p} \tag{22}$$

Which ρ_N,ρ_p and ρ^S are the mass density of nanoshell, piezoelectric layer and surfaces, respectively.

The work done by the external viscous damping, the visco-pasternak effect and the external harmonic excitation can be written as

$$W_c=\frac{1}{2}\int_0^L\int_0^{2\pi}C_w\left(\frac{\partial w}{\partial t}\right)^2Rd\theta dx \tag{23}$$

$$W_{wp}=-\int_0^L\int_0^{2\pi}\{(K_ww-K_p\nabla^2w)w\}Rd\theta dx \tag{24}$$

$$W_f=\int_0^L\int_0^{2\pi}(f\cos\omega t)\,wRd\theta dx \tag{25}$$

The equations of motion and corresponding boundary conditions of the piezoelectric shell can be derived from Hamilton's principle

$$\int_0^t(\delta T-\delta\pi+\delta w_c+\delta w_{wp}+\delta w_f)dt=0, \tag{26}$$

And by taking the variations of displacements u,v and w and then integrating by parts, and by equating the coefficients of δu ، δv and δw to zero, the governing equations of motion are derived as:

$$\delta u:\quad \frac{\partial N_{xx}}{\partial x}+\frac{1}{R}\frac{\partial N_{x\theta}}{\partial\theta}=I\frac{\partial^2u}{\partial t^2}, \tag{27}$$

$$\delta v:\quad \frac{\partial N_{x\theta}}{\partial x}+\frac{1}{R}\frac{\partial N_{\theta\theta}}{\partial\theta}=I\frac{\partial^2v}{\partial t^2}, \tag{28}$$

$$\delta w:\quad \frac{\partial^2M_{xx}}{\partial x^2}+\frac{2}{R}\frac{\partial^2M_{x\theta}}{\partial x\partial\theta}+\frac{1}{R^2}\frac{\partial^2M_{\theta\theta}}{\partial\theta^2}-\frac{N_{\theta\theta}}{R}+N_{xx}\frac{\partial^2w}{\partial x^2}+\frac{\partial N_{xx}}{\partial x}\frac{\partial w}{\partial x}+\frac{N_{\theta\theta}}{R^2}\frac{\partial^2w}{\partial\theta^2}$$
$$+\frac{1}{R^2}\frac{\partial N_{\theta\theta}}{\partial\theta}\frac{\partial w}{\partial\theta}+\frac{2}{R}N_{x\theta}\frac{\partial^2w}{\partial x\partial\theta}+\frac{1}{R}\frac{\partial N_{x\theta}}{\partial x}\frac{\partial w}{\partial\theta}+\frac{1}{R}\frac{\partial N_{x\theta}}{\partial\theta}\frac{\partial w}{\partial x}=I\frac{\partial^2w}{\partial t^2}+C_w\frac{\partial w}{\partial t}+K_ww-K_p\nabla^2w-f\cos\omega t, \tag{29}$$

and boundary conditions are obtained as follows:

$$\delta u=0\quad or\quad N_{xx}n_x+\frac{1}{R}N_{x\theta}n_\theta=0, \tag{30a}$$

$$\delta v=0\quad or\quad N_{x\theta}n_x+\frac{1}{R}N_{\theta\theta}n_\theta=0, \tag{30b}$$

$$\delta w=0\quad or\quad \left(\frac{\partial M_{xx}}{\partial x}+\frac{1}{R}\frac{\partial M_{x\theta}}{\partial\theta}+N_{xx}\frac{\partial w}{\partial x}+\frac{N_{x\theta}}{R}\frac{\partial w}{\partial\theta}\right)n_x \tag{30c}$$
$$+\left(\frac{1}{R}\frac{\partial M_{x\theta}}{\partial x}+\frac{1}{R^2}\frac{\partial M_{\theta\theta}}{\partial\theta}+\frac{N_{x\theta}}{R}\frac{\partial w}{\partial x}+\frac{N_{\theta\theta}}{R^2}\frac{\partial w}{\partial\theta}\right)n_\theta=0,$$

$$\frac{\partial w}{\partial x}=0\quad or\quad M_{xx}n_x+\frac{1}{R}M_{x\theta}n_\theta=0, \tag{30d}$$

$$\frac{\partial w}{\partial\theta}=0\quad or\quad \frac{1}{R}M_{x\theta}n_x+\frac{1}{R^2}M_{\theta\theta}n_\theta=0, \tag{30e}$$

But to solve the problem explicitly and more easily, and the direct use of boundary conditions in equations, the assumed mode method will be used.

With substituting the stresses and moment resultants Appendix A into strain and kinetic energies Eqs. (20) and (21) and using following dimensionless parameters

$$\bar{u}=\frac{u}{h_N},\bar{v}=\frac{v}{h_N},\bar{w}=\frac{w}{h_N},\xi=\frac{x}{L},\bar{b}=\frac{b}{h_N},\bar{A}_{ijN}=\frac{A_{ijN}}{A_{11N}},\bar{B}_{ijN}=\frac{B_{ijN}}{A_{11N}h_N},\bar{D}_{ijN}=\frac{D_{ijN}}{A_{11N}h_N^2},$$
$$\bar{A}_{ijp}=\frac{A_{ijp}}{A_{11N}},\bar{A}_{ij}^*=\frac{A_{ij}^*}{A_{11N}},\bar{B}_{ijp}=\frac{B_{ijp}}{A_{11N}h_N},\bar{B}_{ij}^*=\frac{B_{ij}^*}{A_{11N}h_N},\bar{D}_{ijp}=\frac{D_{ijp}}{A_{11N}h_N^2},\bar{D}_{ij}^*=\frac{D_{ij}^*}{A_{11N}h_N^2},$$
$$\bar{F}_{11N}^*=\frac{F_{11N}^*}{A_{11N}h_N},\bar{F}_{11p}^*=\frac{F_{11p}^*}{A_{11N}h_N},\bar{E}_{11N}^*=\frac{E_{11N}^*}{A_{11N}h_N^2},\bar{E}_{11p}^*=\frac{E_{11p}^*}{A_{11N}h_N^2},\bar{J}_{11N}^*=\frac{J_{11N}^*}{\rho_Nh_N^2},$$
$$J_{11p}^*=\frac{J_{11p}^*}{\rho_Nh_N^2},\bar{G}_{11N}^*=\frac{G_{11N}^*}{\rho_Nh_N^3},G_{11p}^*=\frac{G_{11p}^*}{\rho_Nh_N^3},\bar{N}_{xp}^*=\frac{N_{xp}^*}{A_{11N}},\bar{N}_{\theta p}^*=\frac{N_{\theta p}^*}{A_{11N}},\bar{M}_{xp}^*=\frac{M_{xp}^*}{A_{11N}h_N}, \tag{31}$$
$$\bar{M}_{\theta p}^*=\frac{M_{\theta p}^*}{A_{11N}h_N},\bar{\tau}_0^s=\frac{\tau_0^s}{A_{11N}},m_0=\frac{L}{R},m_1=\frac{L}{h_N},m_2=\frac{h_N}{R}=\frac{1}{\bar{R}},\bar{h}_p=\frac{h_p}{R},m_3=\frac{I}{2\rho_Nh_N},$$
$$m_4=\frac{h_p}{h_N},\tau=t\sqrt{\frac{A_{11N}}{2\rho_Nh_NL^2}}=\Omega t,\bar{\omega}=\frac{\omega}{\Omega},\bar{K}_w=\frac{K_wL^2}{m_3A_{11N}},\bar{K}_p=\frac{K_p}{m_3A_{11N}},\bar{C}_w=\frac{C_w}{I},$$
$$\bar{V}_p=\frac{V_p}{V_0},\bar{F}=\frac{fL^2}{A_{11N}m_3{h_N}^2},$$

Respectively, dimensionless strain and kinetic energies and are obtained as follows:

$$
\begin{aligned}
\pi = \frac{1}{2}\int_0^L\int_0^{2\pi}\Bigg\{ & \alpha_1\left(\frac{\partial\bar{u}}{\partial\xi}\right)^2 + \alpha_2\left(\frac{\partial\bar{u}}{\partial\theta}\right)^2 + \alpha_3\frac{\partial\bar{u}}{\partial\xi}\frac{\partial\bar{v}}{\partial\theta} + \alpha_4\frac{\partial\bar{v}}{\partial\xi}\frac{\partial\bar{u}}{\partial\theta} + \alpha_5\bar{w}\frac{\partial\bar{u}}{\partial\xi} + \alpha_6\frac{\partial\bar{u}}{\partial\xi}\left(\frac{\partial\bar{w}}{\partial\xi}\right)^2 \\
& +\alpha_7\frac{\partial\bar{u}}{\partial\xi}\left(\frac{\partial\bar{w}}{\partial\theta}\right)^2 + \alpha_8\frac{\partial\bar{u}}{\partial\theta}\frac{\partial\bar{w}}{\partial\xi}\frac{\partial\bar{w}}{\partial\theta} + \alpha_9\left(\frac{\partial\bar{v}}{\partial\theta}\right)^2 + \alpha_{10}\frac{\partial\bar{v}}{\partial\theta}\left(\frac{\partial\bar{w}}{\partial\theta}\right)^2 + \alpha_{11}\frac{\partial\bar{v}}{\partial\theta}\left(\frac{\partial\bar{w}}{\partial\xi}\right)^2 + \alpha_{12}\bar{w}\frac{\partial\bar{v}}{\partial\theta} \\
& +\alpha_{13}\left(\frac{\partial\bar{v}}{\partial\xi}\right)^2 + \alpha_{14}\frac{\partial\bar{v}}{\partial\xi}\frac{\partial\bar{w}}{\partial\xi}\frac{\partial\bar{w}}{\partial\theta} + \alpha_{15}\bar{w}^2 + \alpha_{16}\left(\frac{\partial\bar{w}}{\partial\xi}\right)^4 + \alpha_{17}\left(\frac{\partial\bar{w}}{\partial\theta}\right)^4 + \alpha_{18}\left(\frac{\partial\bar{w}}{\partial\xi}\right)^2\left(\frac{\partial\bar{w}}{\partial\theta}\right)^2 \\
& +\alpha_{19}\bar{w}\left(\frac{\partial\bar{w}}{\partial\xi}\right)^2 + \alpha_{20}\bar{w}\left(\frac{\partial\bar{w}}{\partial\theta}\right)^2 + \alpha_{21}\frac{\partial\bar{u}}{\partial\theta}\frac{\partial^2\bar{w}}{\partial\xi\partial\theta} + \alpha_{22}\frac{\partial\bar{u}}{\partial\xi}\frac{\partial^2\bar{w}}{\partial\theta^2} + \alpha_{23}\frac{\partial\bar{u}}{\partial\xi}\frac{\partial^2\bar{w}}{\partial\xi^2} + \alpha_{24}\frac{\partial\bar{v}}{\partial\theta}\frac{\partial^2\bar{w}}{\partial\xi^2} \\
& +\alpha_{25}\frac{\partial\bar{v}}{\partial\xi}\frac{\partial^2\bar{w}}{\partial\xi\partial\theta} + \alpha_{26}\frac{\partial\bar{v}}{\partial\theta}\frac{\partial^2\bar{w}}{\partial\theta^2} + \alpha_{27}\frac{\partial^2\bar{w}}{\partial\xi^2}\left(\frac{\partial\bar{w}}{\partial\theta}\right)^2 + \alpha_{28}\bar{w}\frac{\partial^2\bar{w}}{\partial\xi^2} + \alpha_{29}\frac{\partial^2\bar{w}}{\partial\theta^2}\left(\frac{\partial\bar{w}}{\partial\xi}\right)^2 \\
& +\alpha_{30}\frac{\partial^2\bar{w}}{\partial\xi^2}\left(\frac{\partial\bar{w}}{\partial\xi}\right)^2 + \alpha_{31}\frac{\partial^2\bar{w}}{\partial\theta^2}\left(\frac{\partial\bar{w}}{\partial\theta}\right)^2 + \alpha_{32}\frac{\partial^2\bar{w}}{\partial\xi\partial\theta}\frac{\partial\bar{w}}{\partial\xi}\frac{\partial\bar{w}}{\partial\theta} + \alpha_{33}\bar{w}\frac{\partial^2\bar{w}}{\partial\theta^2} + \alpha_{34}\left(\frac{\partial^2\bar{w}}{\partial\xi^2}\right)^2 \\
& +\alpha_{35}\left(\frac{\partial^2\bar{w}}{\partial\theta^2}\right)^2 + \alpha_{36}\left(\frac{\partial^2\bar{w}}{\partial\xi\partial\theta}\right)^2 + \alpha_{37}\frac{\partial^2\bar{w}}{\partial\xi^2}\frac{\partial^2\bar{w}}{\partial\theta^2} + \alpha_{38}\bar{w} + \alpha_{39}\frac{\partial\bar{u}}{\partial\xi} + \alpha_{40}\frac{\partial\bar{v}}{\partial\theta} + \alpha_{41}\left(\frac{\partial\bar{w}}{\partial\xi}\right)^2 \\
& +\alpha_{42}\left(\frac{\partial\bar{w}}{\partial\theta}\right)^2 + \alpha_{43}\frac{\partial^2\bar{w}}{\partial\xi^2} + \alpha_{44}\frac{\partial^2\bar{w}}{\partial\theta^2} + \alpha_{45}\frac{\partial^2\bar{w}}{\partial\xi^2}\frac{\partial^2\bar{w}}{\partial\tau^2} + \alpha_{46}\frac{\partial^2\bar{w}}{\partial\theta^2}\frac{\partial^2\bar{w}}{\partial\tau^2} + \alpha_{47}\frac{\partial\bar{u}}{\partial\xi}\frac{\partial^2\bar{w}}{\partial\tau^2} \\
& +\alpha_{48}\frac{\partial\bar{v}}{\partial\theta}\frac{\partial^2\bar{w}}{\partial\tau^2} + \alpha_{49}\bar{w}\frac{\partial^2\bar{w}}{\partial\tau^2} \\
& +\alpha_{50}\left(\frac{\partial\bar{w}}{\partial\xi}\right)^2\frac{\partial^2\bar{w}}{\partial\tau^2} + \alpha_{51}\left(\frac{\partial\bar{w}}{\partial\theta}\right)^2\frac{\partial^2\bar{w}}{\partial\tau^2} + \eta_{33}\bar{E}_{zp}^2 h_p\Bigg\} R\,d\theta\,dx,
\end{aligned}
\tag{32}
$$

5. Nonlinear free vibration analysis

The assumed mode method is used for changing the partial differential equations into ordinary differential equations. By applying the assumed mode method, the in-plane, transverse and shear deformations can be expressed as general coordinates and mode shape functions that satisfy the geometric boundary conditions, as follows [27]:

$$
\begin{aligned}
\begin{bmatrix} u(x,\theta,t) \\ v(x,\theta,t) \\ w(x,\theta,t) \end{bmatrix}
&= \sum_{m=1}^{M_1}\sum_{j=1}^{N}\begin{bmatrix} [u_{m,j,c}(\tau)\cos(j\theta) + u_{m,j,s}(\tau)\sin(j\theta)]\chi_{mj}(\xi) \\ [v_{m,j,c}(\tau)\sin(j\theta) + v_{m,j,s}(\tau)\cos(j\theta)]\phi_{mj}(\xi) \\ [w_{m,j,c}(\tau)\cos(j\theta) + w_{m,j,s}(\tau)\sin(j\theta)]\beta_{mj}(\xi) \end{bmatrix} \\
&+ \sum_{m=1}^{M_2}\begin{bmatrix} u_{m,0}(\tau)\chi_{m0}(\xi) \\ v_{m,0}(\tau)\phi_{m0}(\xi) \\ w_{m,0}(\tau)\beta_{m0}(\xi) \end{bmatrix} = \sum_{(i,r,s)=1}^{M_2+M_1\times N}\begin{bmatrix} u_i(\tau)\chi_i(\xi)\vartheta_i(\theta) \\ v_r(\tau)\phi_r(\xi)\alpha_r(\theta) \\ w_s(\tau)\beta_s(\xi)\psi_s(\theta) \end{bmatrix},
\end{aligned}
\tag{35a}
$$

where $\chi_i(\xi)$, $\phi_r(\xi)$ and $\beta_s(\xi)$ are modal functions which satisfy the required geometric boundary conditions. $u_i(\tau)$, $v_r(\tau)$ and $w_s(\tau)$ are unknown functions of time and are related to dynamical response.

Substituting Eqs. (38) into Eqs. (34) and (35) and applying the Lagrange equations:

$$
\frac{\partial}{\partial\tau}\left(\frac{\partial T}{\partial\dot{\bar{q}}_i}\right) - \left(\frac{\partial T}{\partial\bar{q}_i}\right) + \left(\frac{\partial\pi}{\partial\bar{q}_i}\right) + \left(\frac{\partial W_c}{\partial\dot{\bar{q}}_i}\right) = \sum\left(\frac{\partial W}{\partial\bar{q}_i}\right), \quad (i = \bar{u}, \bar{v}, \bar{w}) \tag{36}
$$

Where $W = W_p + W_{wp} + W_e$.

Results in the following reduced-order model of the system:

$$
\begin{aligned}
&[(M)_u^u]\{\ddot{\bar{u}}\} + [(M)_u^w]\{\ddot{\bar{w}}\} + [(K)_u^u]\{\bar{u}\} + [(K)_u^v]\{\bar{v}\} \\
&\quad + [(K)_u^w]\{\bar{w}\} + [(NL)_u^w]\{\bar{w}^2\} \\
&\quad = [\bar{F}_{up}],
\end{aligned}
\tag{37}
$$

$$
\begin{aligned}
&[(M)_v^v]\{\ddot{\bar{v}}\} + [(M)_v^w]\{\ddot{\bar{w}}\} + [(K)_v^u]\{\bar{u}\} + [(K)_v^v]\{\bar{v}\} \\
&\quad + [(K)_v^w]\{\bar{w}\} + [(NL)_v^w]\{\bar{w}^2\} \\
&\quad = [\bar{F}_{vp}],
\end{aligned}
\tag{38}
$$

$$
\begin{aligned}
&\left[(M)_w^w + (K)_{w2}^{\ddot{w}}\{\bar{w}\}\right]\{\ddot{\bar{w}}\} + [(c)_w^w]\{\dot{\bar{w}}\} + [(K)_w^u]\{\bar{u}\} \\
&\quad + [(K)_w^v]\{\bar{v}\} + [(K)_w^w]\{\bar{w}\} \\
&\quad + [(NL)_w^u]\{\bar{w}\bar{u}\} \\
&+[(NL)_w^v]\{\bar{w}\bar{v}\} + [(NL)_{w2}^w]\{\bar{w}^2\} + [(NL)_{w3}^w]\{\bar{w}^3\} \\
&\quad = [\bar{F}_{wp}] + [\bar{F}\cos\bar{\omega}\tau],
\end{aligned}
\tag{39}
$$

where $(M), (K)$ and (NL) are mass, stiffness and the nonlinear stiffness matrixes. Also, $\bar{F}_{up}$, $\bar{F}_{vp}$ and $\bar{F}_{wp}$ are applied loads by piezoelectric voltage and surface stress. All coefficients of mass, stiffness, nonlinear term matrixes and applied loads Eqs. (37)- (39) are presented in Appendix D.

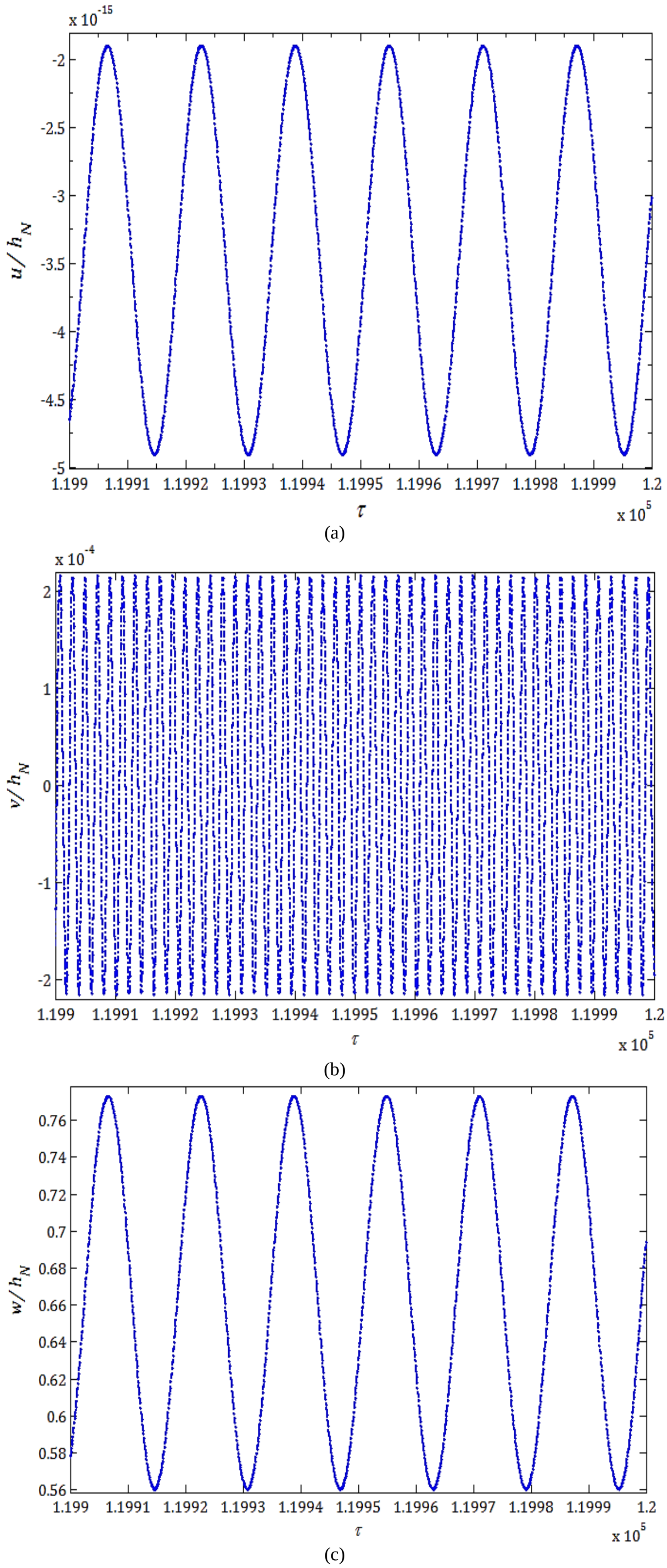

Figure 2. The nonlinear dynamic response of the nano resonator under the harmonic force in SS boundary condition and in three directions: (a) axial (u), (b) tangential (v) and (c) radial (w)

Figure 2(a-c) represents the nonlinear dynamic (the steady state) response of the FG-PCNS for fixed values of the system parameters by ode45 solver. It can be seen from Fig. 2 that the effect of the axial and circumferential inertia terms is so small in comparison with the transverse inertia term that one can ignore it in Eqs. (37) and (38) under an admissive precision. Afterwards, it is feasible from Eqs, (37) and (38) to solve the unknown functions $u_{ij}(\tau)$ and $v_{kl}(\tau)$ in terms of $w_{op}(\tau)$ and by substituting the results into Eq. (39), one can obtain the nonlinear differential equation of transverse motion as

$$\left[(M)_w^w+\begin{bmatrix}(\hat{M})_u^{wu}\\(\hat{M})_v^{wv}\end{bmatrix}\right]\{\ddot{\bar{w}}\} + \left[(K)_{w2}^{\ddot{w}}-[(NL)_w^u](\hat{M})_u^w - [(NL)_w^v](\hat{M})_v^w\right]\{\bar{w}\}\{\ddot{\bar{w}}\}+$$
$$[C_w]\{\dot{\bar{w}}\}+\left[(K)_w^w+\begin{bmatrix}(\hat{K})_u^{wu}\\(\hat{K})_v^{wv}\end{bmatrix}\right]\{\bar{w}\} + \left[[(NL)_w^u]\hat{F}_{up}+[(NL)_w^v]\hat{F}_{vp}\right]\{\bar{w}\} + \tag{40}$$
$$\left\{\begin{bmatrix}(\widehat{NL})_u^{wu}\\(\widehat{NL})_v^{wv}\end{bmatrix}-[(NL)_w^u](\hat{K})_u^w-[(NL)_w^v](\hat{K})_v^w + [(NL)_{w2}^w]\right\}\{\bar{w}^2\}+$$
$$\left\{-[(NL)_w^u](\widehat{NL})_u^w-[(NL)_w^v](\widehat{NL})_v^w+[(NL)_{w3}^w]\right\}\{\bar{w}^3\}+$$
$$\begin{bmatrix}\hat{F}_{wup}\\\hat{F}_{wvp}\end{bmatrix}=\bar{F}_{wp}++\bar{F}cos\bar{\omega}\tau$$

where the all coefficients of Equation (34), i.e.: $(\hat{M})_u^w,(\hat{M})_v^w,(\hat{M})_u^{wu},(\hat{M})_v^{wv},(\hat{K})_u^w,(\hat{K})_v^w,(\hat{K})_u^{wu}$, $(\hat{K})_v^{wv},(\widehat{NL})_u^w,(\widehat{NL})_v^w,(\widehat{NL})_u^{wu},(\widehat{NL})_v^{wv},\hat{F}_{up},\hat{F}_{vp},\hat{F}_{wup},\hat{F}_{wvp}$ are presented in the Appendix 4.

From Eq. (40) the fundamental natural frequencies of vibration of the FG-PCNS can be determined by the relation

$$\bar{\Omega}_n=\sqrt{\left[(K)_w^w+\begin{bmatrix}(\hat{K})_u^{wu}\\(\hat{K})_v^{wv}\end{bmatrix}\right]\Big/\left[(M)_w^w+\begin{bmatrix}(\hat{M})_u^{wu}\\(\hat{M})_v^{wv}\end{bmatrix}\right]}, \tag{41}$$

To study the steady state response of the system, the complex averaging method is applied [29]. For each mode of the nano shell, new complex variables are introduced in the following equation:

$$\zeta_{ln}e^{i\bar{\omega}\tau}=\dot{\bar{w}}_{ln}+i\bar{\omega}\left(\bar{w}_{ln}-\bar{w}_{ln_{st}}\right) \tag{42}$$

By introducing these new variables, dynamics of system is decomposed into fast and slowly varying terms, where ζ_{ln} are the slow term and $\bar{\omega}$ is the fast one. Displacement variable and its derivative can be expressed in terms of these new complex variables. For example:

$$\bar{w}_{ln}=\bar{w}_{ln_{st}}+\bar{w}_{ln_d}=\bar{w}_{ln_{st}}+\frac{\zeta_{ln}e^{i\bar{\omega}\tau}-\zeta_{ln}^*e^{-i\bar{\omega}\tau}}{2i\bar{\omega}},\dot{\bar{w}}_{ln}=\frac{\zeta_{ln}e^{i\bar{\omega}\tau}+\zeta_{ln}^*e^{-i\bar{\omega}\tau}}{2}, \tag{43}$$

$$\ddot{\bar{w}}_{ln}=\dot{\zeta}_{ln}e^{i\bar{\omega}\tau}+i\bar{\omega}\frac{\zeta_{ln}\,e^{i\bar{\omega}\tau}-\zeta_{ln}^*e^{-i\bar{\omega}\tau}}{2},$$

where in the above expression, $\bar{w}_{ln_{st}}$ and $\bar{w}_{ln_d}$ are the static and dynamic part of displacements and the parameters ζ_{ln}^* is the complex conjugate. The complex variable is considered as $\zeta_l=a_l+ib_l$ and $\bar{w}_{l_{st}}$ is considered as q_0 and replaced into Eqs. (43). By substituting $\bar{w}_{ln}$ and its derivative into Eq. (40), a set of complex equations governing the slowly complex amplitude ζ_{ln} is obtained. For solving nonlinear equation of a nonlinear system, the arc-length continuation method is used [14, 15, 29].

Complex averaging method combined with arc-length continuation is used to achieve an approximate solution for the nonlinear frequency response and stability analysis of the system.

6. Results and Discussions

In this section, first, the surface energy effect on the free and linear vibration analysis of a piezoelectric cylindrical nano-shell is investigated. To simplify the presentation, CC, SS, CS and CF represent clamped edge, simply supported edge, clamped-simply supported edge and clamped-free edge, respectively. And, the nonlinear dynamic (the steady state) response of the forced and nonlinear equations of FG-PCNS is solved by *ode45 solver* of MATLAB (numerical simulation).

The nonhomogeneous nano-shell considered in the following examples is composed of stainless steel and nickel and the nonhomogeneous distribution of properties in the thickness direction is varied according to the volume fraction power-law function. The material properties for stainless steel and nickel are shown in Table 1 [30].

Table 1. Properties of stainless steel and nickel

Stainless steel			Nichel		
$E_B(Nm^{-2})$	υ_B	$\rho_B(kg\,m^{-3})$	$E_T(Nm^{-2})$	υ_T	$\rho_T(kg\,m^{-3})$
$\mathbf{2.08\times10^{11}}$	0.381	8166	2.05×10^{11}	0.31	8900

The piezoelectric layer is assumed to be made of PZT-4 material, and the properties of PZT-4 are given in Table 2 [30].

Table 2. Properties of PZT-4

$E_p(Gpa)$	υ_p	$e_{31p}(C/m^2)$	$e_{32p}(C/m^2)$	$\eta_{33p}(10^{-11}\,F/m)$	$\rho_p(kg\,m^{-3})$
95	0.3	−5.2	−5.2	560	7500

The material and geometrical parameters used in all following results are shown in Table 3;

Table 3. The material and geometrical parameters

$R(m)$	L/R	h_N/R	h_p/R	$\lambda^{s_1}(N/m)$	$\mu^{s_1}(N/m)$
$\mathbf{1\times10^{-9}}$	10	0.01	0.01	0.1	0.05
$\tau_0^{s_1}\ (N/m)$	$\rho^{s_1}(kg/m^2)$	$V_p(V)$	$\lambda^{s_2}(N/m)$	$\mu^{s_2}(N/m)$	$\tau_0^{s_2}(N/m)$
$\mathbf{5.5\times10^{-3}}$	3.17×10^{-7}	1×10^{-5}	0.1	0.05	5.5×10^{-3}
$e_{31p}^{s_2}(C/m)$	$e_{32p}^{s_2}(C/m)$	$\rho^{s_2}(kg/m^2)$	$F(N)$	$K_w(pa)$	$K_p(N)$
$\mathbf{-3\times10^{-8}}$	-3×10^{-8}	5.61×10^{-6}	1×10^{-6}	1×10^{15}	1×10^{-2}
$C_w(pa)$					
$\mathbf{6\times10^{-10}}$					

Of course, the geometrical parameters can be varying according to the type of problem. In this paper, the results are presented in dimensionless form and thus the results are not limited to a certain matter. The data presented in the form of sample data to approximate the numbers used in the actual range.

6.1. Comparison and convergence studies

In this subsection, the method proposed in this paper is validated with comparing the available results in literature for nonclassical theories. For this purpose, we compare the results that Rouhi et al. [19] and Ansari et al. [31] presented based on the surface elasticity theory for natural frequencies of nanoscale pipes and cylindrical nanoshell, respectively with material and geometrical parameters; $E = 210\,GP$, $v = 0.24$, $\rho = 2331\,kg\,m^{-3}$, $\lambda^s = -4.488\,N\,m^{-1}$, $\mu^s = -2.774\,N\,m^{-1}$, $\tau_0^s = 0.605\,N\,m^{-1}$, $\rho_s = 3.17 \times 10^{-7}\,kg\,m^{-2}$, $h_N = 1\,nm$, $R\,/h_N = 2.5$, *and* $(m, n) = (3{,}3)$. In this case, we neglect the piezoelectric layer and visco-Pasternak. This comparison is presented in Table 4. It can be observed from Table 4 that the presented results agree very well with the reference solutions, which indicates that the method presented in this accurate with high degree of accuracy and the insignificant differences in the results may be caused by the different shell theories and solution methodology.

Table 4. Comparison of dimensionless natural frequencies calculated for SS shell model and by the models of Rouhi et al. [19] and Ansari et al. [31]

L/R	Present	Surface stress shell model [19]	Surface stress beam model [31]
45	0.2288	0.2363	0.2341
90	0.2138	0.2208	0.2204
135	0.2109	0.2137	0.2126
200	0.2097	0.2083	0.2076

In table 5, the convergence criterion of the present method is examined for the four boundary conditions SS, SC, CC and CF for dimensionless natural frequencies. It is observed from this Table that as the number, N, the Ritz polynomial functions are increased, the convergence is achieved rapidly. It is also seen that convergence of the method is influenced by the type of boundary conditions used.

6.2. Parametric study

The accuracy of the present study was verified in the previous section. Here, some numerical results are presented to explore the effects of involved parameters on the vibration behavior of cylindrical piezoelectric nano-shell. Also, all following results are investigated in the value of mode number $n = 3$ and $m = 1$. According to Eq. 35, the number of natural frequency for mode number $(n, m) = (3{,}1)$ is $(2n + 1) \times m = 7$; i.e. seven (7) natural frequency has in this mode number which consider first, two,…, seven natural frequency ω_i $(i = 1..7)$.

Figures 3 and 4 illustrates the effect of different boundary conditions (SS, CC, CS and CF) on dimensionless natural frequencies ($\omega_n = \bar{\Omega}_n R/L$) and the nonlinear dynamic response of the piezoelectric nano-shell versus length-to-small radius ratio (L/R) based on data of Table 3, respectively. From Figure 3, for all boundary conditions, the fundamental frequency decreases with the increase of the L/R ratio. In addition, the length-to-small radius ratio of cylindrical shell has an important effect on natural frequency. Note that in this figure (Fig. 3), due to the use of all boundary conditions, the results are presented for the first ω_1 and the sixth ω_6 natural frequencies.

Table 5. Convergence of dimensionless natural frequencies $\omega_n = \bar{\Omega}_n R/L$ for SS, SC, CC and CF piezoelectric cylindrical shells

	SS			SC		
n	$N = 1$	$N = 3$	$N = 5$	$N = 1$	$N = 3$	$N = 5$
0	0.16459	0.16459	0.16459	0.16459	0.16459	0.16459
1	0.12762	0.12762	0.12762	0.41303	0.06910	0.05963
2	0.13966	0.13966	0.13966	0.55925	0.13155	0.13067
3	0.25244	0.25244	0.25244	0.67239	0.24995	0.24973
	CC			**CF**		
n	$N = 1$	$N = 3$	$N = 5$	$N = 1$	$N = 3$	$N = 5$
0	0.16459	0.16459	0.16459	0.16459	0.16459	0.16459
1	0.41303	0.06910	0.05963	0.41303	0.06910	0.05963
2	0.55925	0.13155	0.13067	0.55925	0.13155	0.13067
3	0.67239	0.24995	0.24973	0.67239	0.24995	0.24973

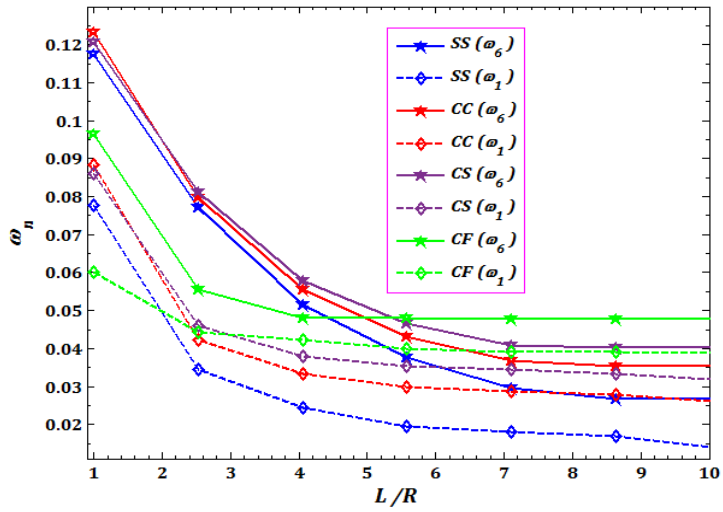

Figure 3. The effect of length-to-small radius ratio L/R on dimensionless natural frequencies of FG-PCNS for different boundary condition with surface energy effects

The reason is that a higher L/R ratio lead to a decrease in the nanoshell stiffness, and cause to lower natural frequencies of nanoshell and the vibrational behavior of the shell with the larger L/R ratio is less sensitive to variations of boundary conditions and by increasing this ratio, the frequency also decreases. The nonlinear dynamic responses of the piezoelectric nano-shell for different boundary conditions (SS, CC, CS and CF) are presented in Figure 4 with $L/R = 10$ and considering of primary resonance $\bar{\omega} = \omega_1$.

In this following, for investigation of the natural frequencies and the nonlinear dynamic response only S-S boundary condition with surface energy effects is considered.

Fig. 5 shows the effects of the ratio thickness L/R on the nonlinear dynamic response of the FG-PCNS in primary resonance $\bar{\omega} = \omega_1$ for SS boundary condition with four cases $L/R = (3,5,10,20)$. As it can be seen, with increasing the length to radius ratio L/R, the oscillation amplitude is less but the number of oscillations increases.

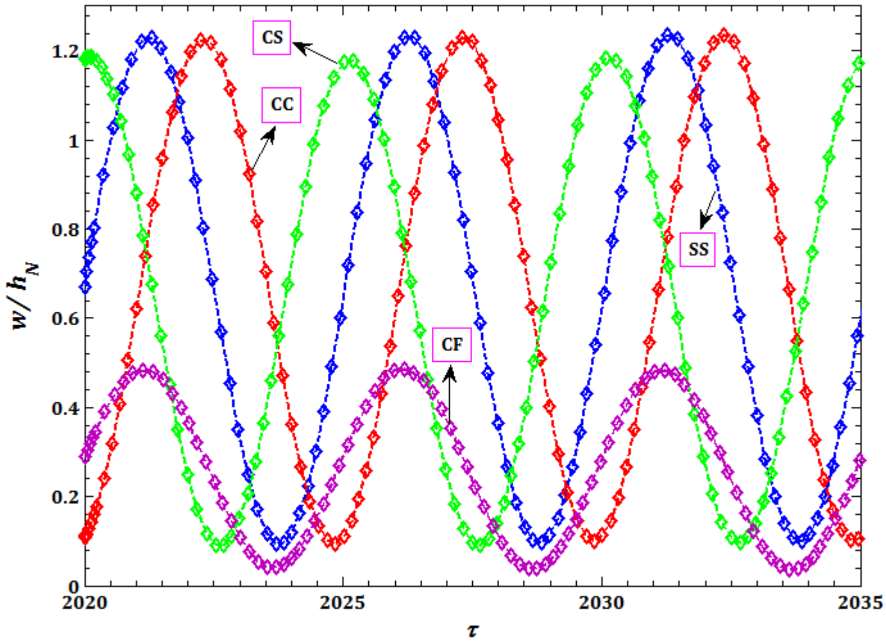

Figure 4. The nonlinear dynamic response of FG-PCNS for different boundary condition with surface energy effects with $L/R = 10$ and in $\bar{\omega} = \omega_1$

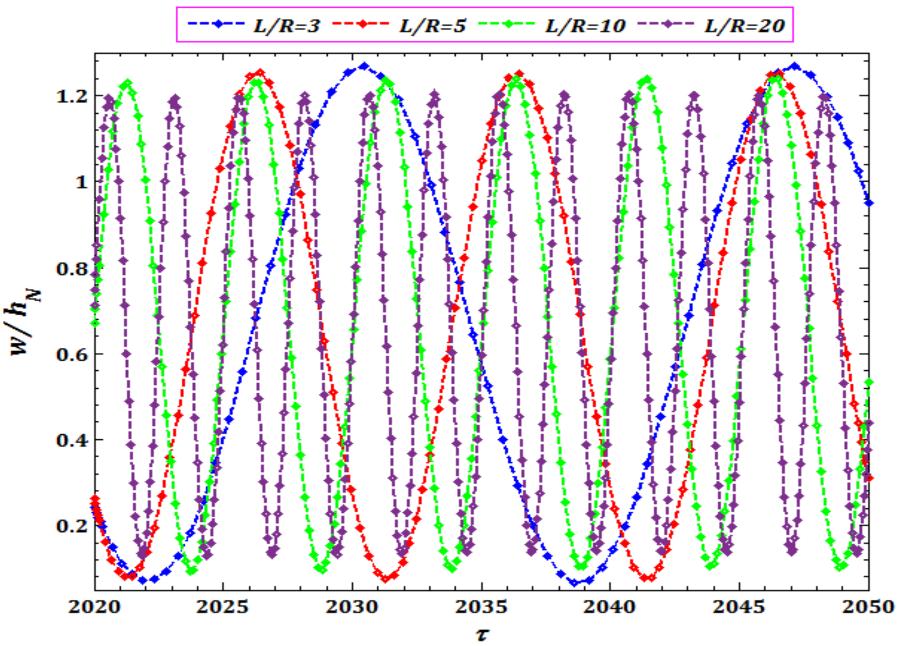

Figure 5. The effects of the ratio thickness L/R on the nonlinear dynamic response of the SS FG-PCNS with surface energy effects

Figure 6 shows the effect of stiffness coefficient of Winkler foundation K_w on the nonlinear dynamic response of the FG-PCNS in primary resonance $\bar{\omega} = \omega_1$ for SS boundary condition with three cases $K_w = (1 \times 10^{10}, 1 \times 10^{15}, 1 \times 10^{16})$. It is quite clear that the increase of the stiffness coefficient of Winkler foundation K_w does not significant effect on the nonlinear dynamic response of the FG-PCNS.

Figure 7 shows the effect of stiffness coefficient of Winkler foundation K_p on the nonlinear dynamic response of the FG-PCNS in primary resonance $\bar{\omega} = \omega_1$ for SS boundary condition with five cases $K_p = (-10, -5, -3, -2, 0.01)$. From the figure 7, we can see that for values of $K_p = (-10, -5, -3)$ the amplitude of nonlinear dynamic response of the FG-PCNS shells are almost constant and by reducing the K_p ratio, the amplitude of nonlinear dynamic response decreases. Or in other words, the K_p has a positive effect on the reduction of the amplitude fluctuation of the FG-PCNS.

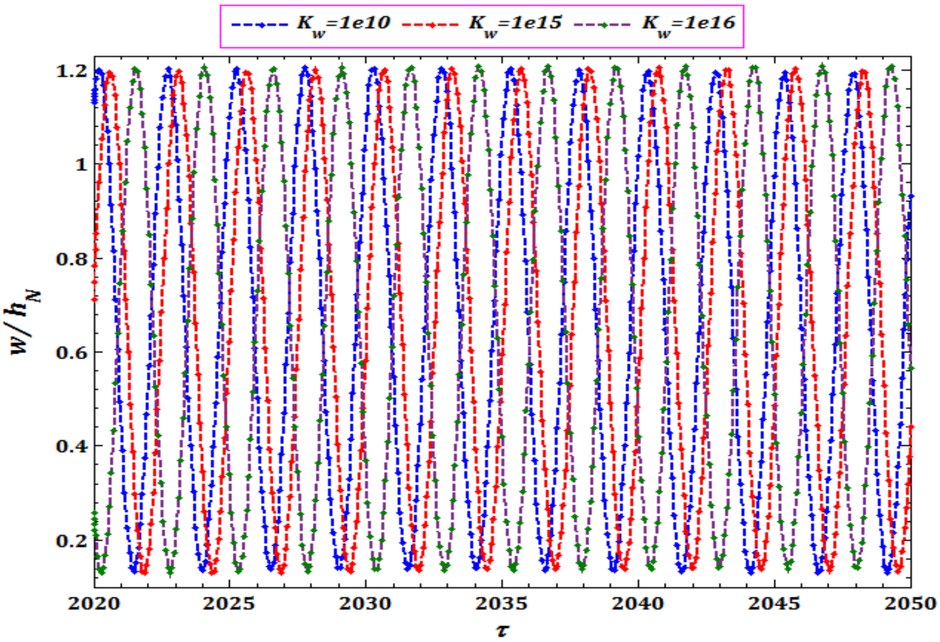

Figure 6. The effect of stiffness coefficient of Winkler foundation K_w on the nonlinear dynamic response of the SS FG-PCNS with surface energy effects

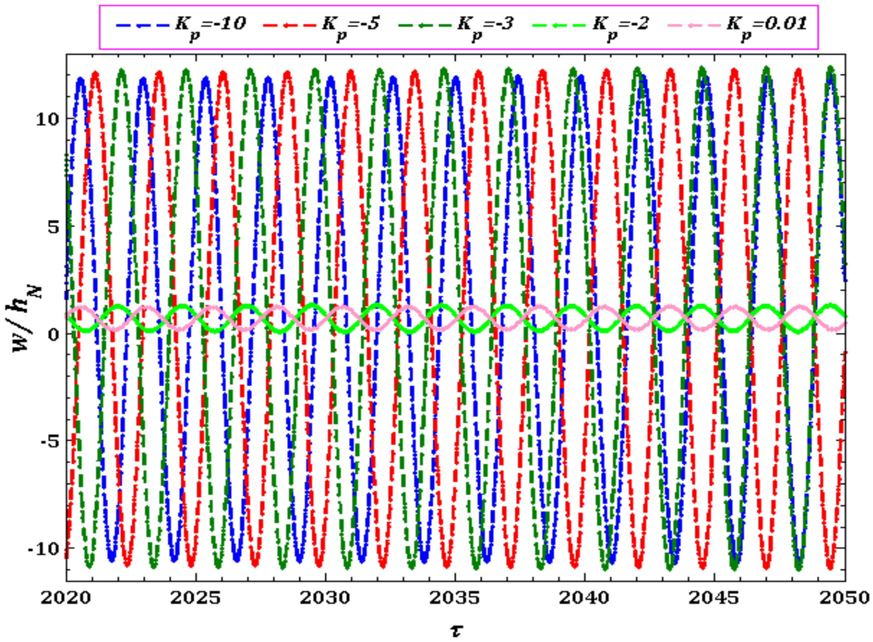

Figure 7. The effect of shear layer of Pasternak foundation K_p on the nonlinear dynamic response of the SS FG-PCNS with surface energy effects

Figure 8 illustrates the effect of thickness shell to small radius ratio h_N/R on dimensionless natural frequencies ($\omega_n = \bar{\Omega}_n R/L$) of the FG-PCNS for SS boundary condition. By increasing the thickness shell to small radius ratio h_N/R, the natural frequency increases which in the higher ratio h_N/R, increase in the frequencies is more evident. For example, in the ratio of $h_N/R = 0.5$, the frequency ω_7 is more than 8 times the first frequency ω_1.

Figure 9 shows the effects of the ratio thickness h_N/R on the nonlinear dynamic response of the FG-PCNS in primary resonance $\varpi = \omega_1$ for SS boundary condition with five cases $h_N/R = (0.009, 0.01, 0.015, 0.02, 0.05)$. From the figure, we can see that the amplitude of nonlinear dynamic response of the FG-PCNS shells decreases when the ratio of h_N/R increase. Or in other words, the h_N/R has a positive effect on the reduction of the amplitude fluctuation of the FG-PCNS.

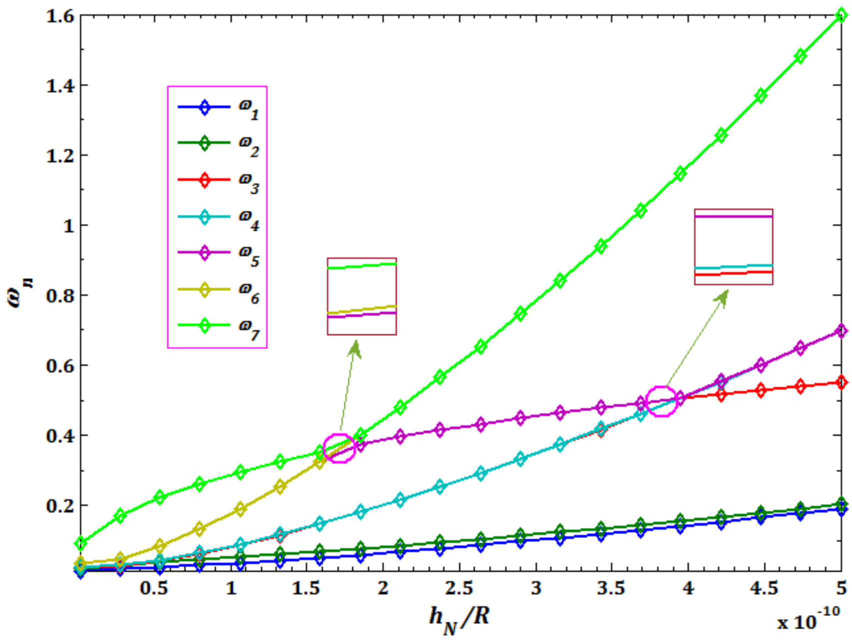

Figure 8. The effect of thickness shell to small radius ratio h_N/R on dimensionless natural frequencies for SS FG-PCNS

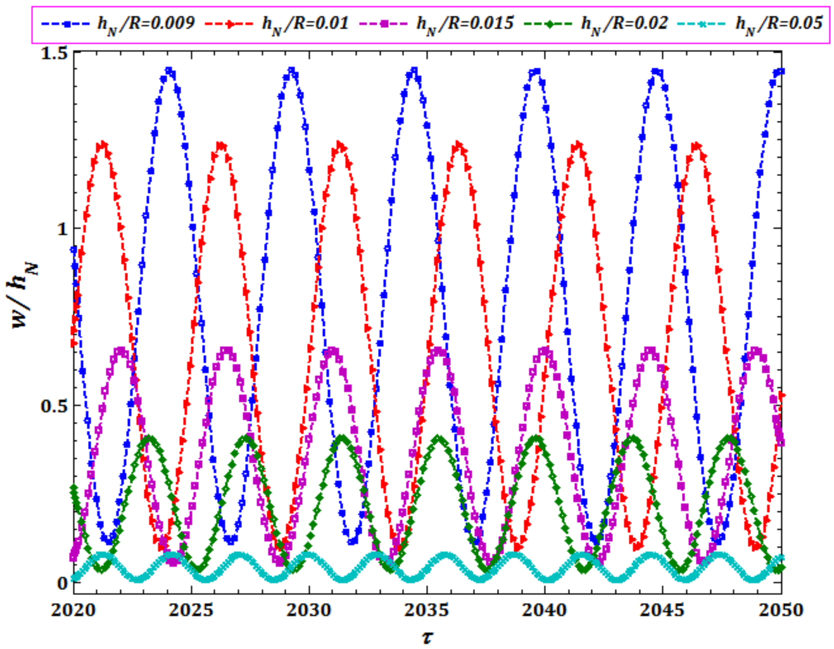

Figure 9. The effect of thickness shell to small radius ratio h_N/R on the nonlinear dynamic response of SS FG-PCNS

The dimensionless natural frequencies ($\omega_n = \bar{\Omega}_n R/L$) of the FG-PCNS versus thickness piezo to small radius ratio (h_p/R) with surface effects for S-S boundary condition is presented in Figure 10. It can be shown that by increasing the ratio h_p/R, the natural frequency increases which in the higher ratio h_p/R, increase in the frequencies is more evident. For example, in the ratio of $h_p/R = 0.5$, the frequency ω_7 is more than 12 times the first frequency ω_1.

Figure 11 shows the effects of the ratio thickness h_p/R on the nonlinear dynamic response of the FG-PCNS in primary resonance $\varpi = \omega_1$ for SS boundary condition with five cases $h_p/R = (0.009, 0.01, 0.015, 0.02, 0.05)$. From the figure, we can see that the amplitude of nonlinear dynamic response of the FG-PCNS shells decreases when the ratio of h_p/R increases. Or in other words, the h_p/R has a positive effect on the reduction of the amplitude fluctuation of the FG-PCNS.

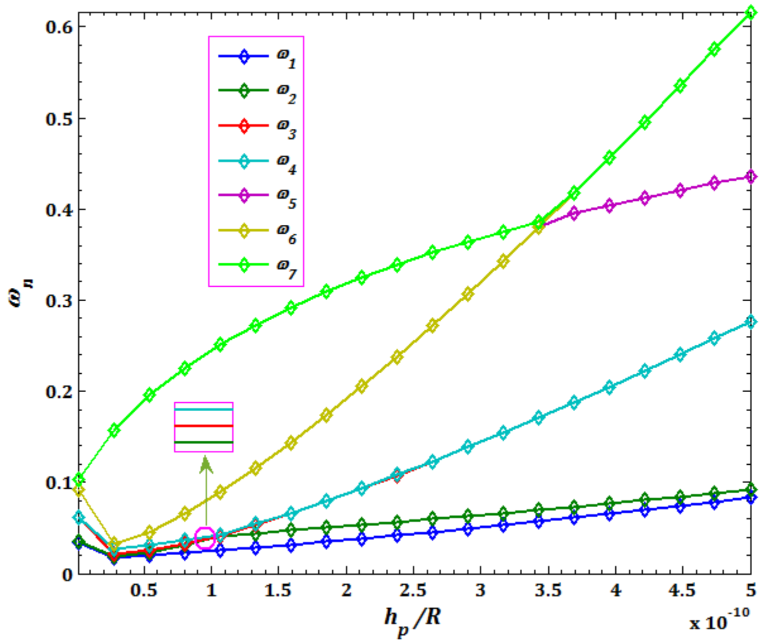

Figure 10. The effect of piezoelectric thickness to small radius ratio h_p/R on dimensionless natural frequencies of SS FG-PCNS

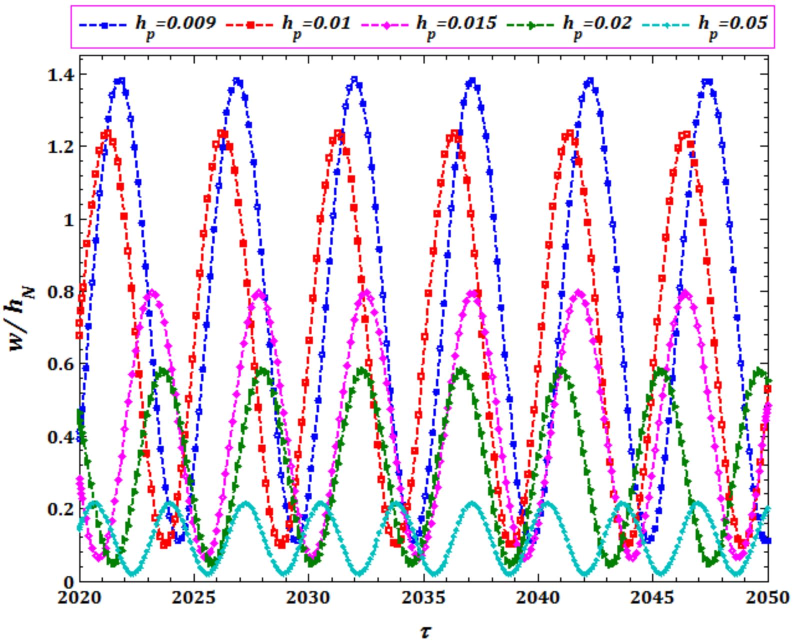

Figure 11. The effect of piezoelectric thickness to small radius ratio h_p/R on the nonlinear dynamic response of SS FG-PCNS

The influence of excitation force F on the nonlinear dynamic response of the FG-PCNS for SS boundary condition illustrate in Figure 12. From Fig. 12, when F is increased, the value of the FG-PCNS amplitude increases and vice versa.

In Figure 13, the effects of different direct electric voltage V_{DC} on the frequency response and stability analysis of SS FG-PCNS are shown. The results show that with increasing of V_{DC} voltage, the oscillation amplitude is increased. Moreover, due to increased amplitude of the DC voltage (and hence increased amplitude of the static deflection), the system displays softening-type nonlinear behaviour with two saddle-node bifurcations.

For stability analysis, if all the eigenvalues of the Jacobian matrix have negative real part, the fixed point is stable and if one or more eigenvalues have positive real part, the fixed point is unstable. Also, if the equation of motion has zero eigenvalue, the fixed point is called a saddle point, which is mathematically unstable [27]. If at bifurcation point, dominate eigenvalues are pure imaginary, Hopf bifurcation is occurred at that condition. Also, the vibration amplitude lean to the left of Ω¯_n, indicating a softening behavior of the system and lean to the right of Ω¯_n, system has hardening behavior [27].

The effect of excitation force F on the nonlinear frequency response and stability analysis of SS FG-PCNS is presented in Figure 14. The results show that with increasing of dimensionless excitation F, the amplitude and the range of the FG-PCNS system's instability increase with saddle-node bifurcations. Also, with increasing of the range of instability and nano shell stiffness, the nonlinear softening behaviour becomes stronger.

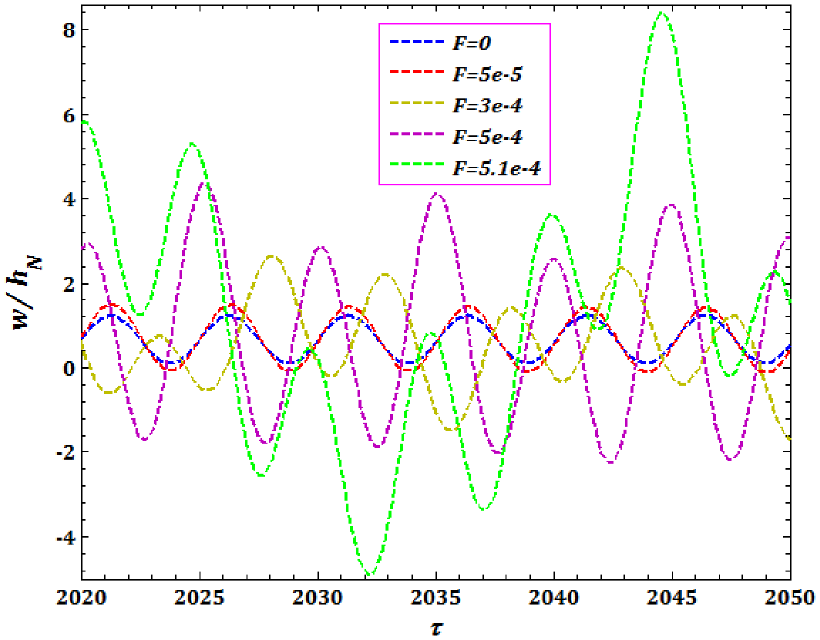

Figure 12. The effect of excitation force F on the nonlinear dynamic response of SS FG-PCNS

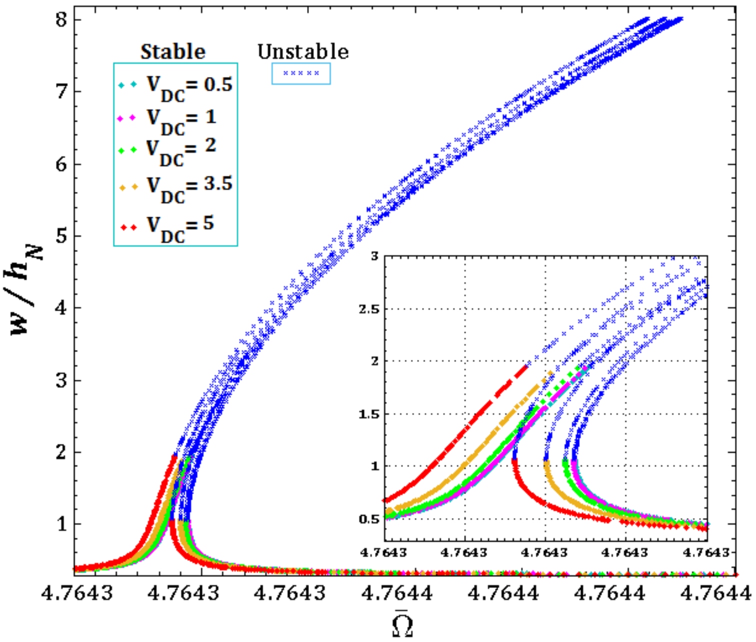

Figure 13. The effect of direct voltage V_{DC} on nonlinear frequency response and stability analysis of SS FG-PCNS

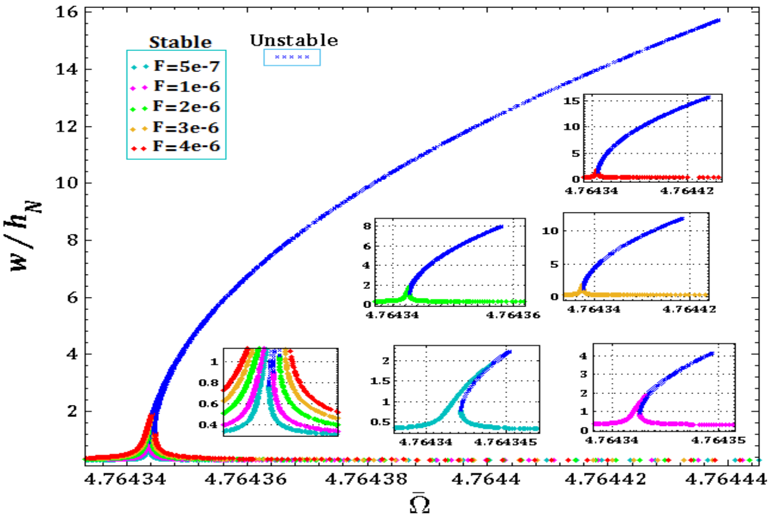

Figure 14. The effect of excitation force F on the nonlinear frequency response and stability analysis of SS FG-PCNS

7. Conclusion

In current work, nonlinear dynamic response and frequency analysis of FG-PCNS embedded in visco-Pasternak medium and harmonic force are investigated using surface energy effects. For this purpose, Hamilton's principle, assumed mode method and Complex averaging method combined with arc-length continuation are used to drive the governing equations and boundary conditions, changing the partial differential equations into ordinary differential equations and to achieve an approximate solution for the nonlinear frequency response and stability analysis of the FG-PCNS. The convergence, accuracy and reliability of the current formulation are validated by comparisons with existing experimental and numerical results published in the literature, with excellent agreements achieved. Also, the effects of geometrical parameters and material properties, visco-Pasternak medium and harmonic force with surface energy effects are studied on natural frequency, nonlinear dynamic response and stability analysis.

Some conclusions are obtained from this study:

- The fundamental frequency decreases with the increase of the L/R ratio. In addition, the length-to-small radius ratio of cylindrical shell has an important effect on natural frequency.
- With increasing the length to radius ratio L/R, the oscillation amplitude is less, but the number of oscillations increases.
- The increase of the stiffness coefficient of Winkler foundation K_w does not have a significant effect on the nonlinear dynamic response of the FG-PCNS.
- The amplitude of nonlinear dynamic response of the FG-PCNS shells is almost constant and by reducing the K_p ratio, the amplitude of nonlinear dynamic response decreases. Or in other words, the K_p has a positive effect on the reduction of the amplitude fluctuation of the FG-PCNS.
- By increasing the thickness shell to small radius ratio h_N/R, the natural frequency increases which in the higher ratio h_N/R, increase in the frequencies is more evident
- The amplitude of nonlinear dynamic response of the FG-PCNS shells decreases when the ratio of h_N/R increase. Or in other words, the h_N/R has a positive effect on the reduction of the amplitude fluctuation of the FG-PCNS.
- By increasing the ratio h_p/R, the natural frequency increases which in the higher ratio h_p/R, increase in the frequencies is more evident. For example, in the ratio of $h_p/R = 0.5$, the frequency ω_7 is more than 12 times the first frequency ω_1.
- The amplitude of nonlinear dynamic response of the FG-PCNS shells decreases when the ratio of h_p/R increase. Or in other words, the h_p/R has a positive effect on the reduction of the amplitude fluctuation of the FG-PCNS.
- When F is increased, the value of the FG-PCNS amplitude increases and vice versa.
- for approximately $K_w = 10^{10} - 10^{17}$ in all resonance frequencies, no changes occur in the amplitude of the FG-PECNS. This means that for this domain, Winkler foundation has no effect in reducing the vibration amplitude. As stiffness increases to the value $K_w > 10^{17}$, the resonance frequencies increase and the amplitude of the piezoelectric nano resonator decreases. According to Fig. 10, $K_w \cong 10^{18}$ is a proper value to decrease the resonance amplitude of FG-PECNS. Also, with increasing K_w, resonance frequencies will be delayed, and this leads to decreasing of nonlinear behavior.
- for approximately $K_p = 10^{-2} - 1$, no significant changes occur in the amplitude of the FG-PECNS. This means that for this domain, Pasternak foundation has no effect in reducing the vibration amplitude. As shear foundation increases to the value $K_p > 1$, the resonance frequencies increase and the resonance amplitude of the piezoelectric nano resonator decreases. Also with increasing K_p, resonance frequencies will be delayed and lead to decreasing of nonlinear behavior. According to Fig. 11, $K_p \cong 2$ is a proper value to decrease the amplitude of SS FG-PECNS.
- with increasing of V_{DC} voltage, the oscillation amplitude is increases and the system displays softening-type nonlinear behavior with two saddle-node bifurcations.
- with increasing of excitation $\bar{F}$, the amplitude and the range of system's instability increase.

Conflict of interest

The authors report no conflict of interest.

Funding Acknowledgement

'This research received no specific grant from any funding agency in the public, commercial, or not-for-profit sectors'.

References

[1] H. Tzou, Piezoelectric Shells: Sensing, Energy Harvesting, and Distributed Control-Second Edition, Springer, New York, 2019.

[2] A. Manbachi, R.S.C. Cobbold, Development and application of piezoelectric materials for ultrasound generation and detection, Ultrasound, 2011; 11(4) 187–96.

[3] Nader Jalili, Piezoelectric-Based Vibration Control: From Macro to Micro/Nano Scale Systems, springer, 2010.

[4] R.D. Mindlin, H.F. Tiersten, Effects of couple-stresses in linear elasticity, Archive for Rational Mechanics and Analysis, 1962; 11(1) 415–48.

[5] A.C. Eringen, Nonlocal polar elastic continua, International Journal of Engineering Science, 1972; 10(1):1–16.

[6] R.D. Mindlin, N.N. Eshel, on first strain-gradient theories in linear elasticity, International Journal of Solids and Structures, 1968; 4(1) 109–24.

[7] R.D. Mindlin, Second gradient of strain and surface-tension in linear elasticity, International Journal of Solids and Structures, 1965; 1(4) 417–38.

[8] M.E. Gurtin, A.I. Murdoch, A continuum theory of elastic material surface, Archive for Rational Mechanics and Analysis, 1975; 57(4):291–323.

[9] M.E. Gurtin, A.I. Murdoch, Surface stress in solids, International Journal of Solids and Structures, 1978; 14(6) 431–40.

[10] X.Q. Fang, C.S. Zhu, J.X. Liu et al., Surface energy effect on free vibration of nano-sized piezoelectric double-shell structures. Physica B: Condensed Matter. 529(2018) 41-56.

[11] X.Q. Fang, C.S. Zhu, J.X. Liu, J. Zhao, Surface energy effect on nonlinear buckling and postbuckling behavior of functionally graded piezoelectric cylindrical nanoshells under lateral pressure, Materials Research Express. 5.4 (2018) 045017.

[12] X.Q. Fang, C.S. Zhu, J.X. Liu, X.L. Liu, Surface energy effect on free vibration of nano-sized piezoelectric double-shell structures, Physica B: Physics of Condensed Matter (2017), DOI: 10.1016/j.physb.2017.10.038.

[13] S.H. Hashemi Kachapi, M. Dardel, H. Mohamadi daniali, A. Fathi, Effects of surface energy on vibration characteristics of double-walled piezo-viscoelastic cylindrical nanoshell, Proceedings of the Institution of Mechanical Engineers, Part C: Journal of Mechanical Engineering Science. 2019, DOI: 10.1177/0954406219845019.

[14] S.H. Hashemi Kachapi, M. Dardel, H. Mohamadi daniali, A. Fathi, Pull-in instability and nonlinear vibration analysis of electrostatically piezoelectric nanoresonator with surface/interface effects, Thin-Walled Structures 143 (2019) 106210.

[15] S.H. Hashemi Kachapi, M. Dardel, H. Mohamadi daniali, A. Fathi, Nonlinear dynamics and stability analysis of piezo-visco medium nanoshell resonator with electrostatic and harmonic actuation, Applied Mathematical Modelling, DOI:10.1016/j.apm.2019.05.035, 2019.

[16] Y. Liu, X. Ji, D. Wang, J. He, Modeling thin structures incorporated with surface effects by using layered shell elements, European Journal of Mechanics - A/Solids. 74 (2019) 139-144.

[17] I. Karimipour, Y. Tadi Beni, H. Zeighampour, Nonlinear size-dependent pull-in instability and stress analysis of thin plate actuator based on enhanced continuum theories including nonlinear effects and surface energy. Microsystem Technology, 24(2018) 1811–1839.

[18] S. M. Pourkiaee, S. E. Khadem, M. Shahgholi, Nonlinear vibration and stability analysis of an electrically actuated piezoelectric nanobeam considering surface effects and intermolecular interactions, Journal of Vibration and Control (2015), DOI: 10.1177/1077546315603270.

[19] H. Rouhi, R. Ansari, M. Darvizeh, Exact solution for the vibrations of cylindrical nanoshells considering surface energy effect, Journal of Ultrafine Grained and Nanostructured Materials. 48(2015) 113-124.

[20] C.S. Zhu, X.Q. Fang, J.X. Liu, Surface energy effect on buckling behavior of the functionally graded nano-shell covered with piezoelectric nano-layers under torque, International Journal of Mechanical Sciences 133 (2017) 662–673.

[21] A Ghorbanpour Arani, A. Fereidoon, R. Kolahchi, Nonlinear surface and nonlocal piezoelasticity theories for vibration of embedded single-layer boron nitride sheet using harmonic differential quadrature and differential cubature methods, Journal of Intelligent Materials Systems and Structures, 2015; 26: 1150–1163.

[22] A Ghorbanpour Arani, R Kolahchi, M Hashemian, Nonlocal surface piezoelasticity theory for dynamic stability of double-walled boron nitride nanotube conveying viscose fluid based on different theories, Proc IMechE Part C: J Mechanical Engineering Science (2014), DOI: 10.1177/0954406214527270.

[23] A. Fereidoon, E. Andalib, A. Mirafzal, Nonlinear Vibration of Viscoelastic Embedded-DWCNTs Integrated with Piezoelectric Layers-Conveying Viscous Fluid Considering Surface Effects, Physica E: Low-Dimensional Systems and Nanostructures, 2016; 81: 205–218.

[24] S. Sahmani, M.M. Aghdam, M. Bahrami, Nonlinear buckling and postbuckling behavior of cylindrical shear deformable nanoshells subjected to radial compression including surface free energy effects, Acta Mechanica Solida Sinica, 2017; 30(2) 209–22.

[25] C.S. Zhu, X.Q. Fang, J.X. Liu, H.Y. Li, Surface energy effect on nonlinear free vibration behavior of orthotropic piezoelectric cylindrical nano-shells. European Journal of Mechanics A/Solids, 66(2017) 423-432.

[26] L. H. Donnell, Beam, Plates and Shells, McGraw-Hill, New York (1976).

[27] M. Amabili, Nonlinear Vibrations and Stability of Shells and Plates, Cambridge University Press, New York (2008).

[28] L.L. Ke, Y.S. Wang, J.N. Reddy, Thermo-electro-mechanical vibration of size-dependent piezoelectric cylindrical nanoshells under various boundary conditions, Composite Structures (2014), doi: http://dx.doi.org/10.1016/j.compstruct.2014.05.048.

[29] A.I. Manevitch, L.I. Manevitch, The mechanics of Nonlinear Systems with Internal Resonance, Imperial College Press, London, 2005.

[30] A.A. Jafari, S.M.R. Khalili, M.Tavakolian, Nonlinear vibration of functionally graded cylindrical shells embedded with a piezoelectric layer, Thin- Walled Structures, 2014; 79:8–15.

[31] R. Ansari, R. Gholami, A. Norouzzadeh, M.A. Darabi, Surface Stress Effect on the Vibration and Instability of Nanoscale Pipes Conveying Fluid Based on a Size-Dependent Timoshenko Beam Model. Acta Mechanica Sinica. 31(2015) 708-719.

Appendix A

The stresses and moment resultants are defined as:

$$(N_{xx}, N_{\theta\theta}, N_{x\theta}) = \int_{-h_N}^{h_N} \sigma_{ijN}\, dz + \int_{h_N}^{h_N+h_p} \sigma_{ijp}\, dz + \sigma_{s_1} + \sigma_{s_2} = (N_{xN}, N_{\theta N}, N_{x\theta N})$$
$$+(N_{xp}, N_{\theta p}, N_{x\theta p}) + \left(\sigma_{xx}, \sigma_{\theta\theta}, \frac{1}{2}(\sigma_{x\theta} + \sigma_{\theta x})\right)_{s_1} + \left(\sigma_{xx}, \sigma_{\theta\theta}, \frac{1}{2}(\sigma_{x\theta} + \sigma_{\theta x})\right)_{s_2} \quad (A.1)$$

$$(M_{xx}, M_{\theta\theta}, M_{x\theta}) = \int_{-h_N}^{h_N} \sigma_{ijN}\, zdz + \int_{h_N}^{h_N+h_p} \sigma_{ijp}\, zdz + \sigma_{s_2}(h_N + h_p) - \sigma_{s_1} h_N$$
$$= (M_{xN}, M_{\theta N}, M_{x\theta N}) + (M_{xp}, M_{\theta p}, M_{x\theta p}) + \left(\sigma_{xx}, \sigma_{\theta\theta}, \frac{1}{2}(\sigma_{x\theta} + \sigma_{\theta x})\right)_{s_2} (h_N + h_p) \quad (A.2)$$
$$-\left(\sigma_{xx}, \sigma_{\theta\theta}, \frac{1}{2}(\sigma_{x\theta} + \sigma_{\theta x})\right)_{s_1} h_N$$

$$N_{xx} = A_{11}\varepsilon_{xx}^0 + A_{12}\varepsilon_{\theta\theta}^0 + B_{11}\kappa_{xx} + B_{12}\kappa_{\theta\theta} - \frac{1}{2}(\tau_0^{s_1} + \tau_0^{s_2})(\frac{\partial w}{\partial x})^2 + (\tau_0^{s_1} + \tau_0^{s_2} - N_{xp})$$
$$+F_{11}^*\left(\frac{\partial^2 w}{\partial x^2} + \frac{1}{R^2}\frac{\partial^2 w}{\partial \theta^2}\right) + J_{11}^*\frac{\partial^2 w}{\partial t^2}, \quad (A.3)$$

$$N_{\theta\theta} = A_{21}\varepsilon_{xx}^0 + A_{22}\varepsilon_{\theta\theta}^0 + B_{21}\kappa_{xx} + B_{22}\kappa_{\theta\theta} - \frac{1}{2}(\tau_0^{s_1} + \tau_0^{s_2})(\frac{2w}{R} + \frac{1}{R^2}(\frac{\partial w}{\partial \theta})^2)$$
$$+(\tau_0^{s_1} + \tau_0^{s_2} - N_{\theta p}) + F_{11}^*(\frac{\partial^2 w}{\partial x^2} + \frac{1}{R^2}\frac{\partial^2 w}{\partial \theta^2}) + J_{11}^*\frac{\partial^2 w}{\partial t^2}, \quad (A.4)$$

$$N_{x\theta} = A_{66}\gamma_{x\theta}^0 + B_{66}\kappa_{x\theta}, \quad (A.5)$$

$$M_{xx} = B_{11}\varepsilon_{xx}^0 + B_{12}\varepsilon_{\theta\theta}^0 + D_{11}\kappa_{xx} + D_{12}\kappa_{\theta\theta} + \tau_0^{s_2}(1 - \frac{1}{2}(\frac{\partial w}{\partial x})^2)(h_N + h_p)$$
$$-\tau_0^{s_1}(1 - \frac{1}{2}(\frac{\partial w}{\partial x})^2)h_N - M_{xp} + E_{11}^*(\frac{\partial^2 w}{\partial x^2} + \frac{1}{R^2}\frac{\partial^2 w}{\partial \theta^2}) + G_{11}^*\frac{\partial^2 w}{\partial t^2}, \quad (A.6)$$

$$M_{\theta\theta} = B_{21}\varepsilon_{xx}^0 + B_{22}\varepsilon_{\theta\theta}^0 + D_{21}\kappa_{xx} + D_{22}\kappa_{\theta\theta} + \tau_0^{s_2}(1 - \frac{1}{2}(\frac{2w}{R} + \frac{1}{R^2}(\frac{\partial w}{\partial \theta})^2))(h_N + h_p)$$
$$-\tau_0^{s_1}(1 - \frac{1}{2}(\frac{2w}{R} + \frac{1}{R^2}(\frac{\partial w}{\partial \theta})^2))h_N - M_{\theta p} + E_{11}^*(\frac{\partial^2 w}{\partial x^2} + \frac{1}{R^2}\frac{\partial^2 w}{\partial \theta^2}) + G_{11}^*\frac{\partial^2 w}{\partial t^2}, \quad (A.6)$$

$$M_{x\theta} = B_{66}\gamma_{x\theta}^0 + D_{66}\kappa_{x\theta}, \quad (A.7)$$

in which

$$A_{ij} = A_{ijN} + A_{ijp} + A_{ij}^*, B_{ij} = B_{ijN} + B_{ijp} + B_{ij}^*, D_{ij} = D_{ijN} + D_{ijp} + D_{ij}^*,$$
$$F_{11}^* = F_{11N}^* + F_{11p}^*, J_{11}^* = J_{11N}^* + J_{11p}^*, E_{11}^* = E_{11N}^* + E_{11p}^*, G_{11}^* = G_{11N}^* + G_{11p}^*, \quad (A.8)$$

Appendix B

$$(A_{ijN}, B_{ijN}, D_{ijN}) = \int_{-h_N}^{h_N} C_{ijN}(1, z, z^2)\, dz, (A_{ijp}, B_{ijp}, D_{ijp}) = \int_{h_N}^{h_N+h_p} C_{ijp}(1, z, z^2)\, dz, \quad (B.1)$$

$$(N_{xp}, N_{\theta p}) = \int_{h_N}^{h_N+h_p} (e_{31p}, e_{32p})\bar{E}_{zp}\, dz + (e_{31p}^s, e_{32p}^s)\bar{E}_{zp}, \quad (B.2)$$

$$(M_{xp}, M_{\theta p}) = \int_{h_N}^{h_N+h_p} (e_{31p}, e_{32p})\bar{E}_{zp}\, zdz + (e_{31p}^s, e_{32p}^s)\bar{E}_{zp}(h_N + h_p), \quad (B.3)$$

$$A_{11}^* = A_{22}^* = (\lambda^{s_1} + 2\mu^{s_1}) + (\lambda^{s_2} + 2\mu^{s_2}), A_{12}^* = A_{21}^* = (\tau_0^{s_1} + \lambda^{s_1}) + (\tau_0^{s_2} + \lambda^{s_2}),$$
$$A_{66}^* = (\mu^{s_1} - \frac{\tau_0^{s_1}}{2}) + (\mu^{s_2} - \frac{\tau_0^{s_2}}{2}), \quad (B.4)$$

$$B_{11}^* = B_{22}^* = (\lambda^{s_2} + 2\mu^{s_2})(h_N + h_p) - (\lambda^{s_1} + 2\mu^{s_1})(h_N),$$
$$B_{12}^* = B_{21}^* = (\tau_0^{s_2} + \lambda^{s_2})(h_N + h_p) - (\tau_0^{s_1} + \lambda^{s_1})(h_N), \quad (B.5)$$
$$B_{66}^* = (\mu^{s_2} - \frac{\tau_0^{s_2}}{2})(h_N + h_p) - (\mu^{s_1} - \frac{\tau_0^{s_1}}{2})(h_N),$$

$$D_{11}^* = D_{22}^* = (\lambda^{s_2} + 2\mu^{s_2})(h_N + h_p)^2 + (\lambda^{s_1} + 2\mu^{s_1})(h_N)^2,$$
$$D_{12}^* = D_{21}^* = (\tau_0^{s_2} + \lambda^{s_2})(h_N + h_p)^2 + (\tau_0^{s_1} + \lambda^{s_1})(h_N)^2, \quad (B.6)$$
$$D_{66}^* = (\mu^{s_2} - \frac{\tau_0^{s_2}}{2})(h_N + h_p)^2 + (\mu^{s_1} - \frac{\tau_0^{s_1}}{2})(h_N)^2,$$

$$F_{11N}^{*}=\int_{-h_N}^{h_N}\frac{\upsilon_N}{(1-\upsilon_N)}\left(\frac{\left(\tau_0^{s_2}-\tau_0^{s_1}\right)}{2}+\frac{\left(\tau_0^{s_2}+\tau_0^{s_1}\right)z}{2h_N+h_p}\right)dz,$$

$$F_{11p}^{*}=\int_{h_N}^{h_N+h_p}\frac{\upsilon_p}{\left(1-\upsilon_p\right)}\left(\frac{\left(\tau_0^{s_2}-\tau_0^{s_1}\right)}{2}+\frac{\left(\tau_0^{s_2}+\tau_0^{s_1}\right)z}{2h_N+h_p}\right)dz, \tag{B.7}$$

$$J_{11N}^{*}=\int_{-h_N}^{h_N}\frac{\upsilon_N}{(1-\upsilon_N)}\left(\frac{(\rho^{s_1}-\rho^{s_2})}{2}-\frac{(\rho^{s_1}+\rho^{s_2})z}{2h_N+h_p}\right)dz,$$

$$J_{11p}^{*}=\int_{h_N}^{h_N+h_p}\frac{\upsilon_p}{\left(1-\upsilon_p\right)}\left(\frac{(\rho^{s_1}-\rho^{s_2})}{2}-\frac{(\rho^{s_1}+\rho^{s_2})z}{2h_N+h_p}\right)dz, \tag{B.8}$$

$$E_{11N}^{*}=\int_{-h_N}^{h_N}\frac{\upsilon_N}{(1-\upsilon_N)}\left(\frac{\left(\tau_0^{s_2}-\tau_0^{s_1}\right)z}{2}+\frac{\left(\tau_0^{s_2}+\tau_0^{s_1}\right)z^2}{2h_N+h_p}\right)dz,$$

$$E_{11p}^{*}=\int_{h_N}^{h_N+h_p}\frac{\upsilon_p}{\left(1-\upsilon_p\right)}\left(\frac{\left(\tau_0^{s_2}-\tau_0^{s_1}\right)z}{2}+\frac{\left(\tau_0^{s_2}+\tau_0^{s_1}\right)z^2}{2h_N+h_p}\right)dz, \tag{B.9}$$

$$G_{11N}^{*}=\int_{-h_N}^{h_N}\frac{\upsilon_N}{(1-\upsilon_N)}\left(\frac{(\rho^{s_1}-\rho^{s_2})z}{2}-\frac{(\rho^{s_1}+\rho^{s_2})z^2}{2h_N+h_p}\right)dz,$$

$$G_{11p}^{*}=\int_{h_N}^{h_N+h_p}\frac{\upsilon_p}{\left(1-\upsilon_p\right)}\left(\frac{(\rho^{s_1}-\rho^{s_2})z}{2}-\frac{(\rho^{s_1}+\rho^{s_2})z^2}{2h_N+h_p}\right)dz, \tag{B.10}$$

Note that, because of geometric symmetry, the expressions B_{ijN} is zero, i.e. $\left(B_{ijN}=0\right)$.

Appendix C

$$\alpha_1=\frac{1}{m_3}\bar{A}_{11},\ \alpha_2=\frac{m_0^2}{m_3}\bar{A}_{66},\ \alpha_3=\frac{m_0}{m_3}(\bar{A}_{12}+\bar{A}_{21}),\alpha_4=\frac{2m_0}{m_3}\bar{A}_{66},\ \alpha_5=\frac{m_0}{m_3}(\bar{A}_{12}+\bar{A}_{21}),$$

$$\alpha_6=\frac{1}{2m_1m_3}\left(2\bar{A}_{11}-\bar{\tau}_0^{s_1}-\bar{\tau}_0^{s_2}\right),\ \alpha_7=\frac{m_0m_2}{2m_3}(\bar{A}_{12}+\bar{A}_{21}),\ \alpha_8=\frac{2m_0m_2}{m_3}\bar{A}_{66},\ \alpha_9=\frac{m_0^2}{m_3}\bar{A}_{22},$$

$$\alpha_{10}=\frac{m_0^2m_2}{2m_3}\left(2\bar{A}_{22}-\bar{\tau}_0^{s_1}-\bar{\tau}_0^{s_2}\right),\alpha_{11}=\frac{m_2}{2m_3}(\bar{A}_{12}+\bar{A}_{21}),\ \alpha_{12}=\frac{m_0^2}{m_3}\left(2\bar{A}_{22}-\bar{\tau}_0^{s_1}-\bar{\tau}_0^{s_2}\right),$$

$$\alpha_{13}=\frac{1}{m_3}\bar{A}_{66},\ \alpha_{14}=\frac{2m_2}{m_3}\bar{A}_{66},\alpha_{15}=\frac{m_0^2}{m_3}\left(\bar{A}_{22}-\bar{\tau}_0^{s_1}-\bar{\tau}_0^{s_2}\right),\ \alpha_{16}=\frac{1}{4m_1^2m_3}\left(\bar{A}_{11}-\bar{\tau}_0^{s_1}-\bar{\tau}_0^{s_2}\right),$$

$$\alpha_{17}=\frac{m_0^2m_2^2}{4m_3}\left(\bar{A}_{22}-\bar{\tau}_0^{s_1}-\bar{\tau}_0^{s_2}\right),\ \alpha_{18}=\frac{m_2^2}{4m_3}(4\bar{A}_{66}+\bar{A}_{12}+\bar{A}_{21}),\ \alpha_{19}=\frac{m_2}{2m_3}(\bar{A}_{12}+\bar{A}_{21}),$$

$$\alpha_{20}=\frac{m_0^2m_2}{m_3}\left(\bar{A}_{22}-\bar{\tau}_0^{s_1}-\bar{\tau}_0^{s_2}\right),\ \alpha_{21}=-\frac{4m_0m_2}{m_3}\bar{B}_{66},\alpha_{22}=\frac{m_0m_2}{m_3}(\bar{F}_{11}-\bar{B}_{12}-\bar{B}_{21}),$$

$$\alpha_{23}=\frac{1}{m_1m_3}(\bar{F}_{11}-2\bar{B}_{11}),\ \alpha_{24}=\frac{m_2}{m_3}(\bar{F}_{11}-\bar{B}_{12}-\bar{B}_{21}),\alpha_{25}=-\frac{4m_2}{m_3}\bar{B}_{66},$$

$$\alpha_{26}=\frac{m_0^2m_2}{m_3}(\bar{F}_{11}-2\bar{B}_{22})\ ,\ \alpha_{27}=\frac{m_2^2}{2m_3}(\bar{F}_{11}-\bar{B}_{12}-\bar{B}_{21}),\alpha_{28}=\frac{m_2}{m_3}(\bar{F}_{11}-\bar{B}_{12}-\bar{B}_{21}),$$

$$\alpha_{29}=\frac{m_2^2}{2m_3}(\bar{F}_{11}-\bar{B}_{12}-\bar{B}_{21}),\ \alpha_{30}=\frac{1}{2m_1^2m_3}\left(\bar{F}_{11}-2\bar{B}_{11}+\bar{\tau}_0^{s_2}(1+m_4)-\bar{\tau}_0^{s_1}\right),$$

$$\alpha_{31}=\frac{m_0^2m_2^2}{2m_3}\left(\bar{F}_{11}-2\bar{B}_{22}+\bar{\tau}_0^{s_2}(1+m_4)-\bar{\tau}_0^{s_1}\right),\alpha_{32}=-\frac{4m_2^2}{m_3}\bar{B}_{66},$$

$$\alpha_{33}=\frac{m_0^2m_2}{m_3}\left(\bar{F}_{11}-2\bar{B}_{22}+\bar{\tau}_0^{s_2}(1+m_4)-\bar{\tau}_0^{s_1}\right),\alpha_{34}=\frac{1}{m_1^2m_3}(\bar{D}_{11}-\bar{E}_{11}),$$

$$\alpha_{35}=\frac{m_0^2m_2^2}{m_3}(\bar{D}_{22}-\bar{E}_{11}),\ \alpha_{36}=\frac{4m_2^2}{m_3}\bar{D}_{66},\alpha_{37}=\frac{m_2^2}{m_3}(\bar{D}_{12}+\bar{D}_{21}-2\bar{E}_{11}),$$

$$\alpha_{38}=\frac{m_0m_1}{m_3}\left(\bar{\tau}_0^{s_1}+\bar{\tau}_0^{s_2}-\bar{N}_{\theta p}\right),\alpha_{39}=\frac{m_1}{m_3}\left(\bar{\tau}_0^{s_1}+\bar{\tau}_0^{s_2}-\bar{N}_{xp}\right),\alpha_{40}=\frac{m_0m_1}{m_3}\left(\bar{\tau}_0^{s_1}+\bar{\tau}_0^{s_2}-\bar{N}_{\theta p}\right),$$

$$\alpha_{41}=\frac{1}{2m_3}\left(\bar{\tau}_0^{s_1}+\bar{\tau}_0^{s_2}-\bar{N}_{xp}\right),\alpha_{42}=\frac{m_0^2}{2m_3}\left(\bar{\tau}_0^{s_1}+\bar{\tau}_0^{s_2}-\bar{N}_{\theta p}\right),\alpha_{43}=\frac{1}{m_3}(\bar{M}_{xp}+\bar{\tau}_0^{s_1}-\bar{\tau}_0^{s_2}(1+m_4)),$$

$$\alpha_{44}=\frac{m_0^2}{m_3}(\bar{M}_{\theta p}+\bar{\tau}_0^{s_1}-\bar{\tau}_0^{s_2}(1+m_4)),\alpha_{45}=-\frac{1}{2m_1^2m_3}\bar{G}_{11}^{*},\alpha_{46}=-\frac{m_2^2}{2m_3}\bar{G}_{11}^{*},\alpha_{47}=\frac{1}{2m_1m_3}\bar{J}_{11}^{*},$$

$$\alpha_{48}=\frac{m_2}{2m_3}\bar{J}_{11}^{*},\alpha_{49}=\frac{m_2}{2m_3}\bar{J}_{11}^{*},\alpha_{50}=\frac{1}{4m_1^2m_3}\bar{J}_{11}^{*},\alpha_{51}=\frac{m_2^2}{4m_3}\bar{J}_{11}^{*},$$

Appendix D

For all following parameters, limits of integrations are $\xi = 0 \dots L$ and $\theta = 0 \dots 2\pi$.

$$(M)_u^u = \iint (\chi_e \chi_i \vartheta_f \vartheta_j) d\xi d\theta \ , (M)_u^w = \frac{1}{2}\alpha_{47} \iint (\chi_e' \beta_o \vartheta_f \psi_l) d\xi d\theta$$

$$(K)_u^u = \iint (\alpha_1 \chi_e' \chi_i' \vartheta_f \vartheta_j + \alpha_2 \chi_e \chi_i \vartheta_f' \vartheta_j') d\xi d\theta \ , (K)_u^v = \frac{1}{2} \iint (\alpha_3 \chi_e' \phi_k \vartheta_f \alpha_l' + \alpha_4 \chi_e \phi_k' \vartheta_f' \alpha_l) d\xi d\theta$$

$$(K)_u^w = \frac{1}{2} \iint (\alpha_5 \chi_e' \beta_o \vartheta_f \psi_l + \alpha_{21} \chi_e \beta_0' \vartheta_f' \psi_l' + \alpha_{22} \chi_e' \beta_o \vartheta_f \psi_l'' + \alpha_{23} \chi_e' \beta_0'' \vartheta_f \psi_l) d\xi d\theta$$

$$(NL)_u^w = \frac{1}{2} \iint (\alpha_6 \chi_e' \beta_0' \beta_t' \vartheta_f \psi_p \psi_v + \alpha_7 \chi_e' \beta_o \beta_t \vartheta_f \psi_p' \psi_v' + \alpha_8 \chi_e \beta_0' \beta_t \vartheta_f' \psi_p \psi_v') d\xi d\theta$$

$$\bar{F}_{up} = \frac{1}{2}\alpha_{39} \iint (\chi_e' \vartheta_i) d\xi d\theta \ , (M)_v^v = \iint (\phi_q \phi_k a_f a_l) d\xi d\theta \ , (M)_v^w = \frac{1}{2}\alpha_{48} \iint (\phi_q \beta_o \alpha_f' \psi_l) d\xi d\theta$$

$$(K)_v^u = \frac{1}{2} \iint (\alpha_3 \phi_q \chi_i' \alpha_f' \vartheta_l + \alpha_4 \phi_q' \chi_i \alpha_f \vartheta_l') d\xi d\theta \ , (K)_v^v = \iint (\alpha_9 \phi_q \phi_k \alpha_f' \alpha_l' + \alpha_{13} \phi_q' \phi_k' \alpha_f \alpha_l) d\xi d\theta$$

$$(K)_v^w = \frac{1}{2} \iint (\alpha_{12} \phi_q \beta_o \alpha_f' \psi_l + \alpha_{24} \phi_q \beta_0'' \alpha_f' \psi_l + \alpha_{25} \phi_q' \beta_0' \alpha_f \psi_l' + \alpha_{26} \phi_q \beta_o \alpha_f' \psi_l'') d\xi d\theta$$

$$(NL)_v^w = \frac{1}{2} \iint (\alpha_{10} \phi_q \beta_o \beta_t \alpha_g' \psi_p' \psi_v' + \alpha_{11} \phi_q \beta_0' \beta_t' \alpha_g' \psi_p \psi_v + \alpha_{14} \phi_q' \beta_0' \beta_t \alpha_g \psi_p \psi_v') d\xi d\theta$$

$$\bar{F}_{vp} = \frac{1}{2}\alpha_{40} \iint (\phi_q \alpha_f') d\xi d\theta$$

$$(M)_w^w = \frac{1}{2} \iint (2\beta_r \beta_o \psi_s \psi_p + \alpha_{45} \beta_r'' \beta_o \psi_s \psi_p + \alpha_{46} \beta_r \beta_o \psi_s'' \psi_p + \alpha_{49} \beta_r \beta_o \psi_s \psi_p) d\xi d\theta$$

$$(C)_w^w = \iint (\bar{C}_w \beta_r \beta_o \psi_s \psi_p) d\xi d\theta$$

$$(K)_w^u = \frac{1}{2} \iint (\alpha_5 \beta_r \chi_i' \psi_s \vartheta_j + \alpha_{21} \beta_r' \chi_i \psi_p' \vartheta_j' + \alpha_{22} \beta_r \chi_i' \psi_s'' \vartheta_j + \alpha_{23} \beta_r'' \chi_i' \psi_s \vartheta_j) d\xi d\theta$$

$$(K)_w^v = \frac{1}{2} \iint (\alpha_{12} \beta_r \phi_k \psi_s \alpha_l' + \alpha_{24} \beta_r'' \phi_k \psi_s \alpha_l' + \alpha_{25} \beta_r' \phi_k' \psi_s' \alpha_l + \alpha_{26} \beta_r \phi_k \psi_s'' \alpha_l') d\xi d\theta$$

$$(K)_w^w = \frac{1}{2} \iint \begin{pmatrix} 2\alpha_{15} \beta_r \beta_o \psi_s \psi_p + \alpha_{28} \beta_r \beta_0'' \psi_s \psi_p + \alpha_{28} \beta_r'' \beta_o \psi_s \psi_p + \alpha_{33} \beta_r \beta_o \psi_s \psi_p'' \\ +\alpha_{33} \beta_r \beta_o \psi_s'' \psi_p + 2\alpha_{34} \beta_r'' \beta_0'' \psi_s \psi_p + 2\alpha_{35} \beta_o \beta_r \psi_s'' \psi_p'' + 2\alpha_{36} \beta_r' \beta_o' \psi_s' \psi_p' \\ +\alpha_{37} \beta_r \beta_o'' \psi_s'' \psi_p + \alpha_{37} \beta_r'' \beta_o \psi_s \psi_p'' + 2\alpha_{41} \beta_r' \beta_o' \psi_s \psi_p + 2\alpha_{42} \beta_r \beta_o \psi_s' \psi_p' \\ +2\bar{k}_w \beta_r \beta_o \psi_s \psi_p - 2\bar{k}_p \beta_r \beta_0'' \psi_s \psi_p - 2\bar{k}_p m_0^2 \beta_r \beta_o \psi_s \psi_p'' - 2\bar{F}_{e2} (K_e)_w^w \end{pmatrix} d\xi d\theta$$

$(K_e)_w^w = \beta_r \beta_o \psi_s \psi_p$,

$$(K)_{w2}^{\bar{w}} = \iint (\alpha_{50} \beta_r' \beta_o \beta_t' \psi_s \psi_p \psi_v + \alpha_{51} \beta_r \beta_o \beta_t \psi_s' \psi_p \psi_v') d\xi d\theta$$

$$(NL)_w^u = \frac{1}{2} \iint \begin{pmatrix} 2\alpha_6 \beta_r' \beta_o' \chi_i' \psi_s \psi_p \vartheta_j + 2\alpha_7 \beta_r \beta_o \chi_i' \psi_s' \psi_p' \vartheta_j \\ +\alpha_8 \beta_r' \beta_o \chi_i \psi_s \psi_p' \vartheta_j' + \alpha_8 \beta_r \beta_o' \chi_i \psi_s' \psi_p \vartheta_j' \end{pmatrix} d\xi d\theta$$

$$(NL)_w^v = \frac{1}{2} \iint \begin{pmatrix} 2\alpha_{10} \beta_r \beta_o \phi_k \psi_s' \psi_p' \alpha_l' + 2\alpha_{11} \beta_r' \beta_o' \phi_k \psi_s \psi_p \alpha_l' \\ +\alpha_{14} \beta_r' \beta_o \phi_k' \psi_s \psi_p' \alpha_l + \alpha_{14} \beta_r \beta_o' \phi_k' \psi_s' \psi_p \alpha_l \end{pmatrix} d\xi d\theta$$

$$(NL)_{w2}^{w}=\frac{1}{2}\iint\begin{pmatrix}\alpha_{19}\beta_r\beta_o'\beta_t'\psi_s\psi_p\psi_v+2\alpha_{19}\beta_r'\beta_o'\beta_t\psi_s\psi_p\psi_v+\alpha_{20}\beta_r\beta_o\beta_t\psi_s\psi_p'\psi_v'\\+2\alpha_{20}\beta_r\beta_o\beta_t\psi_s'\psi_p'\psi_v+\alpha_{27}\beta_r''\beta_o\beta_t\psi_s\psi_p'\psi_v'+2\alpha_{27}\beta_r\beta_o\beta_t''\psi_s'\psi_p'\psi_v\\+\alpha_{29}\beta_r\beta_o'\beta_t'\psi_s''\psi_p\psi_v+2\alpha_{29}\beta_r'\beta_o'\beta_t\psi_s\psi_p\psi_v''+\alpha_{30}\beta_r''\beta_o'\beta_t'\psi_s\psi_p\psi_v\\+2\alpha_{30}\beta_r'\beta_o'\beta_t''\psi_s\psi_p\psi_v+\alpha_{31}\beta_r\beta_o\beta_t\psi_s''\psi_p'\psi_v'+2\alpha_{31}\beta_r\beta_o\beta_t\psi_s'\psi_p'\psi_v''\\+\alpha_{32}\beta_r'\beta_o'\beta_t\psi_s'\psi_p\psi_v'+\alpha_{32}\beta_r'\beta_o'\beta_t\psi_s\psi_p'\psi_v'+\alpha_{32}\beta_r\beta_o'\beta_t'\psi_s'\psi_p\psi_v'\\-2\bar{F}_{e3}(NL_{2e})_w^w\end{pmatrix}d\xi d\theta$$

$$(NL_{2e})_w^w=\beta_r\beta_o\beta_t\psi_s\psi_p\psi_v$$

$$(NL)_{w3}^{w}=\frac{1}{2}\iint\begin{pmatrix}4\alpha_{16}\beta_r'\beta_o'\beta_t'\beta_a'\psi_s\psi_p\psi_v\psi_b+4\alpha_{17}\beta_r\beta_o\beta_t\beta_a\psi_s'\psi_p'\psi_v'\psi_b'\\+2\alpha_{18}\beta_r'\beta_o'\beta_t\beta_a\psi_s\psi_p\psi_v'\psi_b'+2\alpha_{18}\beta_r\beta_o\beta_t'\beta_a'\psi_s'\psi_p'\psi_v\psi_b\\-2\bar{F}_{e4}(NL_{3e})_w^w\end{pmatrix}d\xi d\theta$$

$$(NL_{3e})_w^w=\beta_r\beta_o\beta_t\beta_a\psi_s\psi_p\psi_v\psi_b$$

$$\bar{F}_{wp}=\frac{1}{2}\iint(\alpha_{38}\beta_r\psi_s+\alpha_{43}\beta_r''\psi_s+\alpha_{44}\beta_r\psi_s'')d\xi d\theta$$

$$\bar{F}_w=\bar{F}\iint\beta_r\beta_s\cos\Omega\tau\,d\xi d\theta,$$

Appendix E

$$\begin{bmatrix}(\hat{M})_u^w\\(\hat{M})_v^w\end{bmatrix}=\begin{bmatrix}(K)_u^u&(K)_u^v\\(K)_v^u&(K)_v^v\end{bmatrix}^{-1}\begin{bmatrix}(M)_u^w\\(M)_v^w\end{bmatrix},\begin{bmatrix}(\hat{K})_u^w\\(\hat{K})_v^w\end{bmatrix}=\begin{bmatrix}(K)_u^u&(K)_u^v\\(K)_v^u&(K)_v^v\end{bmatrix}^{-1}\begin{bmatrix}(K)_u^w\\(K)_v^w\end{bmatrix},\begin{bmatrix}(\widehat{NL})_u^w\\(\widehat{NL})_v^w\end{bmatrix}=\begin{bmatrix}(K)_u^u&(K)_u^v\\(K)_v^u&(K)_v^v\end{bmatrix}^{-1}\begin{bmatrix}(NL)_u^w\\(NL)_v^w\end{bmatrix},$$

$$\begin{bmatrix}\hat{F}_{up}\\\hat{F}_{vp}\end{bmatrix}=\begin{bmatrix}(K)_u^u&(K)_u^v\\(K)_v^u&(K)_v^v\end{bmatrix}^{-1}\begin{bmatrix}\bar{F}_{up}\\\bar{F}_{vp}\end{bmatrix},\begin{bmatrix}\hat{F}_{wup}\\\hat{F}_{wvp}\end{bmatrix}=[(K)_w^u\quad(K)_w^v]\begin{bmatrix}\hat{F}_{up}\\\hat{F}_{vp}\end{bmatrix},\begin{bmatrix}(\hat{M})_u^{wu}\\(\hat{M})_v^{wv}\end{bmatrix}=-[(K)_w^u\quad(K)_w^v]\begin{bmatrix}(\hat{M})_u^w\\(\hat{M})_v^w\end{bmatrix},\begin{bmatrix}(\hat{K})_u^{wu}\\(\hat{K})_v^{wv}\end{bmatrix}=$$

$$-[(K)_w^u\quad(K)_w^v]\begin{bmatrix}(\hat{K})_u^w\\(\hat{K})_v^w\end{bmatrix},\begin{bmatrix}(\widehat{NL})_u^{wu}\\(\widehat{NL})_v^{wv}\end{bmatrix}=-[(K)_w^u\quad(K)_w^v]\begin{bmatrix}(\widehat{NL})_u^w\\(\widehat{NL})_v^w\end{bmatrix},$$

JJMIE

Volume 12, Number 4, December. 2018
ISSN 1995-6665
Pages 313 - 321

Jordan Journal of Mechanical and Industrial Engineering

Effects of SiC Particles Parameters on the Corrosion Protection of Aluminum-based Metal Matrix Composites using Response Surface Methodology

Shashi Prakash Dwivedi*, Rohit Sahu

G. L. Bajaj Institute of Technology & Management, Greater Noida, Gautam Buddha Nagar, U.P. 201310, India

Received 3 August. 2018

Abstract

In the automobile industries materials, durability with respect to time (corrosion behavior) of materials is one of the most important factors observed since many past years. In the present investigation, aluminum (AA6061) based metal matrix composite successfully developed using SiC as reinforcement material through electromagnetic stir casting route. Three parameters (preheat temperature, size, weight percent) of SiC were selected to reduce the corrosion rate of metal matrix composite. From the result, it was observed that by increasing the preheat temperature of SiC, corrosion rate decrease. Increasing the particle size and weight percent of SiC, corrosion rate also increases. Regarding optimal values of SiC preheat temperature, SiC particle size and wt. % of SiC were found to be 370.120C, 38.7 µm and 2.94 wt. % respectively for minimum corrosion rate 1.16444 mm/year with desirability one of metal matrix composite using Response Surface Methodology. Microstructure at optimum reinforcement parameters was carried out. Uniform distribution of composite was observed at optimum SiC particles parameters.

Keywords: Preheat temperature, size, weight percent, corrosion rate, RSM;

1. Introduction

Aluminum alloys reinforced with ceramic particulates have considerable potential due to their high specific strength and stiffness as well as low density. The higher specific strength is, the higher strength and lighter weight the material is. It is important to select materials with high specific strength or improve the specific strength to lift buildings' height, reduce structural weight and lower project costs. Stiffness is proportional to the cube of the thickness. To neutralize aluminum being one-third the stiffness of steel, an aluminum part must be made 44 percent thicker than the steel part [1-2]. These properties have made particles reinforced metal matrix composites (MMCs) an attractive material for the use in aerospace, transportation and industrial sectors [3-5]. Aluminum based metal matrix composite is used in various industrial applications where good mechanical properties are required. Its demand in aircraft industries and automobile industries is mainly due to its low cost of processing and a broad range of properties [6-9]. Aluminum based metal matrix composite (AMC) is used in the design of specific aerospace and automotive components such as ventral fins, fuel excess door covers, rotating blades sleeves, gear parts, crankshafts, and suspension arms [10-13]. In the electronics industry, it is used in the processing of integrated heat sinks, microprocessor, microwave, aircraft wings, fuselages frames and landing gears [14-15]. Though, mechanical properties of materials such as hardness and tensile strength are much important factor in the application of materials in various manufacturing sector [16-18]. But from some past years, other factors are also considered by the automobile industries as well as manufacturing industries; this factor is materials' durability with respect to time [19-20].

Pen Jin et al. [21] found the effect of SiC particle size on the structures and properties of Ni–SiC nanocomposites deposited by magnetic pulse electrodeposition technology. Results showed S-30 nanocomposites with fine, compact and uniform structures consisting of fine nickel grains (average size: 381.7 nm) and SiC nanoparticles (average size: 34.2 nm). For SiC particle size of 30 nm, diffraction peaks of Ni and SiC appeared wide with low intensity, indicating S-30 nanocomposites with small-sized Ni grains and SiC nanoparticles. Reza Zare et al. [22] investigated the effect of SiC particles on the physical and thermal properties of Al6061/SiCp composite. It was seen that with increasing the amount of the reinforcement, the density of the samples decreased, while the porosity increased. D. Ahmadkhaniha et al. [23] observed the effect of SiC particle size and heat-treatment on microhardness and corrosion resistance of NiP electrodeposited coatings. It was found that the heat-treatment doubled the

* Corresponding author e-mail: spdglb@gmail.com.

microhardness and changed the anodic polarization behaviour of the coatings from passive to active with respect to the as-plated conditions. S. Vijayabhaskar et al. [24] showed the effect of nano SiC particles on properties and characterization of Magnesium matrix nanocomposites. The results showed that the increase in weight % of nano SiC improves the mechanical properties. Pham Van Trinh et al. [25] investigated the effect of oxidation of SiC particles on mechanical properties and wear behaviour of SiCp/Al6061 composites. The results revealed an improvement in interfacial bond strength between Al6061 and oxidized SiC_p due to the formation of a $MgAl_2O_4$ continuous phase and suppression of brittle Al_4C_3 formation at the interfacial layer. Łukasz Rogal et al. [26] designed novel metal matrix nanocomposites exploring the CoCrFeMnNi high entropy alloy as a matrix and SiC spherical nanoparticles with a diameter of 20–50 nm as a reinforcement phase and manufactured by mechanical alloying followed by hot isostatic sintering. Li Zhang et al. [27] identified the effect of SiC particles and the particulate size on the hot deformation and processing map of AZ91 magnesium matrix composites. Results show that compared with the monolithic AZ91 alloy, the incorporated nano-SiC particles effectively increase the flow stress of the composites by blocking the strain-induced dislocations, while the effect of the micro-SiC particles varies due to the competition between pinning effect and particle stimulating nucleation (PSN) mechanism.

From the literature review, it was observed that very few researchers find out the reinforcement parameters effect on the corrosion rate of aluminum-based MMC. No researchers have given the optimum value of the combination of reinforcement parameters to reduce the corrosion rate using response surface methodology. Keeping these facts in mind, optimum condition of reinforcement parameters was obtained using Response Surface Methodology followed by confirmation experiment which was carried out to identify reduced corrosion rate as compared to the base material.

2. Materials and Methods

2.1. Matrix Material

In this study, aluminum alloy 6061 is chosen as the matrix material. Alloy 6061 is one of the most widely used alloys in the 6000 series. AA6061 is used in the fabrication of various rotating and reciprocating parts such as brake-rotors, driveshafts, piston and in other structural parts which require lightweight and high strength materials [19]. Typical chemical composition of Al 6061 is presented below:

Table 1. Chemical Composition of Aluminum 6061 alloy

Si	Fe	Cu	Mn	Mg	Zn	Ti	Cr	Al
0.4-0.8	0.7	0.15-0.40	0.15	0.8-1.2	0.25	0.15	0.35	Balance

2.2. Reinforcement Material

Silicon Carbide is used as a reinforcement material. Silicon carbide (SiC), also known as carborundum, is a compound of silicon and carbon with chemical formula SiC. Usually, SiC particles in composite improve the tensile strength and hardness of the composite. In this investigation, the effect of SiC addition on corrosion behavior of the composite was investigated [21-23].

2.3. Development of Al/SiC Metal Matrix Composite

In this study, the composite material was developed by using stir casting technique. AA6061/SiC composite was developed with different compositions as shown in Table 2. Argon gas was used at the surface of composite material during the stirring process to avoid porosity and blow holes. The vacuum pump was also used to create the vacuum environment at the time of development of composite. SiC reinforcement particles were preheated before adding into the melt matrix material to obtain proper wettability between the matrix material and reinforcement particles after the solidification process. Matrix material was melted in the muffle furnace. The liquid aluminium alloy at 700^0C temperature was poured into a graphite crucible packed with glass wool between magnetic coils. Current is supplied to provide the magnetic force in the motor. Due to the magnetic force, the melted composite material was begun to rotate as shown in Figure 1. The prepared composite was removed from the graphite crucible after the solidification to observe different properties. Electromagnetic parameters are shown in Table 2.

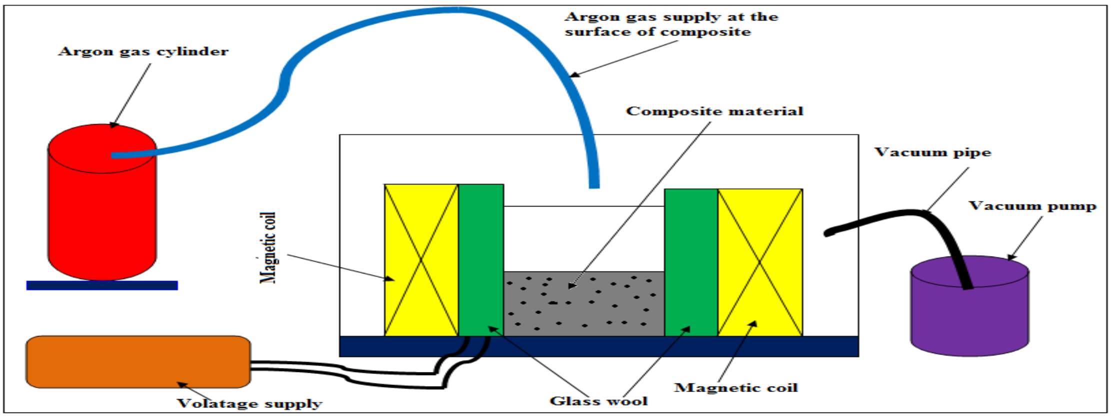

Figure 1.: Electromagnetic Stir Casting Set-Up

Table 2. Electromagnetic stir casting process parameters

S.No	Parameters	Values set as
1	Voltage supply	200 V
2	Current	20 Ampere
3	Stirring speed	200 RPM
4	Stirring time	3 minutes
5	Stirring temperature	700^0C
4	Percentage of SiC	2.5 %- 12.5 %

2.4. Corrosion Test

Corrosion test of all developed metal matrix composite was carried out in high alkalinity bath tub. Corrosion test of each sample were carried out for 120 hours with 3.5 wt. % NaCl in the bath tub. Weight of each sample was kept constant (9 gm). All seventeen samples were kept in the bath tub for 120 hours. After 120 hours, the final weight of each sample was measured. Weight loss of each sample was calculated by subtracting the weight of each sample after corrosion test to the initial weight of samples (9 gm). Corrosion rate was calculated from the given equation [28].

$$\text{Corrosion Rate (CR)} = \frac{\text{Weight loss (g)} * K}{\text{Alloy Density (g/cm}^3) * \text{Exposed Area (A)} * \text{Exposure Time (hr)}}$$

Where, $K = 8.75 \times 10^4$, Exposed area $A = 9$ cm^2, Exposure time = 120 hour

2.5. Design Matrix Table for Corrosion Test

Design matrix table was obtained by using design expert software [29]. The corrosion test specimens were randomly tested for corrosion rate using response surface methodology to avoid any possible bias. For the selection of SiC parameters as reinforcement (SiC Preheat Temperature in degree centigrade, particle size of SiC in µm and SiC wt. %), numerous experiments were conducted. In the pilot run, arbitrarily the SiC preheat temperature was chosen as 100^0C for the development of AA6061/SiC composite material and others reinforcement parameters (particle size of SiC in µm and SiC wt. %) were kept constant. Some porosity was observed. In addition to porosity problem, wettability between the SiC and aluminium was not formed properly. When SiC was preheated to 200^0C, some porosity was disappeared and wettability between the matrix material and SiC was enhanced. Further, SiC preheat temperature was increased to 500^0C, it was observed that some porosity was obtained. After the pilot run investigation, SiC preheat temperature was chosen in the range of 200^0C to 300^0C. The same course of action was conducted to decide the ranges for other reinforcement parameters. Design matrix table with corresponding corrosion rate for each run was shown in Table 3.

Table 3. Design matrix and experimental results for corrosion rate

Standard order	Run	A: SiC Preheat Temperature (Degree centigrade)	B: Particle size of SiC (µm)	C: SiC wt. %	Corrosion rate (mm/year)	Composition of Composites
12	1	300.00	105	12.5	3.4	AA6061+ 12.5% SiC
14	2	300.00	70.00	7.5	2.2	AA6061+ 7.5 % SiC
10	3	300.00	105.00	2.5	1.52	AA6061+ 2.5 % SiC
6	4	400.00	70.00	2.5	1.3	AA6061+ 2.5 % SiC
16	5	300.00	70.00	7.5	2.2	AA6061+ 7.5 % SiC
13	6	300.00	70.00	7.5	2.29	AA6061+ 7.5 % SiC
5	7	200.00	70.00	2.5	2	AA6061+ 2.5 % SiC
15	8	300.00	70.00	7.5	2.25	AA6061+ 7.5 % SiC
9	9	300.00	35.00	2.5	1.2	AA6061+ 2.5 % SiC
4	10	400.00	105.00	7.5	2.8	AA6061+ 7.5 % SiC
3	11	200.00	105.00	7.5	3.4	AA6061+ 7.5 % SiC
17	12	300.00	70.00	7.5	2.27	AA6061+ 7.5 % SiC
7	13	200.00	70.00	12.5	3.4	AA6061+ 12.5% SiC
8	14	400.00	70.00	12.5	2.3	AA6061+ 12.5% SiC
1	15	200.00	35.00	7.5	2.7	AA6061+ 7.5 % SiC
11	16	300.00	35.00	12.5	2.05	AA6061+ 12.5 % SiC
2	17	400.00	35.00	7.5	1.7	AA6061+ 7.5 % SiC

3. Results and Discussion

3.1. Mathematical modelling

From the ANOVA Table 4, it can be seen that the Model F-value of 209.06 implies the model is significant. There is only a 0.01% chance that a "Model F-value" this large could occur due to noise. Values of "Prob > F" less than 0.0500 indicate model terms are significant. In this case, A, B, C, A^2, B^2, C^2, AB, AC, BC are significant model terms. Values greater than 0.1000 indicate the model terms are not significant. If there are many insignificant model terms (not counting those required to support hierarchy), model reduction may improve your model.

The "Lack of Fit F-value" of 4.14 implies the Lack of Fit is not significant relative to the pure error. There is a 10.19% chance that a "Lack of Fit F-value" this large could occur due to noise. Non-significant lack of fit is good -- we want the model to fit.

The "Pred R-Squared" of 0.9537 is in reasonable agreement with the "Adj R-Squared" of 0.9915. "Adeq Precision" measures the signal to noise ratio. A ratio greater than 4 is desirable. The ratio of 45.662 indicates an adequate signal. This model can be used to navigate the design space.

Equation (1) shows the mathematical model for corrosion rate with respect to SiC particles parameters.

Corrosion Rate (mm/year) = +5.10644 - 0.023215 x SiC Preheat Temperature - 0.01867 x Size of SiC + 0.26510 x Weight of SiC +3.07750E-005 x SiC Preheat Temperature^2 + 8.18367E-005 x Size of SiC^2 - 0.011990 x Weight of SiC^2 + 2.85714E-005 x SiC Preheat Temperature x Size of SiC - 2.00000E-004 x SiC Preheat Temperature x Weight of SiC +1.47143E-003 x Size of SiC x Weight of SiC (1)

The diagnostics graph of predicted v/s actual and residual plots are shown in Figure 2 and Figure 3 respectively. The predicted v/s actual graph as well as residual plots show accurate straight line. Both graphs are not showing any definite trend.

Table 4. ANOVA Table for corrosion rate

Source	Sum of square	DF	Mean square	F value	Prob. > F	
Model	7.37	9	0.82	209.06	< 0.0001	Significant
A	1.44	1	1.44	369.09	< 0.0001	
B	1.51	1	1.51	384.45	< 0.0001	
C	3.29	1	3.29	840.26	< 0.0001	
A^2	0.40	1	0.40	101.86	< 0.0001	
B^2	0.042	1	0.042	10.81	0.0133	
C^2	0.38	1	0.38	96.63	< 0.0001	
AB	0.040	1	0.040	10.22	0.0151	
AC	0.040	1	0.040	10.22	0.0151	
BC	0.27	1	0.27	67.75	< 0.0001	
Residual	0.027	7	3.915E-003			
Lack of Fit	0.021	3	6.908E-003	4.14	0.1019	Not significant
Pure Error	6.680E-003	4	1.670E-003	Pure Error		
Cor Total 16	7.39	16				
Std. dev.	0.063	R-Square		0.9963		
Mean	2.29	Adj-R squared		0.9915		
C.V.	2.73	Pred R-squared		0.9537		
Press	0.34	Adeq precision		45.662		

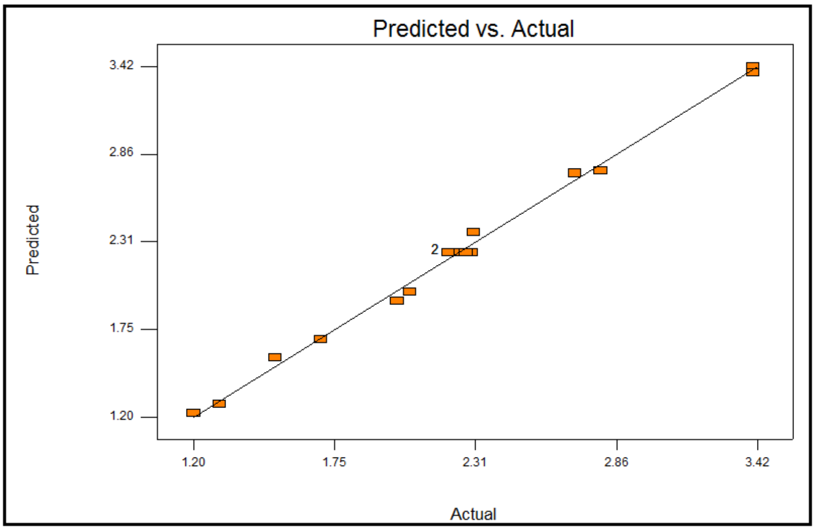

Figure 2. Diagnostics graph of predicted v/s actual

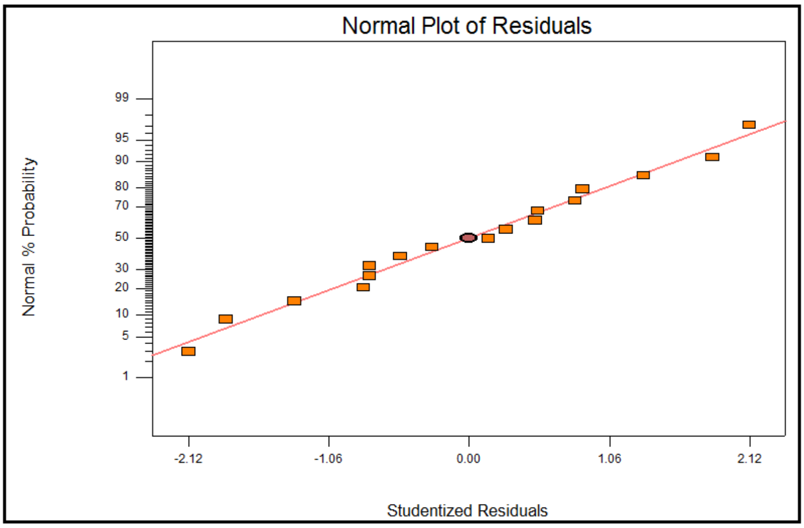

Figure 3. Diagnostics graph of residual plots

3.2. Optimum SiC Particles Parameters for Minimum Corrosion Rate

3.2.1. Effect of SiC preheat temperature on corrosion rate

Effect of SiC preheat temperature on corrosion rate is described with the help of Figure 4. Within the range of SiC preheat temperature; it was observed that the corrosion rate of metal matrix composite decreases by increasing the SiC preheat temperature. Basically, by increasing the preheat temperature of SiC, wettability of SiC particles with aluminium is improved while porosity is reduced. Minimum porosity and good wettability reduce corrosion rate and improve the mechanical properties of composite.

3.2.2. Effect of SiC particle size on corrosion rate

Figure 5 shows the relation between SiC particle size and the corrosion rate of metal matrix composite. From Figure 5, it can be observed that by increasing the SiC particle size, corrosion rate continuously increases. When particle size increases then more porosity is obtained. Porosity is a type of defects due to which more corrosion weight loss occurs. Figure 6 (a) shows the microstructure image of AA6061/3 wt. % SiC composite with particle size 105 µm. Cracks and porosity were observed in the composite material after solidification process. Figure 6 (b) shows the microstructure image of AA6061/3 wt. % SiC composite with particle size 35 µm. Porosity free composite was obtained.

3.2.3. Effect of SiC weight percent on corrosion rate

Figure 7 shows the effect of SiC weight percent on the corrosion rate. It can be observed that by increasing the weight percent of SiC particles corrosion rate continuously increases. When, weight percent of SiC particles increases, electrochemical reactions of the aluminum-based material composite reinforced with SiC may increase. The electrochemical reaction occurs when most or all the atoms on the same metal surface are oxidized, damaging the entire surface. Most metals are easily oxidized: they tend to lose electrons to oxygen in the air or in water. Usually, by increasing the weight percent of SiC particles (more than 12.5 wt. %), blow holes and porosity is formed. This porosity increases the corrosion rate rapidly. Figure 8 (a) shows the microstructure image of AA6061/12.5 wt. % SiC composite material. Microstructure results showed uniform distribution of AA6061/12.5 wt. % SiC composite material. However, the microstructure image of AA6061/15 wt. % SiC composite material showed the agglomeration of SiC particles. These agglomeration produced porosity and cracks inside the composite.

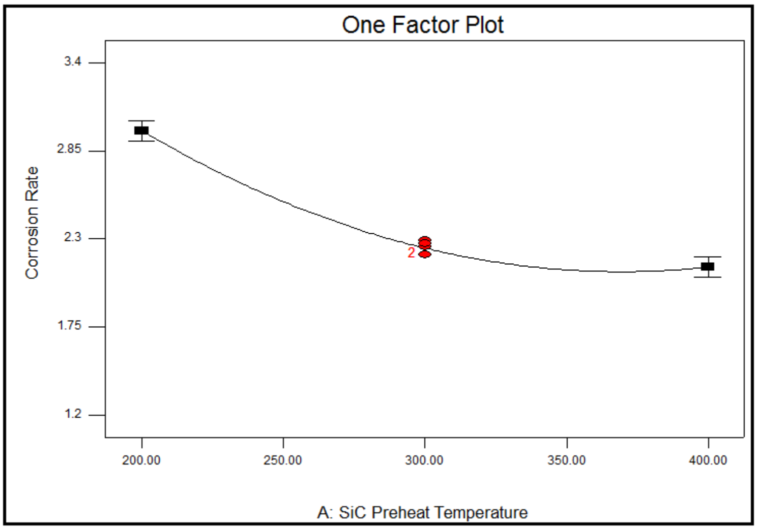

Figure 4. Effect of SiC preheat temperature on corrosion rate

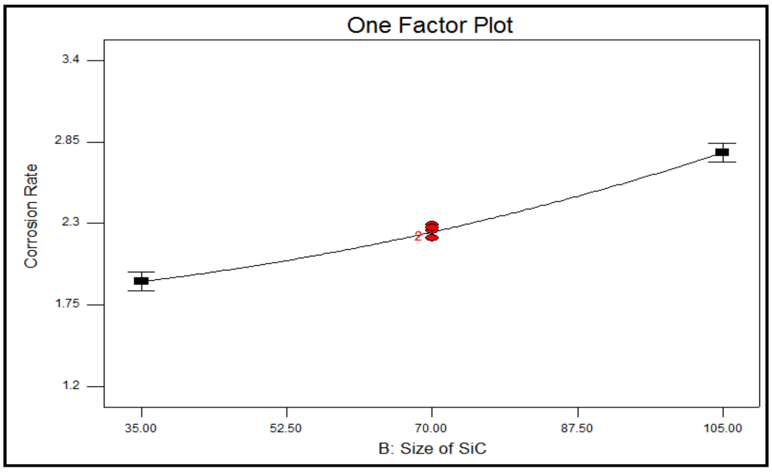

Figure 5. Effect of SiC particle size on corrosion rate

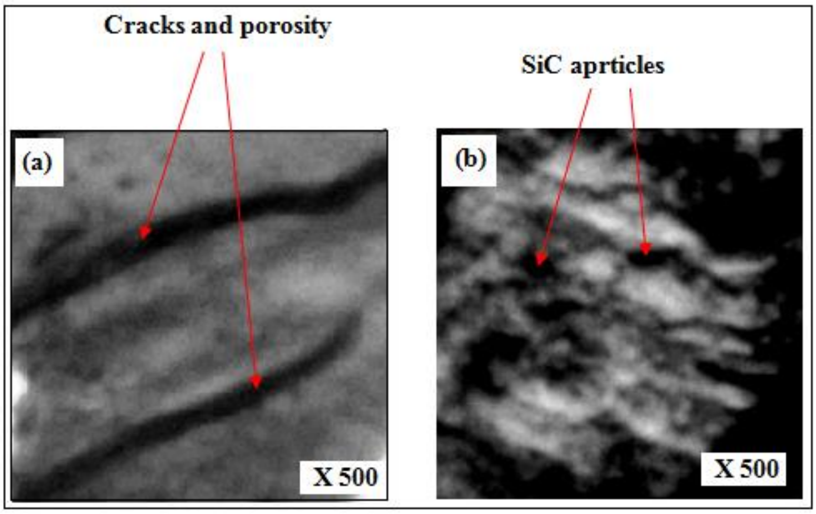

Figure 6. Microstructure image of; (a) AA6061/3 wt. % SiC composite with particle size 105 µm, (b) AA6061/3 wt. % SiC composite with particle size 35 µm

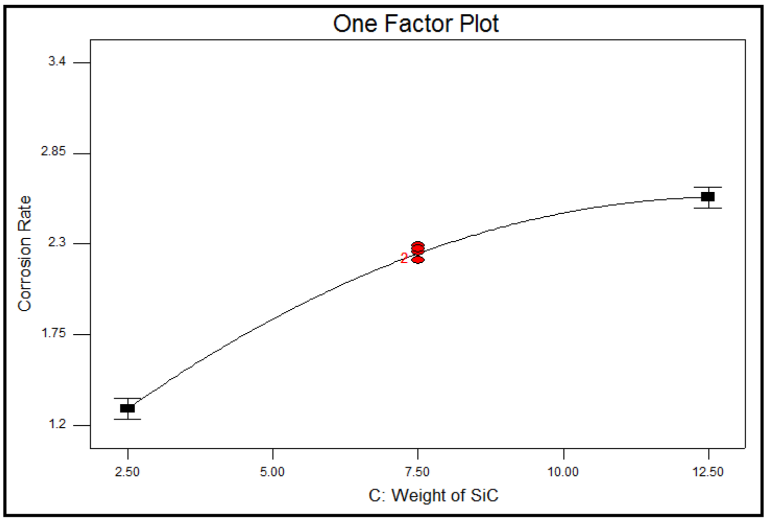

Figure 7. Effect of SiC wt. % on the corrosion rate

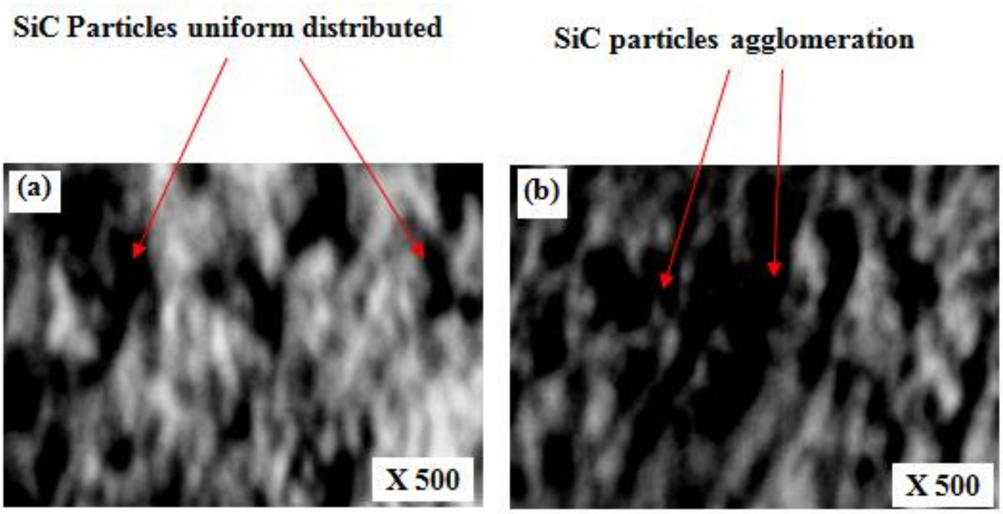

Figure 8. Microstructure image of; (a) AA6061/12.5 wt. % SiC composite, (b) AA6061/15 wt. % SiC composite

3.3. Three Dimensional Interaction of Eggshell parameters

Figure 9, Figure 10 and Figure 11 show the 3D interaction between SiC preheat temperature, SiC particle size and wt. % of SiC with corrosion rate. It can be observed from Figure 7 that with the increase in SiC temperature and size of SiC the corrosion rate decreases and increases respectively. Other interaction effects can be discussed in the same way.

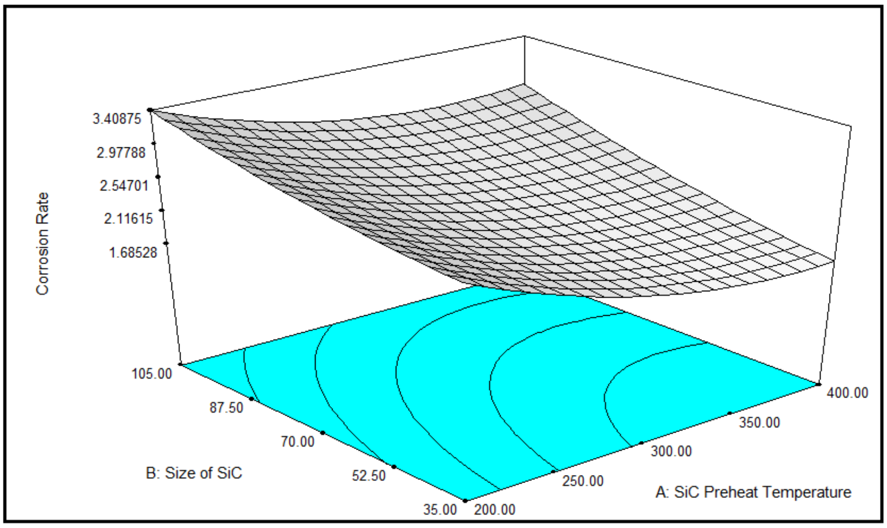

Figure 9. 3D interaction between SiC preheat temperature and SiC particle size with corrosion rate

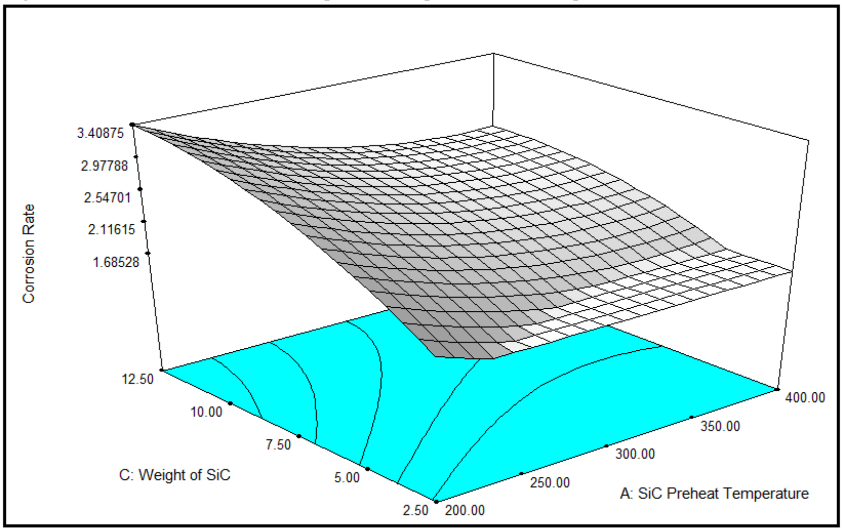

Figure 10. 3D interaction between SiC preheat temperature and wt. % of SiC with corrosion rate

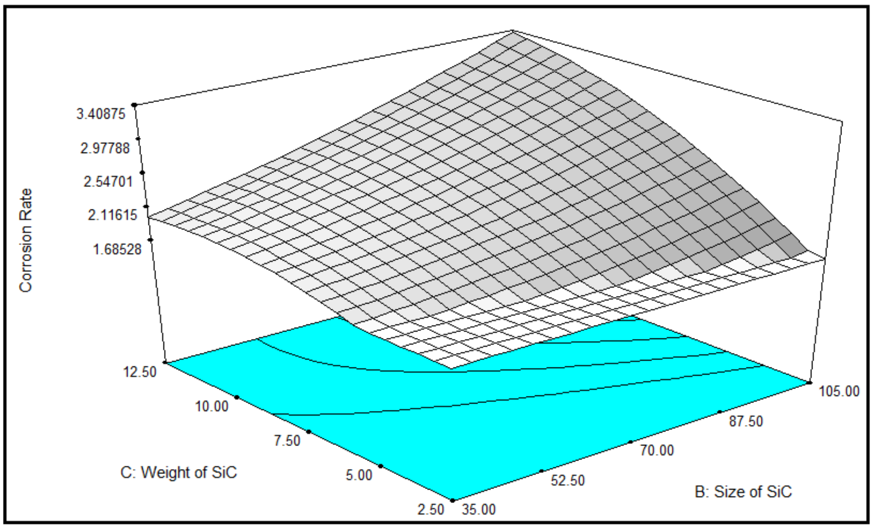

Figure 11. 3D interaction between SiC particle size and wt. % of SiC with corrosion rate

3.4. Validation of RSM Model Development

From the above analysis, optimum values of SiC particles parameters were obtained by using ramp function graph (Figure 12). Results showed that if SiC preheat temperature was kept 370.12^{0}C, size of SiC was kept 38.70 µm and weight of SiC was kept 2.94 % then minimum corrosion rate (1.16444) was obtained with desirability one.

3.5. Microstructure Analysis

From the ramp function graph, optimum SiC particles parameters were identified. At the optimum parameter, a composite sample was prepared. Microstructure of composite sample was taken to identify the distribution of SiC particles in the matrix material. Figure 13 shows the proper distribution of SiC particles in AA6061 aluminum alloy. This proper distribution is fully responsible in the enhancement of wear property, mechanical properties of the composite.

4. Conclusions

Aluminum based metal matrix composite successfully developed using SiC as reinforcement material through Electromagnetic stir casting route. Three parameters (preheat temperature, size, weight percent) of SiC were selected to reduce the corrosion rate of metal matrix composite. It was observed that by increasing the preheat temperature of SiC, corrosion rate decrease. By increasing the particle size and weight percent of SiC, corrosion rate increases. Optimum values of SiC preheat temperature, SiC particle size and wt. % of SiC were found to be 370.120C, 38.7 µm and 2.94 wt. % respectively for minimum corrosion rate 1.16444 mm/year with desirability one of metal matrix composite using Response Surface Methodology (Box-Behnken Design).

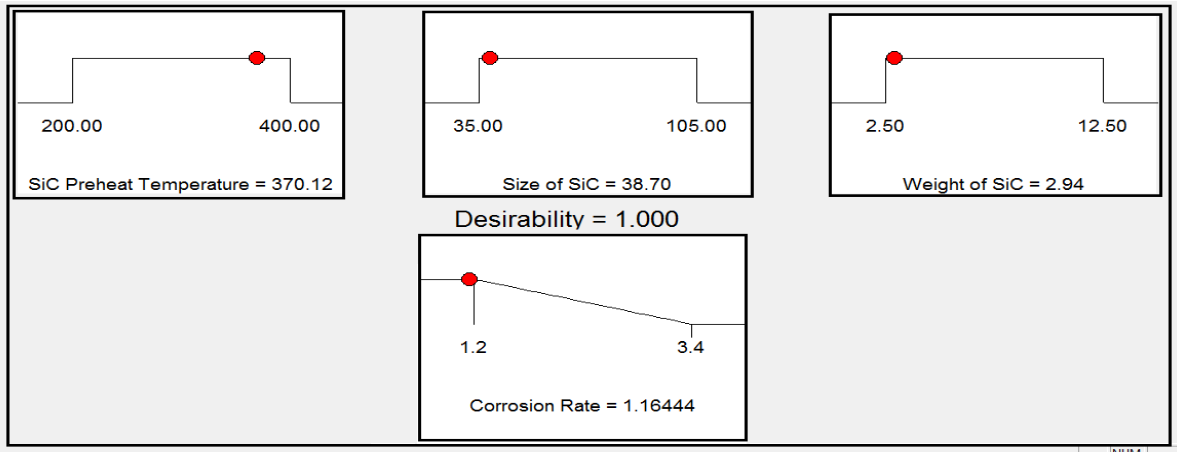

Figure 12. Ramp Function Graph

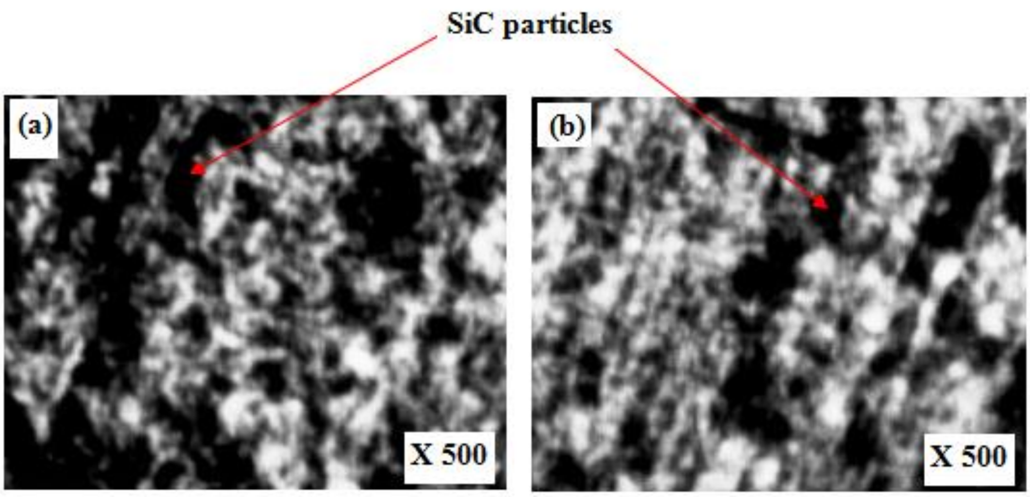

Figure 13. Microstructure of AA6061/3 wt. % SiC metal matrix composite

References

[1] C. S. Ramesh, R. Keshavamurthy, B. H. Channabasappa, S. Pramod, "Friction and wear behaviour of Ni–P coated Si_3N_4 reinforced Al 6061composites" Tribology International, Vol. 43, 2010, 623–634.

[2] D. Cree, M. Pugh, "Dry wear and friction properties of an A356/SiC foam interpenetrating phase composite" Wear Vol. 272, 2011, 88– 96.

[3] S. Gopalakrishnan, N. Murugan, "Production and wear characterization of AA 6061 matrix titanium carbide particulate reinforced composite by enhanced stir casting method" Composites: Part B , Vol. 43 ,2012,302–308.

[4] Pardeep Sharma, Dinesh Khanduna, Satpal Sharma, Parametric Study of Dry Sliding Wear of Aluminium Metal Matrix Composites by Response Surface Methodology, Material Today: Proceedings, Vol. 2, No. 4-5, 2015, 2687–2697.

[5] N. Mathan Kumar, S. Senthil Kumaran, L.A. Kumaraswamidhas, "Wear behaviour of Al 2618 alloy reinforced with Si3N4, AlN and ZrB_2 in situ composites at elevated temperatures" Alexandria Engineering Journal, Vol. 55,2016, 19–36.

[6] N.Ch. Kaushik, R. N. Rao, "Effect of applied load and grit size on wear coefficients of Al6082–SiC–Gr hybrid composites under two body abrasion" Tribology International, Vol. 103 2016,298–308.

[7] A. Pramanik, "Effects of reinforcement on wear resistance of aluminum matrix composites" Transactions of Nonferrous Metals Society of China, Vol. 26, Issue 2, 2016, 348-358.

[8] H.Y. Yue, B. Wang, X. Gao, S.L. Zhang, X.Y. Lin, L.H. Yao, E.J. Guo, "Effect of interfacial modifying on the microstructures, mechanical properties and abrasive wear properties of aluminum borate whiskers reinforced 6061Al composite" Journal of Alloys and Compounds, Vol. 692, 2017, 395–402.

[9] Hu¨lya Kac¸ar Durmus, Cevdet Meric, "Age-hardening behavior of powder metallurgy AA2014 alloy" Materials and Design, Vol. 28, 2007, 982–986.

[10] R. Senthilkumar, N. Arunkumar, M. Manzoor Hussian, "A comparative study on low cycle fatigue behaviour of nano and micro Al_2O_3 reinforced AA2014 particulate hybrid composites" Results in Physics, 2015. http://dx.doi.org/10.1016/j.rinp.2015.09.004

[11] S. Ugender, A. Kumar, A. Somi Reddy, "Experimental investigation of Tool Geometry on Mechanical Properties of Friction Welding of AA2014 Aluminium Alloy" Procedia Materials Science, Vol. 5, 2014, 824 – 831.

[12] Ramanjaneyulu Kadaganchi, Madhusudhan Reddy Gankidi, Hina Gokhale, "Optimization of process parameters of aluminum alloy AA 2014-T6 friction stir welds by response surface methodology" Defence Technology, Vol. 11, 2015, 209-219.

[13] Aziz, I., Qi, Z. and Min, X., "Corrosion Inhibition of SiCp/5A06 Aluminum Metal Matrix Composite by Cerium Conversion Treatment," Chinese Journal of Aeronautics, Vol. 22, 2009, 670-676.

[14] Zakaria, H.M., "Microstructural and corrosion behavior of Al/SiC metal matrix composites," Ain Shams Engineering Journal, Vol. 5, 2014, 831–838.

[15] Seyed Reihani, S.M., "Processing of squeeze cast Al6061–30vol% SiC composites and their characterization" Materials and Design, Vol. 27, 2006, 216–222.

[16] Feng, Y.C., Geng, L., Zheng, P.Q., Zheng, Z.Z., Wang, G.S., "Fabrication and characteristic of Al-based hybrid composite reinforced with tungsten oxide particle and aluminum borate whisker by squeeze casting", Materials and Design, Vol. 29, 2008, 2023–2026.

[17] Ankita Swati, Subrata Hait, "Greenhouse Gas Emission During Composting and Vermicomposting of Organic Wastes– A Review", Clean Soil Air Water, Vol. 46, 2018 https://doi.org/10.1002/clen.201700042.

[18] Haitao Su, Peiyong Guo, Yuxuan Zhang, Jun Deng, Meixian Wang, Yinshi Sun, Yanmei Wu, HongLei Chen, "Effects of Planting Patterns on Trace Metals in Soils Following Wet land Restoration" Clean Soil Air Water, Vol.46, 2018, https://doi.org/10.1002/clen.20170038

[19] Lina M. Shehadeh, Issam S. Jalham, "The Effect of adding Different Percentages of Manganese (Mn) and Copper (Cu) on the Mechanical Behavior of Aluminum", Jordan Journal of Mechanical and Industrial Engineering, Vol. 10, 2016, 19-26.

[20] Saadat Ali Rizvi, S.P. Tewari, "Optimization of Welding Parameters by Using Taguchi Method and Study of Fracture Mode Characterization of SS304H Welded by GMA Welding", Jordan Journal of Mechanical and Industrial Engineering, Vol. 12, 2018, 17-22.

[21] Pen Jin, Chufeng Sun, Chunyu Zhou, Lei Shi, C. Liu, "Effect of SiC particle size on structures and properties of Ni–SiC nanocomposites deposited by magnetic pulse electrodeposition technology", Ceramics International, Vol. 45, 2019, 20155-20164.

[22] Reza Zare, Hassan Sharifi, Mohammad Reza Saeri, Morteza Tayebi, "Investigating the effect of SiC particles on the physical and thermal properties of Al6061/SiCp composite", Journal of Alloys and Compounds, Vol. 801, 2019, 520-528.

[23] D. Ahmadkhaniha, F. Eriksson, P. Leisner, C. Zanella, "Effect of SiC particle size and heat-treatment on microhardness and corrosion resistance of NiP electrodeposited coatings", Journal of Alloys and Compounds, Vol. 769, 2018, 1080-1087.

[24] S.Vijayabhaskar, T. Rajmohan, T.K.Vignesh, H.Venkatakrishnan, "Effect of nano SiC particles on properties and characterization of Magnesium matrix nano composites", Materials Today: Proceedings, Vol. 16, 2019, 853-858.

[25] Pham Van Trinh, Junho Lee, Phan Ngoc Minh, Doan Dinh Phuong, Soon Hyung Hong, "Effect of oxidation of SiC particles on mechanical properties and wear behavior of SiCp/Al6061 composites", Journal of Alloys and Compounds, Vol. 769, 2018, 282-292.

[26] Łukasz Rogal, Damian Kalita, Anna Tarasek, Piotr Bobrowski, Frank Czerwinski, "Effect of SiC nano-particles on microstructure and mechanical properties of the CoCrFeMnNi high entropy alloy", Journal of Alloys and Compounds, Vol. 708, 2017, 344-352.

[27] Li Zhang, Qudong Wang, Guoping Liu, Wei Guo, Haiyan Jiang, Wenjiang Ding, "Effect of SiC particles and the particulate size on the hot deformation and processing map of AZ91 magnesium matrix composites", Materials Science and Engineering: A, Vo. 707, 2017, 315-324.

[28] Benamar Balegh, Habib Trouzine, Youcef Houmadi, "Finite Element Simulation and Prediction of Mechanical and Electrochemical Behavior on Crevice Corrosion in Sheet Pile Steel", Jordan Journal of Mechanical and Industrial Engineering, Vol. 12, 2018, 23-31.

[29] Sivaraos, K.R.Milkey, A.R.Samsudin, A.K.Dubey, P.Kidd, "Comparison between Taguchi Method and Response Surface Methodology (RSM) in Modelling CO_2 Laser Machining", Jordan Journal of Mechanical and Industrial Engineering, Vol. 8, 2014, 35-42.

JJMIE

Volume 12, Number 4, December. 2018
ISSN 1995-6665
Pages 323 - 330

Jordan Journal of Mechanical and Industrial Engineering

Three-Dimensional Stress Analysis around Rivet Holes in a Plate Subjected to Biaxial Loading

Ahmad S. Alshyyab*, Feras H. Darwish

Aeronautical Engineering Department, Jordan University of Science and Technology, Irbid, 22110, Jordan

Received 6 September. 2018

Abstract

The three-dimensional (3-D) stress domain around a countersunk hole in an isotropic plate is exclusively dictated by the dimensions of the hole and its size relative to the plate when subjected to a uniaxial load. The application of a biaxial load would certainly redistribute the stresses around the hole. In this respect, the present research aims to investigate through finite element analysis (FEA) the effect of the biaxial remote stress ratio (R) on the in-plane stress concentration factors (SCF) and the out-of-plane stress constraint factor (C) in the vicinity of a countersunk hole. A finite element code is written by using ANSYS Parametric Design Language (APDL) and is used to build the FE model, apply the boundary conditions, and perform the analysis. Based on the FE results, it is found that the SCF decreases linearly with increasing the biaxial load ratio. It is also found that the maximum value of the stress constraint factor C_max is located at the straight shank part of the hole and its magnitude is bounded by zero for plane stress and one for plane strain.

Keywords: countersunk hole, biaxial loading, finite element analysis, stress concentration factor, stress constraint factor;

1. Introduction

In industrial applications, structural components are normally joined together to form larger assemblies. Riveting is one type of the joining methods that is commonly used in aircraft and marine vessel industries. In this aspect, flush rivets are usually used when aerodynamic smoothness of the external surfaces of the structure is required. Upon their application, flush rivets form countersunk holes through the thickness of the joint. During the service life of such joints, countersunk holes act like stress risers at which micro cracks are likely to nucleate and propagate under different loading conditions. Therefore, stress and strain analyses around such holes should be carefully considered in the design process to reduce the risk of any premature failures and to enhance the strength of the joint.

Numerous studies on the SCF due to notches and holes of different geometries and under different loading conditions are reported in the literature [1]. The failure due to biaxial tensile loading of a quasi-isotropic composite plate with a circular hole was experimentally investigated [2, 3]. General stress functions were obtained to determine the SCF around cutouts in infinite composite laminates subjected to biaxial loading [4]. The upper and lower bounds of the limit loads of plates with elliptical and circular holes under uniaxial and biaxial loading conditions were estimated analytically and compared with the finite element results [5]. A general analytical solution was also obtained for the stresses and deformations around a traction free elliptic hole in an infinite elastic plate subjected to a biaxial load [6]. Experimental failure test results of riveted fuselage lap joint specimens under uniaxial and biaxial loading conditions were reported by the FAA [7]. A finite element investigation was carried out on a stiffened plate with a square cutout under various combinations of biaxial loading conditions [8]. The local stresses around a plane hole in an aluminum specimen were determined experimentally by the birefringent-plastic coating method [9]. The effect of the dimensions of a countersunk hole on the SCF in infinite plates subjected to different types of loading conditions was investigated through finite element analysis [10]. Parametric equations for the stress and strain concentration factors around a countersunk hole in an isotropic plate under uniaxial tension were formulated based on regression analysis of the finite element results [11, 12]. A modified equation for the uniaxial SCF around a countersunk hole was reported as well [13]. A new equation for the SCF around countersunk rivet holes in orthotropic laminated plates subjected to uniaxial load was introduced as a function of the hole and plate geometries and the material orthotropy [14]. The SCF around circular holes in isotropic and orthotropic plates and pressure vessels was investigated through finite element analysis [15]. Finite element investigation of the in-plane stresses generated around two adjacent countersunk holes in isotropic plates subjected to

* Corresponding author e-mail: asalshyyab@just.edu.jo.

uniaxial tension was performed [16]. The results revealed that an increase in the stress concentration occurs as the distance between the holes gets smaller. Analytical solutions for the three-dimensional stress domain around circular and non-circular holes in isotropic plates were presented. It was also shown that the out of plane stress constraint factor depends on the thickness of the plate [17]. A review study showed that there is a strong relevance between the plate thickness which affects the stress constraint factor at the notch and the brittle fracture of the plate components [18]. Three-dimensional finite element study was performed to investigate the elastic notch root fields for plates with different thicknesses and different notch configurations [19]. The effect of the plate thickness and the notch configuration on the SCF, the stress constraint factor and the strain energy density were studied through an analytical solution of the stress domain around the notch [20]. The finite element method was used to study the thorough thickness variation of the SCF along the wall of an elliptic hole in an isotropic plate under tension [21].

The main objective of this research is to study the combined effect of the biaxial stress ratio and the hole configuration on the in-plane SCF and the out-of-plane stress constraint factor at the countersunk hole in an isotropic plate.

2. The geometric model and the boundary conditions

Fig. 1 presents a 3-D illustration of the geometric model of a plate made of an isotropic and homogeneous material and accommodates a centered countersunk hole. The Cartesian x-y-z coordinates are used as a reference frame located at the bottom center of the hole. The plate has a length of 2L, a width of 2w and a thickness t. The straight shank (SS) part of the hole has a radius and thickness of r and b respectively. The largest radius of the countersunk hole r_c is determined by the sinking depth C_s and the countersink angle θ_c. Biaxial remote tension stresses σ_{xo} and σ_{yo} are applied at the boundaries of the plate as shown.

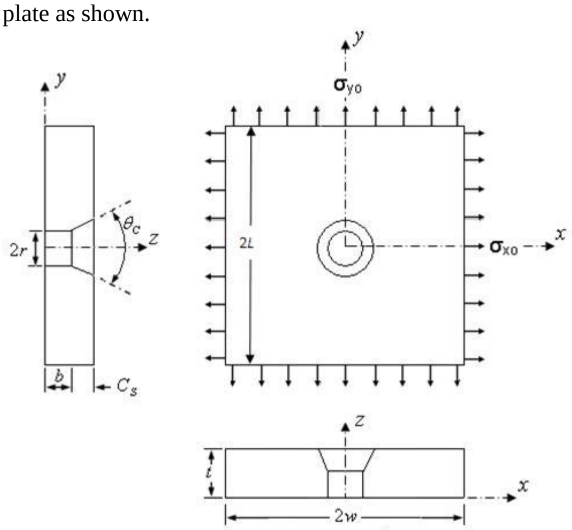

Figure 1. The geometry and boundary conditions of a plate with a centered countersunk hole

Due to the symmetry in the plate's geometry and in the applied stresses across the x- and y-axes, only one quarter of the configuration will be considered for the FE modeling to reduce the number of generated nodes and elements and accordingly to reduce the analysis running time. Fig. 2 shows the split lines and one quarter of the plate. The new generated boundary conditions at the cut line (lines of symmetry) restrain the displacement in the x-direction at the surface at x=0 and the displacement in the y-direction at the surface at y=0. To suppress the rigid mode of body motion in the z-direction, the z-displacement of a one node located at $z = x = 0$ and $y = r$ was restrained.

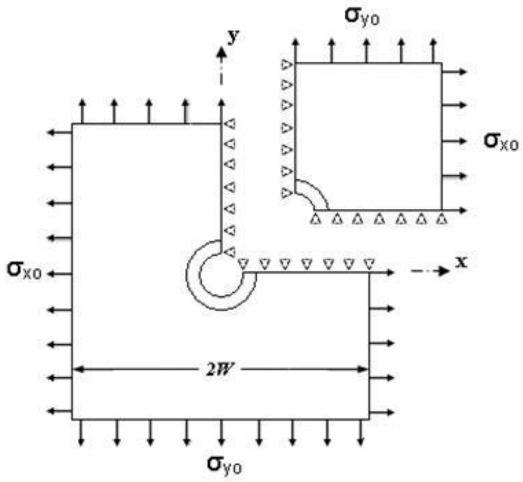

Figure 2. One quarter of the plate and the hole and the resulting boundary conditions

3. Finite Element Modeling

A commercial FEA code, ANSYS Version 13, was used to perform the analysis of the problem. In this respect, APDL batch code was written to generate the FE model, apply the boundary conditions, conduct the solution, and postprocess the results. Three-dimensional solid45 element type was used to generate -through isoperimetric mapping option- the elemental mesh domains for the volumes of the model. Mesh gradation and mesh refinement studies were carefully conducted to generate fine mesh domains at the regions of high stress gradients. The two studies were based on examining the convergence of the solution for different mesh upgrades to assure the accuracy of the results. Fig. 3 illustrates the typical mesh used in the analysis. The number of mesh elements and nodes were 44100 and 48564, respectively.

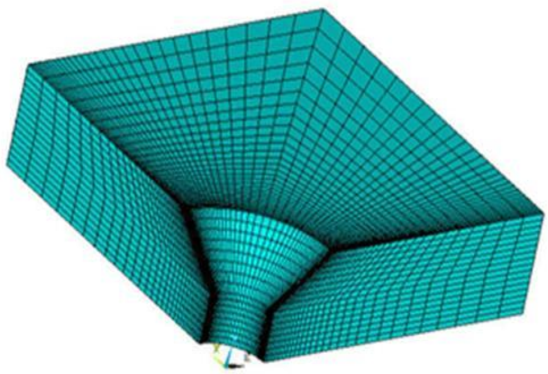

Figure 3. Typical mesh idealization used in the analysis.

In another aspect, as the region around the countersunk hole is expected to experience elevated stresses upon load application, the FE code is designed to save the desired stress results in this region along five paths of interest. As shown in Fig. 4, the five paths are: (i) path ABC formed by the intersection of the hole bore with the *x-z* plane at $y = 0$, (ii) path *DEF* formed by the intersection of the hole bore with the *y-z* plane at $x = 0$, (iii) circular path *CF* of radius r_c formed by the intersection of the hole bore with the *x-y* plane at $z = t$ and (iv, v) two circular paths *AD* and *BE* formed by the intersections of the hole bore with *x-y* plane at $z = 0$ and $z = b$, respectively.

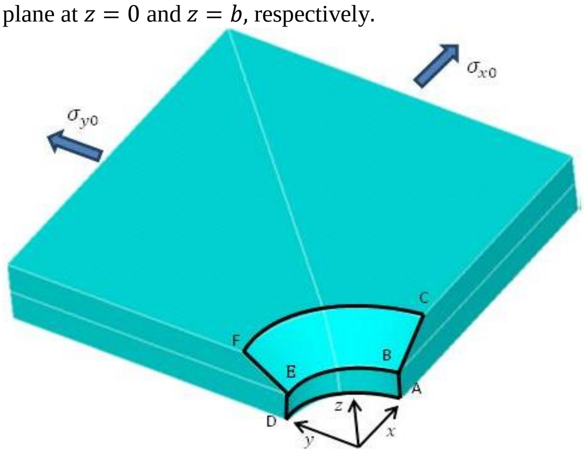

Figure 4. Paths of interest along the edges of the countersunk hole

4. Stress concentration and constraint factors' equations

The SCF is normally defined as the ratio of an elevated local stress due to stress risers to the nominal applied remote stress σ_o. As shown previously in Fig. 1, the plate under consideration is subject to biaxial remote stresses σ_{xo} and σ_{yo} in the *x*- and *y*-directions respectively, for which, the biaxial stress ratio *R* is defined as,

$$R = \frac{\sigma_{xo}}{\sigma_{yo}} \quad (1)$$

Accordingly, in this research, the directional pointwise normal SCF $k_i(z)$ along paths *ABC* and *EDF* are defined in terms of the corresponding local normal stresses $\sigma_i(z)$ and the *y*-direction applied stress σ_{yo}as,

$$k_i(z) = \frac{\sigma_i(z)}{\sigma_{oy}}, \quad i = x, y, z \quad (2)$$

In the above equation, *z* determines a point location through the thickness of the plate at paths *ABC* or *EDF*. Similarly, the SCF at any point on the circular paths *AE*, *BD*, and *CF* is defined as,

$$k_i(\phi) = \frac{\sigma_i(\phi)}{\sigma_{yo}}, \quad i = x, y, z, \quad (3)$$

where the angle ϕ defines the angular position of any point along a specific circular path and it is measured from the *y*-axis as follows:

$$\phi = tan^{-1}\left(\frac{x}{y}\right) \quad (4)$$

In addition, Von Misses stress concentration factor is defined as,

$$k_v(j) = \frac{\sigma_v(j)}{\sigma_{yo}}, \quad (j = z, \phi) \quad (5)$$

The maximum value of k_i along a certain path of interest specifies the stress concentration factor $k_{i,t}$ for that path. Consequently, the maximum of all $k_{i,t}$'s of the prescribed five paths is considered the stress concentration factor k_t of the hole.

The stress constraint factor $C(z)$ is in the 3-D stress analysis of solid structures characterizes the influence of the out-of-plane stress σ_z in a tri-axial stress state and contributes to the fracture mechanics analysis. This factor is defined as,

$$C(z) = \frac{\sigma_z(z)}{v[\sigma_x(z)+\sigma_y(z)]} \quad (6)$$

According to the above definition, the value of $C(z)$ ranges between 0 and 1 for plane stress and plane strain states respectively.

5. Finite element results and discussion

Tremendous number of FE runs was performed to accommodate the results of a wide range of the geometric parameters $(W/r,\ t/r,\ C_s/t)$ and the biaxial loading ratio (R). For this purpose, the ratio of the thickness of the plate to the SS bore radius t/r was varied from 0.1 (plane stress) to 12 (plane strain), the countersink depth to thickness ratio c_s/t was varied from 0 (cylindrical hole) to 1 (knife edge hole) with an increment of 0.05. Similarly, the load ratio R was varied from 0 (uniaxial) to 1 (symmetric biaxial) with an increment of 0.25. The plate was considered square ($W = L$) with a width to bore radius ratio W/r less than 15 (finite size) or greater than 15 (infinite plate) to eliminate the size effect of the plate on the results. Finally, the countersink angle θ_c was maintained constant at the common industrial value of 100°. For each geometric and loading configuration the automated APDL ANSYS batch code defined the five paths of the countersunk hole and stored for each path the three normal stresses, σ_x , σ_y and σ_z and Von Misses stress σ_v.

6. Path ABC

Fig. 5 presents the effect of the biaxial load ratio *R* on the local SCF $k_y(z)$ for an infinite plate $(w/r = 30)$ of thickness defined by the parametric ratio $t/r = 0.1$, and for countersunk holes of bound values $c_s/t = 0$ (regular hole) and $c_s/t = 1$ (knife edge hole). It is shown in

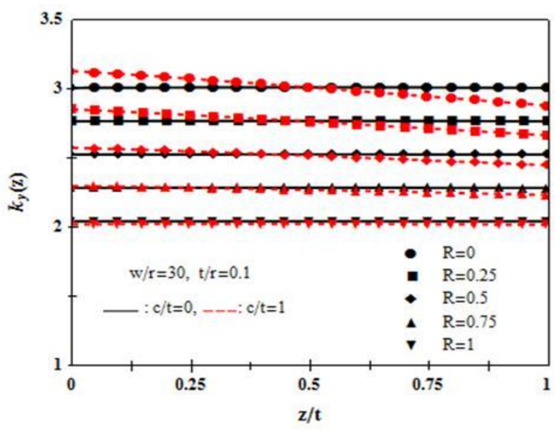

Figure 5. Effect of load ratio R and countersink ratio c_s/t on $k_y(z)$ along path ABC of plane stress problem$t/r = 0.1$

Fig. 5 that for the regular hole, the value of $k_{y,t}$ is found equal to 3 when $R = 0$ and decreases monotonically to 2 as R increases to one which agrees with the theory of elasticity for plane stress state. It is also shown that $k_y(z)$ of the knife edge hole has insignificantly varied from that of the regular hole with $k_{y,t}$ located at the knife edge of the hole. The inverse proportionality between $k_y(z)$ and R can be explained qualitatively as illustrated in Fig. 6, when $R = 0$, the resultant force (F) of the force lines interrupted by the hole is reacted in the y-direction at point A by an equivalent resultant force (F_A) and moment (M_A) in order to maintain equilibrium and compatibility of the plate. On the other hand, by increasing the biaxial load ratio R, the reaction moment of the force lines in the x-direction would counter acts and partially cancels the moment of the main load at point A. Accordingly, when $R = 1$, the reaction moments due to the lever action are cancelled completely, hence, the value of $k_{i,t}$ is minimum.

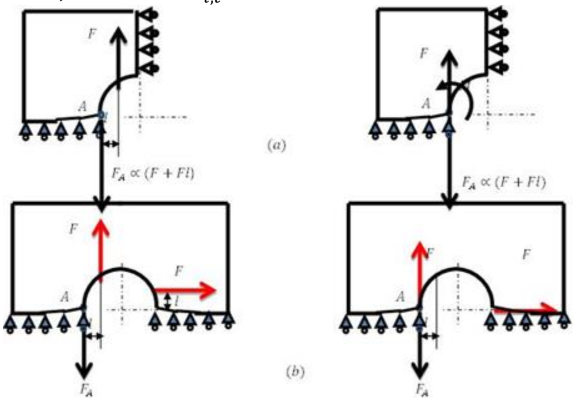

Figure 6. a) $R = 0$, and b) $R = 1$

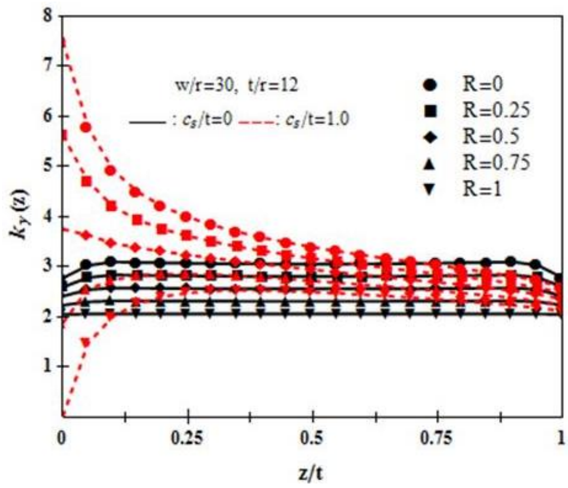

Figure 7. Effect of load ratio R and countersink ratio c_s/t, on $k_y(z)$ along path ABC of plane strain problem $t/r = 12$

Fig. 7 presents the effect or R on $k_y(z)$ for a thick plate ($t/r = 12$) for two cases, $c_s/t = 0$ and $c_s/t = 1$. When $c_s/t = 0$, the results are pretty much similar to those of Fig. 5 with a slight difference at the edges of the hole which reflects the plane strain effect on the stress state. However, for $c_s/t = 1$, the trend of $k_y(z)$ has dramatically changed compared to that of Fig. 5 while maintaining the inverse relationship between R and $k_y(z)$. Here it is observed that the effect of R on the SCF is more significant at the sharp edge side of the hole at z/t=0 than on the other side at z/t=1. It is also found that the SCF at the sharp edge switches from maximum value when R = 0, 0.25 and 0.5 to a minimum value when R = 0.75 and 1, and that it equals to zero at R=1. This result is quite surprising, but it can be referred to the fact that as we increase the thickness of the plate the plane strain effect and hence the transverse stress σ_z which compressive in our case become more pronounced. From mechanics point of view, the resultant force of the transverse stresses in the vicinity of the knife edge hole when R=1 will create compressive moment stress at the sharp edge of the hole that counter acts the applied tension stress and therefore the SCF would be reduced. Fig. 8 presents how the SCF decreases at the sharp edge of the knife edge hole (z/t=0) as t/r increases and for R=1.

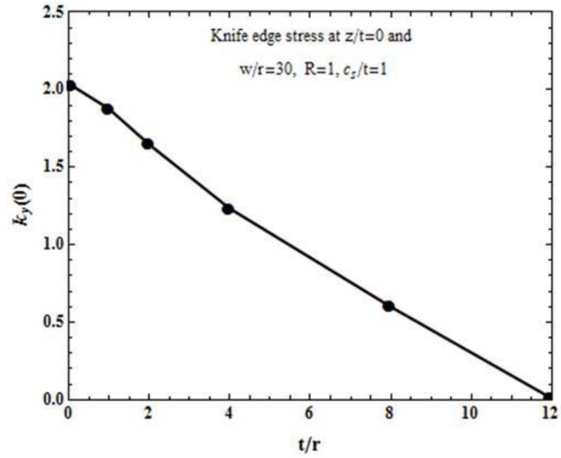

Figure 8. The values of the stress concentration at $z/t = 0$ and $R = 1$.

In Figs 9 and 10 different values of c_s/t (0.25. 0.5, 0.75) are considered to examine the distributions of $k_y(z)$ and $k_v(z)$ respectively for countersunk holes in infinite plates with $t/r = 12$. Both Figs show similar trends with maximum values of $k_v(z)$ and $k_v(z)$ at the

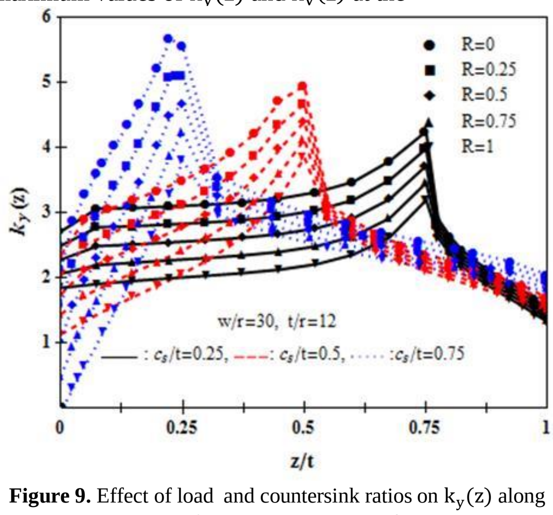

Figure 9. Effect of load and countersink ratios on $k_y(z)$ along path ABC of plane strain problem$t/r = 12$.

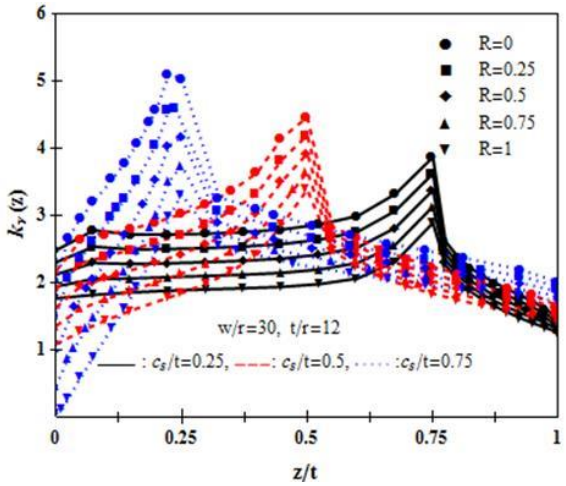

Figure 10. Effect of load ratio R on Von misses stress concentration factor $k_v(z)$ along path ABC, $t/r = 12$

countersink edge($z/t = b/t$). Figs. 11 and 12 present the effect of the load ratio R on $k_y(z)$ of an infinite plate of thickness ratio $t/r = 1$ for different values of c_s/t.

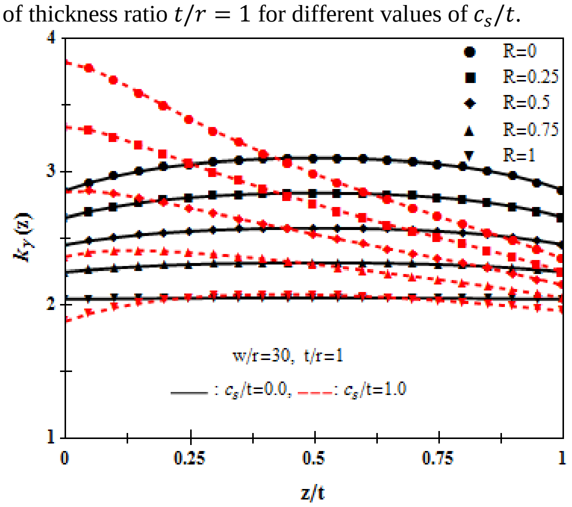

Figure 11. Effect of load ratio R on $k_y(z)$ along path ABC, $t/r = 1$

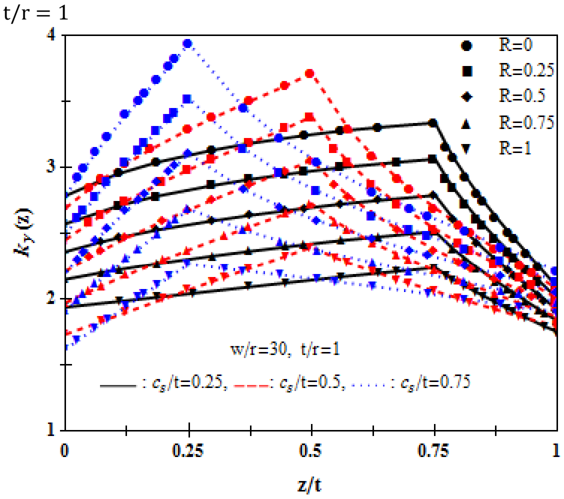

Figure 12. Effect of load ratio R on $k_y(z)$ along path ABC, $t/r = 1$

Figs 13 and 14 present the variations of $k_{y,t}$ and $k_{v,t}$ respectively with increasing the loading ratio R for a wide range of plate thicknesses (t/r=0.1-2.4) and for finite and infinite width plates

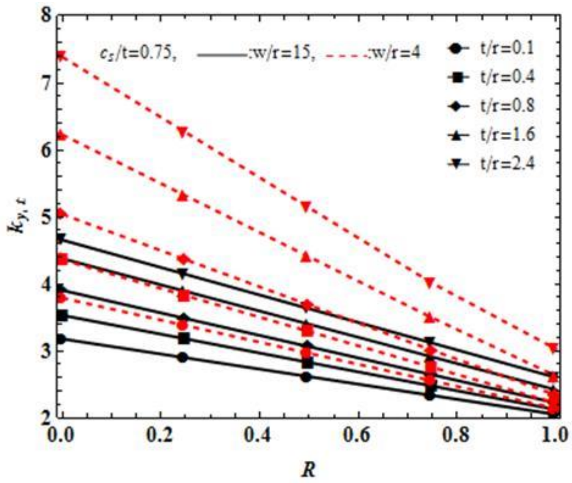

Figure 13. Effect of load ratio R on $k_{y,t}$ for two different bore radius (w/r) and various values of thicknesses (t/r)

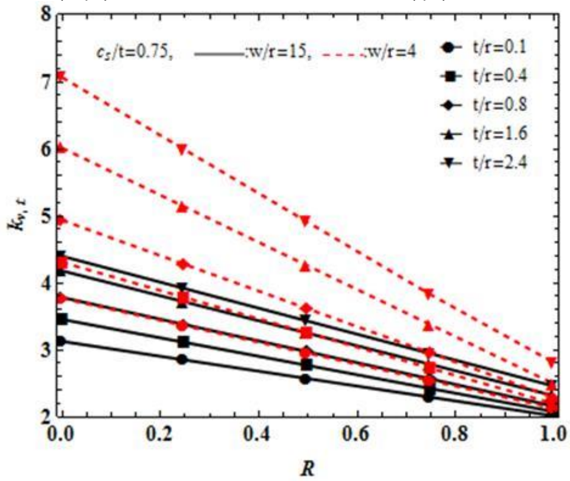

Figure 14. Effect of load ratio R on $k_{v,t}$ for two different bore radius (w/r) and various values of thicknesses (t/r).

(w/r= 4 and 15 respectively). The two **Figs** show that the maximum SCF ($k_{y,t}$or $k_{v,t}$) decreases with increasing R, with increasing the plate's width, and with decreasing the plate's thickness.

The transverse variation of the stress constraint factor $C(z)$ which is expressed in Eq. (6) is shown in **Figs** 15 for two cases; a regular hole ($c_s/t = 0$) and a knife edge hole ($c_s/t = 1$). It is shown that for $c_s/t = 0$, $C(z)$ decreases monotonically with increasing R. This relationship is linked to the faster rate of decreasing σ_z (in the numerator of $C(z)$) than the sum of σ_x and σ_y (in the denominator of $C(z)$) around the hole with increasing R. On the other hand, for $c_s/t = 1$, the relationship is reversed such that $C(z)$ increases with increasing R. This reversal in the relationship between $C(z)$ and R is referred to the tapered geometry of the knife edge hole which in turns affects the tri-axial stress distributions around the hole. As a result, σ_z tends to increase with increasing R and therefore the ratio $C(z)$ increases. Fig. 16 shows the effect of R on σ_z and $\nu(\sigma_x + \sigma_y)$ for both regular and knife edge holes. It is also shown in Fig. 15 that the values of $C(z)$ of a knife-edge hole are smaller than those of a regular hole. For countersunk holes with intermediate values of c_s/t (0.25, 0.5, 0.75), the transverse distribution of $C(z)$ at different R values is shown in Fig. 17. It is shown that the relationship between $C(z)$ and R within the straight shank and sinking portions of the hole is similar to that of the

 © 2018 Jordan Journal of Mechanical and Industrial Engineering. All rights reserved - Volume 12, Number 4 (ISSN 1995-6665)

regular hole and the knife edge hole respectively. The maximum value of $C(z)$ occurs just below the countersunk root in the straight shank part.

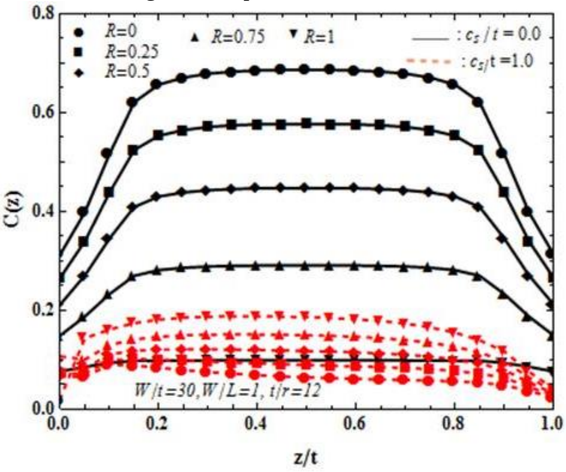

Figure 15. Effect of load ratio R on C(z) for two values of (C_s/t)

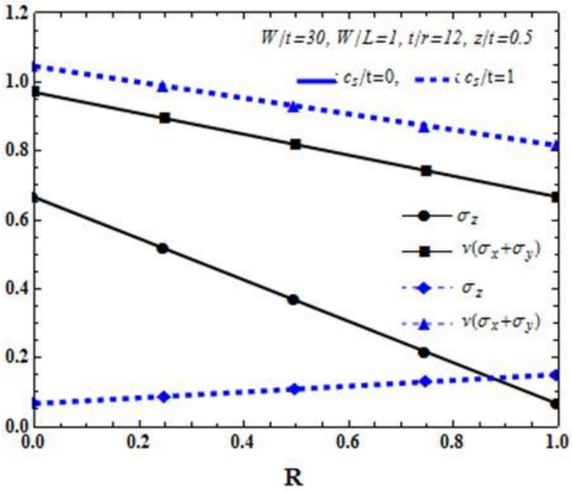

Figure 16. Effect of the biaxial load ratio R on σ_z and ν ($\sigma_x + \sigma_y$)

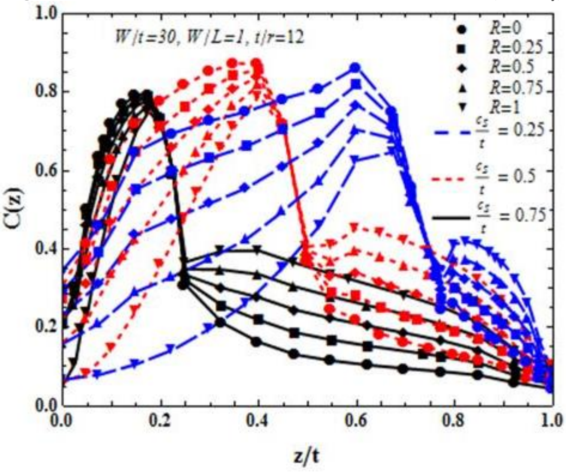

Figure 17. Effect of load ratio R on C(z) for three values of (C_s/t)

Fig. 18 shows that the maximum stress constraint factor C_{max} increases when the thickness of the plate (t/r) increases, and that it approaches zero for very thin plates i.e. $t/r = 0.1$. It is also noticed that C_{max} is greater in value in countersunk holes with c_s/t falling in general between 0.25 and 0.5 than the other hole configurations.

Due to geometrical symmetry of the plate and the hole, any further investigations of the stress concentration factors and the stress constraint factor along the path *DEF* would be redundant.

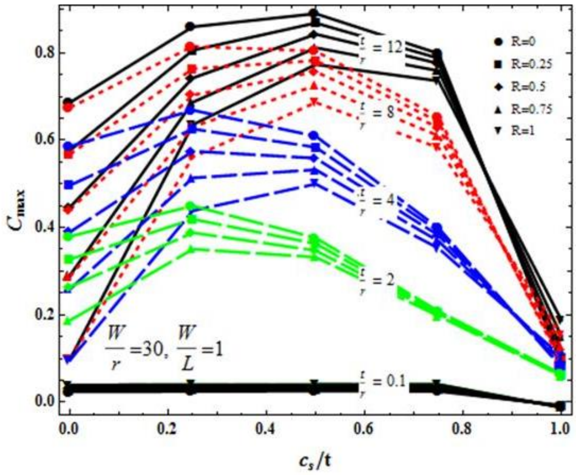

Figure 18. Effect of load ratio R on C_{max}

7. Paths AD, BE and CF

The circular paths *AD*, *BE* and *CF* are defined at the intersections of the countersunk hole surface with the x-y planes at z=0, $z = b$, and $z = t$, respectively. Figs 19-21 show the circumferential distribution of the local stress concentration factors $k_y(\phi)$ along path *BE* for countersunk holes with (c_s/t =0.25, 0.5, 0.75), along path *AD* for regular and knife edge holes, and along path *CF* for regular and knife edge holes respectively in infinite and thick plates at different *R* values.

From Figs. 19 and 21, it is found that the angular position of the maximum stress concentration factor is at $\phi = \pi/2$. It is also noticed that, in general, for each value of (c_s/t) there is a common deflection point (or angle) for the set of curves of different *R* values below which the relation between k_y and *R* is in directly proportionality and beyond which the relation gets reversed.

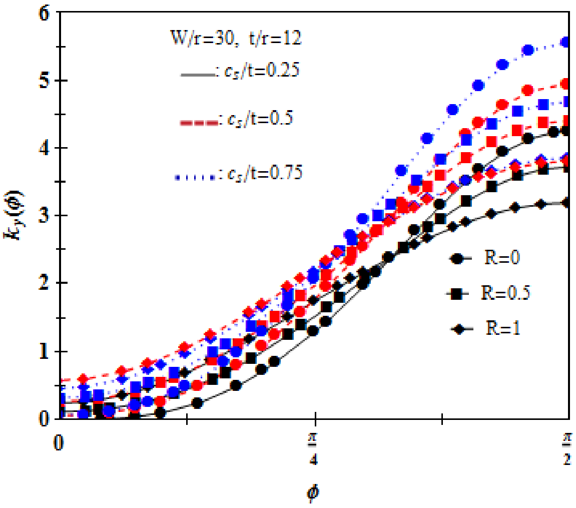

Figure 19. Effect of load ratio R on $k_y(z)$ along path BE, $t/r = 12$.

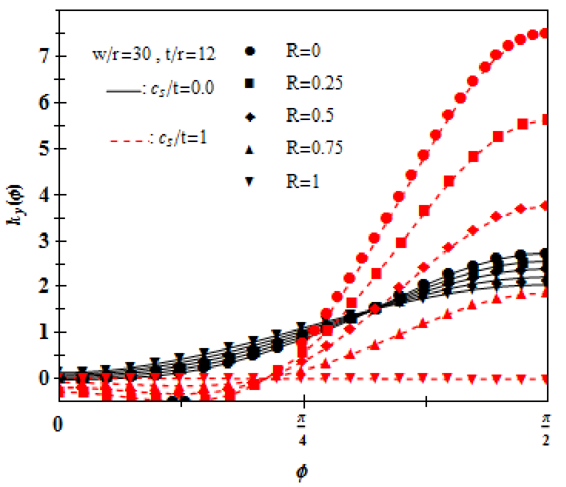

Figure 20. Effect of load ratio R on $k_y(z)$ along path AD, $t/r = 12$.

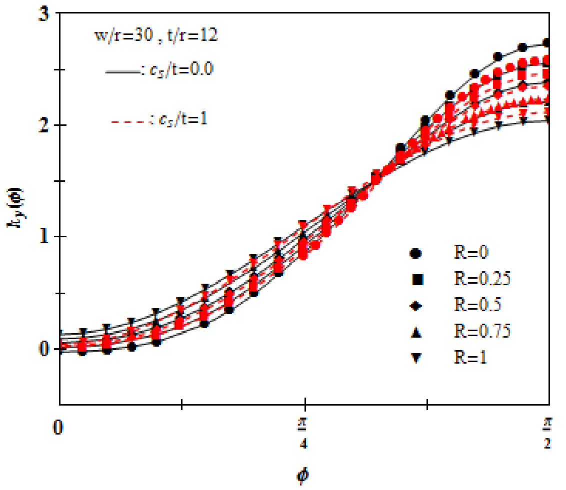

Figure 21. Effect of load ratio R on $k_y(z)$ along path CF, $t/r = 12$.

8. Conclusion

The effect of the biaxial loading ratio R on the magnitudes and locations of the local and global stress concentration factors k_i and $k_{i,t}$, $(i = y, v)$ were investigated along the prescribed five paths of the countersunk hole. As may be anticipated, the increase of the biaxial loading ratio R was found to decrease monotonically the magnitude of k_i, yet magnitudes of $k_{i,t}$ have decreased linearly with increasing R for all considered values of c_s/t and t/r. In addition, the location of the maximum stress concentration k_t was found to be at the root of the countersunk hole at $z = b$ and at an angular location $\phi = \pi/2$. It was also found that at the sharp corner of a knife edge hole the SCF can drop from a maximum value for thin plate (plane stress) when subjected to a uniaxial load to a minimum value that can reach zero for a very thick plate (plane strain) under symmetric biaxial loading.

The study was further extended to examine the influence of the biaxial loading ratio R and the hole geometry on the generated transverse stress σ_z represented by the dimensionless stress constraint factor surrounding the hole. It was found that the magnitude of the local stress constraint factor $C(z)$ attained a severe jump at the root of the countersunk hole (z=b), and its maximum value C_{max} occurred always at the straight shank part of the hole. The maximum stress constraint factor C_{max} was also found a function of c_s/t where in general it attains its maximum value when c_s/t falls between 0.25 and 0.5. Finally, the relationship between the stress constrain factor and the load ratio was found to be in direct proportionality in straight regular holes and that it got reversed in knife edge holes.

References

[1] Pilkey, W.D., Pilkey, D.F., 2008. Peterson's Stress Concentration Factors, third ed. John Wiley & Sons, New York.

[2] Isaac M. Daniel, 1980. Behavior of graphite/epoxy plates with holes under biaxial loading. Experimental Mechanics. 20 (1), 1-8.

[3] Isaac M. Daniel, 1982. Biaxial testing of $[O_2/\pm45]_s$ graphite/epoxy plates with holes. Experimental Mechanics. 22 (5), 188-195.

[4] Dharmendra S Sharma, 2011. Stress concentration around circular/elliptical/triangular cutouts in infinite composite plate. Proceedings of the World Congress on Engineering Vol III WCE, London, U.K.

[5] G.H. Rahimi, R.A. Alashti, 2005. Limit load analyses of plates with a hole under in-plane loads. Scientia Iranica, 12 (4), 442-454.

[6] Xin-Lin Gao, 1996. A general solution of an infinite elastic plate with an elliptic hole under biaxial loading. The International Journal of Pressure Vessels and Piping. 67 (1), 95-104.

[7] H. Vlieger, H.H. Ottens, 1998. Uniaxial and biaxial tests on riveted fuselage lap joint specimens. FAA Final Report, DOT/FAA/AR-98/33.

[8] A.K.L. Srivastava, P.K. Datta, 2006. Elastic stability of square stiffened plates with cutouts under biaxial loading. Int. J. of Applied Mechanics and Engineering, 11 (2), 421-433.

[9] Wharely, R. E., 1965. Stress-concentration factors for countersunk holes. Experimental Mechanics, 5 (8), 257-261.

[10] Shivakumar, K.N., Newman, J.C., 1992. Stress concentrations for straight-shank and countersunk holes in plates subjected to tension, bending, and pin loading. NASA Technical Paper 3192.

[11] Shivakumar, K.N., Bhargava, A., Hamoush, S., 2007. A general equation for stress concentration in countersunk holes. CMC. 6 (2), 71-92.

[12] Bhargava, A., Shivakumar, K.N., 2008. A three dimensional strain concentration equation for countersunk holes. Journal of Strain Analysis for Engineering Design. 43 (2), 75-85.

[13] Darwish, F., Gharaibeh, M., Tashtoush, G., 2012. A modified equation for the stress concentration factor in countersunk holes. European Journal of Mechanics – A/Solids, 36, 94-103.

[14] Feras Darwish, Ghassan Tashtoush, Mohammad Gharaibeh, 2013. Stress concentration analysis for countersunk rivet holes in orthotropic plates. European Journal of Mechanics – A/Solids, 37, 69-78.

[15] Wu, H., Mu, B., 2003. On stress concentrations for isotropic/orthotropic plates and cylinders with a circular hole. Composites: Part B. 34 (2), 127-134.

[16] Feras Darwish, Lubna Al-Nasser, Omar Al-Araidah, 2013. Tensile stress concentration in plates with double countersunk rivet holes. Int. J. Design Engineering, Accepted in-press.

[17] Kotousov, A., Wang, C.H., 2002. Three-dimensional stress constraint in an elastic plate with a notch. International Journal of Solids and Structures. 77, 1665-1681.

[18] Kotousov, A., Lazzarin, P., Berto, F., Harding, S., 2010. Effect of the thickness on elastic deformation and quasi-

brittle fracture of plate components. Engineering Fracture Mechanics. 39, 4311-4326.

[19] Li, .Z., Guo, W., Kuang, Z., 2000. Three-dimensional elastic stress fields near notches in finite thickness plates. International Journal of Solids and Structures. 37, 7617-7631.

[20] Berto, F., Lazzarin, P., Wang, C.H., 2004. Three-dimensional linear elastic distributions of stress and strain energy density ahead of V-shaped notches in plates of arbitrary thickness. International Journal of Fracture. 127, 265-282.

[21] She, C., Guo, W., 2007. Three-dimensional stress concentrations at elliptic holes in elastic isotropic plates subjected to tensile stress. International Journal of Fatigue. 29, 330-335.

المملكة الأردنية الهاشمية

الجامعة الهاشمية

المجلة الأردنية
للهندسة الميكانيكية والصناعية

JJMIE

مجلة علمية عالمية محكمة

تصدر بدعم من صندوق البحث العلمي

http://jjmie.hu.edu.jo/

ISSN 1995-6665

المجلة الأردنية للهندسة الميكانيكية والصناعية

المجلة الأردنية للهندسة الميكانيكية والصناعية: مجلة علمية عالمية محكمة تصدرعن الجامعة الهاشمية بالتعاون مع صندوق دعم البحث العلمي والابتكار- وزارة التعليم العالي والبحث العلمي في الأردن.

ترسل البحوث إلى العنوان التالي

رئيس تحرير المجلة الأردنية للهندسة الميكانيكية و الصناعية

الجامعة الهاشمية
كلية الهندسة
قسم الهندسة الميكانيكية
الزرقاء - الأردن

هاتف : 3903333 5 00962 فرعي 4147

Email: jjmie@hu.edu.jo

Website: www.jjmie.hu.edu.jo